# MODELLING OF MULTI-COMPONENT FUEL DROPLETS HEATING AND EVAPORATION

**AHMED ELSAID YOUSSEF MOHAMMED ELWARDANY**

**PHD** **2012**

# MODELLING OF MULTI-COMPONENT FUEL DROPLETS HEATING AND EVAPORATION

**AHMED ELSAID YOUSSEF MOHAMMED ELWARDANY**

A thesis submitted in partial fulfilment of the
requirements of the University of Brighton
for the degree of Doctor of Philosophy

**January 2012**

**Sir Harry Ricardo Laboratories**
**School of Computing, Engineering and Mathematics**
**University of Brighton**
**UK**

## Abstract

The results of numerical and experimental studies of heating and evaporation of monodisperse fuel droplets in an ambient air of fixed temperature and atmospheric pressure are reported. The numerical model is based on the Effective Thermal Conductivity (ETC) model and the analytical solution to the heat conduction equation inside droplets. It is pointed out that the interactions between droplets lead to noticeable reduction of their heating in the case of ethanol, 3-pentanone, n-heptane, n-decane and n-dodecane droplets, and reduction of their cooling in the case of acetone. A simplified model for bi-component droplet heating and evaporation is developed. The predicted time evolution of the average temperatures is shown to be reasonably close to the measured one (ethanol/acetone mixture). The above-mentioned simplified model is generalised to take into account the coupling between droplets and the ambient gas. The model is applied to the analysis of the experimentally observed heating and evaporation of monodispersed n-decane/3-pentanone mixture droplets at atmospheric pressure. It is pointed out that the number of terms in the series in the expressions for droplet temperature and species mass fractions can be reduced to just three, with possible errors less than about 0.5%. In this case, the model can be recommended for implementation into CFD codes. The simplified model for bi-component droplet heating and evaporation, based on the analytical solutions to the heat transfer and species diffusion equations, is generalised to take into account the effect of the moving boundary and its predictions are compared with those of the model based on the numerical solutions to the heat transfer and species diffusion equations for both moving and stationary boundary conditions. A new model for heating and evaporation of complex multi-component hydrocarbons fuel droplets is developed and applied to Diesel and gasoline fuels. In contrast to all previous models for multi-component fuel droplets with large number of components, the new model takes into account the effects of thermal diffusion and diffusion of components within the droplets.

# Contents

## List of figures

## List of tables

## Acknowledgements

I would like to thank my supervisors Prof. S. S. Sazhin and Prof. M. R. Heikal for their helpful assistance and support throughout this work.

I wish to express my gratitude to Dr. P. A. Krutitskii, Dr. E. M. Sazhina, Dr. Tarsisius Kristyadi, Dr. V. Deprédurand, Dr. G. Castanet and Prof. F. Lemoine for their contributions, support and help.

I acknowledge the European Regional Development Fund Franco-British INTERREG IVA (Project C5, Reference 4005) for the financial support of this project.

Finally, I would like to thank my family for their constant affection and support.

## Declaration

I declare that the research contained in this thesis, unless otherwise formally indicated within the text, is the original work of the author. The thesis has not been previously submitted to this or any other university for a degree, and does not incorporate any material already submitted for a degree.

Signed

Date

# Nomenclature

## English Symbols

| | |
|---|---|
| $a$ | Constant introduced in Eq. (2.4) or parameter introduced in Eqs. (6.16) and (6.17) |
| $A$ | Parameter introduced in Eq. (6.12) |
| $A_k$, $B_k$ | Parameters defined by Eqs. (6.24) |
| $A_\rho$, $B_\rho$, $C_\rho$ | Parameters defined by Eqs. (6.19) |
| $b$ | Constant introduced in Eq. (2.4), parameter introduced in Eqs. (6.16) and (6.17) or parameter defined by Eq. (6.21) |
| $B$ | Parameter introduced in Eq. (6.12) |
| $B_M$ | Spalding mass transfer number |
| $B_T$ | Spalding heat transfer number |
| $c$ | Specific heat capacity [W/(kg.K)] or parameter introduced in Eqs. (6.16) and (6.17) |
| $C$ | Distance parameter, $C = d/(2 \times R_d)$ or parameter introduced in Eq. (6.12) |
| $C_F$ | Coefficient of friction drag defined by Eq. (2.16) |
| $C_m$ | Constant defined by Eq. (6.6) |
| $d$ | Distance between droplets [m] or parameter introduced in Eqs. (6.16) and (6.17) |
| $D$ | Diameter [m] or mass diffusivity [$m^2$/s] |
| $f$ | Frequency of droplet production [Hz] |
| $F$ | Temperature or mass fraction in Eqs. (2.38), (5.17) and (5.18) |
| $f_m$ | Distribution function |
| $Fo$ | Fourier number |
| $F(B_M)$ | Mass film thickness correction factor, defined after Eq. (2.29) |
| $F(B_T)$ | Heat film thickness correction factor, defined after Eq. (2.29) |
| $h$ | Heat transfer coefficient [W/($m^2$.K)] |
| $h_0$ | $= \left(\frac{hR_d}{k_l}\right) - 1,\ = -\left(1 + \frac{\alpha R_d}{\mathrm{D}_l}\right)$ or $\left(\frac{hR_d(t)}{k_l}\right) - 1 - \frac{R'_d(t)R_d(t)}{2\kappa}$ |
| $I$ | Property of the component introduced in Eq. (2.40) and Eq. (6.1) |

| | |
|---|---|
| $I_{1,2}$ | Limiting values of $I$ |
| $k$ | Thermal conductivity [W/(m.K)] |
| $k_B$ | Boltzmann constant [J/K] |
| $k_D$ | Parameter defined at Eq. (5.16) |
| $k_R$ | Parameter introduced at Eq. (2.23) |
| $K$ | Steady-state evaporation constant [$m^2$/s] |
| $L$ | Latent heat of evaporation [J/kg] |
| $L_d$ | Diffusion length [m] |
| Le | Lewis number |
| $M$ | Molecular weight [kg/kmole] |
| $\dot{m}_d$ | Instantaneous droplet vaporization rate [kg/s] |
| $n$ | Parameter introduced in Eq. (2.8) or number of carbon atoms |
| $N$ | Number of moles or number of terms |
| Nu | Nusselt number |
| $p$ | Pressure [Pa] |
| Pe | Peclet number |
| Pr | Prandtl number |
| $Q$ | Power spent on the droplet heating [J/s] |
| $q_n$ | Parameter introduced in Eq. (2.23) or defined by Eq. (4.20) |
| $r^*$ | Normalized radius introduced in Eq. (2.38) |
| $R$ | Distance from the centre of a spherical droplet [m] |
| $\dot{R}_d$ | Rate of change of radius [m/s] |
| $\dot{R}_{dE}$ | Rate of change of radius due to evaporation [m/s] |
| $\dot{R}_{dT}$ | Rate of change of radius due to thermal expansion/contraction [m/s] |
| Re | Reynolds number |
| $R_u$ | Universal gas constant [8.314472 J/( K.mole)] |
| Sc | Schmidt number |
| Sh | Sherwood number |
| $t$ | Time |
| $T$ | Temperature |
| $t_0$ | Time at the beginning of timestep [s] |
| $t_1$ | Time at the end of timestep [s] |
| $t_D$ | Characteristic duration of the process [s] |

| | |
|---|---|
| $t^*$ | Dimensionless time defined by Eq. (5.1) |
| $u$ | Velocity [m/s] |
| $u_1$ | Constant introduced at Eq. (3.7) [m/s] |
| $u_2$ | Constant introduced at Eq. (3.7) [m/(s.ms)] |
| $V$ | Volume [$m^3$] |
| $v_r$ | Radial velocity of the vapour defined by Eq. (5.2) [m/s] |
| $X$ | Mole fraction |
| $Y$ | Mass fraction |

**Greek symbols**

| | |
|---|---|
| $\alpha$ | Parameter of the distribution function or parameter defined by Eq. (4.6) |
| $\alpha_R$ | Parameter defined by Eq. (4.14) |
| $\beta$ | Parameter of the distribution function |
| $\gamma$ | Activity coefficient defined by Eq. (E.3) or parameter of the distribution function |
| $\Delta t$ | Timestep |
| $\delta_{T,M}$ | Thermal and mass film thicknesses defined by Eqs. (5.3) and (5.4) [m] |
| $\epsilon_i$ | Evaporation rate of any of the species *i* defined by Eq. (4.7) |
| $\eta$ | $= \frac{\mathrm{Sh}}{\mathrm{Sh_{iso}}} = \frac{\mathrm{Nu}}{\mathrm{Nu_{iso}}}$ |
| $\theta$ | Dimensionless temperature introduced by Eq. (2.20) |
| $\kappa$ | Thermal diffusivity [$m^2$/s] |
| $\lambda_{0,n}$ | Eigenvalues |
| μ | Dynamic viscosity [Pa.s] |
| $\mu_0(t)$ | Parameter introduced in Eq. (2.23) |
| $\nu$ | Kinematic viscosity [$m^2$/s] |
| $\|v_n\|^2$ | Parameter introduced in Eq. (2.23), defined by Eq. (4.19) or defined by Eq.(4.24) |
| $\xi$ | Parameter introduced in Eq. (2.18) |
| $\rho$ | Density [kg/$m^3$] |

| | |
|---|---|
| $\sigma$ | Minimal distance between molecules [Angstrom] |
| $\varphi$ | Parameter defined by Eq. (2.33) |
| $\chi$ | Parameter introduced in Eq. (2.13) and Eq. (4.8) |
| $\psi$ | Parameter introduced in Eq. (2.18) |

**Subscripts**

| | |
|---|---|
| a | Air |
| atm | Atmospheric |
| av | Average |
| *b* | Boiling |
| *c* | Droplet centre |
| *cr* | Critical |
| *d* | Droplet |
| eff | Effective |
| *f* | Fuel |
| *g* | Gas or region of influence |
| *hu* | Heat-up |
| iso | Isolated droplet |
| *l* | Liquid |
| *ref* | Reference |
| *s* | Droplet surface |
| *st* | Steady-state |
| *T* | Temperature |
| *v* | Vapour |
| *Y* | Species diffusion |
| 0 | Initial or beginning of timestep |
| 1 | End of timestep |
| $\infty$ | Far from the droplet surface |

# 1 General introduction

## 1.1 Background

The practical importance of accurate and computer efficient modelling of fuel droplet heating and evaporation in engineering applications is universally recognised (Sirignano, 1999; Polyanin et al, 2002; Michaelides, 2006; Faghri and Zhang, 2006). The fuels used in automotive engines are supplied to combustion chambers in the forms of sprays. Droplets in these sprays are heated and evaporated and this eventually leads to the ignition of the air/fuel vapour mixture (Sazhina et al, 2000). This thesis focuses on the modelling of the first two stages of this process only.

Sirignano (1999) classified the droplet heating models in order of increasing complexity into the following six categories:

1. Constant droplet temperature model where the droplet temperature is constant throughout the evaporation process ($d^2$-law).
2. Infinite Thermal Conductivity (ITC) model, where the droplet temperature is uniform but time-varying (no temperature gradient inside the droplet).
3. Conduction limit model which considers the transient heating process inside the droplet.
4. Effective Thermal Conductivity (ETC) model which takes the effect of recirculation inside the droplet into account via adjustment of the internal liquid thermal conductivity.
5. Vortex model which describes the droplet heating by considering the internal flow within the droplet (Hill vortex).
6. Model based on the full solution of the Navier–Stokes equations.

The more complex the model, the more accurate the results, but it should be kept in mind that these models have been developed for spray simulation where hundreds of thousands of droplets are considered and the computational cost takes the first priority, Ashgriz (2011).

In most Computational Fluid Dynamics (CFD) codes, the heating process has been modelled assuming that there is no temperature gradient inside droplets (Sazhina et al, 2000). This assumption contradicts direct measurements of the temperature distribution inside droplets (Castanet et al, 2002; 2003; 2005; 2007). Bertoli and Migliaccio (1999) were perhaps the first to draw attention to the fact that

taking into account the temperature gradient inside droplets can considerably increase the accuracy of the CFD modelling of combustion processes in Diesel engines. The analysis by these authors was based on the numerical solution to the heat conduction equation inside droplets. An alternative approach was suggested and developed in (Sazhin et al, 2004; 2005a,b; 2006; 2007; Sazhin, 2006). In these papers both finite liquid thermal conductivity and recirculation inside droplets (via the Effective Thermal Conductivity (ETC) model; Abramzon and Sirignano, 1989) were taken into account by incorporating the analytical solution to the heat conduction equation inside the droplet into the numerical scheme. This approach was shown to be considerably more efficient (from the points of view of both accuracy and computer efficiency) than the one used in Bertoli and Migliaccio (1999).

Among other authors who studied heating and evaporation of mono-component droplets theoretically and experimentally we mention Nomura et al (1996), Sazhin and Krutitskii (2003), Abdelghaffar (2005), Maqua (2007), Maqua et al (2006; 2008a), Elwardany (2009), Deprédurand (2009) and Deprédurand et al (2008; 2010).

All papers, mentioned above, were based on the assumption that fuel droplets are mono-component, while most of the commercial fuels (used in automotive engines) such as gasoline and Diesel fuels are complex mixture of hundreds of hydrocarbons species (Heywood, 1988). Hence, the assumption of mono-component droplets might be not accurate enough for modelling realistic fuel heating and evaporation processes (Zhang and Kong, 2009).

There are two main groups of multi-component droplet heating and evaporation models: the first group is called the Discrete Component (DC) models in which the number of fuel components is reasonably small (Abraham and Magi, 1998; Aggarwal and Mongia, 2002; Maqua et al, 2008b). The second group deals with fuels with large number of components (Continuous Thermodynamics 'CT' theory; Tamim and Hallet, 1995; Lippert and Reitz, 1997; Zhang and Kong, 2009 and the Distillation Curve model; Burger et al, 2003). There are also models which contain features of both groups (Lage, 2007; Ra and Reitz, 2009; Laurent et al, 2009; Zhang and Kong, 2010; Rivard and Brüggemann, 2010).

## 1.2 Objectives

The objectives of this thesis are the following:

1. To perform a comparison between the predictions of the heating and evaporation model, suggested by Sazhin et al (2004), and experimental data similar to those reported by Deprédurand et al (2010) for mono-component droplets, but for a wider range of substances (acetone, ethanol, 3-pentanone, n-heptane, n-decane and n-dodecane) and different experimental conditions. The effect of interaction between droplets on the predicted droplet temperatures and radii will be taken into account.

2. To develop a simplified model for multi-component droplets (small number of components) based on a new analytical solution to the species diffusion equation inside the droplet and validation of this model using the available experimental data (acetone/ethanol mixtures; Maqua et al, 2008b).

3. To perform a comparison between the predictions of the new simplified model for multi-component droplets heating and evaporation, described above, and those based on the numerical solutions to both temperature and species equations.

4. To generalise the above-mentioned model to take into account the effect of varying droplet radius during each individual timestep (effect of the moving boundary).

5. To generalise the above-mentioned simplified model to take into account the effect of coupling between droplets and ambient gas. To validate the new model using the available experimental data (n-decane/3-pentanone mixtures; Deprédurand, 2009). To investigate the accuracy and CPU efficiency of the new model.

6. To develop a new quasi-discrete model for multi-component fuel droplets with large number of components and to apply this model to Diesel and gasoline fuels.

## 1.3 Layout of the thesis

Chapter 2 summarises the previously suggested approaches related to heating and evaporation of fuel droplets. Chapter 3 focuses on the modelling of monodisperse mono-component fuel droplets heating and evaporation. A simplified model for a multi-component droplets heating and evaporation is presented and discussed in Chapter 4. The generalisation of this simplified model to take into account the coupling between droplets and ambient gas and the results of our analysis of its accuracy and CPU efficiency are presented in Chapter 5. A new model for multi-component fuel droplets with large number of components and its application to Diesel and gasoline fuels are presented in Chapter 6. The main results of the thesis and recommendations for future work are summarised in Chapter 7.

## 1.4 Dissemination of the results

The results presented in the thesis have been published in the following journals papers: Kristyadi et al (2010) (Chapter 3), Sazhin et al (2010b) (Chapter 4), Sazhin et al (2011a) , Gusev et al (2012) and Elwardany et al (2012) (Chapter 5), Sazhin et al (2011c) and Elwardany and Sazhin (2012) (Chapter 6) and a number of papers in refereed conferences proceedings (Sazhin et al, 2010c,d; 2011b; Elwardany et al, 2011).

# 2 Literature review

This chapter briefly highlights numerous previous studies related to heating and evaporation of fuel droplets. Section 2.1 focuses on the models of mono-component droplets heating and evaporation. Section 2.2 focuses on the models of multi-component droplets heating and evaporation. Experimental studies related to the heating and evaporation process of fuel droplets are summarised in Section 2.3. A summary of this chapter is presented in Section 2.4.

## 2.1 Mono-component droplet heating and evaporation

Chin and Lefebvre (1983a) studied the effect of ambient pressure and temperature on the evaporation rate of different types of fuels (aviation gasoline, n-heptane, JP4, JP5 and DF2) in air. They provided the following equation to calculate the steady-state evaporation constant $K_{st}$ (see Eq. (2.7)) of the $d^2$-law:

$$K_{st} = \frac{8k_g \ln(1+B_M)}{\rho_l c_{p_g}}, \tag{2.1}$$

where $c_{p_g}$ is the gas specific heat capacity, $k_g$ is the gas thermal conductivity, $\rho_l$ is the liquid fuel density and $B_M$ is the Spalding mass transfer number:

$$B_M = \frac{Y_{vs}-Y_{v\infty}}{1-Y_{vs}} = \left.\frac{Y_{vs}}{1-Y_{vs}}\right|_{Y_{v\infty}=0}, \tag{2.2}$$

where $Y_{vs}$ and $Y_{v\infty}$ are the fuel vapour mass fraction at the droplet surface and in the surroundings respectively. They assumed that $Y_{v\infty} = 0$, while $Y_{vs}$ was calculated from the following equation:

$$Y_{vs} = \left[1 + \left(\frac{p}{p_v} - 1\right)\frac{M_a}{M_f}\right]^{-1}, \tag{2.3}$$

where $p$ is the ambient pressure, $M_a$ is the molecular weight of air, $M_f$ is the molecular weight of fuel and $p_v$ is the fuel vapour pressure (saturation pressure) at the droplet surface calculated from the Clausius-Clapeyron equation:

$$p_v = \exp[a - b/(T_s - 43)], \tag{2.4}$$

where $T_s$ is the droplet surface temperature and $a$, $b$ are constants specified for various types of fuel.

They suggested a numerical procedure for calculation of steady-state evaporation droplet surface temperature $T_{s,st}$ and steady-state evaporation constant $K_{st}$. This procedure is based on the fact that at steady-state evaporation the heat

available for heating the droplet is equal to the heat used in evaporation of the droplet which means that $T_{s,st} = \text{const}$ and $B_M = B_T$, where $B_T$ is the Spalding heat transfer number calculated as:

$$B_T = \frac{c_{p_g}(T_\infty - T_s)}{L}, \tag{2.5}$$

where $L$ is the latent heat of evaporation and $T_\infty$ is the ambient temperature.

After equating $B_M$ and $B_T$, they obtained the following equation:

$$\frac{p}{p_v} - \frac{M_a}{M_f}\frac{L}{c_{p_g}(T_\infty - T_s)} - 1 = 0. \tag{2.6}$$

They began their calculations by choosing a random value of $T_s$ and then calculated all the relevant parameters in Eq. (2.6). Then they substituted these parameters in the left-hand side of Eq. (2.6) and repeated this step for another surface temperature until the left-hand side of Eq. (2.6) became close to 0. The droplet surface temperature that satisfied Eq. (2.6) is the steady-state droplet surface temperature. They used this temperature to calculate the steady-state evaporation constant $K_{st}$ using Eq. (2.1) and calculated the droplet diameter using the $d^2$-law:

$$D^2 = D_0^2 - K_{st}t, \tag{2.7}$$

where $D$ is the droplet diameter at the current timestep, $D_0$ is the initial droplet diameter and $t$ is the time.

It was noticed that the steady-state evaporation constant $K_{st}$ increased with the ambient temperature. Also it was pointed out that the evaporation rates increased with the ambient pressure for high ambient temperatures (> 800 K) and decreased with the ambient pressure for low temperatures (< 600 K). For the intermediate region between 600 and 800 K, evaporation rates were almost independent of the ambient pressure. The pressure dependence of $K_{st}$ was approximated as:

$$K_{st} \propto p^n, \tag{2.8}$$

where $n$ varies between $-0.25$ and $+0.25$. It was shown that the pressure dependence of the evaporation rates was stronger at high pressures than at low pressures. The pressure dependence was shown to be positive for high ambient temperatures and negative for low ambient temperatures.

Chin and Lefebvre (1983b) extended their previous paper and studied the factors affecting the duration of the heat-up period in the fuel droplet evaporation process and the ratio of the heat-up period to the total evaporation time. The factors under consideration were different ambient conditions (air pressure, temperature and

velocity) and fuel droplet size. The heat available for heating up the droplet ($Q_{\mathrm{hu}}$) was calculated as the difference between the heat transferred from the surroundings to the droplet and the heat used for the evaporation of the fuel:

$$Q_{\mathrm{hu}=}\dot{m}_d L\left(\frac{B_T}{B_M}-1\right), \tag{2.9}$$

where $\dot{m}_d$ is the fuel evaporation rate calculated using the following equation:

$$\dot{m}_d = 2\pi D\frac{k_g}{c_{p_g}}\ln(1+B_M) = \frac{\mathrm{d}}{\mathrm{d}t}\left[\frac{\pi}{6}\rho_l D^3\right], \tag{2.10}$$

The rate of change of droplet diameter was calculated as:

$$\frac{\mathrm{d}D}{\mathrm{d}t} = \frac{4k_g\ln(1+B_M)}{\rho_l c_{p_g} D}. \tag{2.11}$$

It was assumed that the droplet has uniform but time-varying temperature (ITC model) and the rate of change of droplet surface temperature was calculated from the following equation:

$$\frac{dT_s}{dt} = \frac{Q_{\mathrm{hu}}}{c_l m_d}, \tag{2.12}$$

where $c_l$ is the specific heat of the fuel droplet, $m_d$ is the fuel droplet mass.

The authors defined the end of the heat-up period as the moment of time when there is no heat available for heating up the droplet ($B_M = B_T$, see Eq. (2.9)). This condition was used to capture the heat-up temperature and radius of the droplet. Although this iterative method was reasonably accurate, it was found to be time-consuming. An alternative method for calculating the heat-up period and steady-state temperature was suggested. The results, predicted by both iterative and alternative method, appeared to be reasonably close.

It was shown that the heat-up period increased with increasing ambient pressure and decreased with increasing ambient temperature. It was also noticed that the increase in initial fuel droplet temperature from 270 K to 370 K reduced the heat-up period by about 20% for a number of ambient temperatures. The results showed that convective effects did not change the steady-state temperature and heat-up period whilst it is possible to enhance the evaporation process by reducing the steady-state evaporation time.

The ratio of the heat-up period to the total evaporation time increased with increasing fuel droplet size and also increased with increasing ambient velocity and pressure. It was demonstrated that, at low pressure this ratio decreased with increasing temperature, whereas at high pressure the opposite trend was observed. It

was also noticed that increasing ambient temperature reduced both heat-up and steady-state periods.

Abramzon and Sirignano (1989) developed a model for mono-component droplets heating and evaporation. This model considered the effects of variable thermophysical properties, the non-unity Lewis number in the gas film, internal recirculation inside the droplet and the transient heating of liquid fuel droplets. They called this model the 'extended model'. It is based on the solution of a two dimensional (axially symmetric) energy equation inside the droplet. The limiting cases of this model are: for small liquid Peclet numbers $\mathrm{Pe}_{d(l)}$ the extended model is reduced to the 'Conduction limit model' while for high liquid Peclet numbers the extended model represents the 'Vortex model'.

It was noticed that the extended model has poor CPU efficiency and is not adequate for implementation into CFD codes. A simplified model was suggested to take into account the effect of recirculation inside droplets via the ETC model, in which the thermal conductivity of liquid is multiplied by the factor $\chi_T$ which allows for the effect of internal circulation on heat transfer within the droplet:

$$k_{\mathrm{eff}} = \chi_T k_l, \tag{2.13}$$

where the coefficient $\chi_T$ varies from 1 (at droplet Peclet number $\mathrm{Pe}_{d(l)} = \mathrm{Re}_{d(l)}\mathrm{Pr}_{d(l)} < 10$) to 2.72 (at $\mathrm{Pe}_{d(l)} > 500$) and it was approximated as:

$$\chi_T = 1.86 + 0.86\tanh\left[2.225\log_{10}\left(\mathrm{Pe}_{d(l)}/30\right)\right], \tag{2.14}$$

where $\mathrm{Re}_{d(l)} = \frac{2\rho_l u_s R_d}{\mu_l}$ is the Reynolds number and $\mathrm{Pr}_{d(l)} = \frac{c_l \mu_l}{k_l}$ is the Prandtl number, based on liquid transport coefficients, $\rho_l$, $\mu_l$, $c_l$ and $k_l$ are liquid density, dynamic viscosity, specific heat capacity and thermal conductivity respectively and $u_s$ is the maximum surface velocity calculated as:

$$u_s = \frac{1}{32}\left|u_g - u_d\right|\left(\frac{\mu_g}{\mu_l}\right)\mathrm{Re}_d C_F, \tag{2.15}$$

where $u_g$ is the gas velocity, $u_d$ is the droplet velocity, $\mu_g$ is the gas dynamic viscosity, $\mathrm{Re}_d$ is the Reynolds number based on gas transport coefficients $\mathrm{Re}_d = 2\rho_g\left|u_g - u_d\right|R_d/\mu_g$ and $C_F$ is the friction drag coefficient:

$$C_F = \frac{12.69}{Re_d^{2/3}(1+B_M)}, \tag{2.16}$$

where $B_M$ is the Spalding mass transfer number defined by Eq. (2.2).

The predictions of the ETC and extended models almost coincided while the extended model results appeared to be in between the results of the ITC and

Conduction limit models. The ETC model does not detail the physical features of the recirculation inside the droplet which are not important in most practical engineering applications but it predicts the global effect of the recirculation on heat transfer within the droplets.

Bertoli and Migliaccio (1999) suggested a numerical solution to the heat conduction equation inside the droplet to take into account the effect of finite thermal conductivity, the 'Conduction limit model'. This model was implemented into KIVA II CFD code to relax the assumption of infinite thermal conductivity of liquid which is originally introduced in the KIVA II 'ITC model', and validated using variant fuels (tetradecane, n-heptane and Diesel fuel). For more volatile fuels, the differences between the predictions of the models were less important than for less volatile fuels. The validation was performed against experimental data for an evaporating droplet in a combustion bomb and evaporating spray in a Direct Injection (DI) Diesel engine. The results referring to droplet radii, liquid tip penetration and in-cylinder pressures showed that the predictions of the Conduction limit model agreed better with the experimental data than those of the ITC model.

Sazhin and Krutitskii (2003) suggested an analytical solution to the heat conduction equation inside spherical droplets assuming that the heat is driven to the droplet by convection only. The results showed that the ITC model, which is a limiting case of their model ($k_l \to \infty$), overpredicted the heating up time of droplets. Dombrovsky and Sazhin (2003a) suggested another approach for convective heating of droplets, considering the effect of finite thermal conductivity. The temperature profile inside the droplet was assumed to be parabolic and was calculated as:

$$T(R,t) = T_c(t) + [T_s(t) - T_c(t)](R/R_d)^2, \tag{2.17}$$

where $T_c$ and $T_s$ are the temperatures at the centre and the surface of the droplet, $R$ is the distance from the droplet centre and $R_d$ is the droplet radius. Eq. (2.17) satisfied the equation of the thermal balance.

The droplet surface temperature was calculated based on:

$$T_s = \left(T_{\mathrm{av}} + 0.2\xi T_g\right)/\psi + 0.2\xi R_d \dot{R}_d(T_s)L/(k_l\psi), \tag{2.18}$$

where $T_{\mathrm{av}}$ is the droplet average temperature, $T_g$ is the gas temperature, $\xi = 0.5\mathrm{Nu}\, k_g/k_l$, $\mathrm{Nu} = 2hR_d/k_g$ is the Nusselt number and $\psi = 1 + 0.2\xi$. It was noticed that the parabolic model predicted the droplet surface temperature with about 10% error relative to the rigorous numerical solution to the heat conduction equation

inside the droplet. To improve the accuracy of this model, a dimensionless temperature $\theta = (T - T_0)/(T_g - T_0)$ was introduced. The dimensionless surface temperature was calculated as:

$$\theta_s = \frac{(\theta_{av} + 0.2\xi)}{\psi}[1 - \exp(-\xi Fo)], \tag{2.19}$$

where $Fo = k_l t/(\rho_l c_l R_d^2)$ is the Fourier number. The model based on Eq. (2.19) was named the 'corrected' parabolic model. The ITC model was also considered, where the droplet temperature was calculated as:

$$\theta = 1 - \exp(-3\xi Fo) \tag{2.20}$$

The results showed that the 'corrected' parabolic model predicts more accurately the surface and average droplet temperatures than the ITC model relative to the results obtained by the rigorous numerical solution to the heat conduction equation inside the droplet.

Sazhin et al (2004) provided three analytical solutions to the heat conduction equation inside spherically-symmetric mono-component droplets:

$$\frac{\partial T}{\partial t} = \kappa\left(\frac{\partial^2 T}{\partial R^2} + \frac{2}{R}\frac{\partial T}{\partial R}\right) , \tag{2.21}$$

where $\kappa = \frac{k_l}{c_l \rho_l}$ is the liquid thermal diffusivity, $k_l$, $c_l$, and $\rho_l$ are the liquid thermal conductivity, specific heat capacity and density respectively. The boundary condition of Eq. (2.21) was written as (without evaporation):

$$h(T_g - T_s) = k_l \left.\frac{\partial T}{\partial R}\right|_{R=R_d-0} , \tag{2.22}$$

and the initial condition $T(t=0) = T_{d0}(R)$, where $T_s = T_s(t)$ is the droplet's surface temperature, $T_g = T_g(t)$ is the ambient gas temperature, $h$ is the convection heat transfer coefficient. The solutions were based on three approximations for the convection heat transfer coefficient $h$; constant, almost constant and arbitrary. Firstly an explicit solution to Eq. (2.21) was obtained for the case of a constant heat transfer coefficient in the form of a convergent series. This solution was used to solve Eq. (2.21) for the case of an almost constant heat transfer coefficient. In the case of an arbitrary (time-dependent) coefficient, the differential heat conduction equation was reduced to the Volterra integral equation of the second kind.

In the case when the convection heat transfer coefficient $h(t) = h$ = const., the solution to Eq. (2.21) for $R_d$ = const. during the timestep and the corresponding

boundary and initial conditions, applied to a small timestep $\Delta t = t_1 - t_0$, gives the following value of temperature at the end of the timestep $t_1$, Sazhin et al (2004):

$$T(R,t_1) = \frac{1}{R}\sum_{n=1}^{\infty}\left\{q_n \exp[-k_R\lambda_n^2 t_1] - \frac{R_d^2 \sin\lambda_n}{\|v_n\|^2\lambda_n^2}\left(\mu_0(t_0) - \frac{\frac{\mathrm{d}\,\mu_0(t)}{\mathrm{d}t}}{k_R\lambda_n^2}\right)\exp[-k_R\lambda_n^2 t_1] - \right.$$

$$\left.\frac{R_d^2 \sin\lambda_n}{\|v_n\|^2\lambda_n^4}\frac{\frac{\mathrm{d}\,\mu_0(t)}{\mathrm{d}t}}{k_R}\right\}\sin\left(\lambda_n\frac{R}{R_d}\right) + T_g(t_1), \qquad (2.23)$$

where a set of positive eigen values $\lambda_n$, numbered in ascending order ($n$=1, 2, . . .) (the trivial solution $\lambda = 0$ was not considered) was found from the solution to the following equation:

$$\lambda\cos\lambda + h_0\sin\lambda = 0, \qquad (2.24)$$

$$\|v_n\|^2 = \frac{R_d}{2}\left(1 - \frac{\sin 2\lambda_n}{2\lambda_n}\right) = \frac{R_d}{2}\left(1 + \frac{h_0}{h_0^2+\lambda_n^2}\right),$$

$$q_n = \frac{1}{\|v_n\|^2}\int_0^{R_d} RT_{d0}(R)\sin\left(\lambda_n\frac{R}{R_d}\right)\mathrm{d}R,$$

$$k_R = \frac{k_l}{c_l\rho_l R_d^2},\ \mu_0(t) = \frac{hT_g(t)R_d}{k_l},\ h_0 = \left(\frac{hR_d}{k_l}\right) - 1.$$

Sazhin et al (2005a) showed that the solution to the heat conduction equation based on the assumption of a constant heat transfer coefficient (2.23) is the most efficient for implementation into CFD codes. It was also shown that the numerical scheme based on Solution (2.23), where the heat transfer coefficient is assumed to be constant, is more effective than the approach based on the numerical solution to the heat conduction equation inside the droplet and more accurate than the numerical scheme based on the parabolic temperature profile inside the droplet.

Sazhin et al (2005b) pointed out that, in the absence of break-up, the difference between the evaporation time predicted by the ETC and ITC models did not exceed a few percent while the ETC model predicted a decrease in the ignition delay. In the presence of break-up, the ETC model predicted significant decreases in the evaporation time and auto-ignition timing compared with the ITC model.

Sazhin et al (2006) presented a comparative analysis between different liquid and gas phase models for fuel droplet heating and evaporation. The analysis was based on two liquid phase models (ITC and ETC models), and seven gas phase models. These were six semi-theoretical models based on various assumptions and a model based merely on the approximation of experimental data.

The first gas phase model, called 'M0', is based on the following approximations for Sherwood (Sh) and Nusselt (Nu) numbers:

$$\mathrm{Sh} = 2\frac{\ln(1+B_M)}{B_M}\left[1 + 0.3\mathrm{Re}_d^{1/2}\mathrm{Sc}_d^{1/3}\right], \tag{2.25}$$

$$\mathrm{Nu} = 2\frac{\ln(1+B_M)}{B_M}\left[1 + 0.3\mathrm{Re}_d^{1/2}\mathrm{Pr}_d^{1/3}\right], \tag{2.26}$$

where $\mathrm{Re}_d$ is the Reynolds number as introduced in Eq. (2.15), $\mathrm{Sc}_d = \frac{\mu_g}{\rho_g D_v}$ is the Schmidt number and $\mathrm{Pr}_d = \frac{c_{pg}\mu_g}{k_g}$ is the Prandtl number. Replacing $B_M$ in Eq. (2.26) with the Spalding heat transfer number $B_T$, the 'M1' model was obtained. $B_T$ was defined as:

$$B_T = \frac{c_{pv}(T_g - T_s)}{L_{\mathrm{eff}}}, \tag{2.27}$$

where $L_{\mathrm{eff}} = L + \frac{Q_L}{\dot{m}_d}$, $Q_L$ is the power spent on the droplet heating, $c_{pv}$ is the specific heat capacity of fuel vapour.

The third model, 'M2', was based on the following approximations:

$$\mathrm{Sh} = 2\frac{\ln(1+B_M)}{B_M}\left[1 + 0.3\frac{\mathrm{Re}_d^{1/2}\mathrm{Sc}_d^{1/3}}{F(B_M)}\right], \tag{2.28}$$

$$\mathrm{Nu} = 2\frac{\ln(1+B_T)}{B_T}\left[1 + 0.3\frac{\mathrm{Re}_d^{1/2}\mathrm{Pr}_d^{1/3}}{F(B_T)}\right], \tag{2.29}$$

where $F(B_{M,T}) = (1 + B_{M,T})^{0.7}\frac{\ln(1+B_{M,T})}{B_{M,T}}$.

The 'M4' model was the one suggested by Abramzon and Sirignano (1989):

$$\mathrm{Sh} = 2\frac{\ln(1+B_M)}{B_M}\left[1 + \frac{(1+\mathrm{Re}_d\mathrm{Sc}_d)^{1/3}\max(1,\mathrm{Re}_d^{0.077}) - 1}{2F(B_M)}\right], \tag{2.30}$$

$$\mathrm{Nu} = 2\frac{\ln(1+B_T)}{B_T}\left[1 + \frac{(1+\mathrm{Re}_d\mathrm{Pr}_d)^{1/3}\max(1,\mathrm{Re}_d^{0.077}) - 1}{2F(B_T)}\right]. \tag{2.31}$$

According to Abramzon and Sirignano (1989), $B_T$ and $B_M$ were linked by the following equation:

$$B_T = (1 + B_M)^{\varphi} - 1, \tag{2.32}$$

$$\varphi = \left(\frac{c_{pv}}{c_{pa}}\right)\left(\frac{\mathrm{Sh}^*}{\mathrm{Nu}^*}\right)\frac{1}{\mathrm{Le}}, \tag{2.33}$$

where $\mathrm{Le} = k_g/(c_{pa}\rho_g D_v)$ is the Lewis number and

$$\mathrm{Sh}^* = 2\left[1 + \frac{(1+\mathrm{Re}_d\mathrm{Sc}_d)^{1/3}\max(1,\mathrm{Re}_d^{0.077}) - 1}{2F(B_M)}\right], \tag{2.34}$$

$$\mathrm{Nu}^* = 2\left[1 + \frac{(1+\mathrm{Re}_d\mathrm{Pr}_d)^{1/3}\max(1,\mathrm{Re}_d^{0.077}) - 1}{2F(B_T)}\right] \tag{2.35}$$

are Sherwood and Nusselt Numbers for non-evaporating droplets respectively. Sazhin et al (2006) assumed that the ratio $\frac{\mathrm{Sh}^*}{\mathrm{Nu}^*}$ is equal to 1.

The model referred to as 'M3' is a limiting case of 'M4' when $F(B_M) = F(B_T) = 1$. When the coefficient 0.3 in Eqs. (2.28) and (2.29) was replaced by 0.276 the model was referred to as 'M5'. The 'M6' model was based on the analysis of the experimental data:

$$\mathrm{Sh} = \frac{2}{B_M}\left[\frac{1+0.435\mathrm{Re}_d^{1/2}\mathrm{Sc}_d^{1/3}}{(1+B_M)^{0.7}}\right], \tag{2.36}$$

$$\mathrm{Nu} = \frac{\ln(1+B_T)}{B_T}\left[\frac{2+0.57\mathrm{Re}_d^{1/2}\mathrm{Pr}_d^{1/3}}{(1+B_F)^{0.7}}\right], \tag{2.37}$$

where $B_F = \frac{C_{pv}(T_g - T_s)}{L}\left(1 - \frac{Q_L}{Q_c}\right)$ and $Q_c$ is the heat transferred to the droplet by convection.

Sazhin et al (2006) pointed out that the 'M4' model predicts the evaporation time closest to the one obtained based on the approximation of experimental data. They showed that the ETC model leads to marginally better agreement with experimental data than the ITC model. This is in agreement with the results of Bertoli and Migliaccio (1999).

Barata (2008) presented a numerical study for evaporation of biofuel droplets injected through a turbulent cross-stream. The effect of interaction between droplets was ignored and the ITC model was used to describe the heating process inside the liquid droplet. This model was applied to the analysis of the evaporation of Diesel 'DF2', Rapeseed Methyl Ester 'RME', ethanol and n-heptane fuel droplets. The results showed that 'RME' has similar evaporation characteristics to 'DF2' fuel which indicates that 'RME' can be used as an alternative fuel to 'DF2'.

Fieberg et al (2009) studied the evaporation process of single isolated droplets and monodisperse droplet chains under Diesel engine conditions. For the liquid phase, they took into account the effect of transient heating of the droplet based on the ETC model and the dependence of the properties on temperature and droplet spacing.

Sazhin et al (2010a) extended the model previously suggested by Sazhin et al (2004), which was based on the assumption of constant droplet radius during each timestep, to take into account the effect of changes in radius during the individual timesteps. The radius was assumed to change linearly with time. The results showed a small difference between the predictions of both models in terms of droplets' temperature and radius.

Mitchell et al (2011) suggested a numerical solution to the heat conduction equation inside the droplet considering the effect of changes in radius during the individual timesteps. The predictions of their model coincided with those of the model based on the analytical solution to this equation provided by Sazhin et al (2010a).

Sazhin et al (2011d) suggested other analytical solutions to the heat conduction equation inside the droplet considering the effect of changes in radius during the individual timesteps, assuming that the time evolution of the droplet radius is known. The predictions of these calculations were compared with the predictions obtained using their previously suggested approach when the droplet radius was assumed to be a linear function of time during individual timesteps (Sazhin et al, 2010a). For sufficiently small timesteps the time evolutions of droplet temperatures and radii predicted by both methods coincided. The solutions, suggested by Sazhin et al (2010a, 2011d), predict lower droplet temperature and slower evaporation when the effects of the reduction of $R_d$ are taken into account.

## 2.2 Multi-component modelling

When modelling multi-component fuel droplets one needs to take into account that different components evaporate at different rates and this leads to concentration gradients and mass diffusion in the liquid phase. Sirignano (1999) considered two limiting cases of liquid diffusivity. The first one refers to the rapid regression or zero-diffusivity limit (also called the Diffusion Limit 'DL' case). The second one refers to the Infinite Diffusivity limit (or 'ID', also called the well mixed case) in which the concentration of the components is uniform. As mentioned in Chapter 1, there are two main groups of models for multi-component droplet heating and evaporation, taking into account the effects of finite species diffusivity inside droplets. These are described below.

### *2.2.1 Discrete component models*

Abraham and Magi (1998) developed a model for multi-component droplet evaporation. The multi-component droplets were treated as a combination of several mono-component droplets with the same size and initial temperature and subject to the same surrounding conditions. The heat flux to each of the mono-component droplets was assumed to be the same as the heat flux to the multi-component droplets. The evaporation rate of each mono-component droplets was calculated and

the mass balance was used to calculate the evaporation rate of the multi-component droplets. The model was then implemented into KIVA 3 CFD code and applied to evaporation of isolated droplets, Diesel spray and Diesel engine conditions. Different droplet mixtures of $C_6H_{14}$, $C_8H_{18}$, $C_{10}H_{22}$ and $C_{16}H_{34}$, under warm operating and cold start conditions, were considered. For the isolated droplet case, the results showed that under warm operating conditions the evaporation rate was fast and the droplet lifetime was short and therefore the diffusion of species vapour was not important. Under cold start conditions the results showed that the evaporation rates had a significant effect on the vapour species distribution.

Aggarwal and Mongia (2002) suggested a model for evaporation of multi-component droplets under high pressure conditions and applied this model to the operating conditions of the gas turbine combustor. Two commonly used liquid heating models were considered: Infinite Diffusion, 'ID', and Diffusion Limit, 'DL'. They compared the vaporization characteristics of bi-component fuel droplets mixture of 50% $C_{10}H_{22}$ – 50% $C_{14}H_{30}$ with mono-component fuel droplets of pure $C_{12}H_{26}$. At ambient pressure of 1 atm, the results showed that as the gas temperature increases from 373 K (represents initial starting and ignition) to 1500 K (represents a typical lean blowout temperature for ground idle condition) the differences between evaporation histories of bi-component droplets and the corresponding mono-component droplets increase as well. They concluded that at high temperatures the evaporation of a bi-component fuel droplet could be represented by an equivalent mono-component droplet (50% boiling point) for the case of the 'DL' model, while for the 'ID' model this replacement leads to discrepancies between the evaporation rates of bi-component and mono-component fuel droplets. For low temperature conditions, the results showed that the evaporation behaviour of bi-component droplets could not be represented by equivalent mono-component fuel droplets using both liquid phase models. It was also noticed that the differences in the vaporization characteristics using the two liquid phase models for bi-component droplets are quite significant while they are negligible for the equivalent mono-component droplets.

Brenn et al (2007) extended the model suggested by Abramzon and Sirignano (1989) for mono-component droplets to enable it to analyse acoustically levitated multi-component droplets. They noticed that the acoustically levitated droplets are well mixed due to the interaction with the acoustic streaming and therefore the droplets have flat temperature profiles. For this reason the ITC model was used to

simulate the heating of the liquid phase. The acoustic levitator was used to carry out experiments on the evaporation behaviour of single droplets of multi-component liquids. In this technique the droplet is suspended without any direct mechanical contact by making use of the quasi-steady sound pressure distribution in a confined space. The experiments were carried out for droplets which consisted of different mixtures of methanol, ethanol, 1-butanol, n-heptane, water and n-decane. The results indicated that the maximum deviation between both computed and measured lifetimes is 5% for simple ternary mixtures and more complex cases of five components.

Sirignano and Wu (2008) presented the analysis of evaporation of eight multi-component (n-heptane, n-octane and n-decane) droplets in a cubic array. The concept of mass flux potential was introduced for both liquid and gas phase calculations. Three models for the liquid diffusion process were considered. The first model is 'transient behaviour' at which heat and mass diffusion times and droplet lifetimes are of the same order of magnitude. The second model is one of the limiting cases of transient behaviour, the 'fast vaporization or well mixed' (ID) model, in which the regression rate of the droplet surface is much greater than characteristic times for heat and mass diffusion. The third model is the other limiting case, the 'slow vaporization or Diffusion Limit' (DL) model, in which the times for liquid phase heat and mass diffusions are very short compared with the droplet lifetime. The results indicated that the isolated droplets evaporate faster than the interactive droplets. At low temperatures, the results indicated that the slow vaporization limit gives acceptable predictions for mono-component droplets but not for multi-component droplets. At high temperatures, the difference between the predictions of slow vaporization limit and transient behaviour became noticeable for both mono- and multi-component droplets.

Gosh et al (2008) studied the evaporation of a dense cluster of bi-component fuel droplets in a spray using a spherical cell model. The spray was assumed to be a cluster of identical droplets; each single droplet evaporates in a single unit spherical cell inside the cluster. The interstitial region between the touching spherical cells, called the ambient region, was assumed to be a common sink for the fuel vapour and the energy source. They validated their model against experimental results of evaporation for tetralin droplets (mono-component) in nitrogen for different cell radii.

Maqua et al (2008b) studied the evaporation process of bi-component droplets (ethanol/acetone) numerically and experimentally under different aerothermal conditions (hot air plume and ambient temperature). The three-colour laser-induced fluorescence (LIF) technique was used to measure the droplet temperature regardless of the composition and the droplet velocity was measured by means of Laser Doppler Anemometry (LDA). The uncertainty of the droplet temperature measurements is about ±1.3 °C. For the numerical part of their study, it was assumed that the droplet is spherically-symmetric. The liquid mass fraction of the $i^{th}$ species $Y_{l,i}$ and the droplet temperature $T$ were calculated based on the following equation:

$$\frac{\partial F}{\partial t} - \frac{r^*}{R}\frac{\mathrm{d}R}{\mathrm{dt}}\frac{\partial F}{\partial r^*} + \frac{1}{R}(\upsilon.\nabla r^*)F = \frac{DF}{R^2}\Delta r^* F, \tag{2.38}$$

where $F$ denotes either the droplet temperature $T$ or the mass fraction $Y_i$, $R$ is the radial distance to the droplet centre, $r^* = R/R_d$ is the normalised radius and $\upsilon$ is the velocity field within the droplet.

They assumed that the internal streamlines of the liquid circulating within the droplet follow the spherical Hill vortex pattern with stream function in the following form:

$$\psi(r^*, \theta, \phi) = -\frac{u_s R^2}{2} r^{*2}\left(1 - r^{*2}\right)\sin^2\theta, \tag{2.39}$$

where $(r^*, \theta, \phi)$ are the spherical coordinates of a point within the droplet and $u_s$ is the maximum surface velocity calculated based on Eq. (2.15).

Good agreement was achieved between the numerical and experimental results in terms of droplet temperature for different initial conditions (droplet radius, velocity, temperatures and compositions).

### *2.2.2 Many components models*

Tamim and Hallett (1995) used the continuous thermodynamics approach for modelling evaporation of multi-component droplets with large number of components. The composition and properties of the mixture, and vapour-liquid equilibrium were described based on the continuous thermodynamics method in which the composition of the mixture is represented by a Probability Density Function (PDF) rather than by discrete components. The function selected for both gas and liquid phases was the Gamma distribution Γ. The distribution function was calculated as:

$$f_m(I) = \frac{(I-\gamma)^{\alpha-1}}{\beta^{\alpha}\Gamma(\alpha)}\exp\left[-\left(\frac{I-\gamma}{\beta}\right)\right], \tag{2.40}$$

where $I$ is the property of the component (they used the molecular weight to represent this property), $I = \gamma$ is the origin , $\alpha$ and $\beta$ are parameters that determine the shape of the distribution and $\gamma$ determines the original shift. They built their analysis of the liquid phase on the 'ID' and 'ITC' models. For the liquid-vapour equilibrium they used Raoult's law with the Clausius-Clapeyron. The model was applied to the analysis of evaporation of Diesel and gasoline fuels.

Lippert and Reitz (1997) applied the continuous thermodynamics approach to multidimensional calculations for droplets and sprays. Similarly to Tamim and Hallett (1995), the Gamma distribution (Eq. (2.40)) was used, the droplets were assumed to have uniform temperature and a well mixed liquid phase (ITC and ID models) and Raoult's law with the Clausius-Clapeyron equation was used. They compared the predictions of their model for the mono-component case (the parameters used for iso-octane were $\alpha = 100.0$, $\beta = 0.1$ and $\gamma = 104$) with the standard model in KIVA CFD code and the mono-component model suggested by Han et al (1996). The results showed good agreement between their model and Han's model. Also the results showed that heavy components appeared at the outer edge of the spray in agreement with the predictions of Abraham and Magi (1998).

Hallett (2000) simplified the model earlier developed by Tamim and Hallett (1995). He assumed that the fuel consists only of n-paraffins and developed a simplified quasi-steady model for evaporation of multi-component droplets by neglecting the gas-phase transients, assuming spherical symmetry and constant properties. The results showed that the simplified model reproduced the predictions of the full model in terms of droplet temperature, the percentage of evaporated mass and fuel vapour mole fraction at the droplet surface for the 'ID' liquid phase model. For the 'DL' liquid phase model, it was noticed that the droplet temperature increased up to the wet bulb temperature and then it remained constant and the steady evaporation appeared clearly, while for the 'ID' model it was noticed that the droplet temperature increased throughout the whole of its lifetime. Despite this difference the droplet lifetimes predicted by both models were very close. The results also showed the applicability of the $d^2$-law for modelling multi-component droplets.

Zhu and Reitz (2002) developed a comprehensive evaporation model for fuel droplets with large number of components in a high pressure environment using the

continuous thermodynamics approach. This model was shown to be independent of the form of the distribution function that is selected for the continuous fuel species and they used the Gamma distribution. They derived the transport equations for the semi-continuous systems. The liquid phase included liquid fuel (continuous) and the ambient gas (discrete) while the gas phase included fuel vapour (continuous) and the ambient gas (discrete). The model was applied to the modelling of evaporation of Diesel fuel with composition parameters similar to those used by Tamim and Hallett (1995) and evaporation of n-tridecane as mono-component fuel with $\alpha = 100.0$, $\beta = 0.1$ and $\gamma = 175.0$ and with the mean molecular weight corresponding to Diesel fuel. The droplets were injected into nitrogen and the results showed that for high pressure conditions the heat of vaporization increases to a maximum value then decreases with increasing temperature. For low pressures the heat of vaporization decreased with increasing temperature. The equivalent mono-component fuel (n-tridecane) predicted smaller heat of vaporization especially at low droplet temperatures and high ambient pressures conditions. They emphasised the importance of considering the composition of multi-component fuels under sub- and super-critical pressure conditions.

Arias-Zugasti and Rosner (2003) introduced spectral representation of the PDF with a number of components (pseudo-components) much smaller than the number of components in the original chemical mixture. They generalised the former method in which the PDF describing the mixture was assumed to have a predetermined mathematical form as in Eq. (2.40). The fuel was considered to be composed only of straight-chain n-alkanes ($C_nH_{2n+2}$) where $n$ is the number of carbon atoms and varies between $n_0$ and $n_f$. For gasoline fuel it varied from 5 to 18 and for Diesel and JP4 fuels it varied from 5 to 25 and from 5 to 16 respectively.

Burger et al (2003) presented an alternative method, known as the Distillation Curve model, for modelling evaporation of multi-component fuel droplets at elevated pressures. This model is based on algebraic equations describing fractional boiling during the droplet evaporation process. It was pointed out that the predictions of the distillation curve for Jet-A1 fuel agreed well with the results of the 'DL' model for Jet-A1 fuel approximated as a bi-component mixture of 44% n-decane and 56% n-tetradecane.

Abdel-Qader and Hallett (2005) compared the two limiting cases of liquid phase mixing (ID and DL models) for evaporation of single droplets using the

continuous thermodynamics technique. They considered two cases of the distribution function. The first was the single distribution function and the second was a sum of two distribution functions with widely differing molecular weights (n-heptane and n-dodecane, a 'dumbbell mixture'). The results using the single distribution function showed that neither temperature nor evaporation rate are significantly affected by internal mixing until near the end of the droplet's lifetime. The results indicated that the largest effects of the liquid mixing models are seen for two discrete components and these effects decrease when the discrete components are replaced by two broad distributions to form a dumbbell mixture.

Lage (2007) developed a pseudo-component model to represent continuous mixtures as a combination of 2 or 3 pseudo-components of each group of components. The model was based on the Gaussian quadrature rule whose weight function is the molar fraction distribution of the complex mixture. He called this model the Quadrature Method of Moments (QMOM). Laurent et al (2009) compared the QMOM with the Gamma-PDF method used to introduce complex hydrocarbons. The QMOM was shown to represent continuous mixtures better than the Gamma-PDF when fuel vapour condenses on the droplet surface.

Zhang and Kong (2009) used the continuous thermodynamics approach for modelling of multi-component fuel droplets. They used the Gamma distribution with molecular weight as a parameter for describing fuel composition. They implemented this model into KIVA 3V CFD code. The initial distribution parameters used for Diesel fuel were: $\alpha = 23.0$, $\beta = 8.15$ and $\gamma = 0.0$ and for gasoline fuel: $\alpha = 5.7$, $\beta = 15.0$ and $\gamma = 0.0$. They selected these parameters to match the distillation curve of the specific fuel based on the linear relationship between boiling point and molecular weight of typical hydrocarbon fuel. The results referring to single droplet evaporation showed that the mean molecular weight of the fuel increases during the droplet's lifetime indicating that the heavier components remain in the droplet until the end of its lifetime. It was noticed that the predicted droplet lifetimes were shorter than those predicted by Lippert and Reitz (1997) for the same conditions.

Ra and Reitz (2009) used the discrete multi-component approach (DC model) to model the evaporation of real fuels with large number of components (gasoline and Diesel fuels). They approximated Diesel fuel as a mixture of six species and gasoline fuel as a mixture of seven components. Their approach took into account

the effect of finite thermal diffusivity but assumed infinite mass diffusivity for the liquid phase. The results showed good agreement with the experimental data.

Zhang and Kong (2010) developed a hybrid vaporization model based on both the continuous thermodynamics approach, to describe petroleum fuels, and the discrete components approach, to represent biofuels and mono-component substances. It was assumed that liquid phase heat and mass diffusivities were infinite. They used Raoult's law for calculation of the vapour surface mass fraction and approximated biodiesel as a mixture of five kinds of fatty acids. For the case of mono-component n-heptane droplets, it was shown that there is good agreement between the predictions of their model and the experimental results by Nomura et al (1996). They also tested their model for the case of evaporation of binary mixture of n-heptane and n-decane and the results showed poor agreement with the experimental results by Gökalp et al (1994). The results for biodiesel droplets were shown to have good agreement with the experimental results by Morin et al (2000). For Diesel-biodiesel mixtures, it was shown that the droplet lifetime increases as the percentage of biodiesel increases. The results also showed that any mixture with up to 20% by volume of biodiesel behaves almost as pure Diesel fuel. For gasoline-ethanol mixtures it was noticed that the ethanol volume fraction increases at the initial stage of the evaporation process and then decreases. This behaviour indicated that part of gasoline components is more volatile than ethanol and so ethanol mass fraction increases until these light components have completely evaporated.

Rivard and Brüggemann (2010) introduced a semi-continuous model of evaporation of pure substance mixed with a continuous mixture (ethanol-gasoline mixture). For the gas phase, they applied Raoult's law. For the liquid phase, they considered three different models: the 'ID' model, the 'DL' model and the combined model where the composition is limited by diffusion. It was pointed out that the difference between the prediction of the three models increases as the ambient temperature decreases. The droplet lifetime predicted by the 'DL' model is shown to be about 30% longer than the one predicted by the 'ID' model. The results of the combined model were shown to always be in between those of the 'ID' and 'DL' models.

Hallett and Legault (2011) used the continuous thermodynamics approach to model biodiesel fuel. They represented the fuel using three distribution functions of three different chemical groups: the fatty acid methyl ester (FAME) fraction

represents the bulk of the fuel, a small light FAME fraction reproduces the early part of the distillation curve and a monoglyceride (MGC) fraction reproduces the partially unconverted feedstock in the fuel. The results demonstrated that the model can reproduce the behaviour of actual biodiesel fuel.

## 2.3 Experimental studies

Nomura et al (1996) studied experimentally the evaporation of an individual suspended n-heptane droplet in a nitrogen atmosphere at high pressures and temperatures under microgravity conditions, which were produced using 5-m and 110-m drop towers and parabolic flights, to prevent natural convection that complicates the phenomena; under microgravity conditions, radial vapour flow occurs instead of natural convection and the vapour layer around the droplet is thicker than under normal gravity conditions. They calculated the temporal variations of droplet diameter for ambient pressure range of 0.1-2.0 MPa with ambient temperatures of 400-800 K and for ambient pressure of 5.0 MPa with ambient temperatures of 400-600 K. For the ambient pressure range of 0.1-2.0 MPa, it was shown that the slope of the squared diameter of the droplet increases with time but later it becomes constant. At 5.0 MPa, this slope becomes less in the latter periods of the evaporation time. The results showed that, at ambient pressure of 0.1 MPa the ratio of heat-up time to the evaporation time was almost independent of ambient temperature and the range of its values was about 0.1 - 0.2. As ambient pressure increased the tendency of this ratio to rise with ambient temperature became noticeable. At ambient temperatures higher than boiling point, the time required to heat the droplet up to the wet bulb temperature increased proportionally to the required time for complete evaporation as ambient temperature increased. For ambient temperatures less than boiling point; the wet bulb temperature and the temperature difference between the droplet and the ambient gas increased as ambient temperature increased. For ambient temperatures above 550 K, the evaporating time decreased as ambient pressure increased while for ambient temperatures below 450 K, the evaporating time increased as the ambient pressure increased and the evaporating time was almost independent of ambient pressure at ambient temperatures of about 480 K.

Two main techniques are used to measure droplet temperature, (Lavieille et al, 2000). The first is the rainbow refractometer method (van Beeck and Riethmuller,

1997), which is based on the variation of the refractive index of the droplet with temperature. A visible laser beam passes through the droplet and produces a rainbow pattern. The rainbow pattern location, which changes with temperature, determines the refractive index. It was noticed that the rainbow technique is reliable when the temperature of the droplet is almost constant and it is not recommended when strong thermal gradients in the droplet exist. The second method uses the droplet Infrared ('IR') emissions to determine its temperature. The droplet stream is placed in front of an extended blackbody, whose temperature can be adjusted. A detector collects the blackbody flux emitted by the droplets. The main difficulty of this technique is determination of the droplet's emissivity. Its limitation is that only a surface temperature is determined.

Lavieille et al. (2000) presented the fundamentals of Laser Induced Fluorescence technique (LIF) for the temperature measurement of monodisperse droplets and delivered the first results on the application from this method. Ethanol fuel (95% ethanol- 5% water) was seeded with an organic dye (rhodamine B) as adequate tracer, due to its strong temperature sensitivity and temperature dependence on the fluorescence of this dye. They also took into account several phenomena such as: the lensing effect for incoming laser light due to the spherical droplet interface with air, since curvature of the interface changes as the droplet size changes; varying focusing of the light and distribution of laser energy through the droplet; changes in droplet size due to thermal expansion or contraction and subsequent fluorescent tracer concentration variation. They measured the droplet temperature at the injection point by the thermocouple and 15 mm downstream from the injection point using the LIF method. It was noticed that the LIF method is able to measure the droplet temperature with errors not more than 1 °C in a monodisperse stream. This technique was found to depend on laser intensity, dye concentration and droplet volume.

Lavieille et al (2001) eliminated the dependence of the laser intensity, dye concentration and droplet volume on the fluorescence signal and they kept the sole effect of temperature on this signal by introducing the two-colour LIF technique. The ratio of the fluorescence signals measured by the two spectral bands eliminates the volume dependence. The effect of the dye concentration was investigated by using two different concentrations of dye and the results showed that decreasing the concentration of the dye to half of its value does not significantly affect the

fluorescence ratio. This ratio was found to be independent of laser power within 1%, corresponding to an error in the temperature of less than 0.5 ºC, and it does not change with the change of the measuring volume size. Lavieille et al (2002a) demonstrated the ability of the two-colour LIF technique to provide average temperature of evaporating and combusting droplets. In a latter paper, Lavieille et al (2002b) determined the temperature distribution inside the droplet by scanning it with a sufficiently small probe volume, compared with the droplet volume, generated by the intersection of two laser beams issuing from the same laser source. They applied this technique to droplets of 200 µm diameter. The intersection volume between the two laser beams was (20×20×90 µm) which is smaller than the droplet volume. The collection volume had a diameter of 68 µm and therefore the resulting probe volume was (20×20×68 µm) (see Fig. 2.1).

The results indicated the existence of convective heating inside the droplets. It was demonstrated that this method was useful for measuring droplet temperatures.

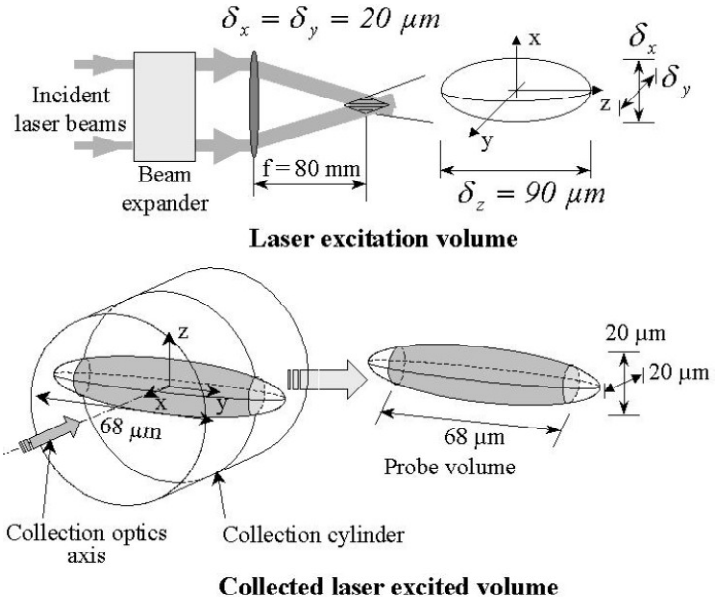


Fig. 2.1 Definition of the probe volume, Lavieille et al (2002b).

In the experiment described by Castanet et al (2002), a linear monodisperse droplet stream was generated by Rayleigh disintegration of a liquid jet undergoing vibrations generated in a piezoelectric ceramic. The fuel was pre-heated in the injector by means of externally heated circulating water. The temperature of the fuel was measured exactly at the injection point with a K type thermocouple situated

within the injector body. For specific frequencies of forced mechanical vibration, the liquid jet broke up into equally spaced and mono-sized droplets.

Castanet et al (2002) implemented electrostatic deviator plates at the injector exit in order to adjust the droplets spacing without changing the droplet diameter. The droplets stream then passed through the thermal boundary layer of a heated vertical plate as shown in Fig. 2.2. The droplet size was measured using a light scattering technique (interferential method) while the droplet velocity was measured by Laser Doppler Velocimetry (LDV). Measured droplet temperature, velocity and size were used to estimate the heat fluxes acting on the evaporating droplets for both heat-up process and steady-state of evaporation. The results showed that the heat convection coefficient for the heat-up process is higher than the one in the steady evaporation case. It was also demonstrated that corrections to the Nusselt number have to be applied to compensate for the effect of interaction between droplets.

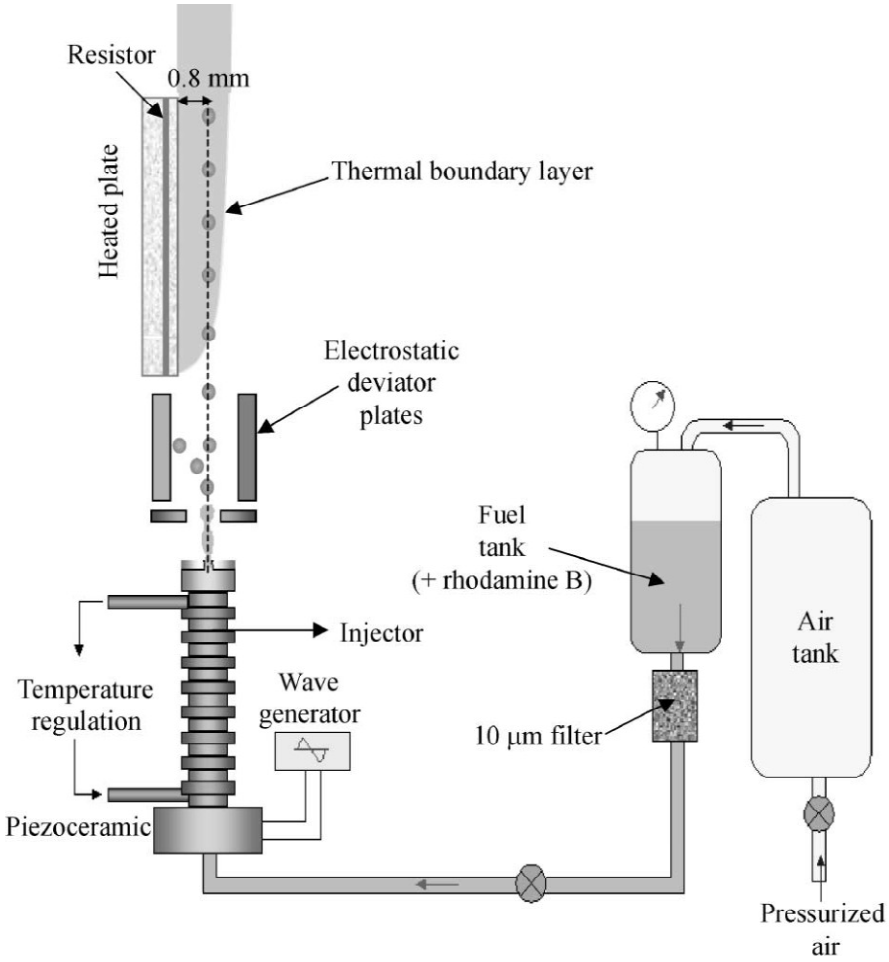


Fig. 2.2 Experimental set-up used by Castanet et al (2002).

Castanet et al (2005) used phase Doppler anemometry for measurement of droplet sizes and calculated the heat fluxes (internal flux, evaporation flux and convective heat flux) acting on evaporating ethanol droplets moving into a flame. The Nusselt and Sherwood numbers were calculated from the heat fluxes and corrections to them were presented to take into account the effect of interaction between droplets in the following form $\eta$:

$$\eta = \frac{\mathrm{Nu}}{\mathrm{Nu_{iso}}} = \frac{\mathrm{Sh}}{\mathrm{Sh_{iso}}} = \tanh(0.36C - 0.82), \tag{2.41}$$

where $C$ is the distance parameter, defined as the droplets spacing divided by their diameter. The subscript $_{\mathrm{iso}}$ refers to isolated droplets. For distance parameters larger than 9, the interaction effects were shown to be negligible. For distance parameters less than 9, the evaporation rate was shown to decrease with increasing values of the distance parameter.

Maqua et al (2008a) extended the experiments described by Castanet et al (2005) to evaporation of ethanol and acetone as mono-component droplets. The measurements were carried out in two different conditions: heating and evaporation of droplets in a hot air flow and in flame. They compared the experimental results with numerical results based on the ETC model and the analytical solution (Eq. (2.23)). The Sherwood and Nusselt numbers for isolated droplets were calculated based on Eqs. (2.30) and (2.31) respectively. Corrections due to droplet interaction were taken into account based on Eq. (2.41). The results showed that there is good agreement between the measured temperature and the predicted average temperature for relatively small droplets (initial radii of 65 μm), while for relatively large droplets (initial radii of 120 μm) the measured temperature was shown to be close to the predicted temperatures at the droplet centre.

There are few available experimental data on the temporal evolution of multi-component droplet temperature due to the lack of measurement techniques available for dealing with multi-component droplets. Maqua et al (2006) developed a technique for measuring multi-component droplet temperature based on three-colour LIF. The fluorescence signal was found to depend on both composition and temperature. They showed that it is possible to separate the dependence of composition and temperature by using a third spectral band for detection. Maqua (2007) and Maqua et al (2008b) produced further experiments for bi-component fuel

droplets. A brief description of these experiments will be presented where they provide validation of our models.

## 2.4 Conclusions of Chapter 2

The classifications of models for fuel droplets heating and evaporation are schematically presented below.

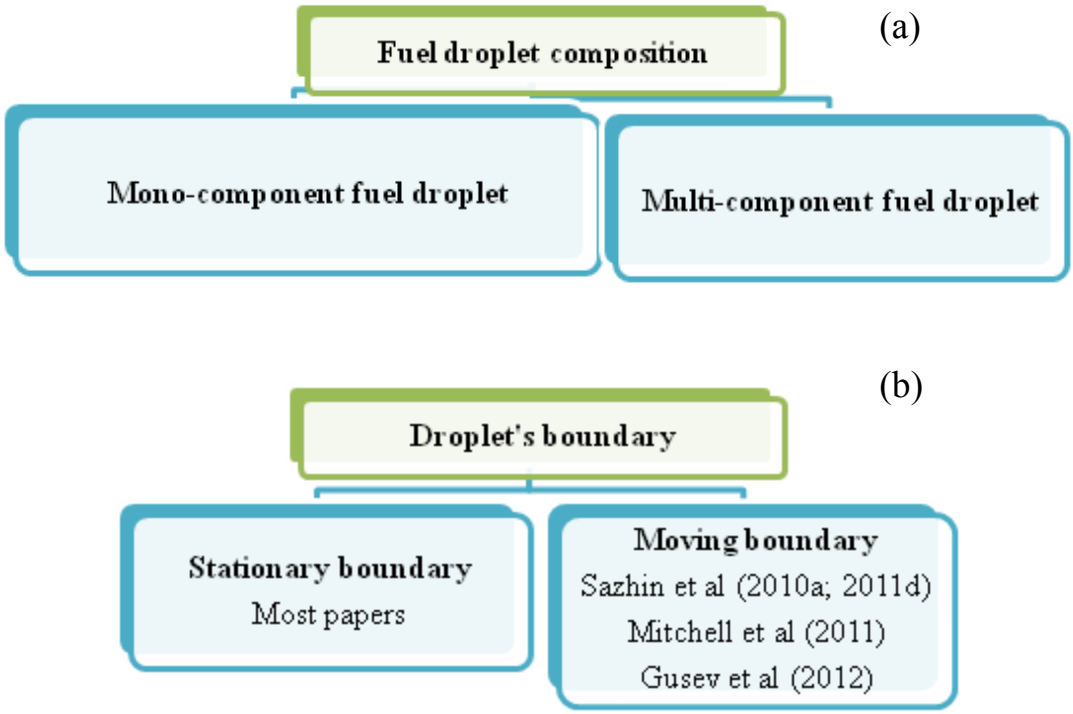


Fig. 2.3 Classifications of fuel droplet heating and evaporation models according to fuel composition (a) and droplet's boundary state (b).

Fig. 2.3a shows the classification of the heating and evaporation models according to the initial fuel composition while Fig. 2.3b shows another classification of the models based on the state of the droplet boundary; either stationary or moving boundary during individual timesteps. The second classification can be applied to mono- and multi-component droplets.

Fig. 2.4 summarises the models for mono- and multi-component fuel droplets heating and evaporation.

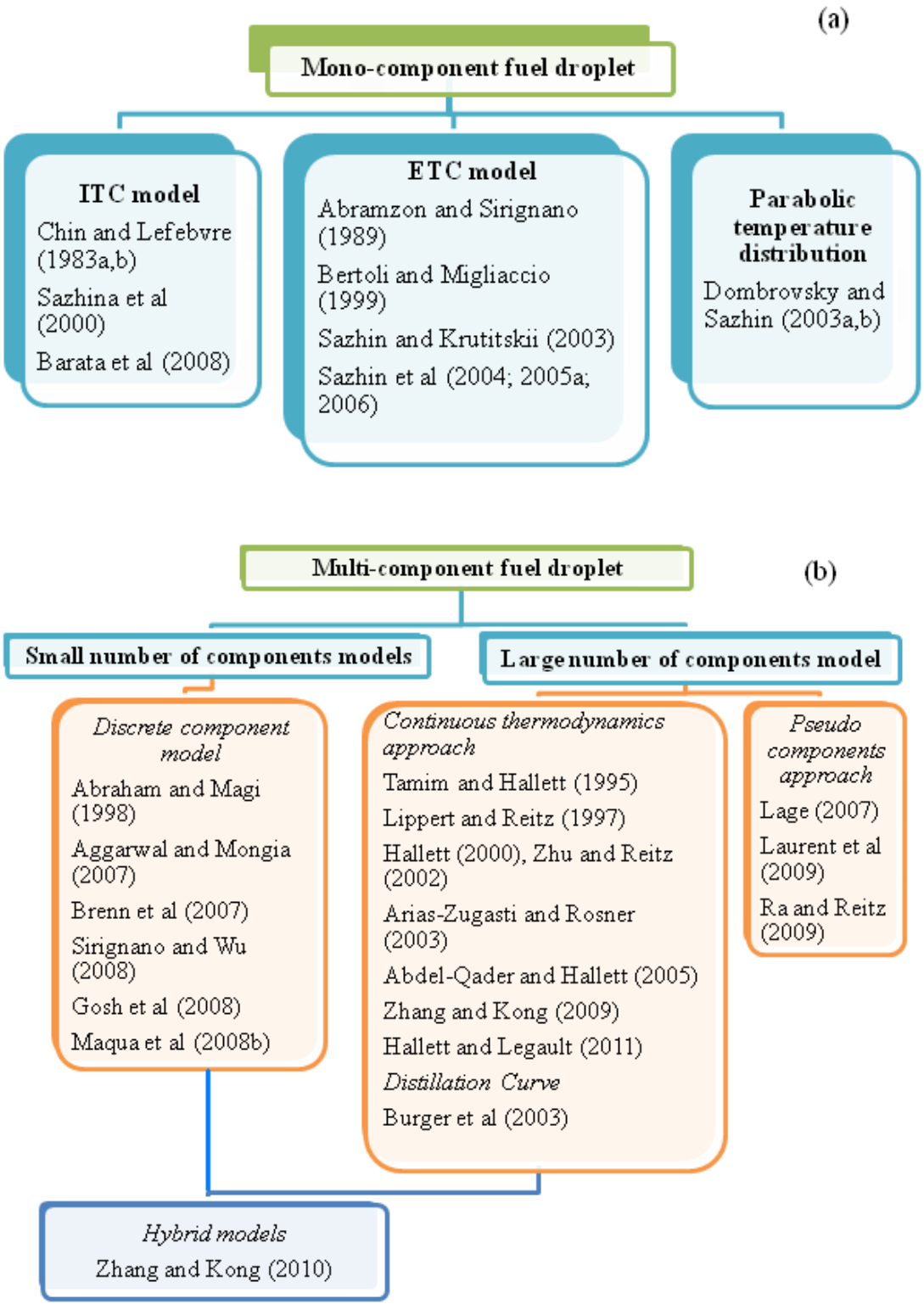


Fig. 2.4 Summary of heating and evaporating models for mono-component droplets (a) and multi-component droplets (b).

The motivation behind the thesis could be summarised as follows:

1. Investigation of the applicability of the model developed by Sazhin et al (2004) to a wider range of substances (acetone, ethanol, 3-pentanone, n-heptane, n-decane and n-dodecane) and different experimental conditions.

2. Development of a new simplified model for multi-component droplets with a small number of components (DC model) based on a new analytical solution to the species diffusion equation inside droplets and validation of this model against available experimental data and the results based on the numerical solution to temperature and species diffusion equations inside droplets.

3. Studying the effect of moving boundaries on the predictions of the simplified model based on the solution provided by Sazhin et al (2010a). Generalising the simplified model to take into account the effect of evaporating droplets on the surrounding gas and validation of the new model against available experimental data. The optimisation of the code.

4. Applying the above simplified model to the case of droplets with large number of components via a new quasi-discrete model.

5. Applying the new quasi-discrete model to the analysis of heating and evaporation of Diesel and gasoline fuels.

# 3 Monodisperse mono-component fuel droplets heating and evaporation

## 3.1 Introduction

The preliminary validation of the model developed by Sazhin et al (2004) against published experimental data was reported in Sazhin et al (2005b). This validation, however, was limited to the comparison of predicted and calculated droplet diameters or global characteristics such as the ignition delay. A more direct validation of the model, based on the comparison of the predictions of the model and the results of simultaneous measurement of average temperatures and diameters of monodisperse mono-component droplets, was reported by Maqua et al (2008a). The latter comparison, however, was limited to just two substances: ethanol and acetone in two different experimental conditions. The aim of this chapter is to perform a comparison between the predictions of the model suggested by Sazhin et al (2004) and the available experimental data, similar to the one reported in Maqua et al (2008a) but for a wider range of substances and different experimental conditions.

The substances to be considered are: acetone, ethanol, 3-pentanone, n-heptane, n-decane and n-dodecane. The experimental data used in this analysis are the same as earlier reported in Deprédurand et al (2010). These data were used in Deprédurand et al (2010) for validation of the model different from the one developed by Sazhin et al (2004). The model used by Deprédurand et al (2010), originally described by Castanet (2004) and Deprédurand (2009), is based on the assumption that both Nu and Sh numbers are estimated based on experimental data. Hence, this chapter is complementary to both earlier published papers (Maqua et al, 2008a; Deprédurand et al, 2010).

The model used in the analysis of this chapter is summarised in Section 3.2. The experimental set-up is briefly described in Section 3.3. In Section 3.4 the predictions of the model are compared with experimental data. The main results of this chapter are summarised in Section 3.5.

## 3.2 Model

The model used in this chapter was developed by Sazhin et al (2004). The equations on which this model is based, their approximations and analytical solutions where possible, are presented and discussed below.

### *3.2.1 Droplet heating*

The process of heating (or cooling) of stationary spherically-symmetric mono-component droplets is described by the transient heat conduction equation for the temperature $T \equiv T(t, R)$ in the liquid phase, Eq. (2.21) (Carslaw and Jaeger, 1986; Sazhin et al, 2004) with boundary condition without evaporation described by Eq. (2.22).

Solution (2.23) is valid for $h_0 > -1$, which is satisfied, remembering the physical background of the problem ($h > 0$). When deriving Solution (2.23) it was assumed that it is applied to individual short timesteps. In this case Sazhin et al (2004) ignored the time dependence of $h$ and $\frac{\mathrm{d}\,\mu_0(t)}{\mathrm{d}t}$ during the timesteps and assumed that $\frac{\mathrm{d}\,\mu_0(t)}{\mathrm{d}t} \approx \langle\frac{\mathrm{d}\,\mu_0(t)}{\mathrm{d}t}\rangle \equiv \mu_0'$. Note that $\mu_0$ depends on time via $T_g$ only. Ten terms in the series (2.23) were used in calculations.

To take into account the effect of droplet evaporation in analytical solution (2.23), gas temperature should be replaced by the so-called effective temperature defined as (Sazhin et al, 2004):

$$T_{\mathrm{eff}} = T_g + \frac{\rho_l L \dot{R}_d}{h}, \tag{3.1}$$

where $L$ is the latent heat of evaporation, $h$ is the convection heat transfer coefficient, linked with the Nusselt number Nu via the equation: $\mathrm{Nu} = 2R_d h/k_g$ and the value of $\dot{R}_d$ can be taken from the previous timestep and estimated based on Eq. (3.2).

The average surface temperature in a moving droplet can still be correctly predicted by Eq. (2.21), with appropriate boundary conditions, and its solution (2.23) if the liquid thermal conductivity $k_l$ is replaced by the so-called effective thermal conductivity $k_{\mathrm{eff}}$ via Eq. (2.14) but with $\mathrm{Re}_{d(l)} = \frac{2\rho_l|u_d - u_g|R_d}{\mu_l}$.

The ETC model was developed mainly for the estimation of the average surface temperature of droplets, which controls droplet evaporation (Abramzon and Sirignano, 1989; Abramzon and Sazhin, 2005; 2006). It cannot predict adequately the details of the distribution of temperature inside droplets, which include vortex

structures for non-zero droplet velocities, but these are not required in most practical engineering applications. Hence, the applicability of this model can be justified.

The actual change of droplet radius $\dot{R}_d$ is calculated as:

$$\dot{R}_d = \dot{R}_{dT} + \dot{R}_{dE}, \tag{3.2}$$

where $\dot{R}_{dT}$ is the change of droplet radius due to thermal expansion/contraction and can be calculated based on the following equation (Sazhin et al, 2005a):

$$\dot{R}_{dT} = \frac{R_d(T_{\mathrm{av},0})}{\Delta t}\left[\left(\frac{\rho_l(T_{\mathrm{av},0})}{\rho_l(T_{\mathrm{av},1})}\right)^{1/3} - 1\right], \tag{3.3}$$

where $T_{\mathrm{av},0}$ and $T_{\mathrm{av},1}$ are average droplet temperatures at the beginning $t = t_0$ and the end of the timestep $t = t_1$ and $\Delta t = t_1 - t_0$. The value of $\dot{R}_{dE}$ is controlled by fuel vapour diffusion from the droplet surface to the ambient gas. It can be found from the following equation (Sazhin, 2006):

$$\dot{R}_{dE} = \frac{\dot{m}_d}{4\pi R_d^2 \rho_l}, \tag{3.4}$$

where $\dot{m}_d$ is the droplet evaporation rate, as discussed in Section 3.2.2.

The value of $\mathrm{Nu_{iso}}$ for an isolated moving droplet is estimated based on the so-called 'M4' model via Eq. (2.31) (Abramzon and Sirignano, 1989; Sazhin et al, 2006).

### *3.2.2 Droplet evaporation*

In the case of isolated droplets, their evaporation rate is given by the following equation (Castanet et al, 2002):

$$\dot{m}_d = -2\pi R_d D_v \rho_g B_M \,\mathrm{Sh_{iso}}, \tag{3.5}$$

where $\rho_g$ is the gas density, $D_v$ is the binary diffusion coefficient of vapour in air and it is estimated as described in Appendix A and $B_M$ is the Spalding mass transfer number defined by Eq. (2.2). The mass fractions of vapour near the droplet surface $(Y_{vs})$ and in the ambient gas $(Y_{v\infty} = 0.0)$ are calculated from the Clausius–Clapeyron equation (Kuo, 1986):

$$p_v = p_{amb}\exp\left[\frac{LM}{R_u}\left(\frac{1}{T_b} - \frac{1}{T_s}\right)\right], \tag{3.6}$$

where $M$ is the molar mass, $L$ is the latent heat of evaporation of fuel, $T_b$ is the boiling temperature of the fuel and $p_{amb}$ is the ambient pressure. When deriving Eq. (3.6) it was taken into account that $p_v$ is equal to the ambient pressure when $T_s = T_b$. Note that there are typos in Eqs. (135) and (136) of Sazhin (2006).

The value of $Sh_{iso}$ for an isolated moving droplet is estimated based on the so-called 'M4' model via Eq. (2.30) (Abramzon and Sirignano, 1989; Sazhin et al 2006).

The values of the transport coefficients were taken for air at the reference temperature $T_{ref} = T_g + (T_g - T_s)/3$ (Incropera and DeWitt, 2002; Sazhin, 2006). The contribution of fuel vapour to the transport properties of air and the effects of droplets on air are ignored at this stage.

## 3.3 Experimental set-up

Droplet diameters and average temperatures were measured using the experimental set-up at the University of Nancy (France), which is described in a number of papers and theses, including (Deprédurand, 2009; Deprédurand et al, 2010). This will be only briefly summarised below.

Linear monodisperse droplet streams were generated by Rayleigh disintegration of a liquid jet undergoing vibrations generated in a piezoelectric ceramic. The fuel was pre-heated in the injector by means of externally heated circulating water. The temperature of the fuel was measured exactly at the injection point with a K type thermocouple situated within the injector body. For specific frequencies of forced mechanical vibration, the liquid jet broke up into equally spaced and mono-sized droplets. The droplets were then injected into an enclosure fed with hot air coming from an electrical heater. In order to limit the thermal losses, a resistive electrical wire was inserted within the enclosure wall so that the wall temperature could be regulated to match that of the entering air (see Fig. 3.1). A temperature of up to 673 K could be reached. The air velocity was maintained at between 0.1 and 0.3 m/s and the air flow was quietened by forcing it to go through a drilled wall and metallic foam. An estimate of the diffusion length $L_d$ could be obtained taking into account that the diffusivity $D_v$ is of the order of $10^{-5}$ $m^2/s$ and maximal diffusion duration $t$ is equal to 25 ms. The latter corresponds to the time required for a droplet to be transported through the enclosure. Based on these data, diffusion length can be estimated as $L_d = \sqrt{D_v t} \approx 0.5$ mm which is negligible compared to the inner radius of the enclosure (10 cm). This ensures non-saturated conditions. Additionally, glass windows were mounted in the wall to provide optical access. The two-colour laser-induced thermometry was used to characterize the droplet temperature, Lavieille et al (2001). The method involved the seeding of the

liquid fuel with a small quantity of a fluorescent tracer, pyromethene 597- C8. An interesting feature of pyrromethene 597-C8 relates to its temperature sensitivity that is almost unchanged when dissolved into any of the selected fuels (Deprédurand et al, 2008). The ratio of the fluorescence intensity detected in two spectral bands is a function of the temperature regardless of laser intensity, time-dependent tracer concentration, and measurement volume (Deprédurand et al, 2008). The velocity of the droplets was measured by Laser Doppler Velocimetry using the same laser light source as for the fluorescence excitation. The droplet size reduction was determined using the light scattering in the forward direction, where a stationary interference pattern is created.

Six liquid fuels were tested: acetone, ethanol, 3-pentanone, n-heptane, n-decane and n-dodecane. All physical properties of fuels are described in Appendix B.

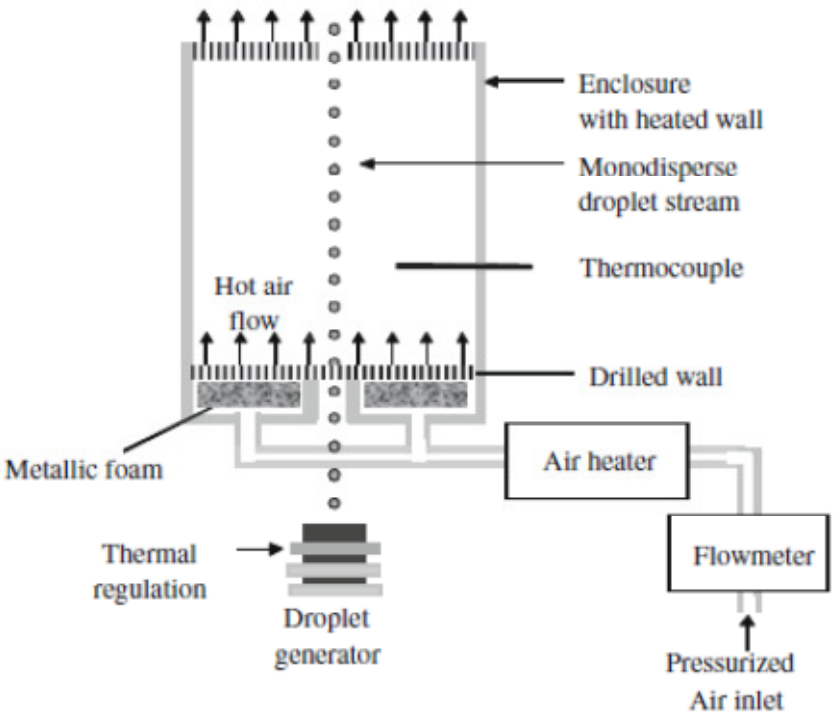


Fig. 3.1 Layout of the heated enclosure and the droplet generator used by Deprédurand et al (2010).

An investigation of a number of droplet streams was performed. The temperature, velocity and diameter of the droplets were measured simultaneously at each measurement point. The periodicity of the droplets in the chain and the steady-state nature of their stream allowed the conversion of the droplet distance from the injector into time. The focus of this analysis is based on the evolution of droplets'

temperatures and radii, starting from the moment when the first droplet was observed near the entrance to the enclosure. By placing a thermocouple at different locations it was established that air temperature $T_g$ did not vary inside the chamber. Hence, it was considered to be constant during each experiment in the modelling. The droplet absolute velocities were approximated as linear functions of time (measured from the moment of injection):

$$u_d = u_1 - u_2 t, \tag{3.7}$$

where constants $u_1$ and $u_2$ were determined for each experiment (Table 3.1), alongside the ratios $\eta_{\mathrm{Nu}} = \mathrm{Nu}/\mathrm{Nu}_{\mathrm{iso}}$ and $\eta_{\mathrm{Sh}} = \mathrm{Sh}/\mathrm{Sh}_{\mathrm{iso}}$ , describing the effects of interaction between droplets in the stream, where the subscript $_{\mathrm{iso}}$ refers to isolated droplets. The error of determination of $u_d$ is comparable with the ambient air velocities up to 0.3 m/s. This justifies the assumption that the absolute droplet velocities, estimated by Eq. (3.7), are equal to droplet velocities relative to ambient air. These velocities were used for the estimation of the Nusselt and Sherwood numbers for isolated droplets, Deprédurand et al (2010).

The values of the Nusselt and Sherwood numbers were estimated based on simultaneous measurements of droplet sizes and mean temperatures. These measurements allowed the evaluation of heat fluxes responsible for droplet heating and evaporation rates. These rates, alongside the measured time evolution of droplet mean temperatures, were used for the estimate of the convective heat flux, responsible for droplet heating, and mass flux of fuel vapour leaving the droplet. The main difficulty in converting these estimates into the estimates of the Nusselt and Sherwood numbers relates to the fact that the surface droplet temperatures $T_s$ were not directly measured and had to be estimated. This issue is addressed in (Deprédurand, 2009; Deprédurand et al, 2010), where an iterative approach based on a simplified analysis of the energy balance of evaporation was used. After the droplet surface temperatures were estimated, the values of the Nusselt and Sherwood numbers were derived from the estimated heat and mass fluxes. Using the values of these numbers for isolated droplets, calculated from the Abramzon and Sirignano (1989) model, the values of $\eta_{\mathrm{Nu}}$ and $\eta_{\mathrm{Sh}}$, presented in Table 3.1, were calculated.

Three experiments were performed with each fuel, except 3-pentanone, for which only two experiments were performed. The values of $T_g$, distance parameter *C* (ratio of the distance between droplets and their diameter), initial droplet diameters

$D_{d0}$ (measured directly when the first droplets near the entrance to the enclosure were observed), $\eta_{\mathrm{Nu}}$, $\eta_{\mathrm{Sh}}$, $u_1$ and $u_2$ for each experiment are presented in Table 3.1, alongside boiling and critical temperatures ($T_b$ and $T_{cr}$) for each substance (Poling et al, 2000). The values of $C$ are shown to indicate the closeness of droplets in these experiments.

| Case | Parameter | Acet | Ethan | 3-Pen | n-Hep | n-Dec | n-Dod |
|---|---|---|---|---|---|---|---|
| | $T_b$ (K) | 329.22 | 351.80 | 375.14 | 371.57 | 477.30 | 489.48 |
| | $T_{cr}$ (K) | 508.10 | 513.92 | 561.50 | 540.20 | 617.70 | 658.00 |
| **1** | $T_g$ (K) | 640 | 643 | 634 | 644 | 643 | 643 |
| | $C$ | 4.5 | 4.3 | 4.9 | 4.4 | 3.7 | 4.6 |
| | $D_{0d}$ ($\mu$m) | 122.6 | 119.6 | 118.2 | 131.1 | 121.5 | 110.0 |
| | $\eta_{\mathrm{Nu}}$ | 0.42 | 0.26 | 0.23 | 0.38 | 0.18 | 0.19 |
| | $\eta_{\mathrm{Sh}}$ | 0.43 | 0.38 | 0.53 | 0.57 | 0.18 | 0.19 |
| | $u_1$ (m/s) | 11.16 | 9.869 | 10.86 | 12.8 | 9.59 | 9.246 |
| | $u_2$ (m/(s.ms)) | 0.198 | 0.214 | 0.254 | 0.329 | 0.220 | 0.281 |
| **2** | $T_g$ (K) | 645 | 643 | 645 | 645 | 645 | 644 |
| | $C$ | 5.5 | 6.1 | 4.0 | 5.3 | 4.4 | 6.9 |
| | $D_{0d}$ ($\mu$m) | 132.2 | 130.28 | 123.3 | 134.2 | 128.37 | 129.0 |
| | $\eta_{\mathrm{Nu}}$ | 0.43 | 0.42 | 0.22 | 0.35 | 0.24 | 0.22 |
| | $\eta_{\mathrm{Sh}}$ | 0.42 | 0.82 | 0.33 | 0.84 | 0.24 | 0.22 |
| | $u_1$ (m/s) | 14.12 | 12.64 | 9.454 | 15.44 | 11.88 | 13.14 |
| | $u_2$ (m/(s.ms)) | 0.276 | 0.268 | 0.224 | 0.446 | 0.329 | 0.573 |
| **3** | $T_g$ (K) | 647 | 644 | n/a | 647 | 647 | 643 |
| | $C$ | 3.3 | 3.1 | n/a | 3.8 | 5.4 | 3.0 |
| | $D_{0d}$ ($\mu$m) | 107.2 | 112.4 | n/a | 122.8 | 124.8 | 98.99 |
| | $\eta_{\mathrm{Nu}}$ | 0.35 | 0.36 | n/a | 0.28 | 0.18 | 0.22 |
| | $\eta_{\mathrm{Sh}}$ | 0.26 | 0.38 | n/a | 0.50 | 0.18 | 0.22 |
| | $u_1$ (m/s) | 7.122 | 6.889 | n/a | 10.56 | 13.55 | 6.091 |
| | $u_2$ (m/(s.ms)) | 0.113 | 0.123 | n/a | 0.244 | 0.307 | 0.218 |

Table 3.1 The values of $T_g$, $C$, $D_{d0}$, $\eta_{\mathrm{Nu}}$, $\eta_{\mathrm{Sh}}$, $u_1$ and $u_2$ for three experiments with acetone, ethanol, 3-pentanone, n-heptane, n-decane and n-dodecane droplets (abbreviated as acet, ethan, 3-pen, n-hep, n-dec and n-dod). In the case of n-decane and n-dodecane, the values of $\eta_{\mathrm{Sh}}$ were not estimated experimentally, but assumed to be equal to $\eta_{\mathrm{Nu}}$.

The uncertainties in the measurement of the droplet diameters were expected to be about ±0.5 μm in most cases and the uncertainties in the temperature measurements were expected to be about ±1 K. Depending on the fuel and the experimental conditions, the uncertainties in the estimates of $\eta_{\mathrm{Sh}}$ and $\eta_{\mathrm{Nu}}$ were expected to be between 2% and 25% (Deprédurand et al, 2010). However, in the case of n-decane and n-dodecane, which have particularly low volatility, the mass loss due to evaporation was so low that it was not possible to determine accurately a

value for $\eta_{\mathrm{Sh}}$. Therefore, for these cases, the values of $\eta_{\mathrm{Sh}}$ were not estimated experimentally and they were assumed to be equal to $\eta_{\mathrm{Nu}}$.

### 3.4 Results

The plots of temperature versus time for Case 1 for all fuels under consideration calculated using the described model and obtained in the experiment (reproduced from Deprédurand et al, 2010) are shown in Figs. 3.2-3.7. The values of parameters shown in Table 3.1 were used in calculations. The calculations were performed ignoring the interaction between droplets (indicated by subscript $_{\mathrm{iso}}$) and taking them into account, based on the values of $\eta_{\mathrm{Sh}}$ and $\eta_{\mathrm{Nu}}$ given in Table 3.1. Time in all figures is measured from the moment of injection.

The calculations started at the time when the droplets were first observed near the entrance to the chamber. The observed temperatures and radii of these droplets were used as the initial temperatures and radii in the model. It was assumed that initially there was no temperature gradient inside droplets.

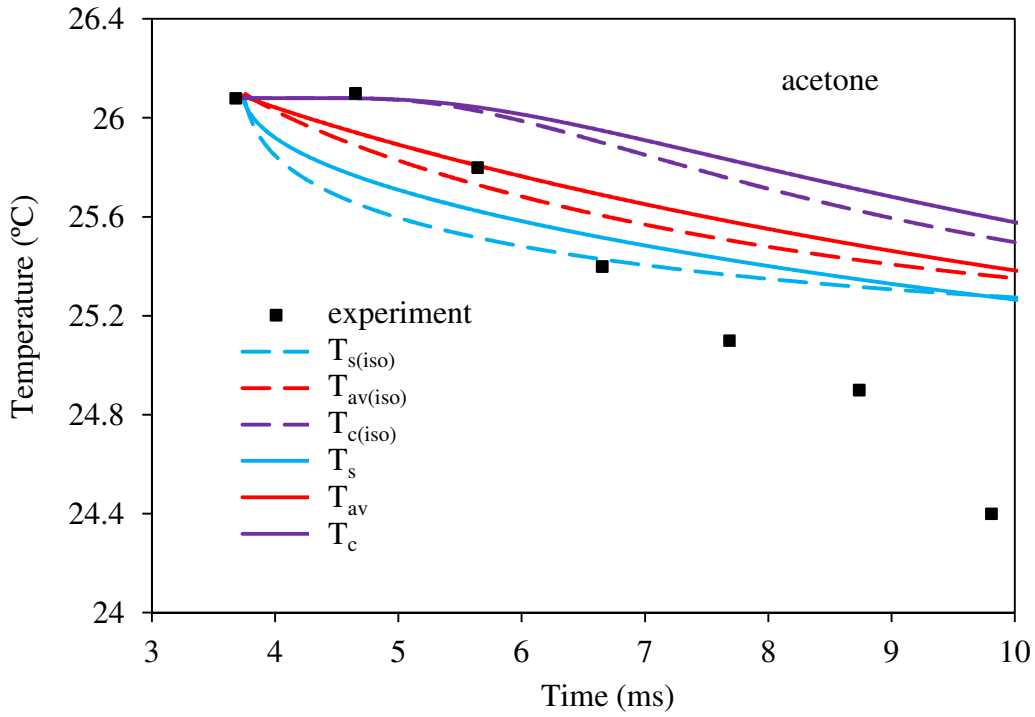


Fig. 3.2 The plots of the time evolution of the experimentally observed temperatures of acetone droplets for Case 1, and temperatures at the surface of these droplets ($T_s$), average temperatures in the droplets ($T_{\mathrm{av}}$) and the temperatures at the centre of the droplets ($T_c$), predicted by the models ignoring the interactions between droplets (indicated by the subscript $_{\mathrm{iso}}$), and taking into account these interactions. The input parameters of the models were taken from Table 3.1.

As follows from Figs. 3.2-3.7, the plots referring to interacting and non-interacting (isolated) droplets are noticeably different for all substances. Similarly, the plots referring to the temperatures at the centres of the droplets, average temperatures, and the temperatures at the surfaces of the droplets are well separated. This result is similar to the one reported by Maqua et al (2008a), and it shows the limitation of the assumption, which is widely used in CFD codes, that the gradient of temperature inside droplets can be ignored.

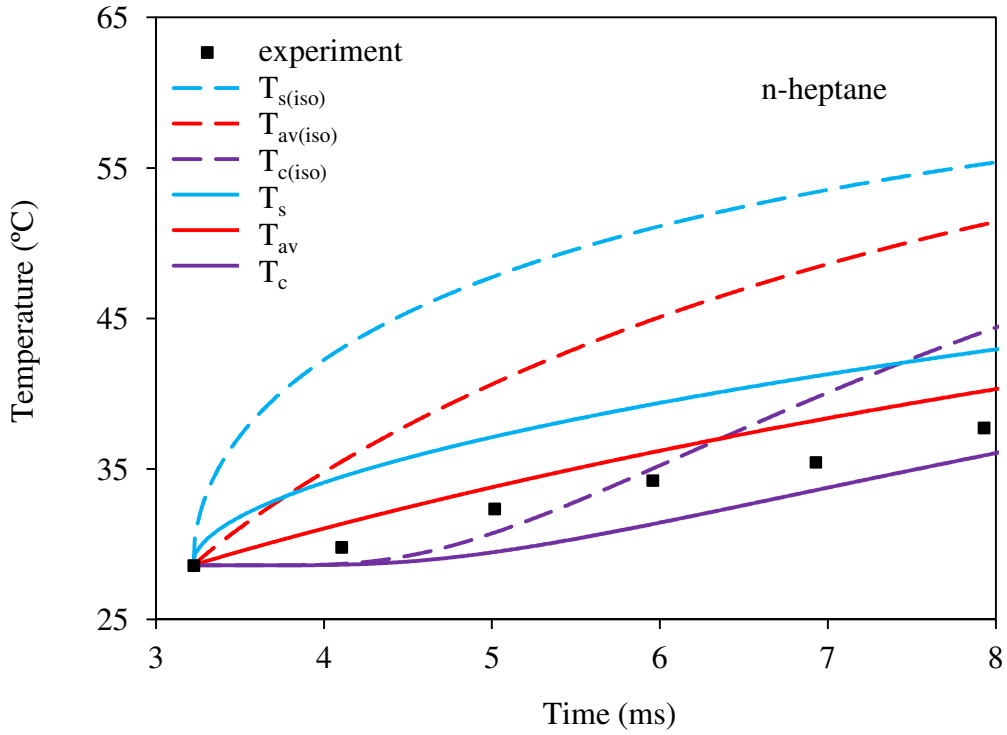


Fig. 3.3 The same as Fig. 3.2 but for n-heptane droplets.

The observed temperatures of acetone droplets, shown in Fig. 3.2, look rather different from the ones predicted by the model. Note, however, that the difference between the average temperature, predicted by the model, taking into account the interaction between droplets ($T_{\mathrm{av}}$), and the experimentally observed temperatures is always less than 1 °C, and can be naturally attributed to the uncertainty of the measurements, and uncertainties of the input parameters used in calculations.

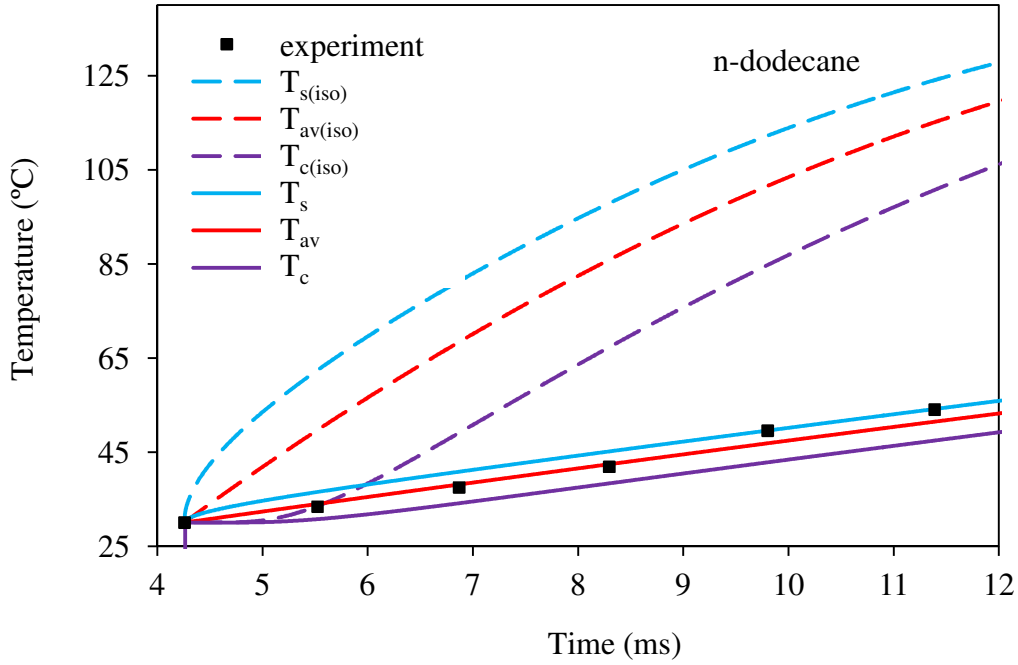


Fig. 3.4 The same as Fig. 3.2 but for n-dodecane droplets.

In the case of n-heptane and n-dodecane droplets shown in Figs. 3.3 and 3.4, the closeness between the experimentally observed temperatures and $T_{av}$ was the most visible, compared with other droplets. However, even in this case, the actual deviation between these temperatures sometimes exceeds 1 °C. This means that the model cannot predict the observed average droplet temperatures with errors less than about 1 °C. For both of these substances, the experimentally observed temperatures always lie between the temperatures $T_s$ and $T_c$ , predicted by the model, taking into account the interaction between droplets.

In the case of ethanol droplets shown in Fig. 3.5, the experimentally observed temperatures were closer to the ones predicted by the model, taking into account the interaction between droplets, than the ones ignoring this interaction. However, the deviation between the experimental points and $T_{av}$ for these droplets (up to about 3 °C) was larger than in the case of acetone, n-heptane and n-dodecane droplets.

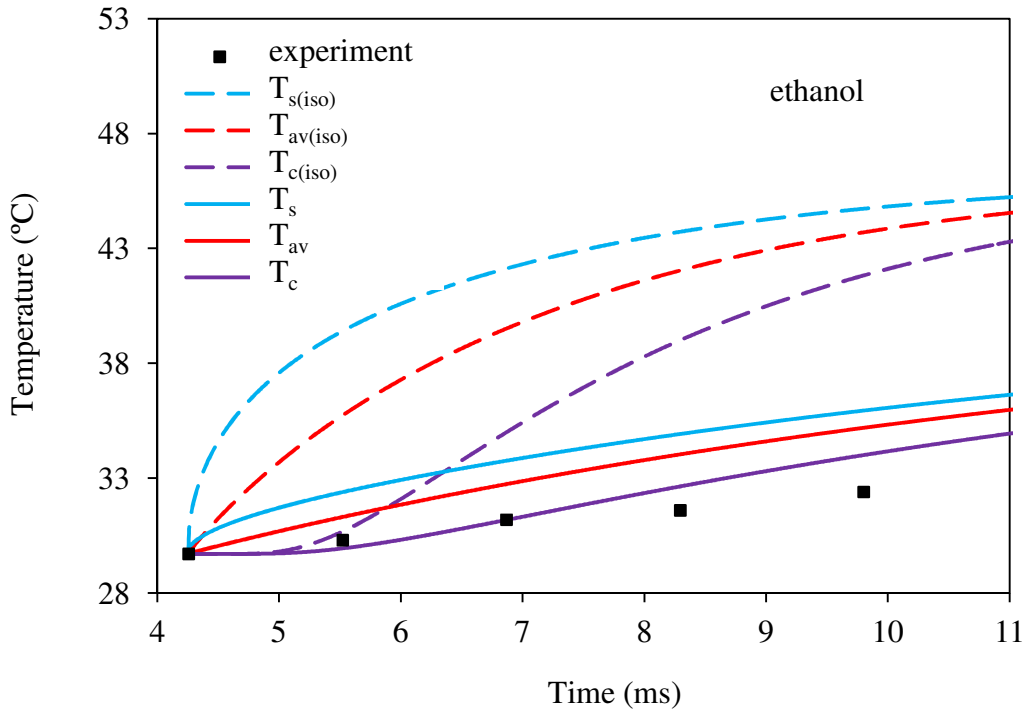


Fig. 3.5 The same as Fig. 3.2 but for ethanol droplets.

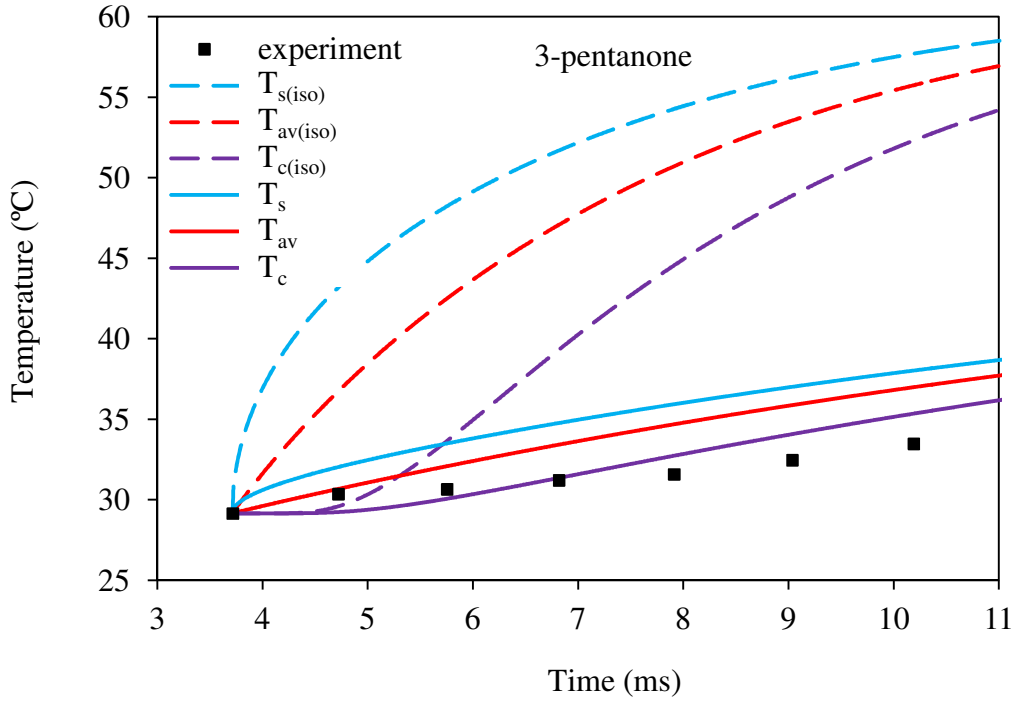


Fig. 3.6 The same as Fig. 3.2 but for 3-pentanone droplets.

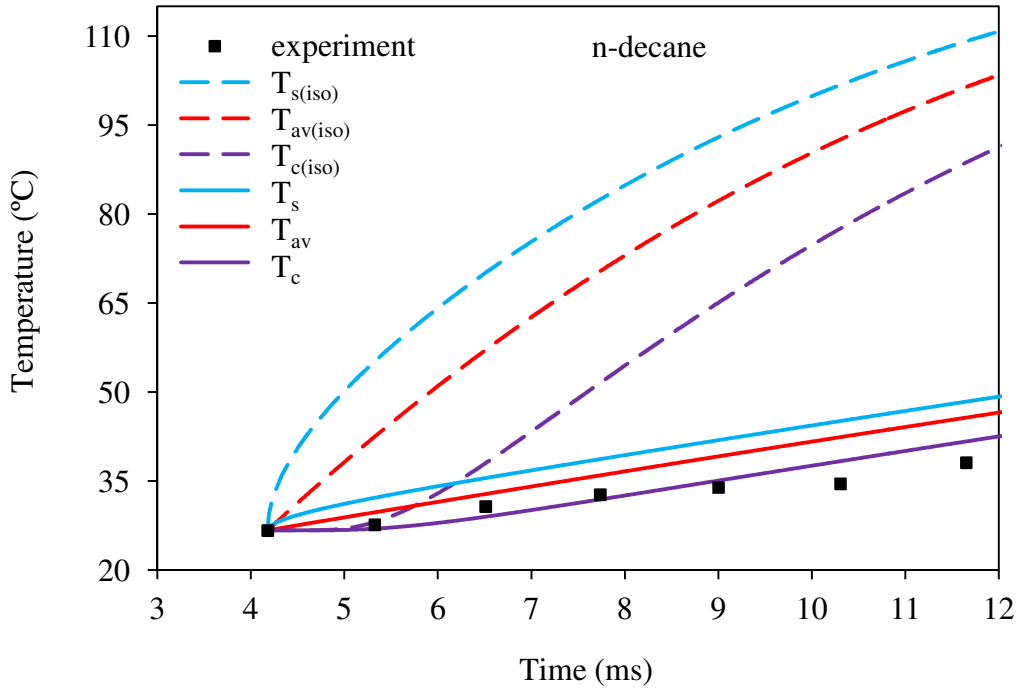


Fig. 3.7 The same as Fig. 3.2 but for n-decane droplets.

The temperatures for 3-pentanone and n-decane shown in Figs. 3.6 and 3.7 were generally similar to those for ethanol, with the maximal deviation between the experimental points and $T_{\mathrm{av}}$ about 3 °C for 3-pentanone and about 6 °C for n-decane.

The plots of normalised droplet radii $R_d/R_{d0}$ versus time for Case 1 for all six substances, calculated using the described model and obtained in the experiment, are shown in Figs. 3.8 and 3.9. The initial values of droplet radii were taken to be equal to those for the droplets for which the first measurements of droplet temperature were taken. When calculating the time evolution of $R_d$, both droplet evaporation and thermal expansion were taken into account based on Eq. (3.2). The values of parameters used for these calculations are given in Table 3.1. Note that in contrast to Deprédurand et al (2010), the plots of the ratios of radii rather than the ratios of radii squared are presented. The latter would have been justified if the analysis had been focused on droplet evaporation beyond the heat-up period, when the $d^2$-law is valid. In our case, the focus is on the heat-up period itself.

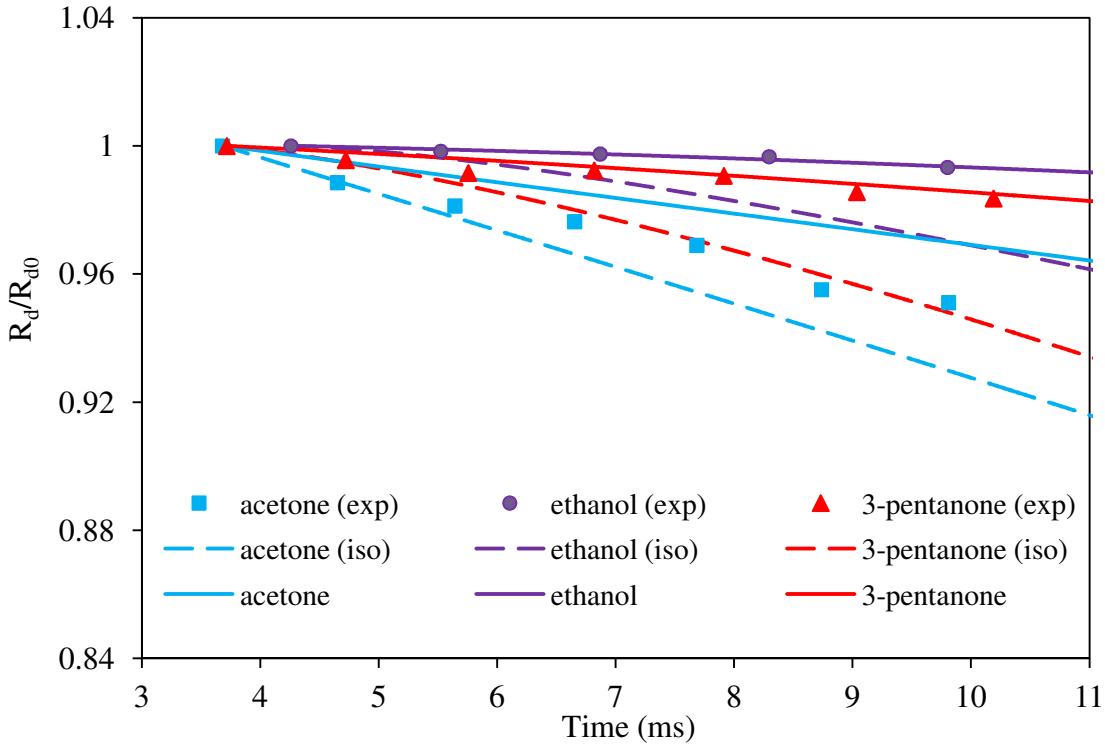


Fig. 3.8 The plots of the time evolution of the experimentally observed (symbols) and modelled (curves) normalised droplet radii $R_d/R_{d0}$ for acetone, ethanol and 3-pentanone droplets for Case 1. Models ignoring the interactions between droplets (indicated by the subscript $_{iso}$), and taking into account these interactions, were used. The input parameters of the models were taken from Table 3.1.

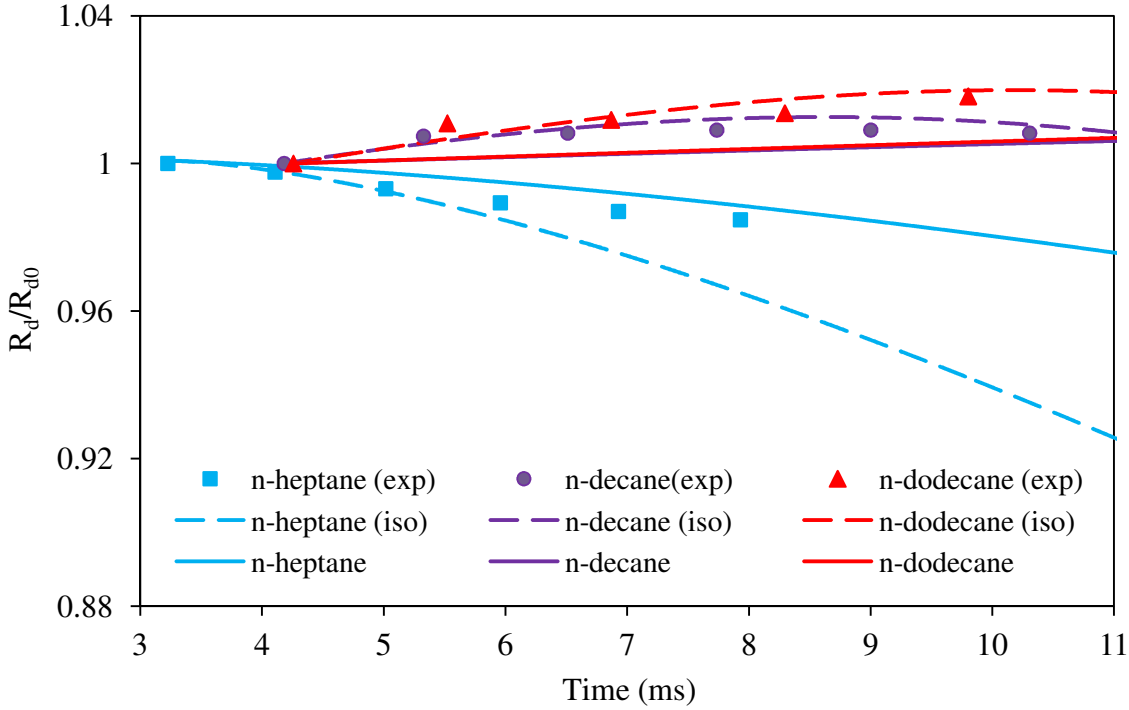


Fig. 3.9 The same as Fig. 3.8 but for n-heptane, n-decane and n-dodecane droplets.

As follows from Figs. 3.8 and 3.9, the effects of interaction between droplets lead to a decrease in the rate of reduction of their radii in the case of acetone,

ethanol, 3-pentanone and n-heptane, but to a slowing down of the increase of these radii in the case of n-decane and n-dodecane in agreement with Castanet et al (2005). In the latter case, the effect of the thermal expansion of droplets dominates over the effects of evaporation. In the case of ethanol, 3-pentanone, n-heptane and n-decane the agreement between experimental plots and predictions of the model, taking into account the interaction between droplets, looks almost ideal. However, for acetone and n-dodecane the experimental data lie between the predictions of the models ignoring the interaction between droplets and taking them into account. Even in the case of these two substances, the deviation between the experimental results and the predictions of the model, taking into account the interaction between droplets, does not exceed about 2%.

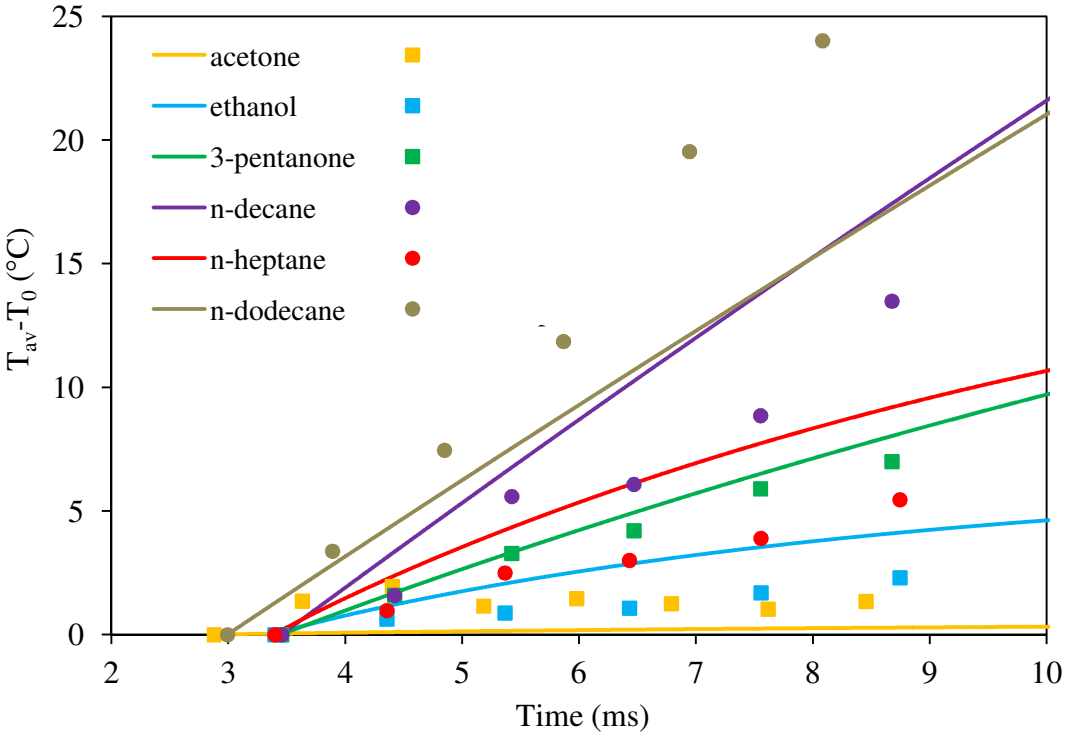


Fig. 3.10 The plots of the time evolution of the experimentally observed droplet temperatures $T_{av}$ - $T_0$, where $T_0$ are the initial droplet temperatures and the average temperatures of droplets $T_{av}$, predicted by the model taking into account the interaction between droplets. The results for acetone, ethanol, 3-pentanone, n-heptane, n-decane and n-dodecane droplets for Case 2 are shown. The input parameters of the models were taken from Table 3.1.

For the results referring to Cases 2 and 3, the analysis is restricted to comparison of the experimental data with the average temperatures and $R_d/R_{d0}$ predicted by the model taking into account the interaction between droplets, as was done by Deprédurand et al (2010). Instead of the actual droplet average temperatures

$T_{av}$, studied for Case 1, the analysis for Cases 2 and 3 is focused on the difference between these temperatures and the initial droplet temperatures $T_0$. The corresponding plots for $T_{av}$ - $T_0$ versus time for Case 2 for all six substances are shown in Fig. 3.10. As follows from this figure, although the trends predicted by the model are similar to the ones observed experimentally, there are noticeable deviations between the actual values of predicted and observed average droplet temperatures. The maximal deviation between them is seen for n-decane and n-dodecane droplets. The minimal deviation between them is seen for 3-pentanone droplets.

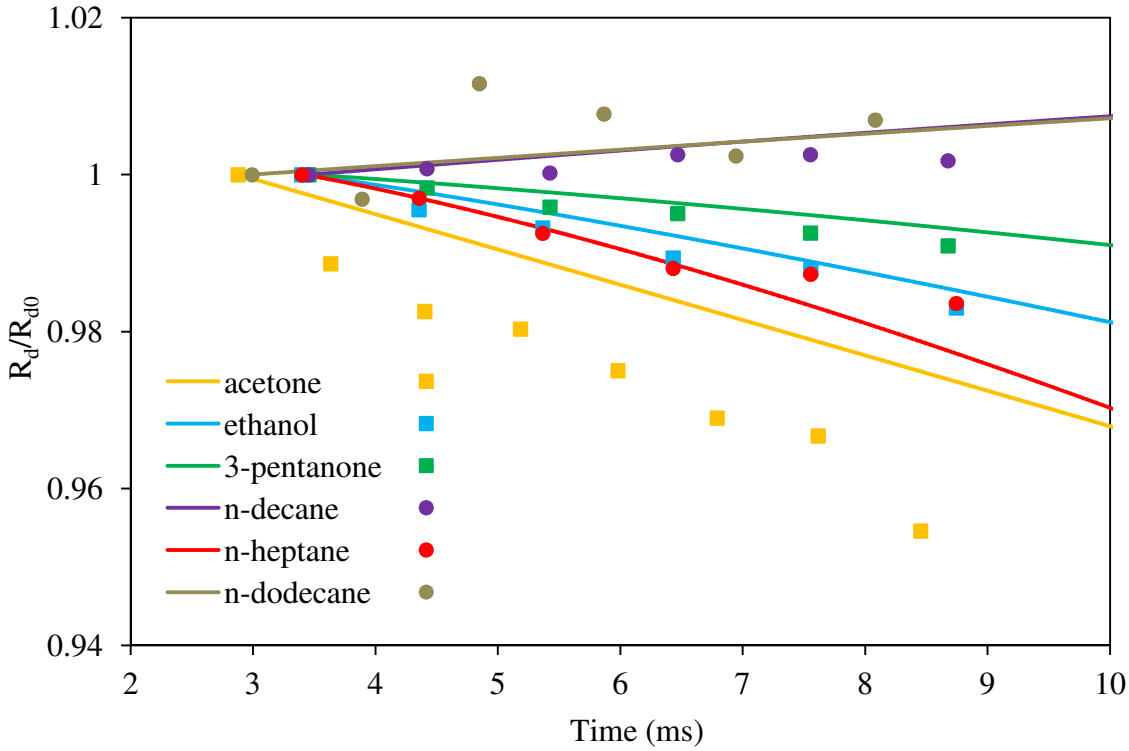


Fig. 3.11 The same as Fig. 3.10 but for $R_d/R_{d0}$.

The plots of $R_d/R_{d0}$ versus time for Case 2 for the same substances as in Fig. 3.10, are shown in Fig. 3.11. As one can see from this figure, the trends predicted by the model are similar to the ones observed experimentally, but there are noticeable deviations between the observed and predicted values of this ratio, as in the case of Fig. 3.10. The maximal deviation between these ratios (up to almost 2%) is seen for acetone droplets. The minimal deviation between these ratios is seen for 3-pentanone droplets. Hence, for Case 2 the best agreement between experimental and modelled results for both temperatures and radii is observed for 3-pentanone droplets.

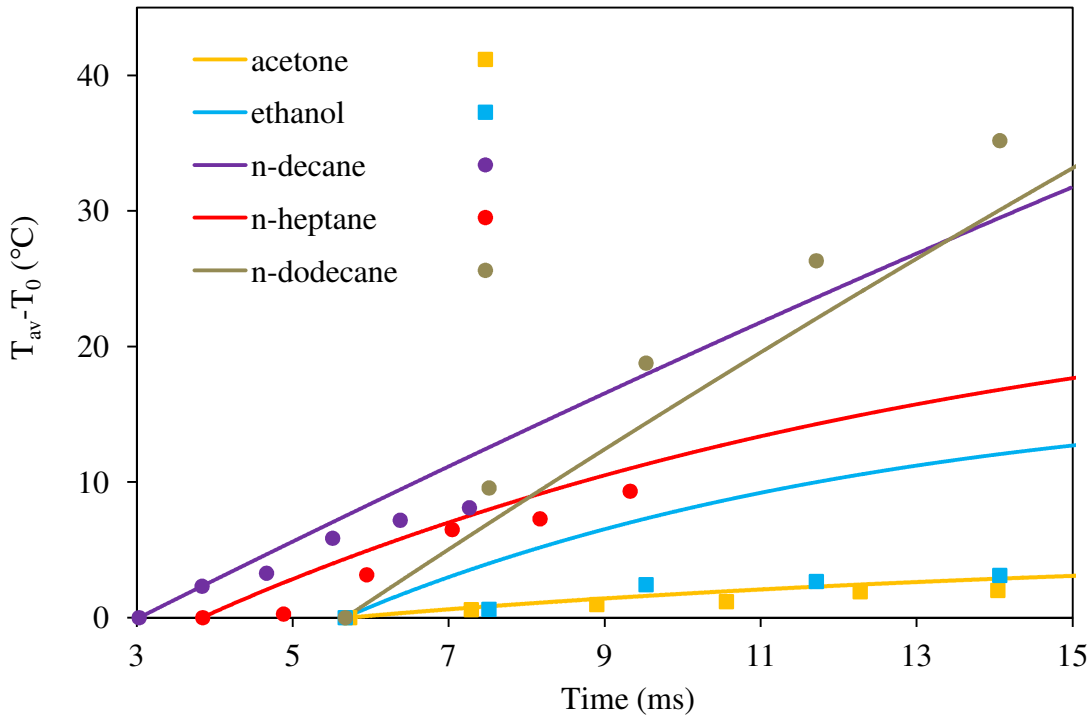


Fig. 3.12 The same as Fig. 3.10 but for Case 3, except without the results for 3-pentanone.

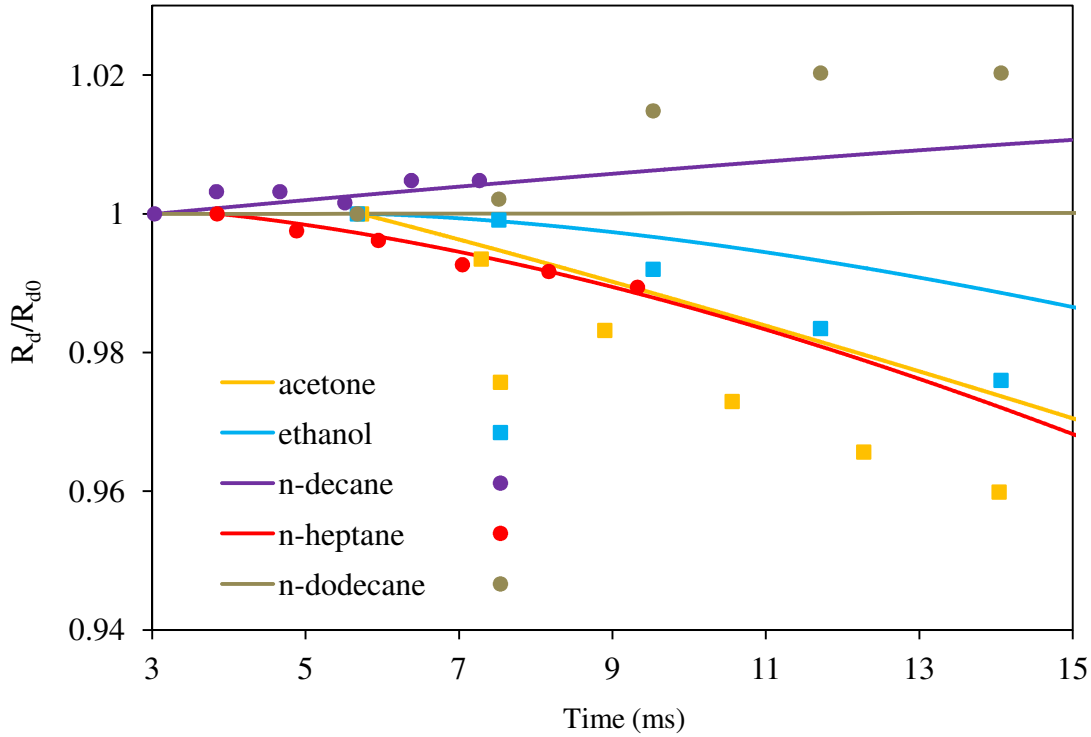


Fig. 3.13 The same as Fig. 3.12 but for $R_d/R_{d0}$.

The plots for $T_{av}$ -$T_0$ versus time for Case 3 for acetone, ethanol, n-heptane, n-decane and n-dodecane (there is no data for 3-pentanone for Case 3) are shown in Fig. 3.12. As one can see from this figure, the agreement between experimental and

modelled results is very good for acetone, while the deviation between the experimentally observed temperatures and those predicted by the model could reach more than about 5 °C for ethanol and n-dodecane (although the observed and predicted trends for both substances are the same). The plots of $R_d/R_{d0}$ versus time for Case 3 for the same substances as in Fig. 3.12 are shown in Fig. 3.13. As can be seen from this figure, the best agreement between experimental and modelled results can be seen for n-decane and n-heptane, and the worst for acetone and n-dodecane. However, even in the case of acetone and n-dodecane, both experimental and modelled results show the same trends and the deviation between them does not exceed 2%.

## 3.5 Conclusions of Chapter 3

Heating and evaporation of monodisperse acetone, ethanol, 3-pentanone, n-heptane, n-decane and n-dodecane droplets in ambient air at fixed temperature and atmospheric pressure have been studied numerically and validated against available experimental results. Droplet initial diameters varied from 99 to 135 $\mu$m, while ambient air temperatures varied from 634 to 647 K. The numerical model took into account the finite thermal conductivity of droplets and recirculation inside them based on the Effective Thermal Conductivity model and the analytical solution to the heat conduction equation inside droplets. The initial values of droplet temperatures and radii were assumed to be equal to those observed experimentally for the first recorded droplet. It was assumed that initially there was no temperature gradient inside droplets.

It is pointed out that the interactions between droplets lead to noticeable reduction of their heating in the case of ethanol, 3-pentanone, n-heptane, n-decane and n-dodecane droplets, and reduction of their cooling in the case of acetone. The interaction between droplets leads to a decrease in the rate of reduction of their radii in the case of acetone, ethanol, 3-pentanone and n-heptane, but to a slowing down of the increase of these radii in the case of n-decane and n-dodecane. In the latter case, the effect of the thermal expansion of droplets dominates over the effects of evaporation.

Although the trends of experimentally observed droplet temperatures and radii are the same as predicted by the model, taking into account the interaction between droplets, the values of the predicted droplet temperatures can differ from the

observed ones by up to about 8 °C, and the actual values of the predicted droplet radii can differ from the observed ones by up to about 2%. Combining the above results and those reported previously by Maqua et al (2008a), it could be concluded that the ETC model, based on the analytical solution to the heat conduction equation inside droplets, can predict the observed average temperature of droplets with possible errors not exceeding several °C, and observed droplet radii with possible errors not exceeding 2% in most cases. These results confirm the previous conclusions of Sazhin et al (2005a,b; 2006) that this model can be recommended for implementation into CFD codes and used for multidimensional modelling of spray heating and evaporation based on these codes.

# 4 A simplified model for bi-component droplet heating and evaporation

## 4.1 Introduction

The focus of this chapter is on the extension of the model developed by Sazhin et al (2004; 2005a), described in Chapters 2 and 3, for mono-component droplets to the case of multi-component droplets. At this stage only the simplest case of bi-component droplets is considered, as in (Klingsporn and Renz, 1994; Lage et al, 1995; Maqua et al, 2008b), which allows developing a better understanding of the underlying physics of the processes involved. The new model is much simpler than the previously suggested models (Maqua et al, 2008b) which make it potentially attractive for implementation into CFD codes. The new model is based on the assumption that the droplet radius remains constant during each timestep. The predictions of the model are compared with the available experimental data (the measured time evolution of droplet temperatures in monodisperse bi-component (ethanol/acetone) droplet streams reproduced from Maqua et al, 2008b). The new model is based on the analytical solutions to heat conduction and species diffusion equations within the droplet. These analytical solutions are then incorporated into a numerical code. The results based on the analytical solutions to the above-mentioned equations will be compared with the results based on the numerical solutions to these equations.

Sazhin et al (2010a; 2011d) and Mitchell et al (2011) showed that the assumption of constant droplet radius during the timestep is not at first borne out and can lead to noticeable deviations from the results predicted by the models, taking into account this effect. In the current chapter, the new simplified model will be generalised to take into account this effect. The results will be compared with those predicted by the model ignoring this effect. Finally a sensitivity study of the results with respect to the choice of the correlation for the gas binary diffusion coefficient will be investigated. The analysis will be focused on bi-component droplets, but the results can be easily generalised to the case of multi-component droplets (Discrete Component model).

The basic equations and approximations of the new simplified model are described in Section 4.2. The experimental set-up (used for validation of our new

models) for measurements of droplet temperatures in monodisperse bi-component (ethanol/acetone) droplet streams is briefly described in Section 4.3. In Section 4.4, some results of the numerical solutions to the basic equations for the values of parameters relevant to the experimental set-up described in Section 4.3 are presented. In Section 4.5 the results, based on the analytical and numerical solutions to the equations of heat transfer and species diffusion inside droplets, are compared for experimental conditions described in Section 4.3. In Section 4.6 the results, taking and not taking into account the effects of the moving boundary, predicted by the model based on the analytical solutions to the equations of heat transfer and species diffusion inside droplets, are compared for the values of parameters relevant to experimental set-up described in Section 4.3 and other related conditions. The effect of the choice of the binary diffusion coefficient correlation on droplet heating and evaporation for experimental conditions described in Section 4.3 is discussed in Section 4.7. The main results of this chapter are summarised in Section 4.8.

## 4.2 Basic equations and approximations

The model developed in this chapter is based on the equations describing liquid phase heating and evaporation, species diffusion in the liquid phase and species mass fractions at the surface of the droplets. These equations and their approximations and analytical solutions, where appropriate, are presented and discussed below.

### *4.2.1 Droplet heating*

The process of heating (or cooling) for stationary spherically-symmetric multi-component droplets is the same as in the case of mono-component droplets (Sazhin et al, 2004), described in Chapters 2 and 3, where the temperature of the droplet $T \equiv T(t, R)$ can be calculated from Eq. (2.23). This model is equally applicable to mono-component and multi-component droplets. The physical properties of multi-component droplets are calculated as described in Appendix C. The physical properties of acetone and ethanol are described in Appendix B.

### *4.2.2 Droplet evaporation*

In the case of multi-component droplets the problem of modelling droplet evaporation is complicated by the fact that different species diffuse at different rates, and the evaporation rate of one of the species is affected by the evaporation rate of

other species. In Deprédurand et al (2010), the analysis of evaporation of multi-component droplets led to the following expression for $\dot{m}_d$ (total evaporation rate):

$$\dot{m}_d = -2\pi R_d D_{vi} \rho_g B_{Mi}\, \mathrm{Sh}_{\mathrm{iso}(i)}, \tag{4.1}$$

where $B_{Mi}$ is the species Spalding mass transfer number defined as:

$$B_{Mi} = \frac{Y_{vis} - Y_{vi\infty}}{\epsilon_i - Y_{vis}}, \tag{4.2}$$

where $D_{vi}$ is the diffusion coefficient of species $i$ in air, $\mathrm{Sh}_{\mathrm{iso}(i)}$ is defined by (2.30) replacing $B_M$ by $B_{Mi}$ and $D_v$ by $D_{vi}$ and $\epsilon_i$ is the evaporation rate of species $i$ defined by Eq. (4.7). As follows from Eq. (4.7) one can see that $B_M = B_{Mi}$. Hence, for stationary droplets this leads to the paradox that the same value of $\dot{m}_d$ is predicted by Eq. (4.1) for different $D_{vi}$. This paradox is resolved by the fact that although Eq. (4.1) is correct, the value of $\mathrm{Sh}_{\mathrm{iso}(i)}$ cannot be approximated by the analogue of Eq. (2.30) which is implicitly based on the assumption that the evaporating species do not affect each other.

The analysis of $\dot{m}_i = \epsilon_i \dot{m}_d (\dot{m}_d = \sum_i \dot{m}_i)$ in this chapter is based on Eq. (3.5), assuming that the mixture of vapour species can be treated as a separate gas, similar to treating the mixture of nitrogen, oxygen and carbon dioxide as air ($Y_{vs} = \sum_i Y_{vis}$). The value of $D_v$ is estimated as described in Section 4.4.4 based on the so-called Wilke-Lee formula (Eq. (4.33)).

The calculations of $\mathrm{Sh}_{\mathrm{iso}}$ and $\mathrm{Nu}_{\mathrm{iso}}$ are based on Eqs. (2.30) and (2.31) respectively. The corrections to $\mathrm{Sh}_{\mathrm{iso}}$ and $\mathrm{Nu}_{\mathrm{iso}}$ due to the finite distance between droplets are calculated as (Castanet et al, 2007; Maqua et al, 2008b; Deprédurand et al, 2010):

$$\eta = \frac{\mathrm{Sh}}{\mathrm{Sh}_{\mathrm{iso}}} = \frac{\mathrm{Nu}}{\mathrm{Nu}_{\mathrm{iso}}} = 1 - 0.57\left(1 - \frac{1-\exp[-0.13(C-6)]}{1+\exp[-0.13(C-6)]}\right), \tag{4.3}$$

where $C$ is the distance parameter. Note that, there is a typo in this equation at Maqua et al (2008b). For the mixtures under consideration, the values of $C$ are presented in Table 4.1.

### *4.2.3 Species diffusion in the liquid phase*

Assuming that the processes inside droplets are spherically-symmetric (no recirculation), equations for mass fractions of liquid species $Y_{li} \equiv Y_{li}(t, R)$ can be presented in the following form (Sirignano, 1983; Sazhin, 2006):

$$\frac{\partial Y_{li}}{\partial t} = D_l \left(\frac{\partial^2 Y_{li}}{\partial R^2} + \frac{2}{R}\frac{\partial Y_{li}}{\partial R}\right), \tag{4.4}$$

where $i$ = 1,2 (refers to all species), $D_l$ is the liquid mass diffusivity. It is calculated as described in Appendix C.

Eq. (4.4) is solved for the following boundary condition (Sirignano, 1983; Sazhin, 2006):

$$\alpha(\epsilon_i - Y_{lis}) = -D_l \frac{\partial Y_{li}}{\partial R}\Big|_{R=R_d-0}, \tag{4.5}$$

and the initial condition $Y_{li}$ ($t$=0) = $Y_{li0}$($R$), where $Y_{lis}$ = $Y_{lis}$($t$) are liquid components' mass fractions at the droplet surface,

$$\alpha = \frac{|\dot{m}_d|}{4\pi\rho_l R_d^2} = \left|\dot{R}_{dE}\right|. \tag{4.6}$$

Assuming that species concentrations in the ambient gas are equal to zero, the values of $\epsilon_i$ can be found from the following relation (Faeth, 1983; Continillo and Sirignano, 1991):

$$\epsilon_i = \frac{Y_{vis}}{\sum_i Y_{vis}}, \tag{4.7}$$

where the subscript $v$ indicates the vapour phase. $\epsilon_i$ is assumed to be constant and determined by the values of $Y_{vis}$ at the beginning of the timestep. The conditions $\epsilon_i$ = const. and α = const. can always be guaranteed for sufficiently small timesteps.

As in the case of Eq. (2.21), we are interested only in a solution which is continuously differentiable twice in the whole domain. This implies that $Y_{li}$ should be bounded for $0 \le R < R_d$. Moreover, the physical meaning of $Y_{li}$, as the mass fraction, implies that $0 \le Y_{li} \le 1$.

Eq. (4.4) with boundary condition (4.5) has essentially the same structure as Eq. (2.21) with boundary condition (2.22). The former equations can be obtained from the latter by replacing $T$ with $Y_{li}$, $\kappa$ with $D_l$, $T_g$ with $\epsilon_i$, $T_s$ with $Y_{lis}$ and $k_l/h$ with $-D_l/\alpha$. However, although Eq. (4.4) looks rather similar to Eq. (2.21), the solution of Eq. (2.21) (see Expression (2.23)) cannot be used for (4.4). The reason for this is that solution (2.23) is valid only for $h_0 > -1$. At the same time the boundary condition for Eq. (4.4) at $R = R_d$ (see Eq. (4.5)) leads to the situation in which $h_0 < -1$. The solution of Eq. (4.4) is given in Appendix D.

The average mass fraction of species in a moving droplet can still be correctly predicted by Eq. (4.4), with appropriate boundary condition (4.5), if the liquid diffusivity $D_l$ is replaced with the so-called effective diffusivity $D_{\text{eff}}$, Sirignano (1999):

$$D_{\text{eff}} = \chi_Y D_l, \tag{4.8}$$

where the coefficient $\chi_Y$ varies from 1 (at droplet mass diffusion Peclet number $\mathrm{Pe}_{d(l)} = \mathrm{Re}_{d(l)}\mathrm{Sc}_{d(l)} < 10$) to 2.72 (at $\mathrm{Pe}_{d(l)} > 500$) and can be approximated as:

$$\chi_Y = 1.86 + 0.86\tanh\left[2.225\log_{10}\left(\mathrm{Re}_{d(l)}\mathrm{Sc}_{d(l)}/30\right)\right], \quad (4.9)$$

where $\mathrm{Sc}_{d(l)} = \frac{\nu_l}{D_l}$ is the liquid Schmidt number, $\nu_l$ is the liquid kinematic viscosity and $\mathrm{Re}_{d(l)}$ is the same as discussed in Chapter 3 (Section 3.2.1).

Eq. (4.8) allows the application of solution to Eq. (4.4) to the case of moving droplets by replacing $D_l$ with $D_{\mathrm{eff}}$, assuming that α = const. Following Sirignano (1999), this model is called the Effective Diffusivity 'ED' model. As in the case of the ETC model, this model cannot describe the details of species mass fractions inside droplets, including vortex structures in the moving droplets, but this information is not required in most engineering applications. A more complex approach based on the analysis of Hill vortices, based on Eq. (2.39), is discussed in a number of publications including (Sirignano, 1999; Maqua et al, 2008b). The contribution of fuel vapour to the transport properties of air and the effects of droplets on air are ignored. The air properties are presented in Appendix B.

### *4.2.4 Species mass fractions at the surface of the droplets*

To calculate the species mass evaporation rate $\dot{m}_i$ and the values of the evaporation rate of species $\epsilon_i$ based on Eq. (4.7), the values of $Y_{vis}$ need to be calculated first. The latter depend on the partial pressure of species $i$ in the vapour state in the immediate vicinity of the droplet surface; Atkins and de Paula, (2002):

$$p_{vis} = X_{lis}\gamma_i p^*_{vis}, \quad (4.10)$$

where $X_{lis}$ is the molar fraction of the $i^{\mathrm{th}}$ species in the liquid near the droplet surface, $p^*_{vis}$ is the partial vapour pressure of the $i^{\mathrm{th}}$ species in the case when $X_{lis} = 1$, $\gamma_i$ is the activity coefficient.

In the limit when $\gamma_i = 1$, Eq. (4.10) describes Raoult's law. A more accurate approximation for $\gamma_i$ for the ethanol/acetone mixture is described in Appendix E, following (Maqua, 2007; Maqua et al, 2008b). This approximation will be used in the analysis of this chapter. Remembering the Clausius–Clapeyron equation (Atkins and de Paula, 2002), Eq. (4.10) can be re-written as:

$$p_{vis} = X_{lis}\gamma_i p_{amb}\exp\left[\frac{L_i M_i}{R_u}\left(\frac{1}{T_{bi}} - \frac{1}{T_s}\right)\right], \quad (4.11)$$

where $M_i$ is the molar mass, $T_{bi}$ is the boiling temperature of the $i^{\mathrm{th}}$ species, $p_{amb}$ is the ambient pressure and $L_i$ is the latent heat of evaporation of species $i$. The values

of $L_i$ for ethanol and acetone are calculated as described in Appendix B. When deriving Eq. (4.11) it was taken into account that $p_{vi}^*$ is equal to the ambient pressure when $T_s = T_{bi}$.

Eq. (4.11) can be re-written for the molar fractions of species $i$ in the vapour phase:

$$X_{vis} = X_{lis}\gamma_i \exp\left[\frac{L_i M_i}{R_u}\left(\frac{1}{T_{bi}} - \frac{1}{T_s}\right)\right]. \quad (4.12)$$

Eq. (4.11) is the generalisation of Eq. (3.6) to the case of multi-component droplets.

### *4.2.5 Moving boundary effects*

The effect of the moving boundary, due to thermal expansion/contraction and evaporation, on the solutions to Eqs. (2.21) and (4.4) is taken into account based on the analytical solutions to these equations assuming that the droplet radius is a linear function of time during each timestep (Sazhin et al, 2010a):

$$R_d(t) = R_{d0}(1 + \alpha_R t), \quad (4.13)$$

where the value of $\alpha_R$ takes into account both effects of evaporation and thermal swelling/contraction.

$$\alpha_R = \frac{\dot{R}_d}{R_{d0}}, \quad (4.14)$$

where $\dot{R}_d$ is calculated based on Eq. (3.2). For $R_d(t)$ defined by (4.13) the solution to Eq. (2.21), subject to the correspondence boundary and initial conditions, can be presented in the form, Sazhin et al (2010a):

$$T(R,t) = \frac{1}{R\sqrt{R_d(t)}} \exp\left[-\frac{\alpha_R R_{d0} R^2}{4\kappa R_d(t)}\right]\left[\sum_{n=1}^{\infty} \Theta_{\rm n}(t) \sin\left(\lambda_n \frac{R}{R_d(t)}\right) + \frac{\mu_0(t)}{1+h_0}\frac{R}{R_d(t)}\right], \quad (4.15)$$

where $\kappa$ is the liquid thermal diffusivity as introduced in Eq. (2.21), $\lambda_n$ are the positive solutions to Eq. (2.24) while the parameter $h_0$ is calculated as :

$$h_0 = \left(\frac{hR_d(t)}{k_l}\right) - 1 - \frac{R_d'(t)R_d(t)}{2\kappa}, \quad (4.16)$$

where $R_d'(t) = \dot{R}_d$ for moving boundary condition and zero otherwise.

$$\Theta_{\rm n}(t) = q_n \exp\left[-\frac{\kappa\lambda_n^2 t}{R_{d0}R_d(t)}\right] + f_n\mu_0(t) - f_n\,\kappa\lambda_n^2 \int_0^t \frac{\mu_0(\tau)}{R_d^2(\tau)} \times \exp\left[\frac{\kappa\lambda_n^2}{\alpha_R R_{d0}}\left(\frac{1}{R_d(t)} - \frac{1}{R_d(\tau)}\right)\right] {\rm d}t, \quad (4.17)$$

$$\mu_0(t) = \tilde{\mu}(t)\sqrt{R_d(t)} \exp\left[\frac{R_d'(t)R_d(t)}{4\kappa}\right], \quad (4.18)$$

$$\tilde{\mu}(t) = M(t)R_d^2(t),\ M(t) = \frac{h}{k_l}T_g + \frac{\rho_l}{k_l}L\dot{R}_{dE},\ f_n = -\frac{\sin\lambda_n}{\|v_n\|^2\lambda_n^2},$$

$$\|v_n\|^2 = \frac{1}{2}\left(1 - \frac{\sin 2\lambda_n}{2\lambda_n}\right) = \frac{1}{2}\left(1 + \frac{h_0}{h_0^2+\lambda_n^2}\right), \quad (4.19)$$

$$q_n = \frac{1}{\|v_n\|^2}\int_0^1 W_0(r)v_n(r)\mathrm{d}r, \tag{4.20}$$

$$r = \frac{R}{R_d(t)},\ v_n(r) = \sin(r\lambda_n),$$

$$W_0(r) = R_{d0}^{3/2} r T_0(rR_{d0}) \exp\left[\frac{R_d'(t)R_{d0}}{4\kappa}r^2\right]. \tag{4.21}$$

We should notice the difference between the parameters $h_0$, $\|v_n\|^2$ and $q_n$ introduced here and those introduced in Eq. (2.23). This solution was obtained under the assumption that parameter $h_0$ is a constant greater than -1 during the timestep. In the general case of a time dependent $h_0$ the solution of the differential heat conduction equation was reduced to the solution of the Volterra integral equation of the second kind (Sazhin et al, 2010a).

For $R_d(t)$ defined by (4.13) the solution to Eq. (4.4), subject to the correspondence boundary and initial conditions, can be presented in the form, Gusev et al (2012):

$$Y_{li}(R,t) = \frac{\alpha\epsilon_i \exp\left[\frac{\alpha_R R_{d0}}{4D_l}\left(\frac{R_{d0}R_d(t)-R^2}{R_d(t)}\right)\right]}{\alpha+\frac{\alpha_R R_{d0}}{2}}\frac{R_{d0}^{5/2}}{R_d^{5/2}(t)} + \frac{1}{R\sqrt{R_d(t)}}\exp\left[-\frac{\alpha_R R_{d0}R^2}{4D_l R_d(t)}\right]\times\left[\sum_{n=1}^{\infty}[q_{Yn} + f_{Yn}\ \mu_{Y0}(0)]\exp\left[-\frac{D_l\lambda_n^2 t}{R_{d0}R_d(t)}\right]\sin(r\lambda_n) + \sum_{n=1}^{\infty}[q_{Y0} + f_{Y0}\mu_{Y0}(0)]\exp\left[-\frac{D_l\lambda_0^2 t}{R_{d0}R_d(t)}\right]\sinh\ (r\lambda_0)\right], \tag{4.22}$$

where

$$f_{Yn} = \frac{1}{\|v_n\|^2}\int_0^1 f_Y(r)v_{Yn}(r)\mathrm{d}r = \begin{cases}\frac{1}{\|v_0\|^2\lambda_0^2}\sinh\lambda_0 & \text{when } n=0\\ \frac{1}{\|v_n\|^2\lambda_n^2}\sin\lambda_n & \text{when } n\geq 1\end{cases} \tag{4.23}$$

$$\|v_n\|^2 = \begin{cases}\frac{-1}{2}\left(1+\frac{h_{Y0}}{h_{Y0}^2-\lambda_0^2}\right) & \text{when } n=0\\ \frac{1}{2}\left(1+\frac{h_{Y0}}{h_{Y0}^2+\lambda_n^2}\right) & \text{when } n\geq 1\end{cases} \tag{4.24}$$

$$q_{Yn} = \frac{1}{\|v_n\|^2}\int_0^1 W_{Y0}(r)v_{Yn}(r)\mathrm{d}r, \tag{4.25}$$

$$W_{Y0}(r) = \sum_{n=1}^{\infty} q_{Yn}\, v_{Yn}(r), \tag{4.26}$$

$v_{Yn}(r) = \sin(r\lambda_n),\ v_{Y0}(r) = \sinh\ (r\lambda_0)$

$$\mu_{Y0}(t) = -\frac{\alpha\epsilon_i\left(R_d(t)\right)^{5/2}}{D_l}\exp\left[\frac{R_d'(t)R_d(t)}{4D_l}\right], \tag{4.27}$$

$$h_{Y0} = \left(-\frac{\alpha R_d(t)}{D_l}\right) - 1 - \frac{R_d'(t)R_d(t)}{2D_l}, \tag{4.28}$$

$\lambda_0$ is the solution to the equation:

$$\lambda\cosh\ \lambda + h_{Y0}\sinh\ \lambda = 0. \tag{4.29}$$

A countable set of positive solutions to this equation (positive eigenvalues) are arranged in ascending order, as in the case of Solutions (2.23), (D.38) and (4.15).

### *4.2.6 Numerical solutions*

We will use two solutions to heat transfer and species diffusion equations; the one based on the analytical solutions to Eqs. (2.21) and (4.4) and the other based on the numerical solutions to these equations. These are referred to as Solutions A and B respectively.

The Cranck-Nicholson method is used to solve numerically Eqs. (2.21) and (4.4). This classical approach has already been used in several papers, including Abramzon and Sirgnano (1989) and Maqua et al (2008b), to describe the droplet heating and the change of its composition.

In this chapter, the results of the numerical solutions are provided by Dr. Guillaume Castanet. The timestep is set at 0.01 ms and the radius of the droplet is divided into 200 elements of identical size, which appears to be sufficient to ensure a good accuracy in the results. The dependence of liquid properties on temperature and composition is taken into account while the gas properties are assumed to be the same as air and they depend on temperature. At each timestep, the temperature and the liquid mass fractions are calculated iteratively with updated values of the physical properties and the iterations are stopped when:

$$\left|T_{s,j}(t+\Delta t) - T_{s,j-1}(t+\Delta t)\right| < 0.01 \text{ K}, \tag{4.30}$$

$$\frac{\left|\dot{m}_{s,j}(t+\Delta t) - \dot{m}_{s,j-1}(t+\Delta t)\right|}{\dot{m}_{s,j}(t+\Delta t)} < 0.01, \tag{4.31}$$

where $j$ refers to the $j^{\text{th}}$ iteration. Typically two or three iterations have been sufficient to satisfy these conditions.

## 4.3 Experimental data and input parameters

The experimental results are reproduced from Maqua et al (2006; 2008b), in what follows a brief description of the experimental set-up and input parameters used in our calculations will be presented.

The experimental set-up used for validation of the model is the same as described in Section 3.3. The two-colour laser-induced fluorescence technique, previously used for the measurement of droplet temperatures, was further developed to include the third colour band. This additional band is required for the analysis of bi-component droplets (Maqua et al, 2006). In this new technique, droplets were

seeded with a low concentration of a fluorescent dye and illuminated by laser beams having a wavelength tuned on the absorption spectrum of the tracer. The fluorescence signal was detected over specific spectral bands of emissions. The ratio of the intensity of these bands depends on the temperature and, to a lesser extent, on the droplet composition, while the fluorescence dependencies on tracer concentration, probe volume dimensions, laser intensity and optical layout were eliminated (Maqua et al, 2006). The probe volume (intersection between the laser beams and the detection field of view) was about 150 × 150 × 1200 $\mu m^3$. It was larger than the droplet in order to provide a global excitation of the whole droplet volume. The signal was averaged over the total time of droplet transit in the probe volume (Maqua et al, 2006; 2008b).

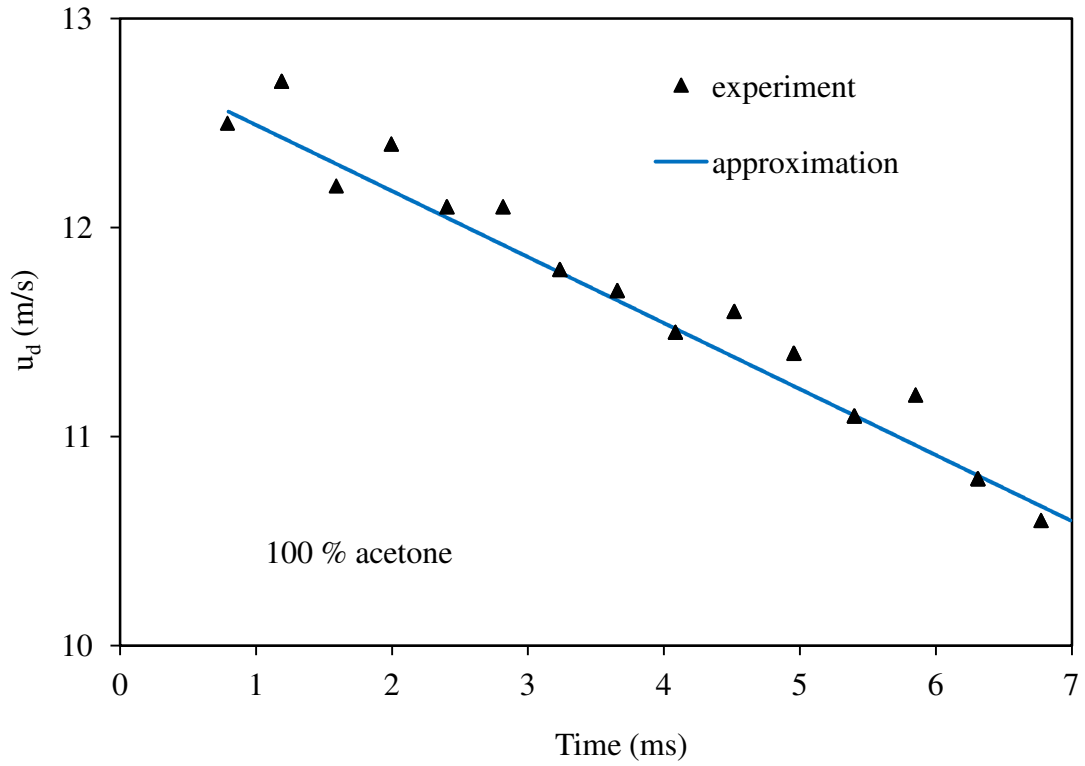


Fig. 4.1 Experimentally observed velocities for pure acetone droplets (triangles) approximated by Eq. (3.7).

The measured time evolution of the droplet velocities for pure acetone is shown in Fig. 4.1. In the same figure, the linear approximation (Eq. (3.7)) of the experimental results is shown. Similar plots were obtained for pure ethanol and various mixtures of acetone and ethanol (shown in Appendix F). In all cases the linear approximations of the experimental results, similar to the one shown in Fig. 4.1, were used. These are summarised in Table 4.1.

| Substance | $u_1$ (m/s) | $u_2$ (m/(s.ms)) | $C$ | $T_g$ (°C) | $T_d$ (°C) | $D_{0d}$ ($\mu$m) |
|---|---|---|---|---|---|---|
| **100 % acetone** | 12.81 | 0.316 | 7.1 | 21.5 | 34.8 | 143.4 |
| **100 % ethanol** | 12.30 | 0.344 | 7.1 | 22.0 | 38.0 | 140.8 |
| **25 % ethanol + 75 % acetone** | 12.75 | 0.370 | 8.7 | 21.1 | 32.8 | 133.8 |
| **50 % ethanol + 50 % acetone** | 12.71 | 0.448 | 7.53 | 20.8 | 37.5 | 142.7 |
| **75 % ethanol + 25 % acetone** | 12.28 | 0.306 | 7.53 | 21.6 | 38.6 | 137.1 |

Table 4.1 The values of $u_1, u_2$, $C$, $T_g$, $T_d$ and $D_{d0}$ for five different initial mass fractions of acetone and ethanol droplet. The droplet velocities in m/s are approximated as Eq. (3.7) where $t$ is in ms.

## 4.4 Results

This section is divided into four parts. The first one shows the results of Solution A with the stationary boundary (Eqs. (2.23) and (D.38)). The second one shows the results of Solutions A and B with the stationary boundary. The third one shows the results of Solution A with the moving boundary (Eqs. (4.15) and (4.22)). The fourth one shows the effects of the binary diffusion coefficient on the time evolution of droplet temperature.

### *4.4.1 Solution A based on stationary boundary*

The plots of the time dependence of the temperatures for pure acetone and ethanol are shown in Figs. 4.2 and 4.3 respectively. The experimentally observed average droplet temperatures are shown by filled triangles in these figures. The results of calculations are shown by purple, red and blue curves referring to the central, average and surface temperatures. The calculations started with the first observed droplets approximately 1 ms after the start of injection. At the earlier times, the liquid fuel formed an unstable jet the temperature evolution of which cannot be interpreted using the model under consideration. Also, it is assumed that there is no temperature gradient inside droplets at the initial moment of time as in calculations in Chapter 3.

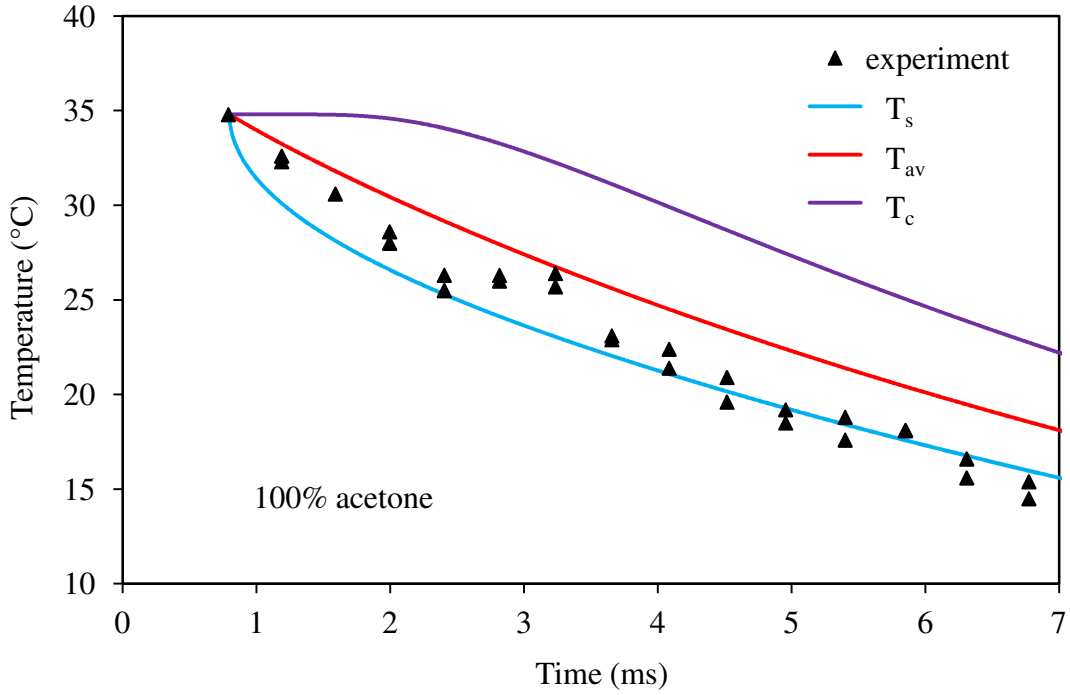


Fig. 4.2 The time evolution of droplet surface, average and centre temperatures ($T_s$, $T_{av}$, and $T_c$) and experimentally observed temperatures for pure acetone droplets with initial diameter 143.4 µm and homogeneous temperature 34.8 °C in an ambient gas at temperature equal to 21.5 °C.

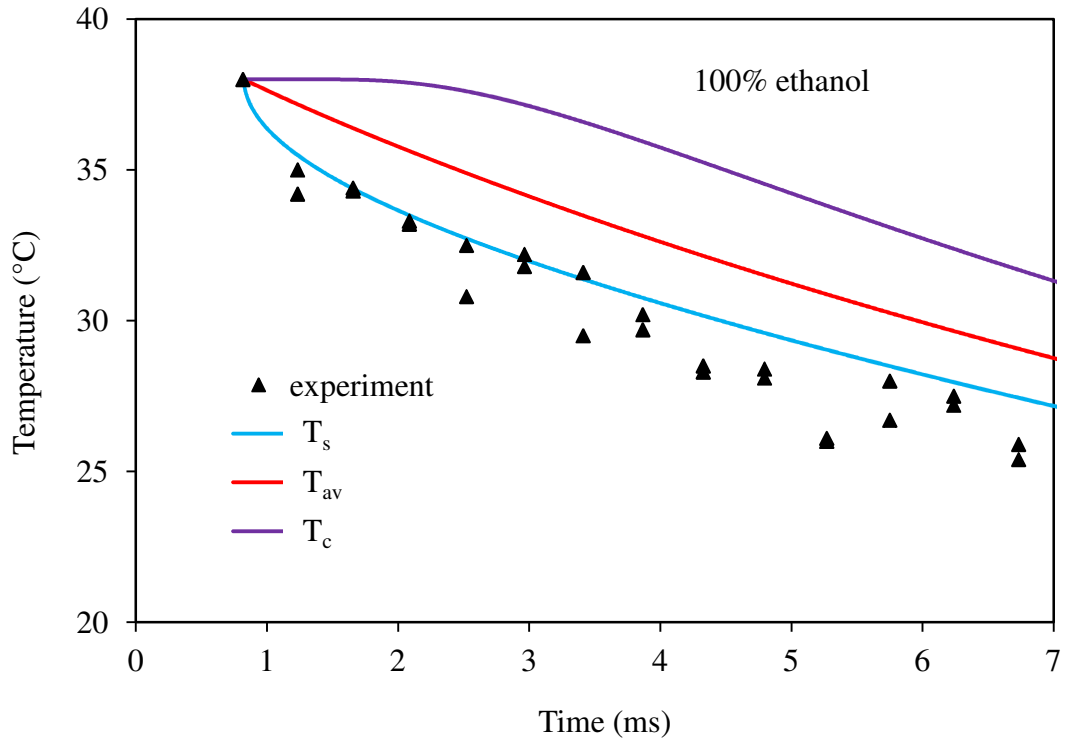


Fig. 4.3 The same as Fig. 4.2 but for pure ethanol droplets with initial diameter 140.8 µm, homogeneous temperature 38.0 °C and ambient gas temperature equal to 22.0 °C.

As follows from Figs. 4.2 and 4.3, all three temperatures are well separated for both acetone and ethanol. Hence, the difference between them needs to be taken into account in the analysis of experimental data. In the case of acetone there seems to be a reasonable agreement between the values of average temperature of the droplets and experimental data. Data on the time evolution of droplet radii were not available. Note that the Effective Thermal Conductivity and Effective Diffusivity models, on which the analysis of this chapter is based, are primarily designed to predict correctly the average surface temperature and species mass fractions of droplets, but not their average temperature and species mass fractions.

In the case of pure ethanol shown in Fig. 4.3, the experimentally observed temperatures lie below the surface temperature predicted by the model. Note that the temperature scale in Fig. 4.3 is much finer than in Fig. 4.2. Hence, the overall agreement between experimental data and predictions of the model looks reasonably good. This level of agreement between the model and experimental data is similar to the one reported by Maqua et al (2008b) for the case of the vortex model (see their Fig. 7). Hence, the application of the new simplified model can be justified in this case. Note that despite the overall agreement between the results of modelling and experimental data, the observed rate of temperature decrease at the later times is lower than predicted by the model.

Plots similar to those shown in Figs. 4.2 and 4.3, but for the mixtures of ethanol and acetone, are presented in Figs. 4.4-4.6. The calculations were performed for the cases of the ideal mixture ($\gamma_i = 1$ in Eqs. (4.10) and (4.11)) and the non-ideal mixture ($\gamma_i$ in Eqs. (4.10) and (4.11)) was calculated based on Eq. (E.3)). As can be seen from these figures, in all cases the predictions of the temperatures by the ideal and non-ideal models are noticeably different (by up to several degrees), especially at later times. However, both these models predict about the same trend in the evolution of temperature with time. The ideal model can be used if the prediction errors of several degrees can be tolerated.

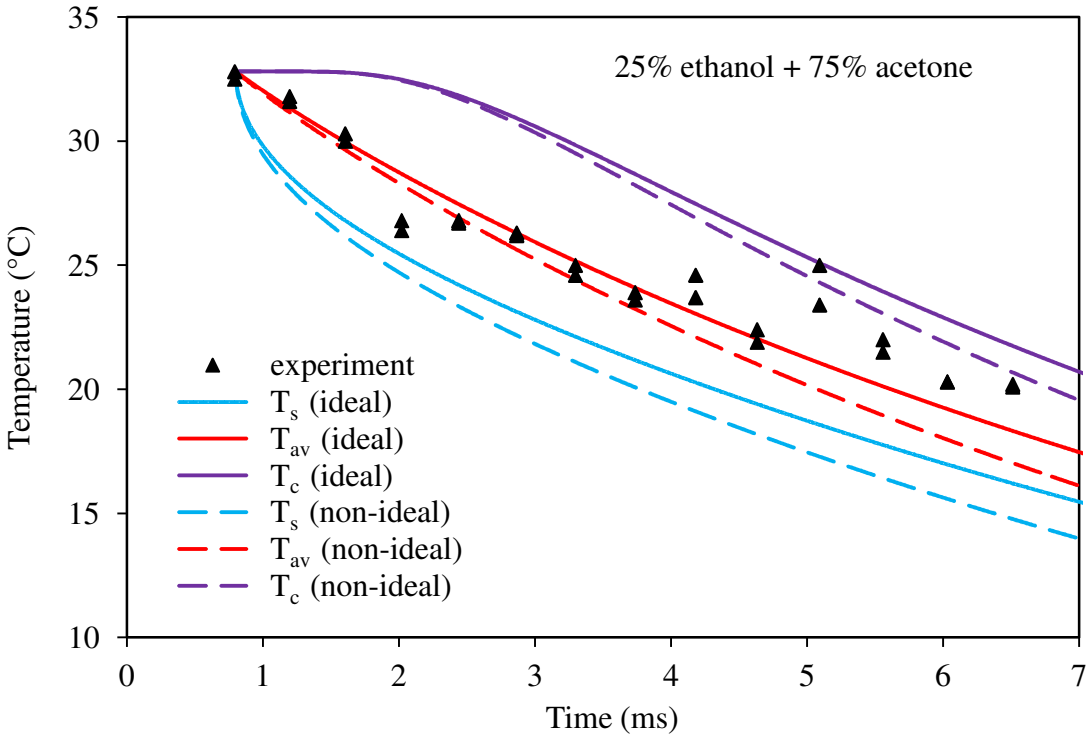


Fig. 4.4 The same as Figs. 4.2 and 4.3 but for the 25% ethanol–75% acetone mixture droplets with initial diameter 133.8 μm, homogeneous temperature 32.8 °C and ambient gas temperature equal to 21.1 °C. The results of calculations based on the ideal ($\gamma_i = 1$) and non-ideal models are presented.

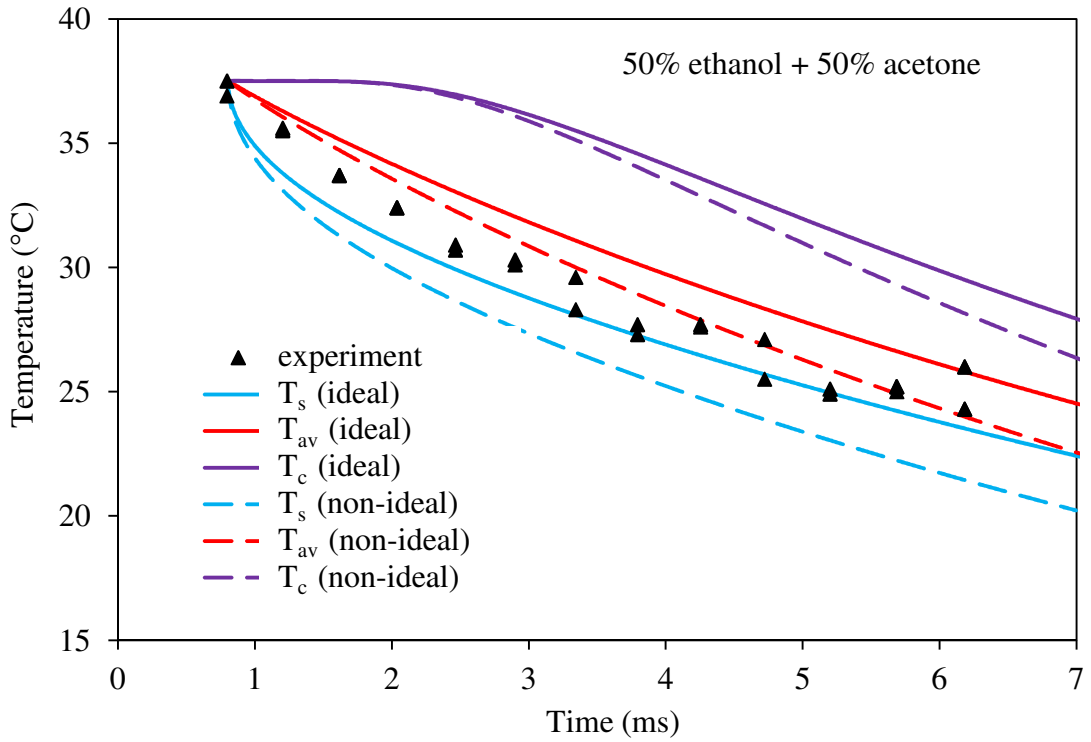


Fig. 4.5 The same as Fig. 4.4 but for the 50% ethanol–50% acetone mixture droplets with initial diameter 142.7 μm, homogeneous temperature 37.5 °C and ambient gas temperature equal to 20.8 °C.

In Fig. 4.4 (25% ethanol - 75% acetone; the case of acetone dominated mixture), the agreement between the observed and predicted average droplet temperatures, for both ideal and non-ideal models, is reasonably good, although the scatter of experimental data in this case is more noticeable than in the case of pure acetone shown in Fig. 4.2.

In Fig. 4.5 (the case of the 50% ethanol - 50% acetone mixture), the experimentally observed temperatures lie between the average and surface temperatures predicted by both ideal and non-ideal models. These temperatures are closer to the average temperatures predicted by the non-ideal model than to those predicted by the ideal model.

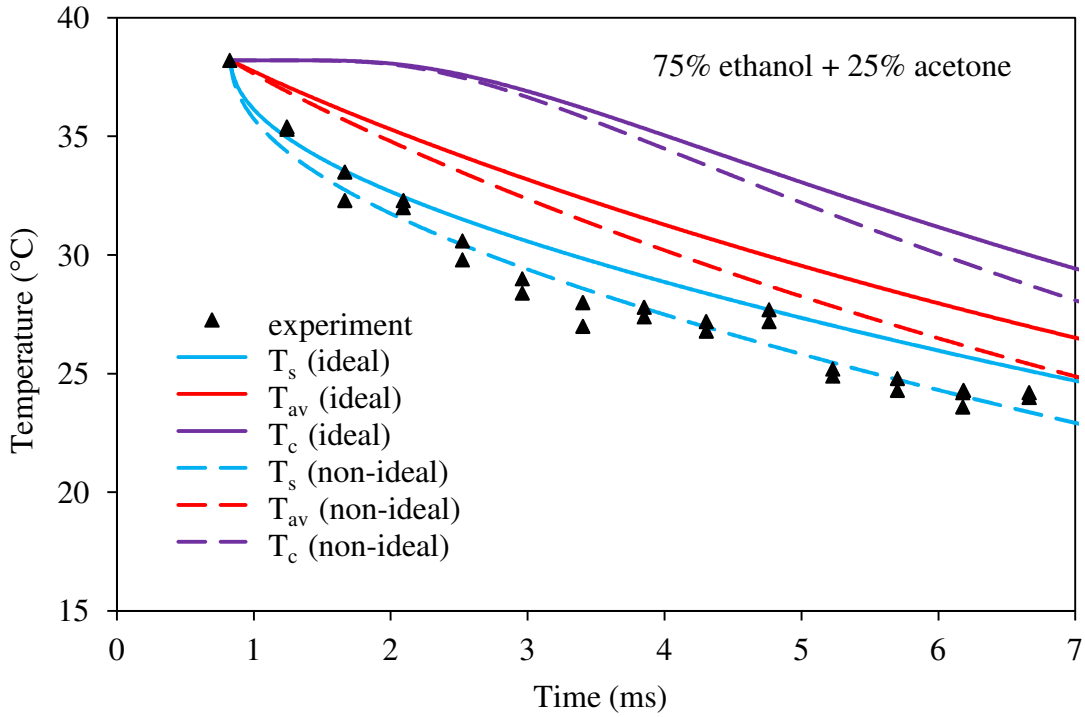


Fig. 4.6 The same as Figs. 4.4 and 4.5 but for the 75% ethanol–25% acetone mixture droplets with initial diameter 137.1 µm, homogeneous temperatures 38.6 °C and ambient gas temperature equal to 21.6 °C.

In Fig. 4.6 (the case of the 75% ethanol - 25% acetone mixture), the experimentally observed temperatures lie well below the average temperatures predicted by both ideal and non-ideal models, although they are closer to the average temperatures predicted by the non-ideal model than to those predicted by the ideal model, as in the case of the 50% ethanol - 50% acetone mixture shown in Fig. 4.5. The reason for this deviation between the measured and predicted temperatures, which could reach up to 5 °C, is not clear.

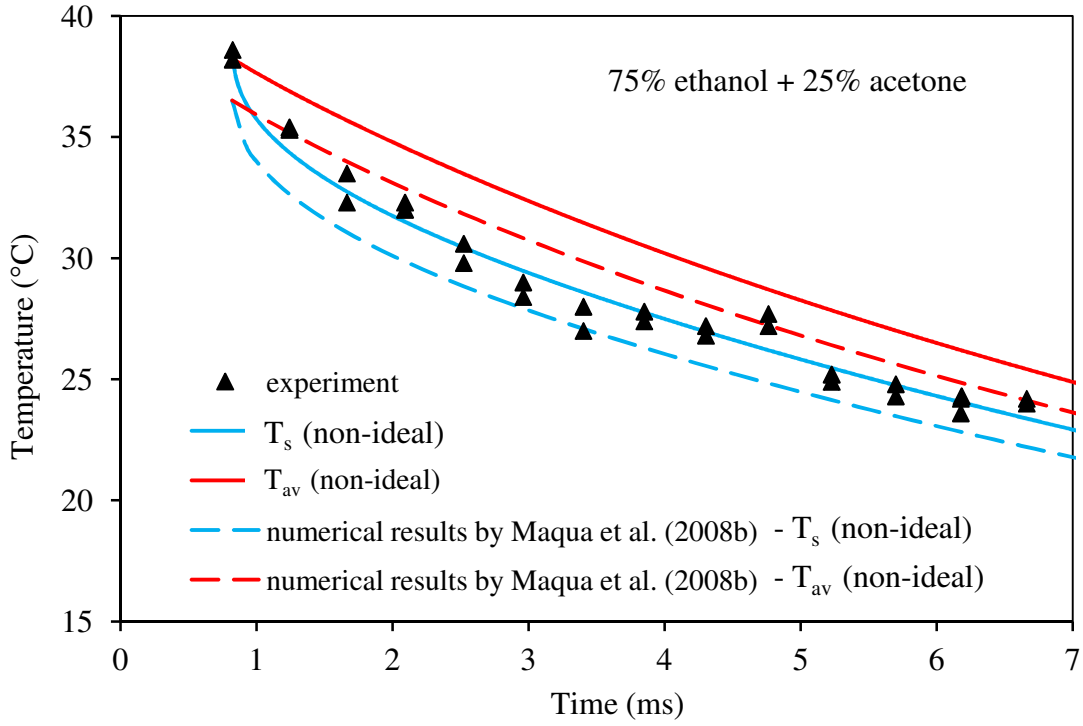


Fig. 4.7 The same as Fig. 4.6 but including additional results of calculations of $T_s$ and $T_{av}$ (based on the vortex model, as reported in Maqua et al, 2008b) instead of the results referring to $T_c$.

In Fig. 4.7 the predictions of the new simplified model and the predictions of the vortex model, reported in Maqua et al (2008b) are compared. As one can see from this figure, the experimental results agree better with the predictions of the average temperature by the vortex model than by the new simplified model. It seems, however, that this was achieved by the choice of the lower initial droplet temperature in the vortex model (which could be used as a fitting parameter). If the values of this temperature were taken to be the same, one would expect that the predictions of the simplified and vortex models would be very close.

The plots of time evolution of droplet radius for the same mixture as in the case of Figs. 4.6 and 4.7, inferred from the new simplified model and the numerical results reported in Maqua et al (2008b), are shown in Fig. 4.8. As follows from this figure, the vortex model predicts a slightly lower evaporation rate than the simplified model. In both cases, the non-ideal model predicts higher evaporation rate than the ideal one.

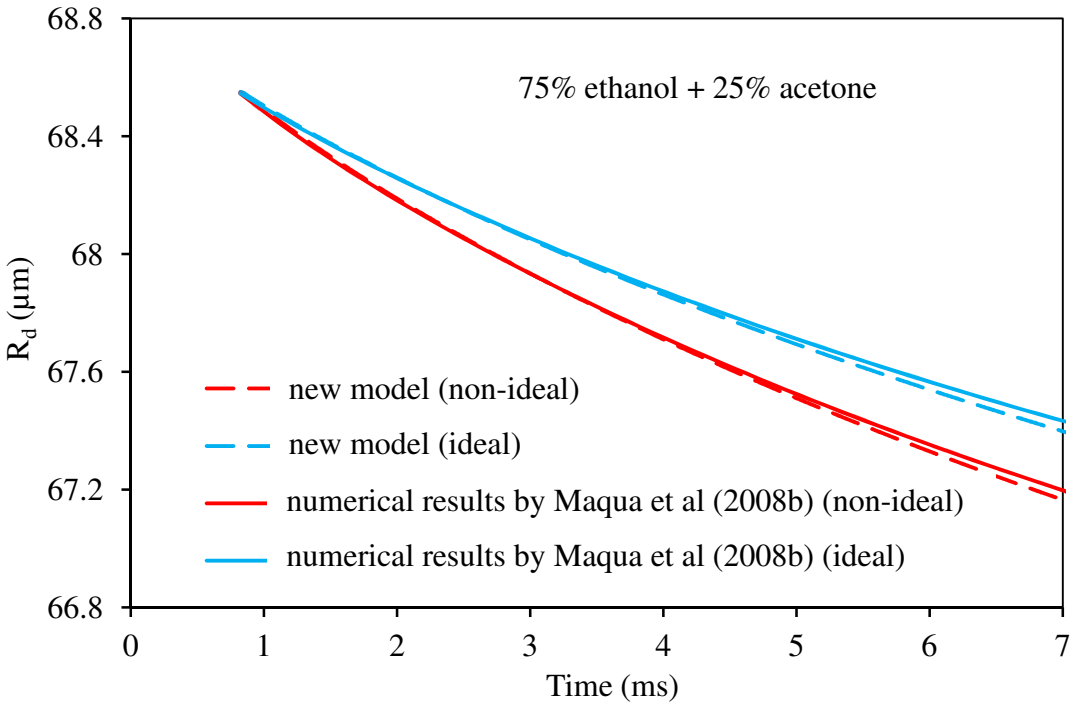


Fig. 4.8 The plots of $R_d$ versus time predicted by the ideal ($\gamma_i = 1$) and non-ideal, simplified and vortex models for the same droplets as in Figs. 4.6 and 4.7.

The plots of temperature distribution inside droplets at various moments of time after the start of calculations for the 75% ethanol – 25% acetone mixture for the same conditions as in Figs. 4.6-4.8 are shown in Fig. 4.9. The values of central and surface temperatures inferred from this figure are the same as shown in Fig. 4.6. Note that at times greater than about 2 ms, the distribution of temperature inside droplets is close to parabolic. This could justify the application of the so-called parabolic model to take into account the gradient of temperature inside droplets (Dombrovsky and Sazhin, 2003a,b). Note that these plots do not describe the actual distribution of temperature inside the moving droplets, as they are based on the ETC model. Only the temperatures near the surface of the droplets have physical meaning. The plots of temperature distribution inside droplets for other mixtures turned out to be rather similar to the ones shown in Fig. 4.9.

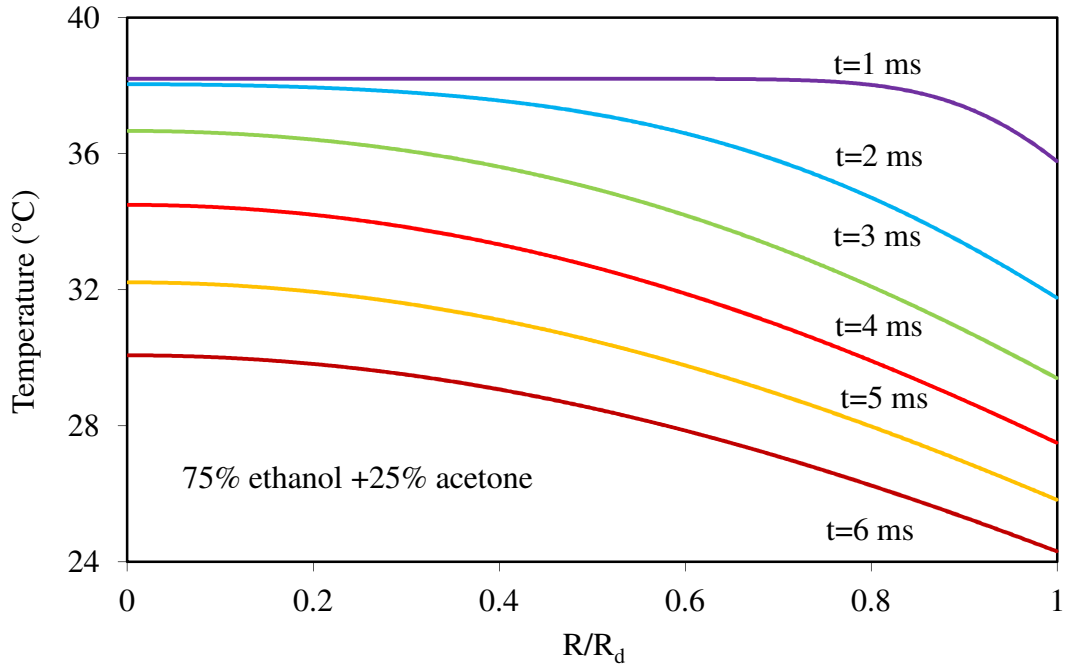


Fig. 4.9 The plots of $T$ versus $R/R_d$ for six moments of time after the start of calculations for the same droplets as in Figs. 4.6-4.8.

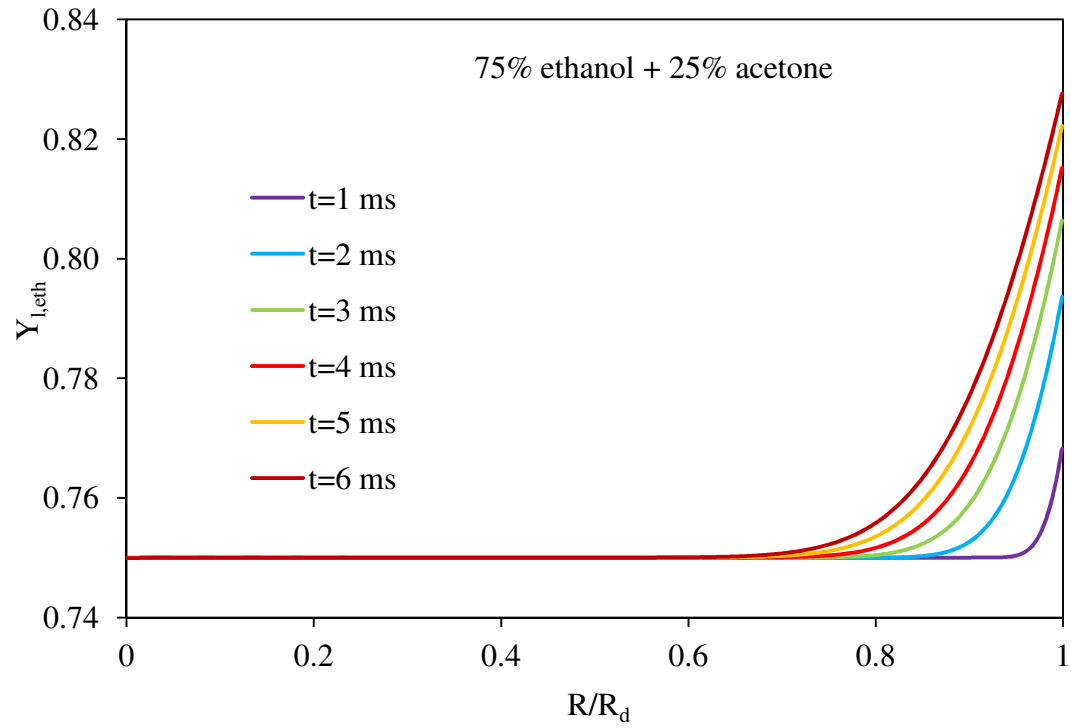


Fig. 4.10 The plots of the ethanol mass fraction $Y_{l,eth}$ versus $R/R_d$ for six moments of time after the start of calculations for the same droplets as in Figs. 4.6-4.9.

The plots of the distribution of mass fraction of ethanol inside droplets for the same mixture as shown in Fig. 4.9 at various moments of time after the start of calculations are shown in Fig. 4.10. As expected, the mass fraction of ethanol near the surface of the droplet increases with time. This is related to the dominant acetone evaporation due to its high volatility. The distribution of mass fraction of ethanol

presented in this figure clearly indicates that the models, based on the assumptions of zero or infinitely large diffusivities inside droplets, are not applicable in this particular case. Note that these plots do not describe the actual distribution of mass fraction inside the moving droplets, as they are based on the ED model. Only the mass fractions near the surface of the droplets have physical meaning. The radial distribution of the ethanol mass fraction shown in Fig. 4.10 is expected to predict the trends of this distribution but not its quantitative characteristics. The plots of ethanol mass fraction distribution inside droplets for other mixtures showed the same trends as Fig. 4.10.

### *4.4.2 Solutions A and B (stationary boundary)*

In the previous section the value of the distance parameter $C$ was assumed to be constant and equal to its initial value. The analysis of this part takes into account the changes in $C$ from the previous to the current timestep based on the following equation:

$$C_{\text{new}} = C_{\text{old}} \frac{u_{d,\text{new}}}{u_{d,\text{old}}} \frac{R_{d,\text{old}}}{R_{d,\text{new}}}, \tag{4.32}$$

where subscripts $_{\text{new}}$ and $_{\text{old}}$ refer to the values of variables at the previous timestep and one timestep behind respectively. In this case the values of $R_{d,\text{old}}$ and $R_{d,\text{new}}$ are known at the current timestep.

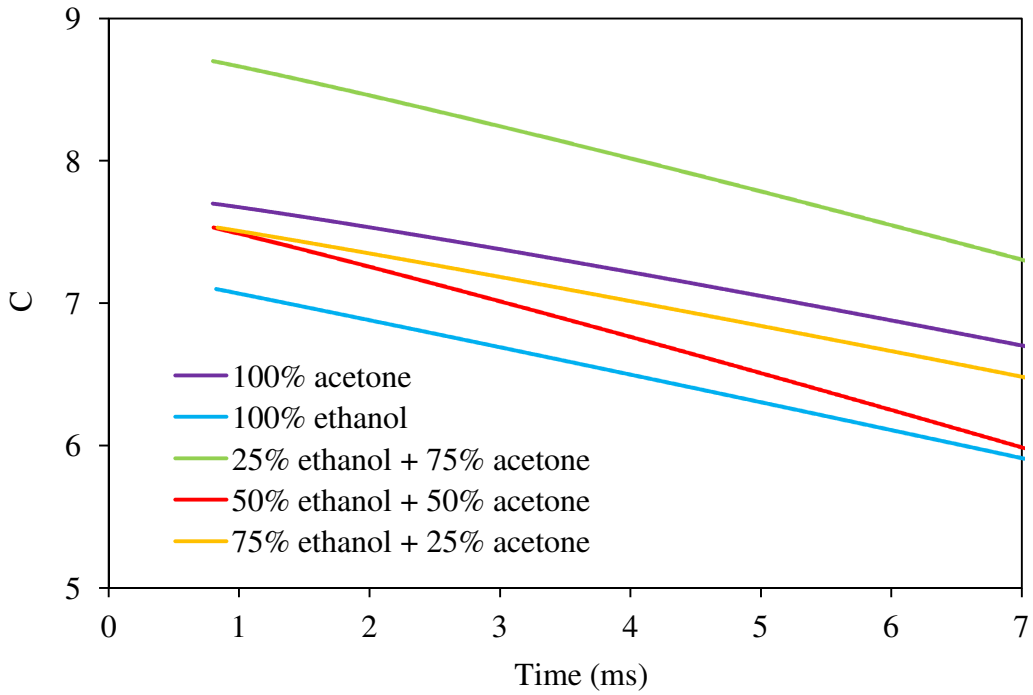


Fig. 4.11 The time evolution of the distance parameter for acetone and ethanol droplets and their mixtures, calculated based on the parameters in Table 4.1 and Eq. (4.32).

The plots of $C$ versus time for all cases shown in Table 4.1 are presented in Fig. 4.11. As can be seen from this figure, the changes in $C$ during the experiments are noticeable in all cases and cannot be ignored.

In the previous sections of this chapter the Reynolds number for liquid droplet '$\mathrm{Re}_{d(l)}$' was calculated as in Chapter 3, where $\Delta u \equiv |u_g - u_d|$ is the relative velocity between ambient gas and droplets, which is a crude assumption. Following Abramzon and Sirgnano (1989) it is calculated here based on the maximum surface velocity $u_s$ introduced by Eq. (2.15).

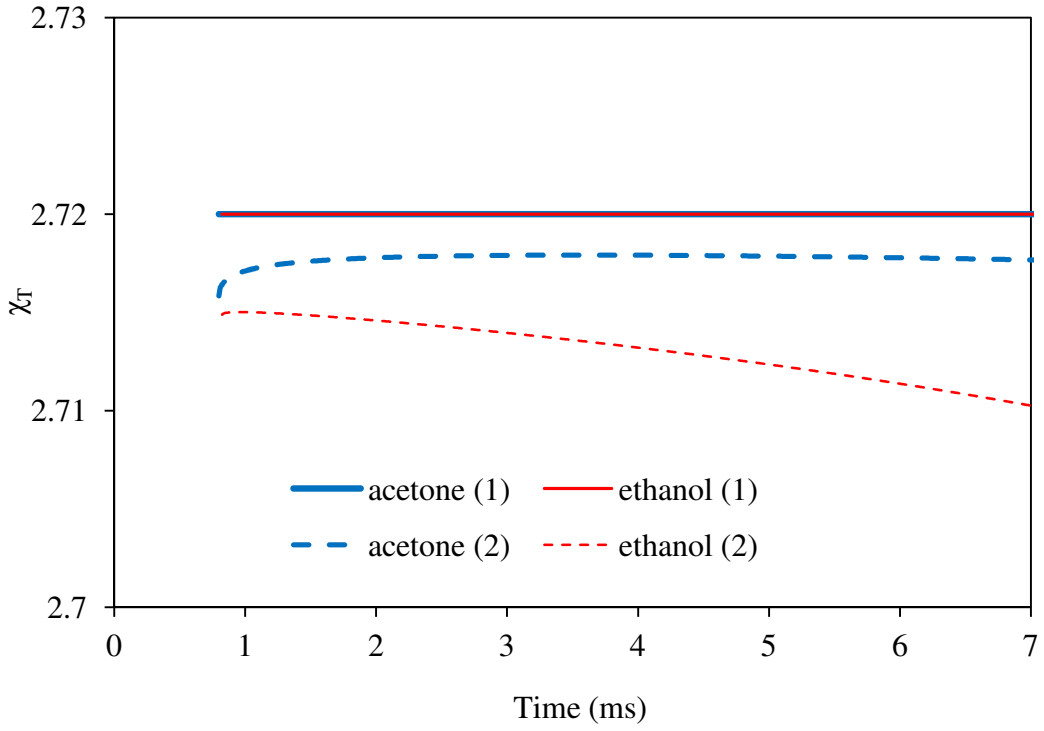


Fig. 4.12 The time evolution of the parameter $\chi_T$ for pure acetone and ethanol, calculated based on parameters in Table 4.1 and Eq. (2.14), and the assumption that $u_s = \Delta u$ (curves 1) and Eq. (2.15) (curves 2).

The values of correction factor of thermal conductivity '$\chi_T$' predicted based on a crude assumption that $u_s = \Delta u$ (curve 1) and Eq. (2.15) (curve 2) for acetone and ethanol are shown in Fig. 4.12. As one can see from this figure, for both acetone and ethanol the predicted values of $\chi_T$ based on these approximations differ by less than 0.5% which can be safely ignored in most practical engineering applications. The plots, based on the assumption that $u_s = \Delta u$ for acetone and ethanol, coincide within the accuracy of plotting.

The main focus of this section is the comparison of the results of calculations based on the analytical solutions to the equations for heat transfer and species

diffusion inside droplets (Eqs. (2.21) and (4.4)) (Solution A), and those based on the numerical solutions to these equations (Solution B). The effects of the movement of the droplet surface due to evaporation and thermal swelling/contraction during individual timesteps are ignored.

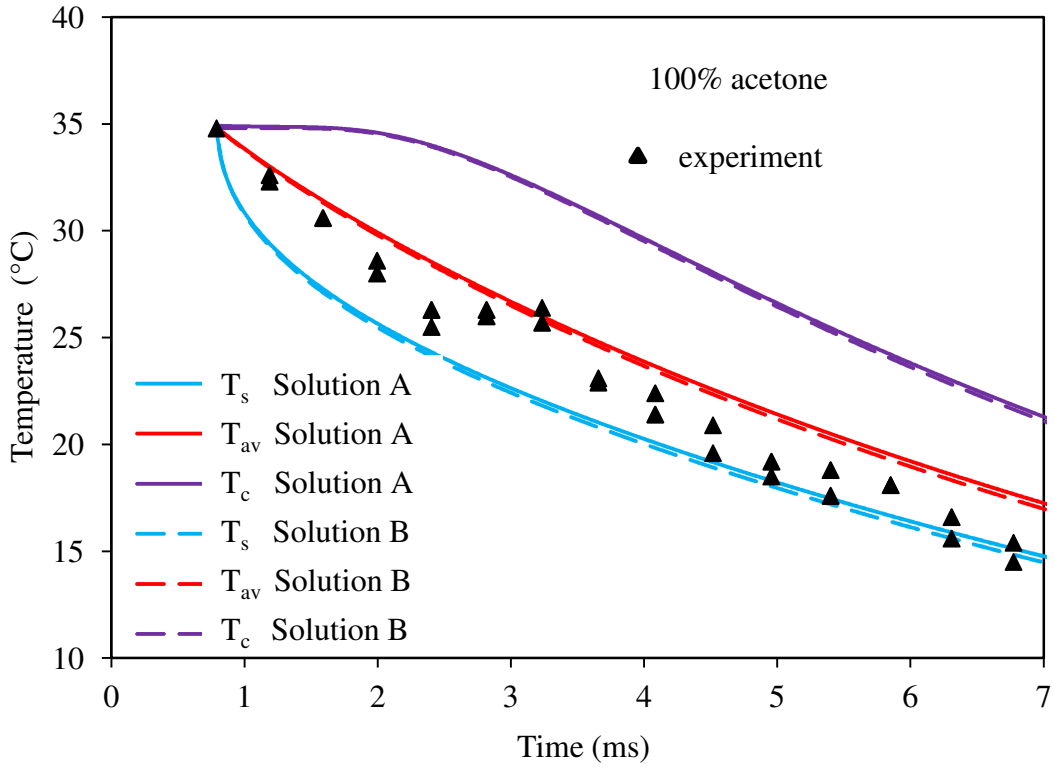


Fig. 4.13 The same as Fig. 4.2 but for both of Solutions A and B. The distance parameter is calculated based on Eq. 4.32.

The plots of the time dependence of the temperatures for pure acetone and ethanol, obtained based on Solutions A and B, are shown in Figs. 4.13 and 4.14 respectively. The experimentally observed average droplet temperatures are shown by filled triangles in these figures. As follows from these figures, all three temperatures are well separated for both acetone and ethanol. Hence, the difference between them needs to be taken into account in the analysis of experimental data. The results predicted by Solutions A and B coincide within the accuracy of plotting, which gives us confidence in the results predicted by both solutions.

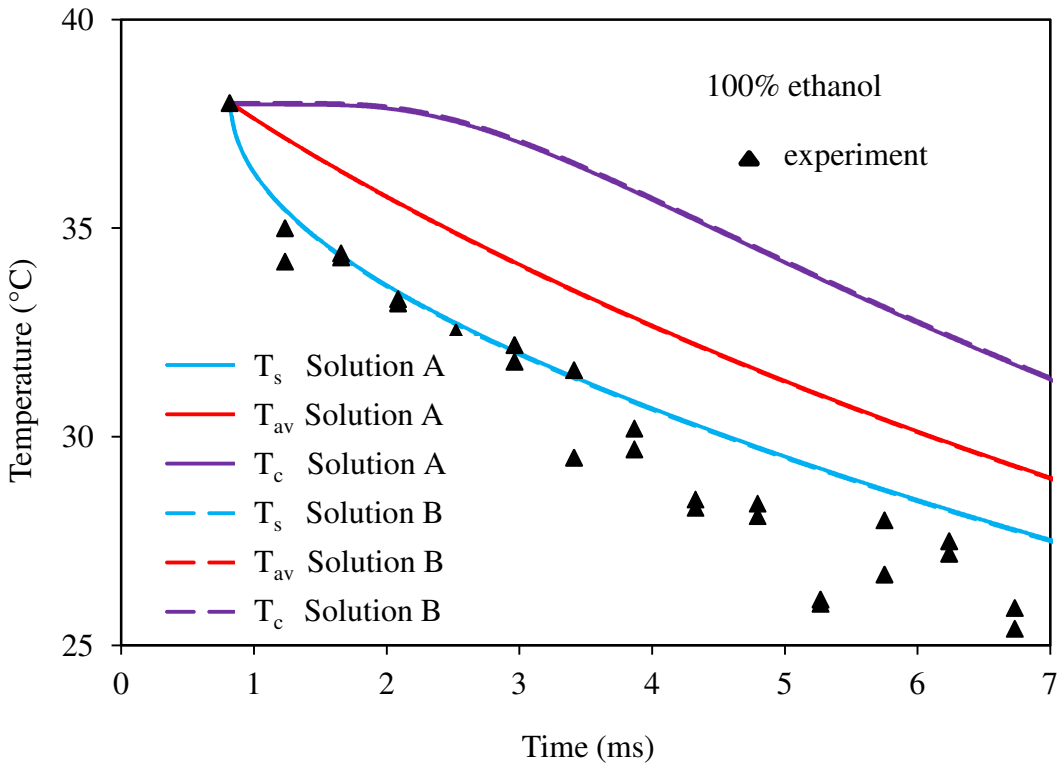


Fig. 4.14 The same as Fig. 4.13 but for pure ethanol droplets.

In the case of acetone (see Fig. 4.13), the observed temperature values lie close to the average temperatures. In the case of ethanol (see Fig. 4.14), the observed temperatures are close to or below the surface temperature of the droplets. Hence, for both acetone and ethanol, the trends of predicted temperatures agree with experimental observations, but there is a rather poor agreement between the values of observed and predicted temperatures for both acetone and ethanol, in agreement with results shown in Figs. 4.2 and 4.3, as the measured temperatures are expected to be the volume-averaged droplet temperatures with systematically more weighting in the zones near the centres of the droplet (see Section 4.3). The reason for this lack of quantitative agreement is not clear to us.

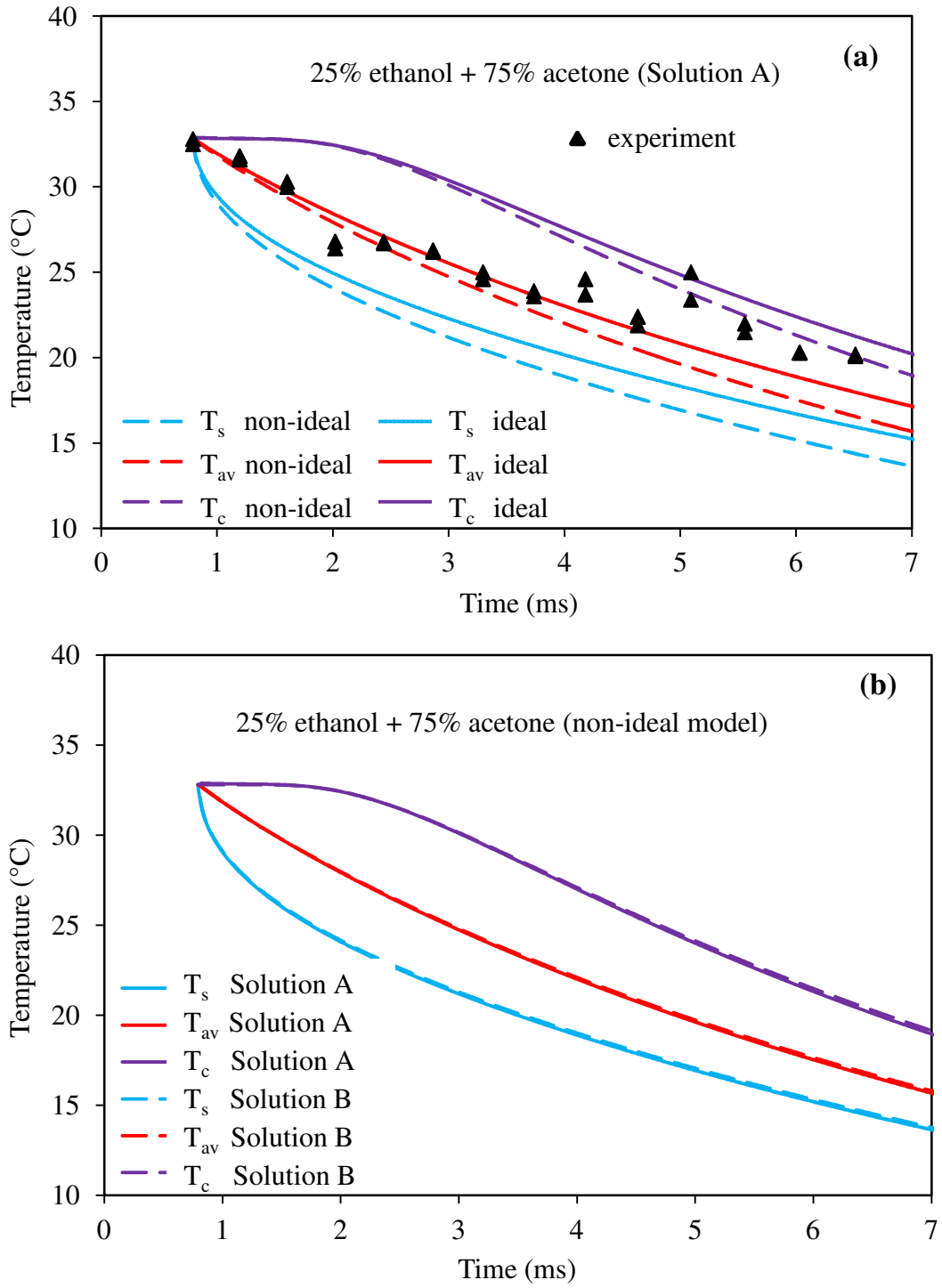


Fig. 4.15 The same as Fig. 4.4 predicted by Solution A, but with variable *C*, for ideal and non-ideal models and experimentally observed temperatures (a); the same as (a), predicted by Solutions A and B for the non-ideal model (b).

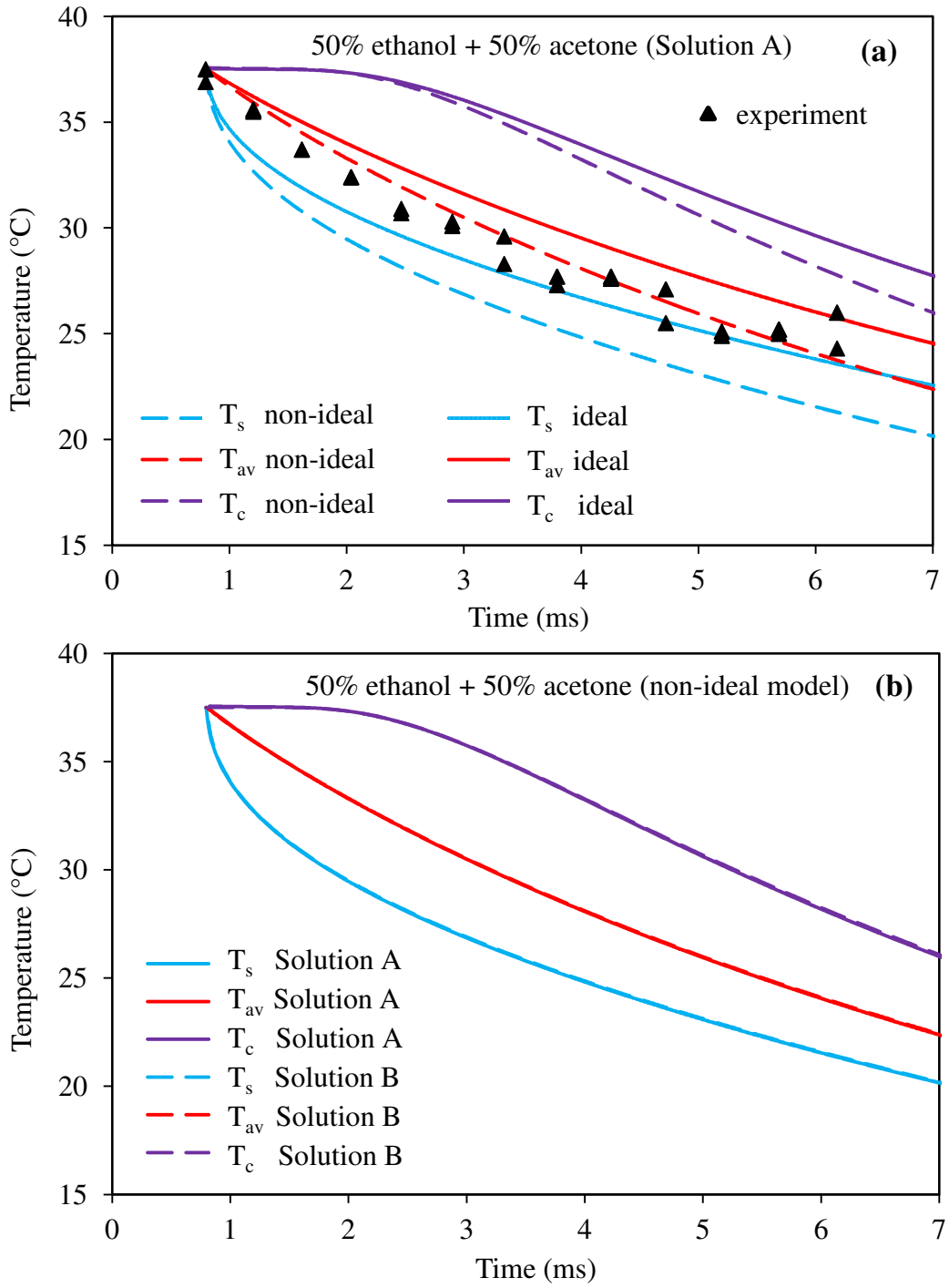


Fig. 4.16 The same as Fig. 4.15 but for the 50% ethanol – 50% acetone mixture droplets.

Plots similar to those shown in Figs. 4.13 and 4.14, but for mixtures of ethanol and acetone, are presented in Figs. 4.15–4.17. The calculations were performed for cases of the ideal mixture ($\gamma_i = 1$ in Eq. (4.10)) and the non-ideal mixture ($\gamma_i$ in Eq. (4.10) is calculated by Eq. (E.3)). As can be seen from these figures, in all cases the predictions of the temperatures by the ideal and non-ideal models are noticeably different (by up to several degrees), especially at later times.

However, both these models predict about the same trend in the evolution of temperature with time. The ideal model can be used if the prediction errors of several degrees can be tolerated. This seems to be our case where the random errors of the estimates of droplet temperatures appear to be about 2-3 degrees. As in the cases shown in Figs. 4.13 and 4.14, the results predicted by Solutions A and B coincide within the accuracy of plotting, which gives us confidence in the results predicted by both solutions.

In the case of an acetone dominated mixture (25% ethanol – 75% acetone: see Fig. 4.15), the agreement between the observed and predicted average droplet temperatures, for both ideal and non-ideal models, is reasonably good. Most of the observed temperatures lie between average and central temperatures, although the scatter of experimental data in this case is more noticeable than for pure acetone (see Fig. 4.13).

In the case of the 50% ethanol– 50% acetone mixture (see Fig. 4.16), the experimentally observed temperatures lie close to the average temperatures predicted by the non-ideal model. For the 75% ethanol – 25% acetone mixture (see Fig. 4.17), the experimentally observed temperatures are close to the surface temperatures predicted by the non-ideal model. As with pure acetone and ethanol, the reason for this deviation between the measured and predicted temperatures is not clear to us.

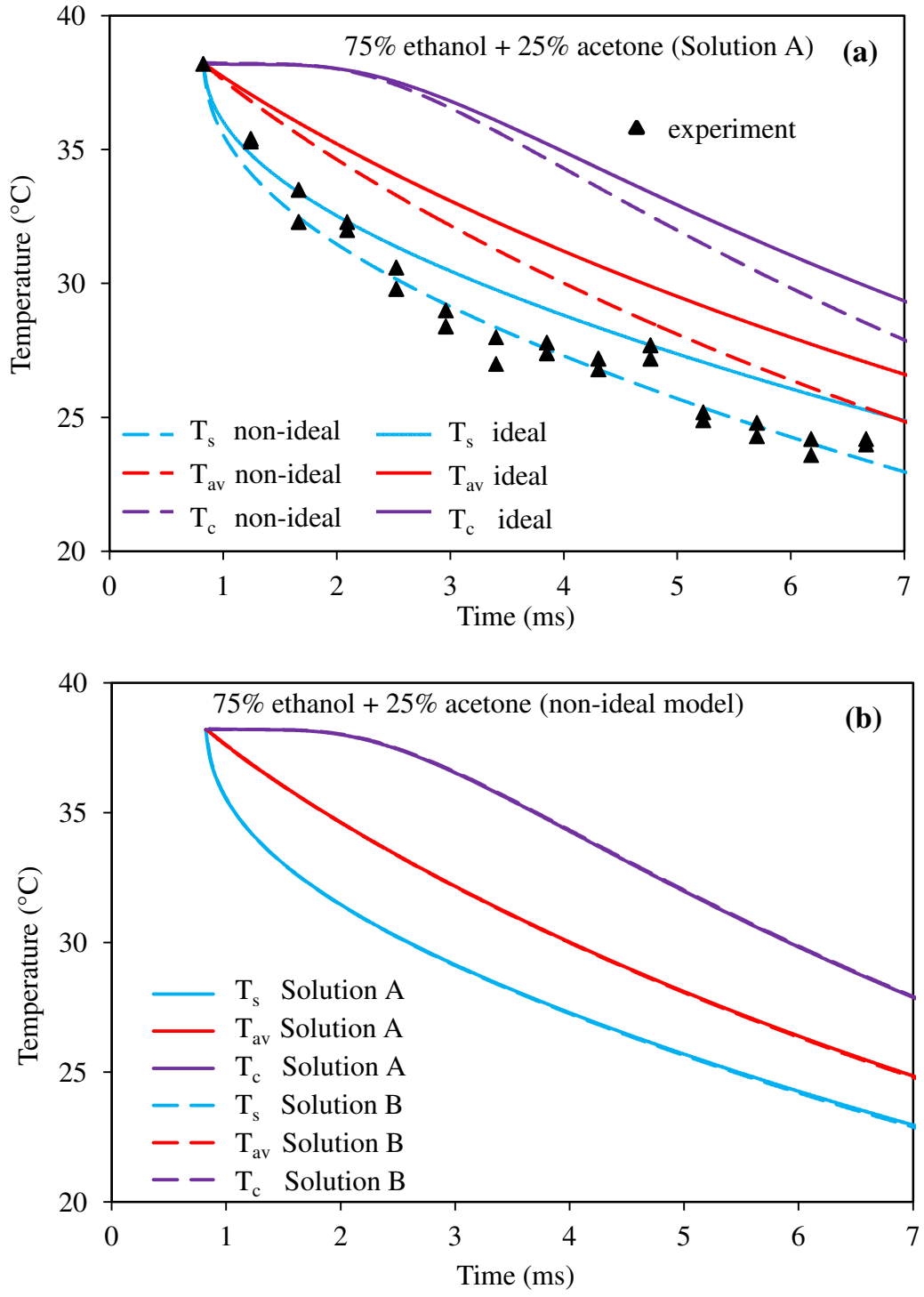


Fig. 4.17 The same as Figs. 4.15 and 4.16 but for the 75% ethanol – 25% acetone mixture droplets.

### *4.4.3 Solution A based on moving boundary*

As mentioned in the Introduction, in a number of papers (Sazhin et al, 2010a; 2011d; Mitchell et al, 2011) it was shown that the assumption that the droplet radius is fixed during the timestep can lead to noticeable deviations from the results predicted by the models which take into account the changes of this radius during the timesteps. The cases tested in the above-mentioned papers refer to droplet heating and evaporation in a hot gas and the moving boundary was linked only with droplet evaporation. The effects of thermal swelling/contraction were ignored in these papers. Also, only mono-component droplets were considered, in which case the moving boundary only had an effect on the heat conduction equation inside droplets. In this section the effect of the moving boundary on both heat transfer and species diffusion equations will be taken into account based on Eqs. (4.15) and (4.22). The model will first be applied to the case of droplets considered in Section 4.3. Then other related cases will be considered.

The plots of time evolutions of the temperatures at the centre and the surface of the droplets and the average droplet temperatures, predicted by the models not taking into account the effect of the moving boundary and taking into account this effect for both temperature and species diffusion for the 25% ethanol – 75% acetone and 50% ethanol – 50% acetone mixture droplets, are shown in Fig. 4.18. As can be seen from this figure, the effect of the moving boundary on the predicted temperatures can be safely ignored in the analysis of experimental data described in Section 4.3. The same conclusion can be drawn for the case of the 75% ethanol – 25% acetone mixture droplets.

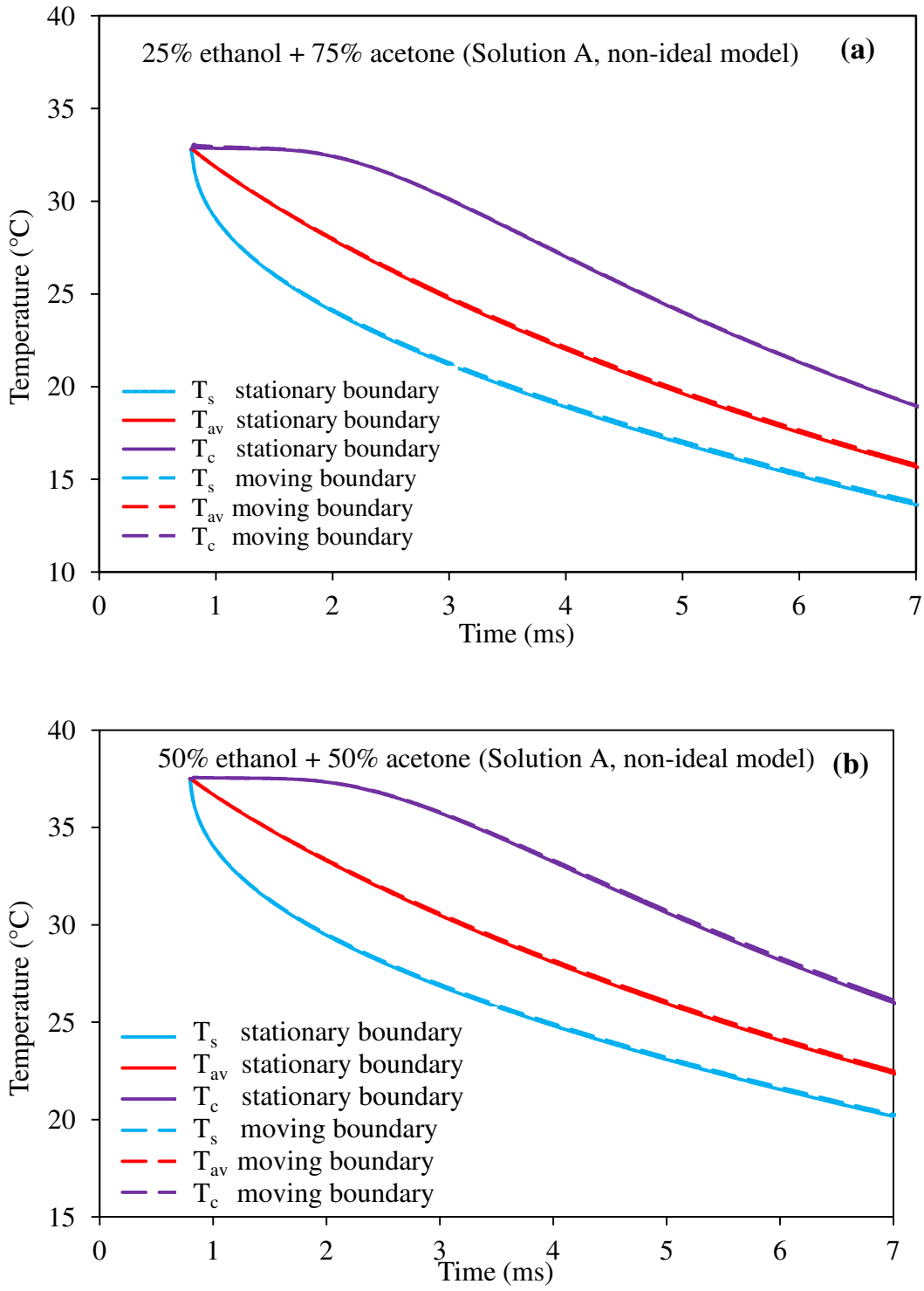


Fig. 4.18 The time evolution of droplet surface, average and centre temperatures ($T_s$, $T_{av}$ and $T_c$), predicted by Solution A for the non-ideal model, taking and not taking into account the effects of moving boundary during individual timesteps (moving and stationary boundaries) on the solutions to both heat transfer and species diffusion equations for the 25% ethanol – 75% acetone mixture droplets with the values of the initial parameters, droplet velocity and gas temperature given in Table 4.1 (a); the same as (a) but for the 50% ethanol – 50% acetone mixture droplets (b).

In Fig. 4.19 a hypothetical case is shown when the 50% ethanol – 50% acetone mixture droplets are cooled down or heated and evaporated until complete evaporation takes place. Both plots for the droplet surface temperature and droplet radius are shown. The same values as shown in Table 4.1 for the initial droplet temperature, diameter, distance parameter and gas temperature are used, but in contrast to the case shown in Table 4.1, it is assumed that the droplet velocity remains constant and equal to 12.71 m/s. The cases of the stationary boundary during individual timesteps, the cases when the effects of the moving boundary are taken into account for the heat transfer and species diffusion equations separately during individual timesteps, and the case when these effects are simultaneously taken into account for heat transfer and species diffusion are shown.

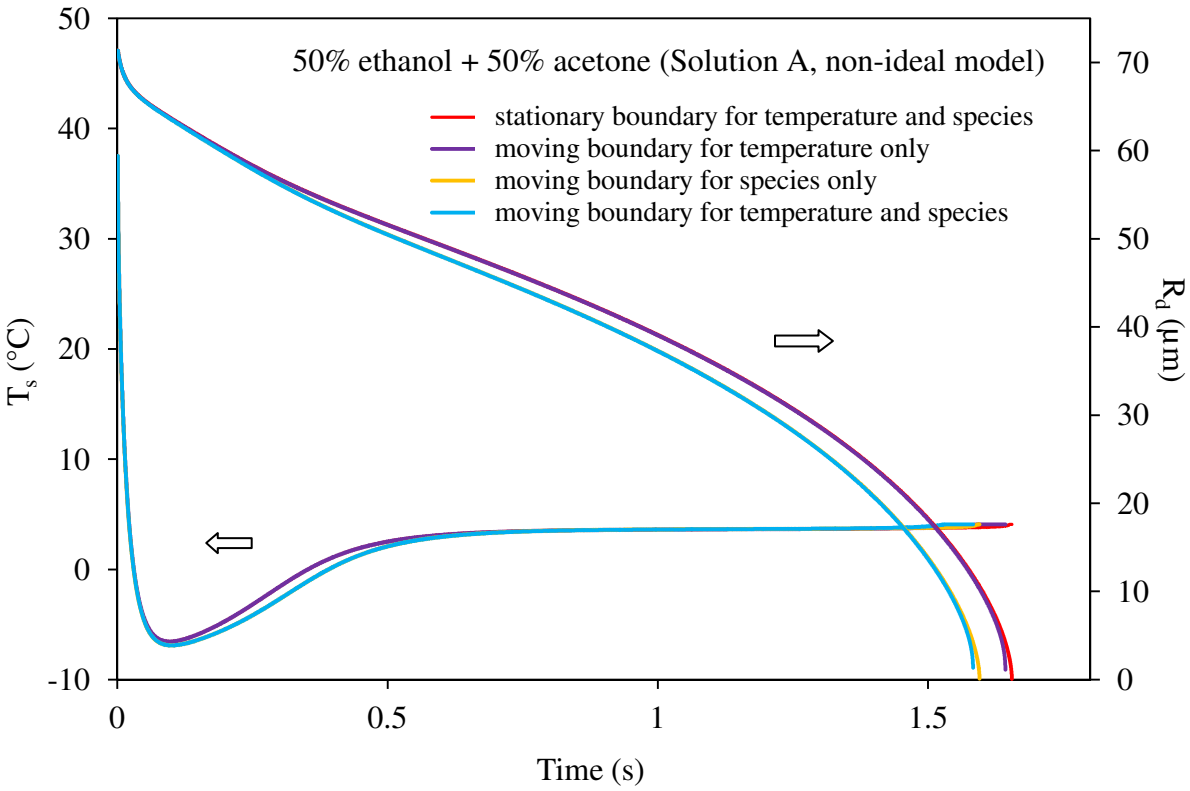


Fig. 4.19 The time evolution of droplet surface temperatures ($T_s$) and radius ($R_d$), predicted by Solution A for the non-ideal model, taking and not taking into account the effects of moving boundary during individual timesteps on the solutions to the heat transfer equation only, species diffusion equation only and both heat transfer and species diffusion equations for the 50% ethanol – 50% acetone mixture droplets with the values of the initial parameters, and gas temperature given in Table 4.1, assuming that the droplet velocity is constant and equal to 12.71 m/s.

As can be seen from Fig. 4.19, the plots taking into account the effects of the moving boundary on the heat transfer equation only, and ignoring this effect altogether practically coincide. That means that this effect can be safely ignored for this case. Also, the plots taking into account the effects of the moving boundary on the solution to the species diffusion equation, and taking it into account for both solutions to the heat transfer and species diffusion equations practically coincide, but the difference between both these curves and the ones ignoring this effect altogether can be clearly seen after about 0.1 s. The effect of the moving boundary is a reduction of the predicted droplet surface temperature between about 0.1 to 0.6 s. During this period the droplet surface temperature is below the ambient gas temperature. Hence the reduction of the droplet surface temperature is expected to increase the heat flux from the ambient gas to the droplets, leading to the acceleration of droplet evaporation. This agrees with the predicted time evolution of the droplet radius, taking and not taking into account the effect of the moving boundary, shown in Fig. 4.19.

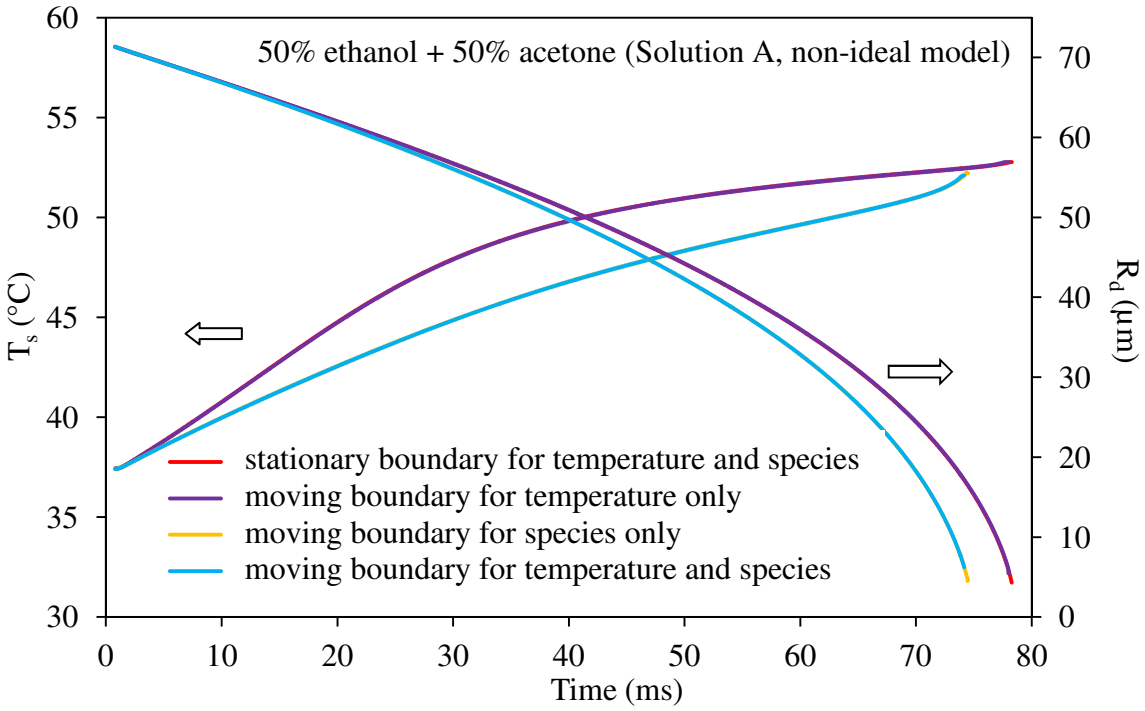


Fig. 4.20 The same as Fig. 4.19 but for gas temperature equal to 1000 K.

In Fig. 4.20 the case similar to the one shown in Fig. 4.19, but for gas temperature equal to 1000 K, is shown. In this case, droplet surface temperature increases during the whole period of droplet heating and evaporation, in contrast to the case shown in Fig. 4.19. As one can see from Fig. 4.20, the plots taking into

account the effects of the moving boundary on the solution to the heat transfer equation, and ignoring this effect altogether practically coincide, as in the case shown in Fig. 4.19. Also, similarly to the case shown in Fig. 4.19, the plots taking into account the effects of the moving boundary on the solution to the species diffusion equations, and taking it into account for both heat transfer and species diffusion equations practically coincide, but the difference between both these curves and the ones ignoring this effect altogether can be clearly seen after about 5 ms. This difference between the plots is much more visible than in the case shown in Fig. 4.19. As in the case shown in Fig. 4.19, the effect of the moving boundary is to reduce the predicted droplet surface temperature leading to the increase of the heat flux from the ambient gas to the droplets and acceleration of droplet evaporation. This agrees with the predicted time evolution of droplet radius, taking and not taking into account the effect of the moving boundary, shown in Fig. 4.20.

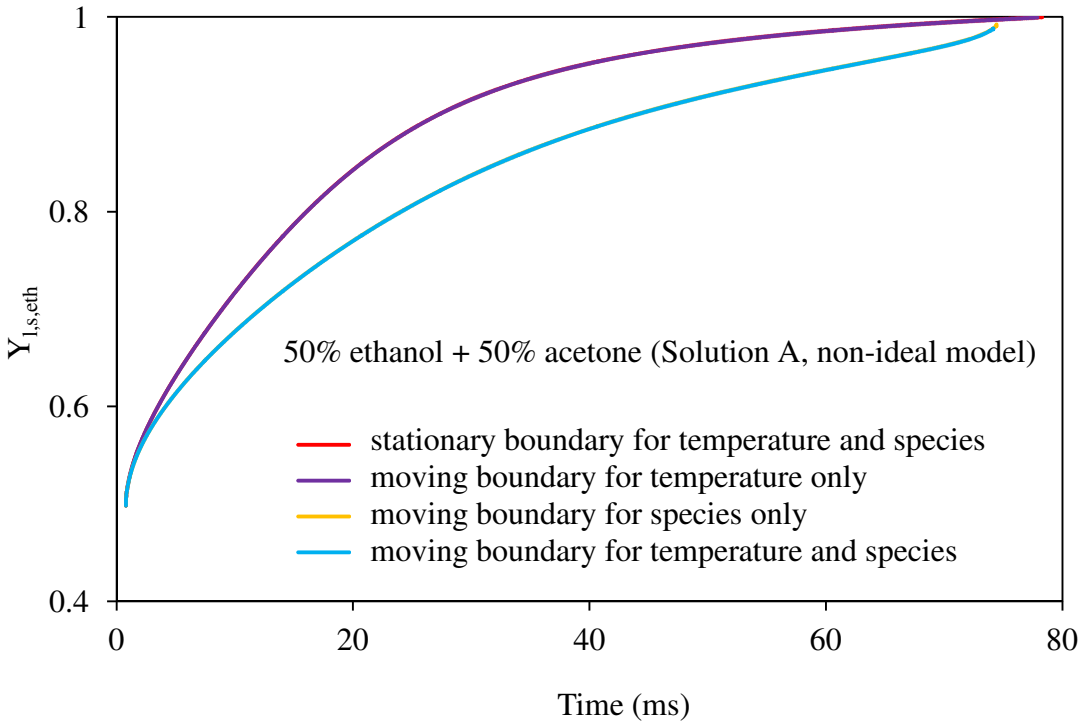


Fig. 4.21 The same as Fig. 4.20 but for the mass fraction of ethanol at the surface of the droplet.

The plots of time evolution of the surface mass fraction of ethanol $Y_{l,s,\mathrm{eth}}$ for the same case as shown in Fig. 4.20, are shown in Fig. 4.21. Similarly to the case shown in Fig. 4.20, the main effect of the moving boundary on the solution to the species diffusion equation is its influence on the values of $Y_{l,s,\mathrm{eth}}$. This effect leads to visible

reductions of the values of $Y_{l,s,\mathrm{eth}}$ until the complete evaporation of the droplet takes place.

### *4.4.4 Effects of the binary diffusion coefficient*

One would expect that the deviation between the predictions of the models and experimental data can be attributed not only to the accuracy of the models and experimental data, but also to the accuracy of the input parameters in the models. As shown before in Sazhin et al (2006), one of the crucial parameters which is expected to affect the predicted time evolution of droplet temperature and radius is the binary diffusion coefficient of fuel vapour in air. The Wilke-Lee formula (Poling et al, 2000) for this diffusion coefficient was used in the previous sections of this chapter:

$$D_v = \frac{\left[3.03-\left(0.98/M_{va}^{1/2}\right)\right]10^{-7}T^{3/2}}{pM_{va}^{1/2}\sigma_{va}^2\Omega_D(T^*)}\ , \tag{4.33}$$

where $D_v$ is in m$^2$/s, $T$ is temperature in K,

$$M_{va} = 2\left(\frac{1}{M_v}+\frac{1}{M_a}\right)^{-1},$$

$M_v$ and $M_a$ are molar masses of vapour and air respectively, $p$ is in atm, $\sigma_{va} = (\sigma_v + \sigma_a)/2$ is the minimal distance between molecules in Angstrom, $\Omega_D$ is the collision integral defined by Eq. (A.2), the values of which depends on the normalised temperature $T^* = k_B T/\varepsilon_{va}$, $k_B$ is the Boltzmann constant, $\varepsilon_{va} = \sqrt{\varepsilon_v \varepsilon_a}$. The values of these parameters are shown in Table A.1. In the case of the mixture of vapour components, all input parameters (molar masses and Lennard–Jones parameters) are calculated as molar averaged, taking into account their relative molar concentrations $X_{\mathrm{eth}}/(X_{\mathrm{eth}} + X_{\mathrm{acet}})$ and $X_{\mathrm{acet}}/(X_{\mathrm{eth}} + X_{\mathrm{acet}})$.

In this section, the sensitivity of some results, reported in the previous sections, with respect to the choice of the approximation for $D_v$ will be investigated. The following approximations for $D_v$, alongside Eq. (4.33) have been chosen.

The Chapman-Enskog approximation, Giddings (1965):

$$D_v = \frac{2.63\times10^{-7}T^{3/2}}{pM_{va}^{1/2}\sigma_{va}^2}. \tag{4.34}$$

The Gilliland approximation, Gilliland (1934)

$$D_v = \frac{4.3\times10^{-7}T^{3/2}}{p\left(V_v^{1/3}+V_a^{1/3}\right)^2}\sqrt{\frac{2}{M_{va}}}, \tag{4.35}$$

where $V_v$ and $V_a$ are molar volumes of vapour and air in cm$^3$ respectively. They are calculated as Polling et al (2000):

$$V_{v,a} = \left(\sigma_{v,a}/1.18\right)^3.$$

The Hirschfelder-Bird-Spotz approximation, Hirschfelder et al (1949):

$$D_v = \frac{1.86\times10^{-7}T^{3/2}}{p\sigma_{va}^2\Omega_D(T^*)}\sqrt{\frac{2}{M_{va}}}. \quad (4.36)$$

The Fuller-Schettler-Giddings approximation, Fuller et al (1966):

$$D_v = \frac{1.43\times10^{-7}T^{1.75}}{\sqrt{2}p\left((\sum v)^{1/3}+(\sum a)^{1/3}\right)}\sqrt{\frac{2}{M_{va}}}, \quad (4.37)$$

where the diffusion volumes $\sum v$ and $\sum a$ are determined by summing the atomic contributions for vapour and air as described in Table 11.1 of Poling et al (2000); $\sum a = 19.7$ cm$^3$, $\sum \text{eth} = 51.77$ cm$^3$ and $\sum \text{acet} = 67.67$ cm$^3$.

The values of $D_v$ in Eqs. (4.33)-(4.37) are in m$^2$/s; $p$ is in atm and $M_{va}$ is in kg/kmole. Eqs. (4.33)-(4.37) are reproduced from Polling et al (2000) and Eslamloueyan and Khademi (2010).

The plots of $D_v$ versus $T$, based on Eqs. (4.33)-(4.37) for acetone and ethanol, are shown in Fig. 4.22. As one can see from this figure, the values of $D_v$, predicted by these formulae are noticeably different especially for ethanol at high temperatures. Note that the predictions of Eq. (4.35) (Gilliland approximation) for acetone and ethanol are almost identical, in contrast to predictions of other equations. This is related to the fact that Eq. (4.35) does not contain $\sigma_{va}$ while masses and molar volumes of acetone and ethanol are about the same. At room temperatures, relevant to the experiments described in Section 4.3, the values of $D_v$, predicted by all approximations, except the one suggested by Chapman and Enskog for acetone and Gilliland for ethanol, are rather close. The values of $D_v$ for the mixtures of acetone and ethanol are expected to lie between those shown in Fig. 4.22. In the following analysis we investigate how this relatively small difference in $D_v$ affects the predicted values of the average temperatures for pure acetone and ethanol.

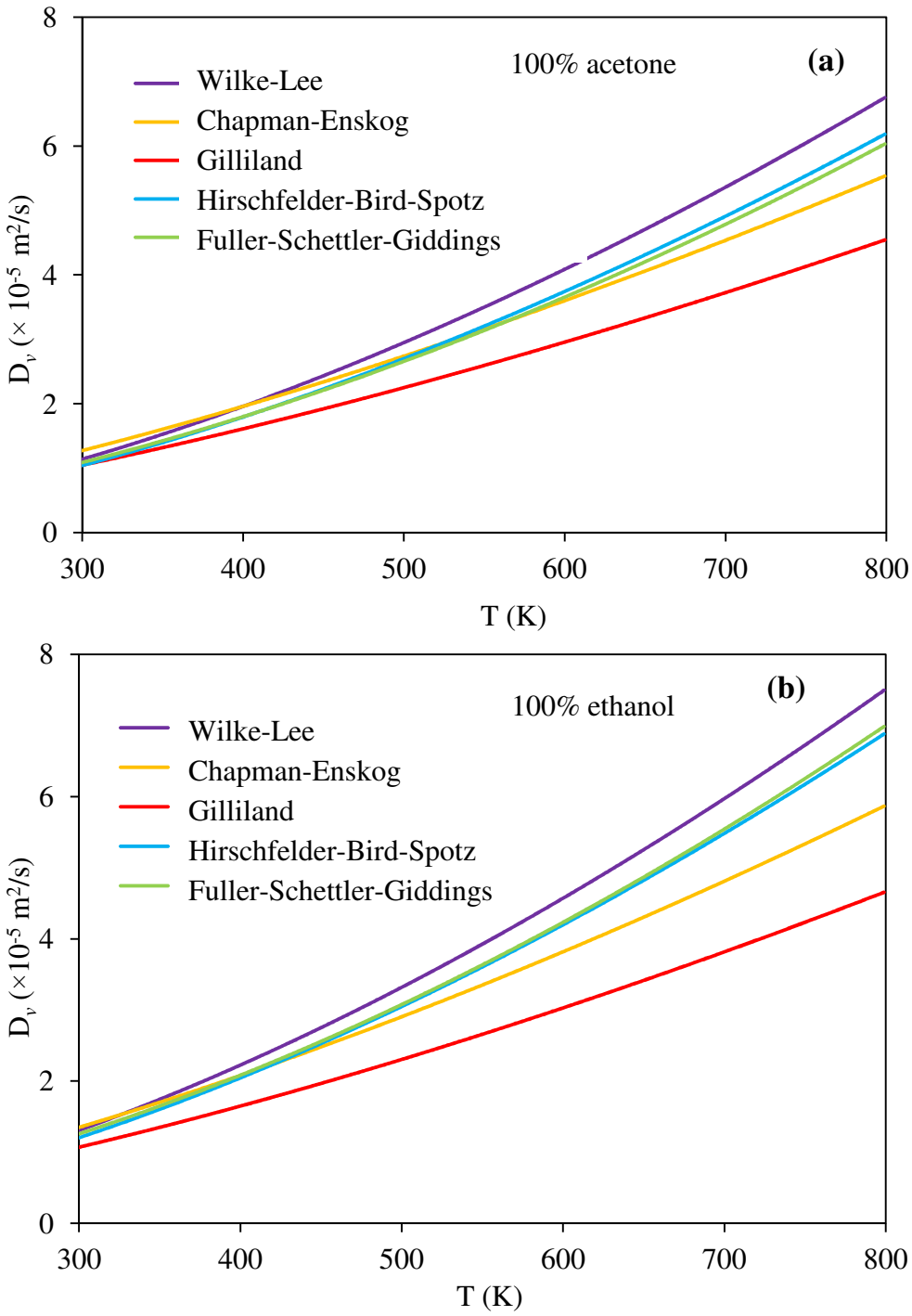


Fig. 4.22 The temperature dependence of the diffusion coefficient of acetone (a) and ethanol (b) for the models described in Section 4.4.4.

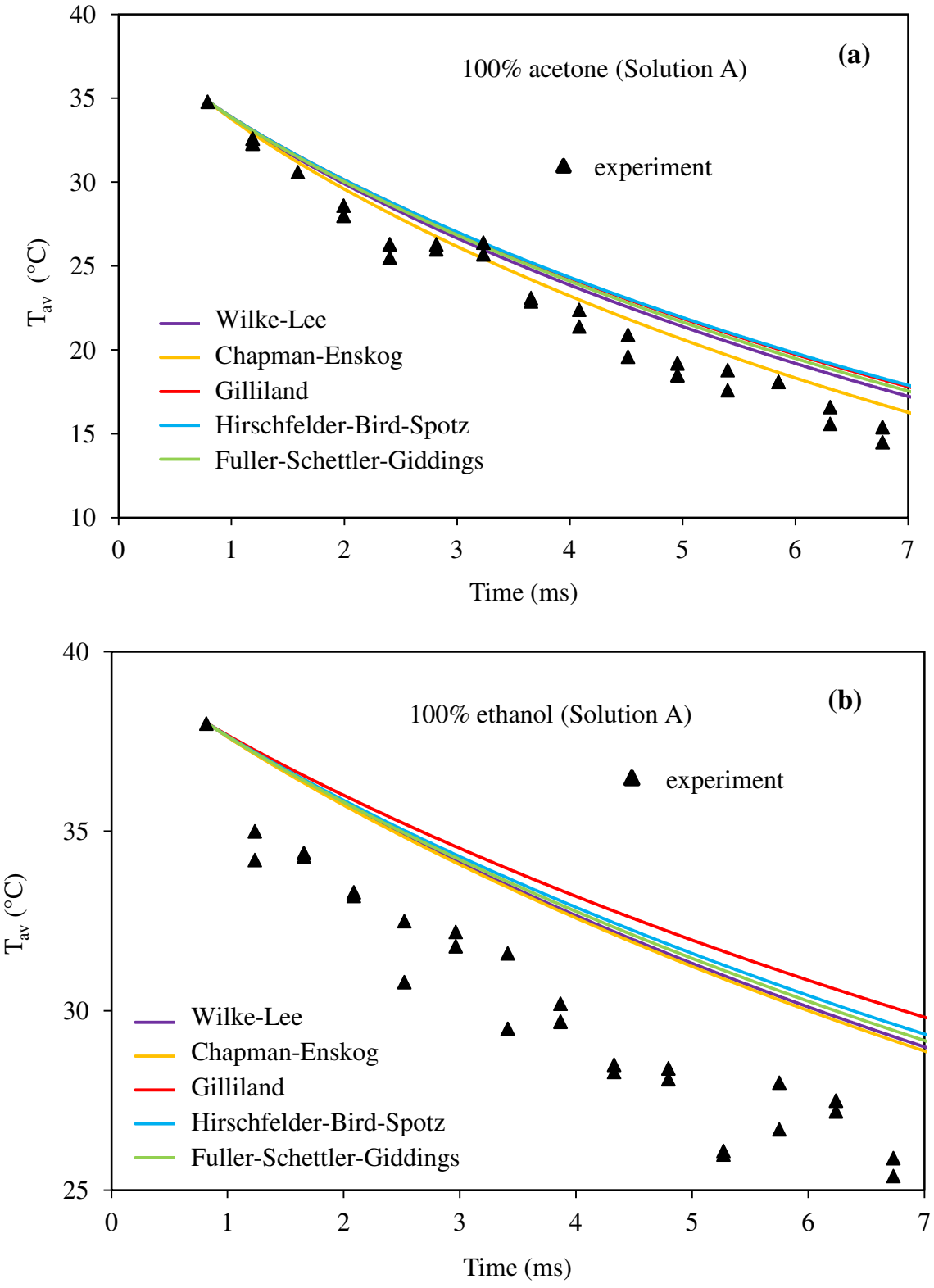


Fig. 4.23 The time evolution of droplet average temperatures ($T_{av}$), predicted by Solution A, using the diffusion coefficients predicted by Eqs. (4.33)-(4.37) and shown in Fig. 4.22, and experimentally observed temperatures for pure acetone (a) and ethanol (b) droplets with the values of the initial parameters, droplet velocity and gas temperature given in Table 4.1.

The plots of the time dependence of the droplet average temperatures for pure acetone and ethanol, obtained based on Solution A, using Eqs. (4.33)-(4.37) are shown in Fig. 4.23. As before, experimentally observed average droplet temperatures are shown by filled triangles. As one can see from this figure, the values of the average temperatures predicted by all approximations turned out to be rather close. Hence, the predictions of the model are not expected to be sensitive to the values of $D_v$. The same conclusion is expected for the mixtures of acetone and ethanol (the plots are not shown).

Finally we check the validity of the parameter $\varphi$, defined by Eq. (2.33) to correlate the heat transfer number $B_T$ with the mass transfer number $B_M$, based on the assumption that $\frac{\mathrm{Sh}^*}{\mathrm{Nu}^*} = 1$, Sazhin et al (2006).

This is done by direct comparison between the values of $T_{\mathrm{av}}$, predicted by the Solution A, using the general equation of $\varphi$ (Eq. (2.33)) and the simplified $\varphi$ based on the assumption that $\mathrm{Sh}^*/\mathrm{Nu}^* = 1$. The results for pure acetone and ethanol are shown in Fig. 4.24. The actual values of $\mathrm{Sh}^*/\mathrm{Nu}^*$ for acetone and ethanol are also shown in the same figure. As can be seen from this figure the values of $\mathrm{Sh}^*/\mathrm{Nu}^*$ for both acetone and ethanol are close to 1, while the values of $T_{\mathrm{av}}$, predicted using both formulae, practically coincide. We anticipate that the same coincidence takes place for the mixtures of acetone and ethanol. This justifies our original assumption that the value of $\varphi$ can be estimated using the simplified $\varphi$ based on the assumption that $\mathrm{Sh}^*/\mathrm{Nu}^* = 1$.

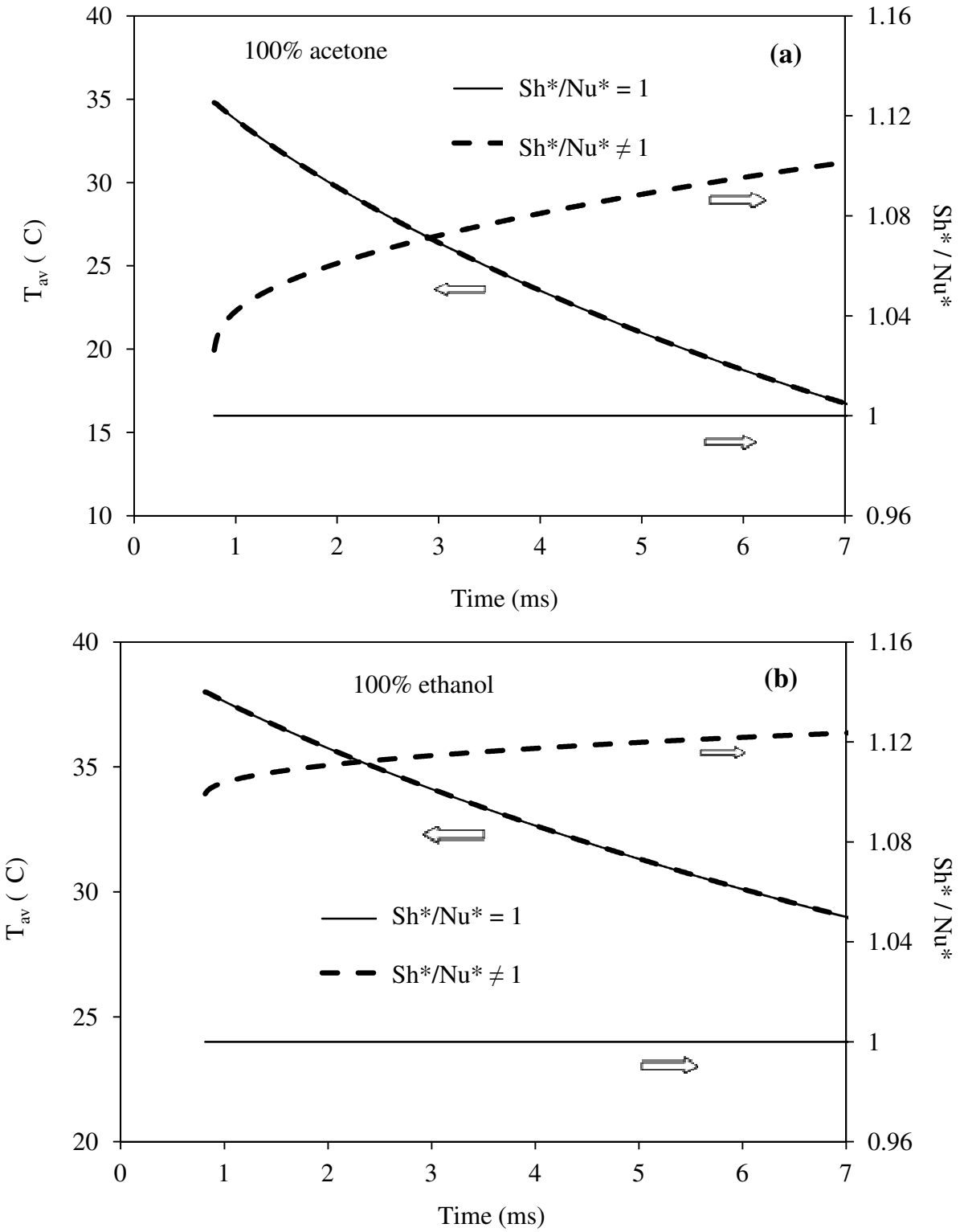


Fig. 4.24 The plots of the time evolution of Sh*/Nu* and $T_{av}$, predicted by Solution A, Eq. (2.33) (dashed curves) and using parameter based on Sh*/Nu* = 1 (solid curves) for pure acetone (a) and ethanol (b).

## 4.5 Conclusions of Chapter 4

A simplified model for bi-component droplet heating and evaporation is suggested. This model takes into account droplet heating by convection from the ambient gas, the distribution of temperature inside the droplet, diffusion of liquid species inside the droplet, droplet swelling or contraction due to changing average temperature, effects of the non-unity activity coefficient (ideal and non-ideal models), the effects of the moving boundary and the effects of the interaction between moving droplets due to the finite distance parameter. The effects of recirculation in the moving droplets on heat and species diffusions within them are taken into account using the ETC and ED models. The previously obtained analytical solution to the transient heat conduction equation has been incorporated in the numerical code alongside the original analytical solution to the species diffusion equation inside droplets.

The predicted time evolutions of surface, average and central droplet temperatures have been compared with the results of direct measurements of droplet average temperatures for the case of various mixtures of ethanol and acetone. There is a general agreement between the predicted and observed average temperatures in the case of pure acetone and acetone-rich mixtures. In the case of ethanol, 50% ethanol - 50% acetone and 75% ethanol - 25% acetone mixture droplets the predicted average droplet temperature was several degrees (up to 5 °C) higher compared with the observed one. It has been shown that the temperatures predicted by the simplified model and the earlier reported vortex model were reasonably close. Also, the temperatures predicted by the ideal and non-ideal models differ by not more than several degrees. This can justify the application of the simplified model with the activity coefficient equal to 1 for the interpretation of the time evolution of temperatures measured with similar errors.

It is pointed out that the predictions of the models based on the analytical and numerical solutions to the heat transfer and species diffusion equations inside droplets are almost identical (both models are based on the assumption that the location of the droplet surface is fixed during the timestep), which gives confidence in both solutions.

It is pointed out that for the conditions of the experiment described in Section 4.3, the predictions of the models, taking and not taking into account the effects of the moving boundary during the timestep on the solutions to the heat transfer and

species diffusion equations are very close. The deviation between the predictions of these models can be ignored in this case. At the same time, the difference in the predictions of these models needs to be taken into account when the whole period of droplet evaporation up to the complete evaporation of droplets is considered. The effect of the moving boundary is shown to be much stronger for the solution to the species diffusion equation than for the solution to the heat conduction equation inside droplets.

The effect of the choice of the approximation of the diffusion coefficient for the ethanol/acetone vapour in air is shown to be small for the conditions of the experiment considered in this chapter, and can be ignored in most engineering applications.

# 5 Coupled solution and code optimisation

## 5.1 Introduction

Although the simplified model for bi-component droplets heating and evaporation, suggested in Chapter 4, was recommended for incorporation into CFD codes, there are still a number of issues which need to be addressed. The original model suggested in Chapter 4, took into account the effect of ambient gas on droplets but ignored the effects of droplets on gas. Furthermore, the issue of optimisation of the code was not addressed in Chapter 4. The choice of the number of terms in the analytical solutions was based exclusively on the numerical values of the ignored terms, without taking into account the computational cost. These two issues will be addressed in this chapter. Also, the model suggested in Chapter 4 will be generalised to arbitrary number of species and validated against experimental data different from those used in Chapter 4. The new analytical solution to species diffusion equation is the same as in Chapter 4 for stationary boundaries and it is described at Appendix D. The analytical solution to heat transfer equation within the droplet is the same as used in Chapters 3 and 4, originally developed by Sazhin et al (2004). It is presented in Chapter 2.

Basic equations and approximations are briefly summarised in Section 5.2. Our approach to the coupled solution and the numerical algorithm are described in Sections 5.3 and 5.4 respectively. Section 5.5 is focused on the input parameters. The results of calculations are compared with experimental data in Section 5.6. In Section 5.7, the accuracy of the model predictions versus the CPU efficiency of the code are investigated. The main results of this chapter are summarised in Section 5.8.

## 5.2 Basic equations and approximations

Most basic equations and approximations used in the analysis of this chapter are essentially the same as used in Chapters 2 and 3 for heat conduction equation inside the droplet and the same as used in Chapter 4 for species diffusion equation inside the droplet for the case of stationary boundaries. New equations, not used in Chapter 3 or 4, are described below.

The values of $Sh_{iso}$ and $Nu_{iso}$ and are calculated based on Eqs. (2.30) and (2.31) respectively. In Chapter 3, the corrections to $Sh_{iso}$ and $Nu_{iso}$ due to the finite distance

between droplets were calculated based on the experimental results (see Table 3.1 and Section 3.3) while in Chapter 4, these corrections were calculated based on the empirical correlation, which was the function of the distance parameter (see Eq. (4.3)). However, as shown by Deprédurand et al (2010), this correlation does not always work, mainly due to the fact that it does not account for fuel volatility which influences the interaction between droplets.

Following Deprédurand et al (2010), we introduce the dimensionless time $t^*$ defined as:

$$t^* = \frac{\delta f}{v_r}, \tag{5.1}$$

where $f$ is the frequency of droplet production (in Hz) (set up for each particular experiment and directly linked with the distance parameter), $\delta$ is the film thickness, which is different for mass and thermal boundary layers ($\delta_M$ and $\delta_T$), $v_r$ is the radial velocity of the vapour released at the droplet surface estimated as:

$$v_r = \frac{\dot{m}_d}{4\pi\rho_v R_d^2}, \tag{5.2}$$

where $\rho_v$ is the density of vapour and $\dot{m}_d$ is the total evaporation rate of the droplet calculated based on Eq. (3.5). Parameter $t^*$ takes into account the contributions of both the distance parameter (via $f$) and the volatility of fuel (via $v_r$).

The values for $\delta_M$ and $\delta_T$ for mono-component droplets were estimated based on the model suggested by Abramzon and Sirignano (1989):

$$\delta_T = F(B_T)\frac{2R_d}{\mathrm{Nu}_0 - 2}, \tag{5.3}$$

$$\delta_M = F(B_M)\frac{2R_d}{\mathrm{Sh}_0 - 2}, \tag{5.4}$$

where $F(B_{M,T})$ are the same as introduced in Eqs. (2.28) and (2.29). $\mathrm{Nu}_0$, $\mathrm{Sh}_0$ are Nusselt and Sherwood numbers for non-evaporating droplet respectively. They can be defined following Abramzon and Sirignano (1989) as:

$$\mathrm{Nu}_0 = 1 + (1 + \mathrm{Re}_d\mathrm{Pr}_\mathrm{d})^{1/3} f(\mathrm{Re}_d), \tag{5.5}$$

$$\mathrm{Sh}_0 = 1 + (1 + \mathrm{Re}_d\mathrm{Sc}_\mathrm{d})^{1/3} f(\mathrm{Re}_d), \tag{5.6}$$

where $f(\mathrm{Re}_d) = 1$ at $\mathrm{Re}_d \leq 1$ and $f(\mathrm{Re}_d) = \mathrm{Re}_d^{0.077}$ at $1 < \mathrm{Re}_d \leq 400$. $\mathrm{Re}_d$, $\mathrm{Pr}_\mathrm{d}$ are Reynolds and Prandtl numbers, based on the gas transport coefficients (Eq. (2.26)).

These definitions of $\delta_M$, $\delta_T$ and $\upsilon_r$ were generalised to the case of multi-component droplets, via introduction of the average density and mass averaged values of transport coefficients.

Having introduced the concept of $t^*$, Deprédurand et al (2010) suggested the following correlations for $\eta_{\mathrm{Nu}} = \frac{\mathrm{Nu}}{\mathrm{Nu_{iso}}}$ for acetone, ethanol, 3-pentanone, n-decane, n-dodecane and n-heptane, and $\eta_{\mathrm{Sh}} = \frac{\mathrm{Sh}}{\mathrm{Sh_{iso}}}$ for ethanol, 3-pentanone and n-heptane ($\eta_{\mathrm{Sh}}$ for acetone was approximated by the same correlation as for $\eta_{\mathrm{Nu}}$):

$$\eta_{\mathrm{Nu}} = \frac{\mathrm{Nu}}{\mathrm{Nu_{iso}}} = \frac{1-0.155335}{(1.416767t^*+1)^{0.535026}} + 0.155335, \tag{5.7}$$

$$\eta_{\mathrm{Sh}} = \frac{\mathrm{Sh}}{\mathrm{Sh_{iso}}} = \frac{1-0.155335}{(6.503406\times10^{-7}t^*+1)^{54302.36}} + 0.155335. \tag{5.8}$$

Although Eqs. (5.7) and (5.8) were derived for a limited number of substances; it can be assumed that they are valid for a wider range of substances and their mixtures. They will be applied to the analysis of droplets of the mixture of n-decane and 3-pentanone.

## 5.3 The coupled solution

The model, described in the previous chapter, could be generalised to take into account the effects of droplets on gas and then incorporated into any CFD code (e.g. KIVA by Amsden et al, 1987). This analysis, however, is beyond the scope of this chapter. Instead, a simplified model, capturing the essential features of coupling between droplets and ambient gas will be described with a view to a specific application to the analysis of the experimental data, similar to those described by Maqua et al (2008a,b) and Deprédurand et al (2010) (Sections 3.3 and 4.3). In these experiments, ambient gas pressure remained the same and equal to the atmospheric pressure. Let us assume that the droplet exchanges heat and mass with a certain volume $V_g$, surrounding it. Following Tonini et al (2008), we call it the region of influence. The shape of this region can be either spherical, in the case of isolated droplets, or cylindrical, in the case of droplets stream, considered by Maqua et al (2008a,b) and Deprédurand et al (2010). In both cases, the cross-section of this region in the arbitrary direction for the spherical region and the cross-section perpendicular to the axis of the cylinder is schematically shown in Fig. 5.1. For the spherical and cylindrical regions, their volumes can be estimated based on the following equations:

$$V_g = \frac{4}{3}\pi\left(R_g^3 - R_d^3\right) \tag{5.9}$$

and

$$V_g = \pi R_g^2 d - \frac{4}{3}\pi R_d^3 \tag{5.10}$$

respectively, where $d$ is the distance between droplets. The choice of $R_g$ will be discussed in Section 5.3.3.

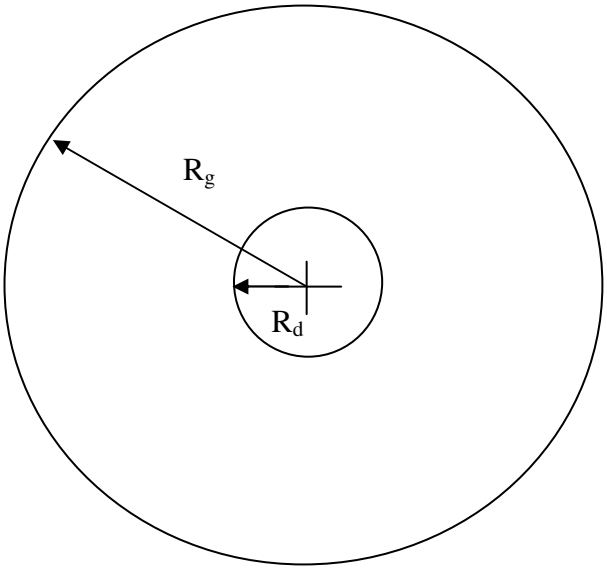


Fig.5.1 Schematic diagram for the spherical region of influence or the plane perpendicular to the cylinder axis for the cylindrical region of influence.

This model will be applied to the analysis of the experiments by Deprédurand et al (2010), where the droplets' velocities were determined from the experiments and not calculated. Hence, the momentum transfer between the region of influence and the droplets is not considered in the model.

This region of influence is assumed to be large enough to allow us to ignore heat exchange between it and the ambient gas, and escape of fuel vapour from this region to the ambient gas. Let's first focus on the mass transfer process.

### *5.3.1 Mass balance*

The total number of moles of gas inside volume $V_g$ can be obtained from the ideal gas law:

$$N_{\text{total}} = \frac{p_{\text{atm}} V_g}{R_u T}, \tag{5.11}$$

where $R_u$ is the universal gas constant. Initially, there is no vapour in $V_g$ and $N_{\text{total}} = N_a$ (number of moles of air) at $T = T_0$. Once the evaporation process has started then a certain number of moles of vapour $N_v = \sum_{i=1}^{N} N_{vi}$, where $N$ is the total number of species, penetrates into volume $V_g$. Simultaneously the temperature changes from the

initial temperature $T_0$ to $T_1$. The number of moles of air in this case reduces (or increases if $T_1$ is sufficiently lower than $T_0$) to:

$$N_{\text{total}} = \frac{p_{\text{atm}} V_g}{R_u T_1} - \sum_{i=1}^{N} N_{vi}. \tag{5.12}$$

Thus the mass fraction of vapour inside the cell can be estimated as:

$$Y_{v(\text{cell})} = \frac{\sum_{i=1}^{N} M_{vi} N_{vi}}{\sum_{i=1}^{N} M_{vi} N_{vi} + M_a N_a}, \tag{5.13}$$

where $M_a$ is the molar mass of air, $M_{vi}$ are molar masses of vapour species. We assume that $Y_{v\infty} = Y_{v(\text{cell})}$. In the one-way solution, described in Chapters 3 and 4, it was assumed that $Y_{v\infty} = 0$. When deriving Eqs. (5.12) and (5.13) it was assumed that fuel vapour cannot escape from volume $V_g$, which is justified if this volume is large enough, and the duration of the process is short ($\Delta t \ll R_g^2/D_v$, where $D_v$ is the diffusion coefficient for vapour, described by Wilke-Lee Formula Eq. (4.33)). For sufficiently small timesteps, we can assume that $T_1 = T_0$ in Eq. (5.12) and updated at the next timestep.

The calculation continues until $Y_{v(\text{cell})} = Y_{vs}$. Once this happens, the droplet stops evaporating ($B_M = 0$). Apart from $Y_{v(\text{cell})}$, Eqs. (5.12) and (5.13) are used for calculation of physical properties of the mixture of vapour and air.

### *5.3.2 Heat balance*

Assuming that gas temperature inside volume $V_g$ is homogeneous, the time evolution of this temperature can be described by the equation:

$$\frac{\mathrm{d}\left(m_g c_{pg} T_g\right)}{\mathrm{d}t} = -2\pi k_g \mathrm{Nu} R_d \left(T_g - T_s\right), \tag{5.14}$$

where $m_g$ is the total mass of gas (mixture of air and vapour) in volume $V_g$, Nu is the Nusselt number for evaporating droplets (taking into account the heating/cooling of the vapour).

Eq. (5.14) was solved at each timestep. The value of $m_g$ in this equation is the mass of the mixture of air and fuel vapour as calculated at the previous timestep. The values of $k_g$ and $c_{pg}$ were calculated for the mixture of air and fuel vapour as described in Appendix C. The physical meaning of Eq. (5.14) is obvious: this is the mathematical expression of the statement that the energy lost by the gas is spent on droplet heating and evaporation. Possible effects of gas temperature gradients near the droplet surface were considered by Sazhin et al (2007).

### *5.3.3 Size of the region of influence*

In CFD codes the results of calculations should not depend on the cell sizes for sufficiently small cells, since the ordinary differential equations in individual cells are solved alongside partial differential equations describing mass, momentum and energy transfer between cells. Although this is true in the case of the Eulerian approach, the results usually start depending on the grid size for sufficiently small cells in the case of the Lagrangian/Eulerian approach widely used for spray simulation. This problem was extensively discussed by Tonini et al (2008), where the concept of the region of influence was first introduced. The main idea of this concept is to allow droplets to exchange mass, momentum and energy not only with gas in a cell, in which a droplet is located, but with gas in a wider *a priori* determined region (region of influence). Essentially the same idea is used in this chapter. The size of this region is considered as a free parameter, within a certain range, which can be adjusted to get the best fit with experimental data. In the case of very large $V_g$, the coupled solution reduces to the one-way solution. For small $V_g$, an unphysical solution can be obtained, since in this case the interaction of gas in $V_g$ and the surrounding air, ignored in our analysis, can play the dominant role.

We assume that $R_g$ can be approximately estimated as:

$$R_g = R_d + \sqrt{k_D t_D}, \tag{5.15}$$

where $t_D$ is the characteristic duration of the process,

$$k_D = \max\left(\frac{k_g}{c_{pg}\rho_g}, D_v\right), \tag{5.16}$$

where the first term in the latter equation describes the heat diffusivity in volume $V_g$, while the second term describes diffusion coefficient of the fuel vapour in the gas inside the region of influence. Since $R_g$ is considered as a fitting parameter in our model, we ignore its possible increase during the experiments (displacement of droplets away from the nozzle).

## 5.4 Numerical algorithm

The numerical scheme outlined below is specifically focused on the application of the model for interpretation of the experimental results similar to those reported by Maqua et al (2008a,b) and Deprédurand et al (2010). In the experiments reported in these papers ambient pressure was constant. The time evolution of droplet velocities was directly measured and these were used as input parameters of

the model at each timestep. In contrast to Chapters 3 and 4, the effects of droplets on the gas phase were taken into account (coupled solution). These are the main steps of the numerical algorithm:

1. Assume the initial distribution of temperature and mass fractions of species inside the droplet or use the distributions obtained at the previous timestep (the initial distributions of both were assumed homogeneous). Recalculate the mass fractions of species into molar fractions of species.

2. Calculate the values of liquid thermal conductivity and effective thermal conductivity of the droplet. Use the values of the droplet velocities from the experimental data.

3. Calculate species partial pressures and molar fractions in the gas phase from Raoult's law (Eqs. (4.11) and (4.12)).

4. Calculate maximum of the thermal and mass diffusivities; calculate $R_g$ according Eq. (5.15) with $t_D$ = 12 ms (typical transit time of droplets). This step is applied to the first timestep only.

5. Calculate the interaction volume based on Eq. (5.9) for the spherical volume and Eq. (5.10) for the cylindrical volume. Calculate the concentration of vapour of all species in the region of influence.

6. Calculate the values of heat capacity (Appendices B and C), diffusivity of the mixture of vapour species in the air (Eq. (4.33)), species evaporation rates $\epsilon_i$ based on Eq. (4.7) and the value of the Spalding mass transfer number based on Eq. (4.2).

7. Calculate the values of Sherwood and Nusselt numbers for isolated droplets $Sh_{iso,}$ $Nu_{iso}$ based on Eqs. (2.30) and (2.31) respectively.

8. Calculate the values of Nusselt and Sherwood numbers for droplets, taking into account the interaction between them (Eqs. (5.7) and (5.8)).

9. Calculate the total change of mass of the evaporating droplet during the timestep $\Delta t$, taking into account the interaction between droplets and the change in liquid density (Eq. (3.5)).

10. Calculate the rate of change of droplet radius based on Eq. (3.2).

11. Calculate the distribution of temperature inside the droplet based on Eq. (2.23).

12. Calculate the distribution of species inside the droplet based on Eq. (D. 38).

13. Recalculate the droplet's radius at the end of the timestep $\Delta t$. In our analysis the droplets never fully evaporated, but the program was designed to deal with the case when the complete evaporation takes place, if necessary. If this radius is negative then the timestep is reduced and the calculations are repeated. If the ratio of this radius to the initial radius is less than an *a priori* chosen small number $\varepsilon_s = 10^{-6}$, then the remaining part of the droplet is assumed to be evaporated with all liquid species transferred into the gas phase with the corresponding decrease in gas temperature. If this ratio is greater than $10^{-6}$ then go to the next step.

14. Recalculate the distributions of temperature and species for the new radius (e.g. $T(R) = T(RR_{d2}/R_{d1}) = T(\tilde{R})$, where $R_{d1,2}$ are droplet radii at the beginning and the end of the timestep, $\tilde{R}$ is the new $R$ used at the second timestep, $T$ are the values of temperature at the end of the timestep).

15. Return to Step 1 and repeat the calculations for the next timestep.

## 5.5 Input parameters

The experimental set-up used for validation of the model is the same as described in Chapters 3 and 4. Three sets of experimental data referring to the mixtures of decane and 3-pentanone will be used in this chapter analysis. These are 95% decane – 5% 3-pentanone, 90% decane – 10% 3-pentanone and 85% decane – 15% 3-pentanone mixture droplets, which will be referred to as Cases 1, 2 and 3

respectively. Droplet initial diameters, temperatures, ambient temperatures, distance parameters, injection frequencies and the experimentally observed time evolutions of droplet velocities for these cases are presented in Table 5.1.

| Parameter | Case 1<br>95% n-decane –<br>5% 3-pentanone | Case 2<br>90% n-decane –<br>10% 3-pentanone | Case 3<br>85% n-decane –<br>15% 3-pentanone |
|---|---|---|---|
| **Initial diameter** | 122.7 µm | 126.1 µm | 127.7 µm |
| **Initial temperature** | 28.66 °C | 25.6 °C | 26.3 °C |
| **Ambient temperature** | 370 °C | 374 °C | 374 °C |
| **Distance parameter** | 3.78 | 3.84 | 3.8 |
| **Injection frequency** | 20600 Hz | 20600 Hz | 20500 Hz |
| $u_1$**, Eq. (3.7)** | 8.51 (m/s) | 10.35 (m/s) | 10.0 (m/s) |
| $u_2$**, Eq. (3.7)** | 0.174 (m/(s.ms)) | 0.278 (m/(s.ms)) | 0.209 (m/(s.ms)) |

Table 5.1 Droplet initial diameters, temperatures, ambient temperatures, distance parameters, injection frequencies and the droplet velocities in m/s are approximated by Eq. (3.7) where $t$ is in ms, for the 95% n-decane – 5% 3-pentanone mixture droplets (Case 1), 90% n-decane – 10% 3-pentanone mixture droplets (Case 2) and 85% n-decane – 15% 3-pentanone mixture droplets (Case 3); Deprédurand (2009).

## 5.6 Results

A crucial parameter which needs to be considered in the coupled solution is the volume of gas where the interaction between droplets and gas is taken into account, or even more important the ratio of this volume and the volume of the droplet $r \equiv V_g/V_d$. For spherical and cylindrical cells these volumes are linked with parameter $R_g$ via Eqs. (5.9) and (5.10) respectively. A crude estimate of this parameter is given by Eq. (5.15). Taking $t_D$ in this equation equal to 12 ms (characteristic transit time of droplets), $R_d$ = 61.35 µm (see Table 5.1), $d$ = 463.806 $\mu$m (based on the distance parameter equal to 3.78 (see Table 5.1), and estimating $k_D$ as 3.61 × $10^{-5}$ $m^2$/s, $R_g$ = 7.2004 × $10^{-4}$ m ≈ 720 $\mu$m is obtained. This gives $r \approx 1615$ for the spherical cell, and $r \approx 780$ for the cylindrical one. The latter is more appropriate for the experimental results considered in this chapter. Remembering that this estimate was made for the maximal $t_D$, and is rather crude by its nature, the actual value of this parameter could be taken a bit less than 780 in the coupled solution, but not too small to affect the assumptions of the model.

The calculations were performed for $r \equiv V_g/V_d = 600$ (coupled solution) and $r = 5\times10^4$ (it was shown that for this $r$ the results predicted by the coupled solution are indistinguishable from the results predicted by the one-way solution, described in Chapters 3 and 4). The choice of the ratio $r$ will be investigated in Section 5.7. Twenty terms in the series in the analytical solutions to temperature and species equations were used in the calculations (the sensitivity of the results with respect to the choice of the number of terms will be investigated in Section 5.7). As in Chapters 3 and 4, in both cases the temperatures at the centre of the droplets, the surface of the droplets and the average droplet temperatures were calculated. The values of ambient gas temperature and droplet velocities were the input parameters of the model. Note that although the ambient gas temperature remained constant during each experiment, in the case of the coupled solution gas temperature inside the volume $V_g$ was allowed to change with time, although no temperature gradients were allowed to develop in this volume. As in Chapters 3 and 4, the calculations started at the moment when droplets were first observed. The initial droplet temperatures were assumed equal to the measured temperatures of the first observed droplets.

The timestep in the calculations was taken equal to $10^{-5}$ s, and the number of points along the radius inside droplets, where the temperatures were stored, was taken equal to 2000. The latter number controls the accuracy of the calculation of the spatial derivatives of the temperature and species mass fractions, used in boundary conditions for $T$ and $Y_{li}$ (see Eqs. (2.22) and (4.5)). The reason for this choice of the timestep and the number of points will be discussed later in Section 5.7.

The plots of time evolutions of the temperatures at the centre of the droplets, the surface of the droplets and the average droplet temperatures, predicted by the coupled and one-way solutions for the 95% n-decane – 5% 3-pentanone mixture droplets (Case 1), are shown in Fig. 5.2. As follows from this figure, all three temperatures under consideration are well separated, as in the cases, considered in Chapters 3 and 4. Also, the coupled solutions show visibly slower rates of droplet heating, compared with the predictions of the one-way solution. All experimental plots lie between the average droplet temperature and the temperature at the centre of the droplet predicted by the coupled solution.

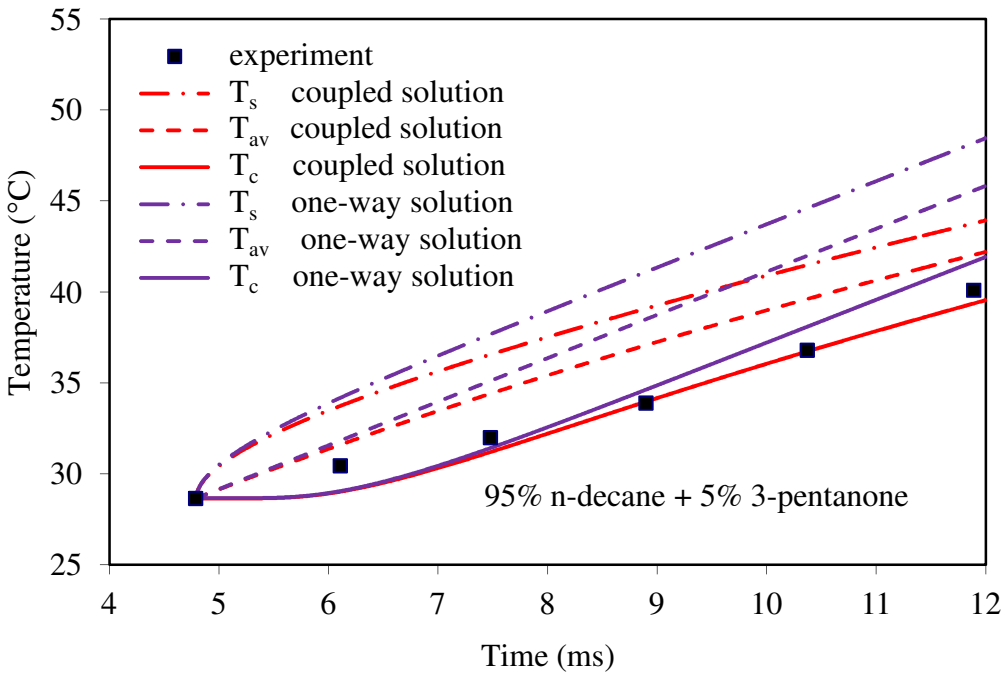


Fig. 5.2 The time evolution of the droplet surface, average and central temperatures ($T_s$, $T_{av}$ and $T_c$), as predicted by the coupled and one-way solutions, and experimentally observed temperatures for the 95% n-decane – 5% 3-pentanone mixture droplets with initial diameters 122.7 $\mu$m and homogeneous temperature 28.66 $^{o}$C injected into an ambient gas at constant temperature equal to 370 $^{o}$C (see Table 5.1). Zero time corresponds to the start of injection.

The plots similar to those shown in Fig. 5.2 but for the 90% n-decane – 10% 3-pentanone mixture droplets (Case 2) and the 85% n-decane – 15% 3-pentanone mixture droplets (Case 3) are shown in Figs. 5.3 and 5.4 respectively. The trends of all curves in these figures are rather similar to those shown in Fig. 5.2. In both cases experimental plots lie between the average droplet temperature and the temperature at the centre of the droplet predicted by the coupled solution, as in the case shown in Fig. 5.2, except three experimental points in Fig. 5.4. Even in the latter case, however, the deviation between the predicted temperatures at the centre of the droplet and the ones obtained experimentally is well within the experimental error. In all three cases, the one-way solution predicts unrealistically high average droplet temperatures, well above those observed experimentally. Hence, the effects of coupling need to be taken into account for the accurate prediction of droplet temperatures.

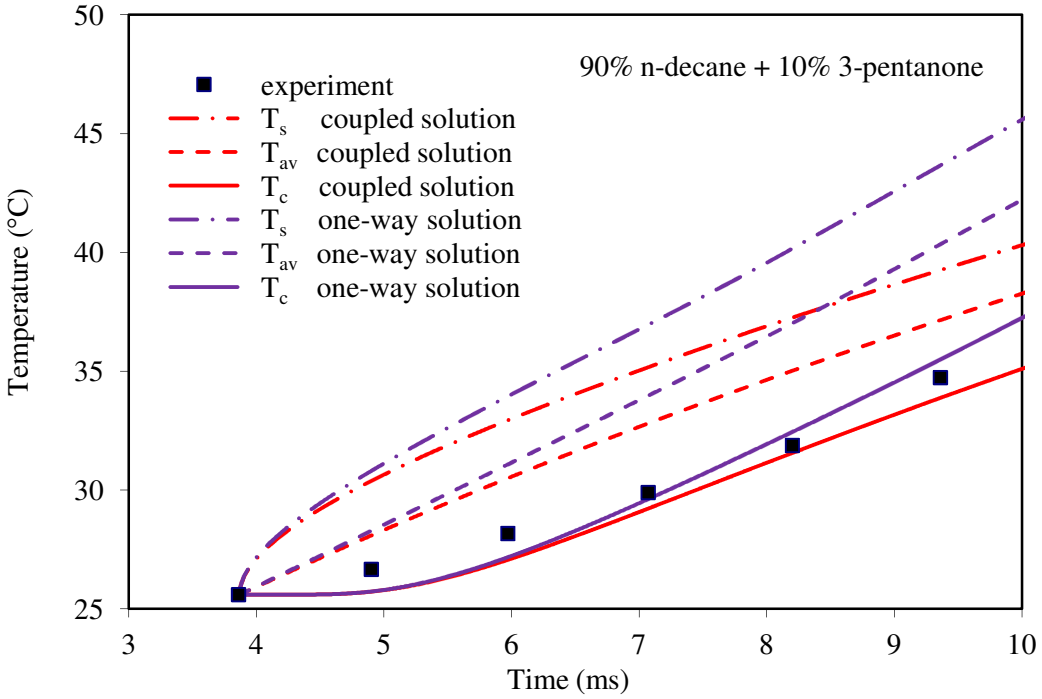


Fig. 5.3 The same as Fig. 5.2 but for the 90% n-decane – 10% 3-pentanone mixture droplets with initial diameters 126.1 $\mu$m, homogeneous temperature 25.6 $^{o}$C injected into an ambient gas at constant temperature equal to 374 $^{o}$C (see Table 5.1).

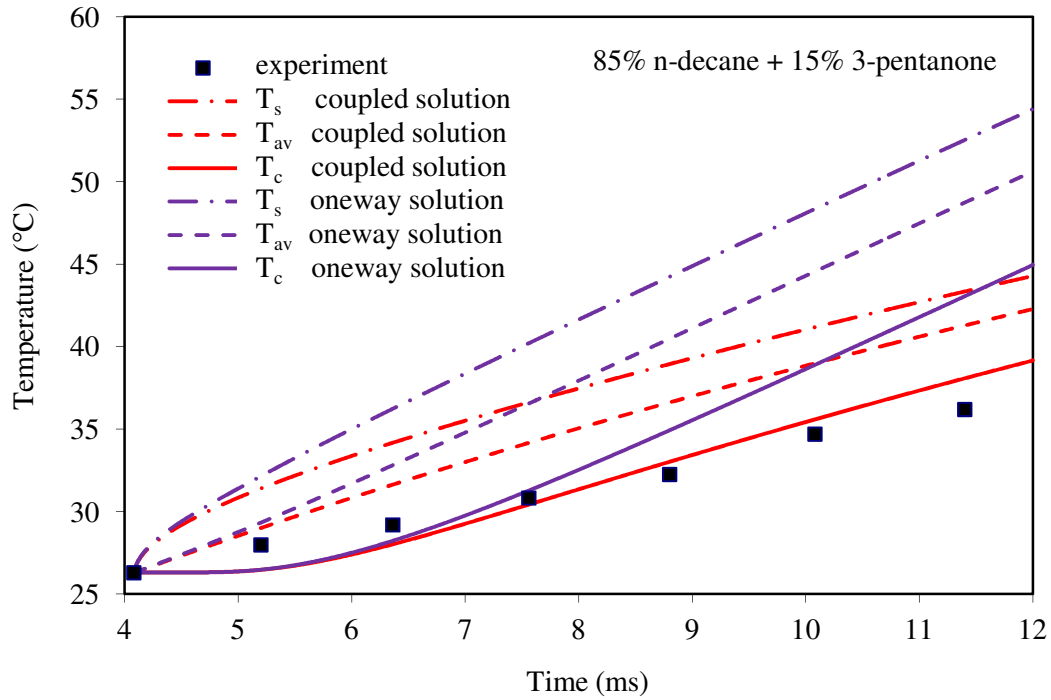


Fig. 5.4 The same as Figs. 5.2 and 5.3 but for the 85% n-decane 15% 3-pentanone mixture droplets with initial diameters 127.7 $\mu$m, homogeneous temperature 26.3 $^{o}$C injected into an ambient gas at constant temperature equal to 374 $^{o}$C (see Table 5.1).

The plots of time evolutions of the gas temperatures in the region of influence for all three cases, as predicted by the coupled solution, are shown in Fig. 5.5. In the case of the one-way solution, this temperature remained constant. As can

be seen from Fig. 5.5, the drop in the gas temperature during droplet heating could reach up to about 70 $^{o}$C and this leads to a visible reduction of the rate of increase of droplets temperatures predicted by the coupled solution. This drop in gas temperature is expected to produce much stronger effect due to the coupled solution, compared with the addition of fuel vapour to the region of influence.

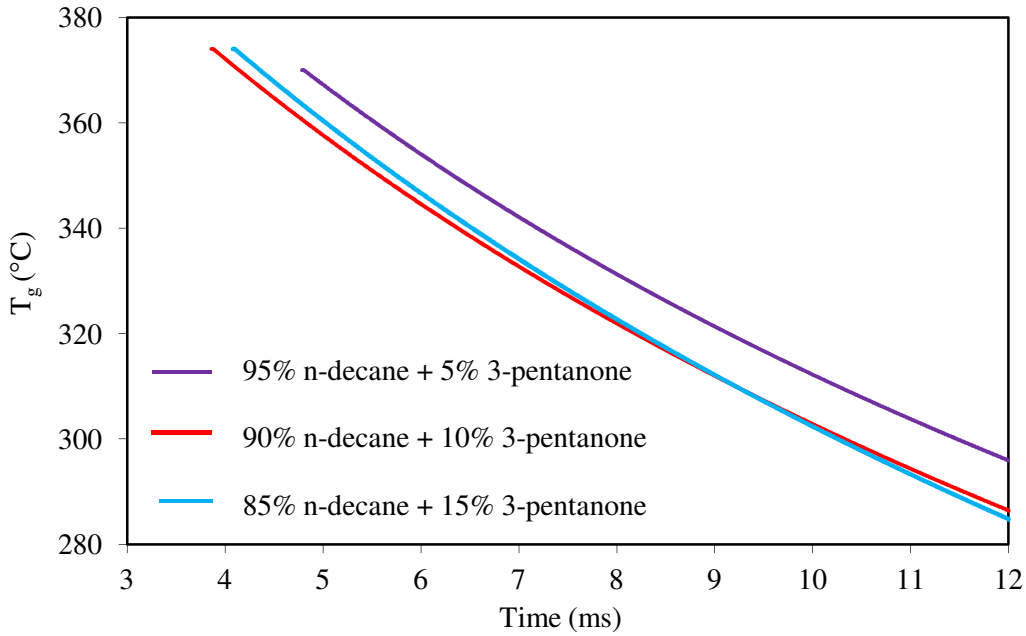


Fig. 5.5 The time evolution of gas temperature in the region of influence for three mixtures of n-decane and 3-pentanone. The droplets and the ambient gas parameters are the same as used in Figs. 5.2-5.4.

The plots similar to those shown in Figs. 5.2-5.4, but for droplet radii, are shown in Figs. 5.6-5.8. As one can see from these figures, neither coupled solutions nor one-way solutions can predict the observed trends in the time evolution of droplet radii. At the same time, one can see from these figures that the deviation between the predicted and observed droplet radii is less than about 0.5 $\mu$m in most cases, which is within the margins of experimental errors. Hence, the deviations between the predicted and observed droplet radii cannot undermine the validity of the model.

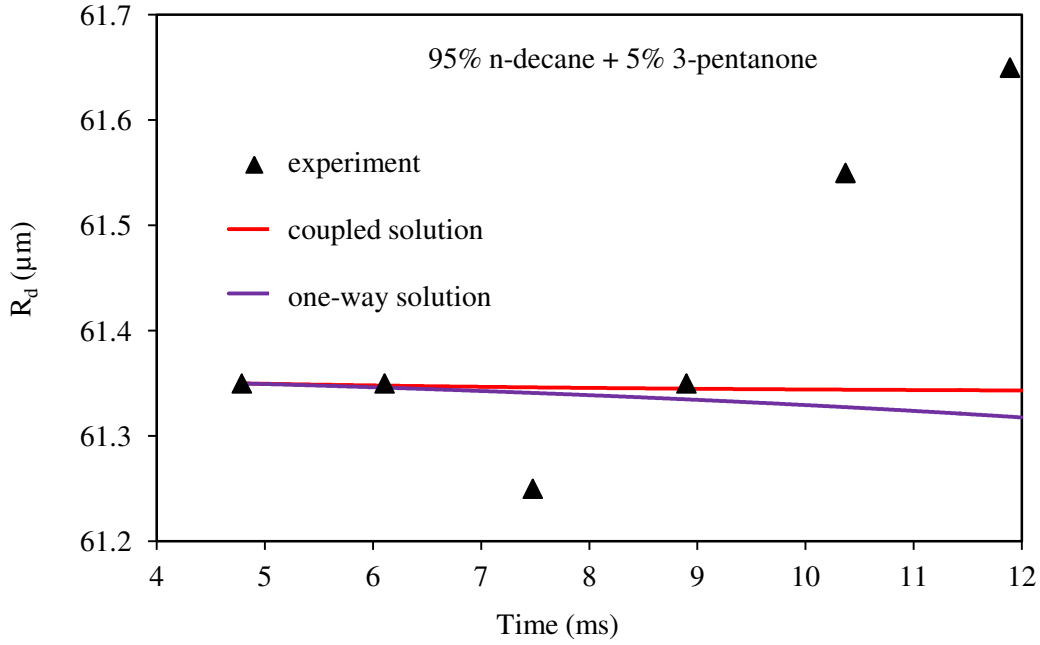


Fig. 5.6 The plots of $R_d$ versus time predicted by the one-way and coupled solutions for the same conditions as in Fig. 5.2.

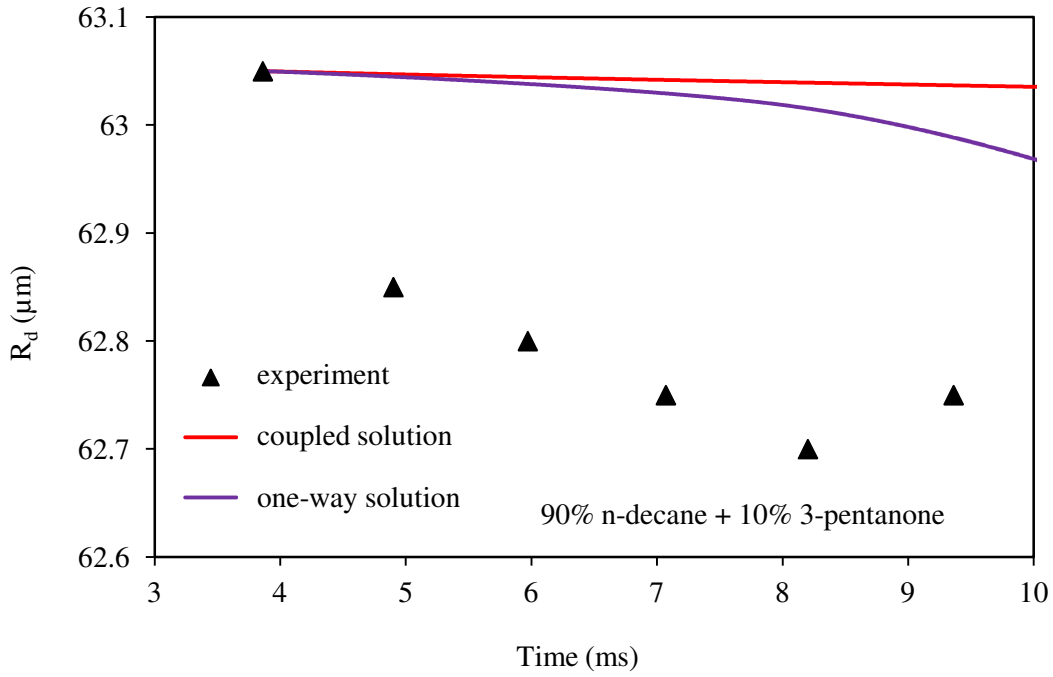


Fig. 5.7 The plots of $R_d$ versus time predicted by the one-way and coupled solutions for the same conditions as in Fig. 5.3.

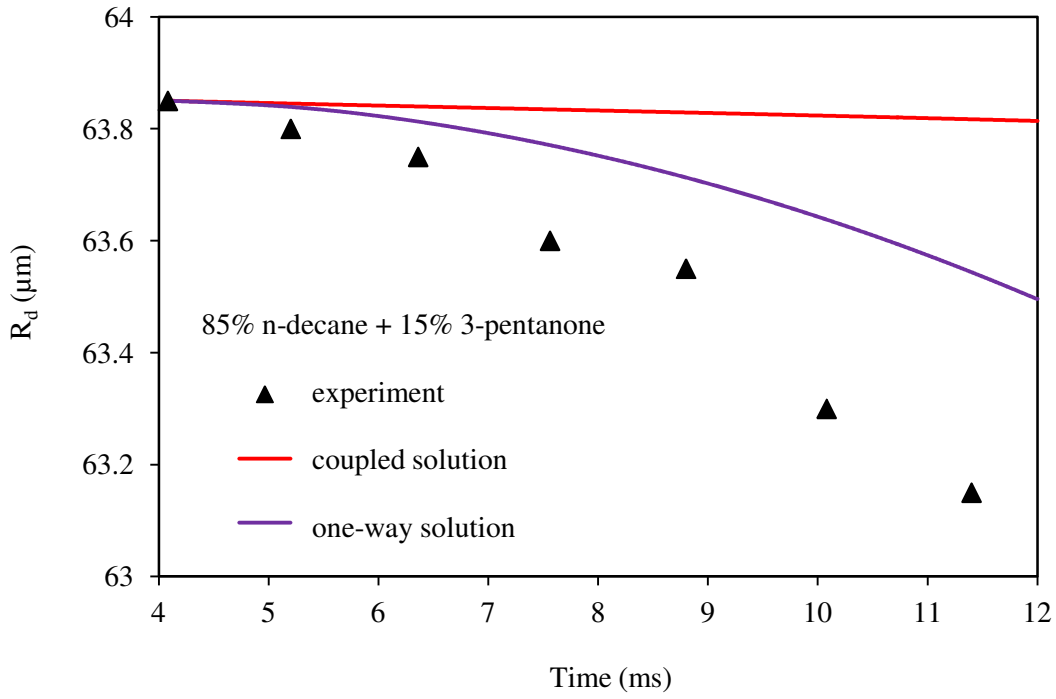


Fig. 5.8 The plots of $R_d$ versus time predicted by the one-way and coupled solutions for the same conditions as in Fig. 5.4.

Four sets of plots are presented below, which cannot be validated against experimental data at the moment, but show the underlying physics of the processes involved.

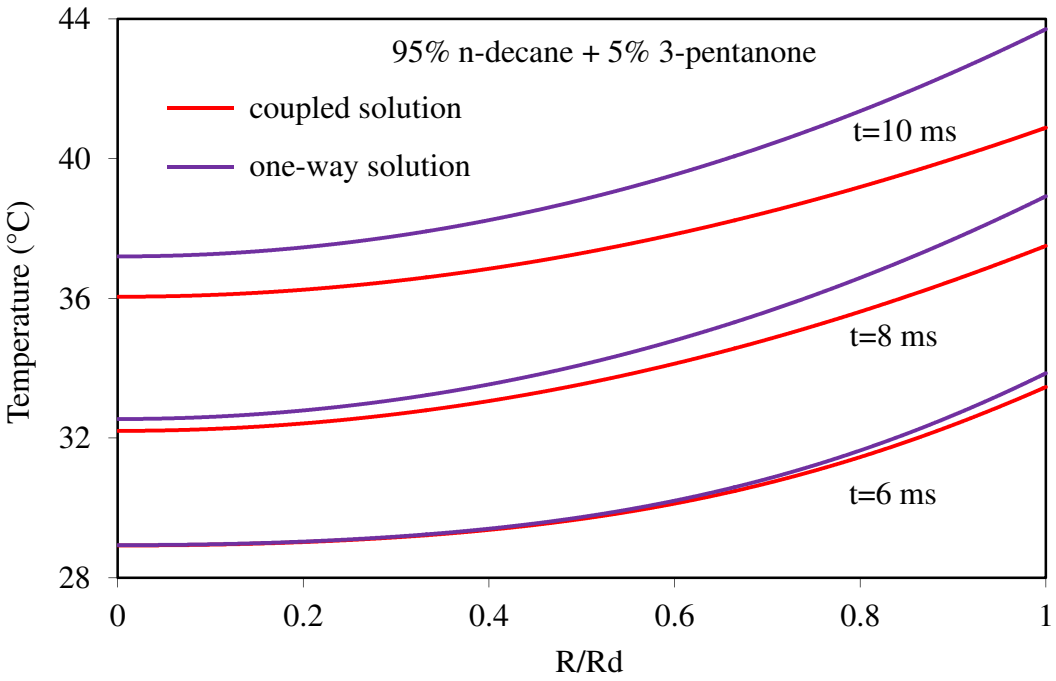


Fig. 5.9 The plots of $T$ versus $R/R_d$ for three moments of time after the start of calculations predicted by the one-way and coupled solutions and for the same conditions as in Fig. 5.2.

The temperature distribution inside the 95% decane – 5% 3-pentanone mixture droplets (Case 1) at three moments of time, as predicted by the coupled and one-way solutions, is presented in Fig. 5.9. As can be seen from this figure, at all times the temperature increases with the distance from the centre of the droplets, as expected. The temperature gradient is less important for case predicted by the coupled solution compared with the one-way solution. The deviation between the temperatures in all areas of the droplets, predicted by the coupled and one-way solutions, increases with time.

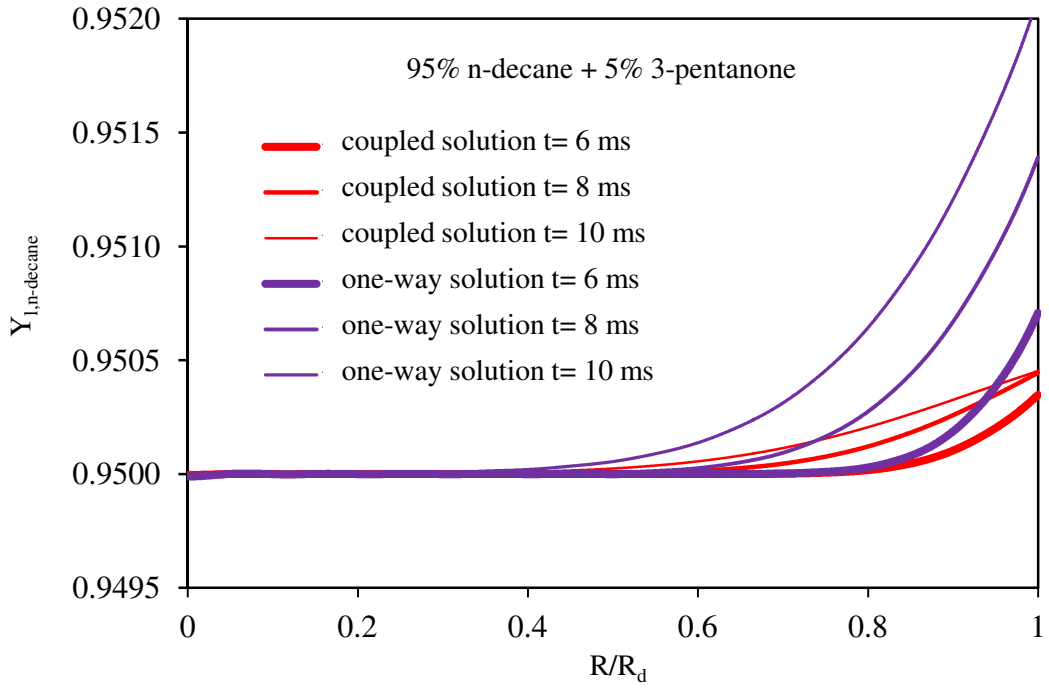


Fig. 5.10 The plots of the n-decane mass fraction $Y_{l,\text{n-decane}}$ versus $R/R_d$ for three moments of time after the start of calculations predicted by the one-way and coupled solutions and for the same conditions as in Fig. 5.2.

Plots similar to those shown in Fig. 5.9, but for the mass fraction of n-decane, are presented in Fig. 5.10. As can be seen from this figure, the mass fraction of n-decane in the areas close to the surface of the droplet, predicted by the coupled and on-way solutions, increases with time. This is related to higher volatility of 3-pentanone, compared with n-decane. As in the case of temperature, shown in Fig. 5.9, the rate of increase of the mass fraction of n-decane, predicted by the coupled solution, is slower than the one predicted by the one-way solution. The deviation between the results predicted by these solutions increases with time. This can be related to the fact that in the coupled solution, vapour in the region of influence is

partially saturated and the temperature in this region is lower than that in the surrounding gas.

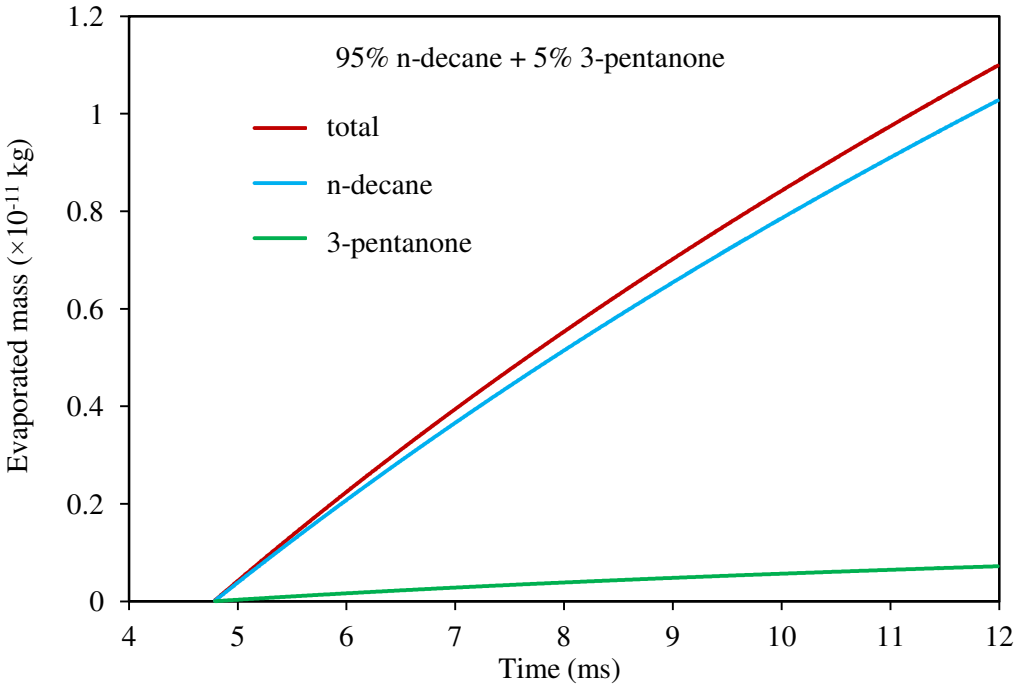


Fig. 5.11 The plots of the evaporated masses of n-decane, 3-pentanone and the total evaporated mass versus time predicted by the coupled solution for the same conditions as in Fig. 5.2.

The time evolution of evaporated masses of 3-pentanone, n-decane and the total vapour mass in the region of influence is shown in Fig. 5.11. As one can see from this figure, evaporated masses of both substances increase with time. This can be related to the fact that no condensation takes place during the period under consideration, and to the assumption that no vapour escapes from the region of influence into ambient gas. The predicted mass of n-decane is always greater than that of 3-pentanone, despite higher volatility of 3-pentanone, compared with n-decane (cf. Fig. 5.10). This is related to the fact that the original amount of n-decane in droplets is 20 times more than the amount of 3-pentanone.

The time evolution of masses of air and the total mass of the mixture of air and vapour in the region of influence is shown in Fig. 5.12. The increase of the mass of air with time is related to the decrease of temperature in the interaction volume with time (cf. Fig. 5.5) at constant pressure. Note that for a fixed temperature, part of air should have been removed from the interaction volume by the evaporating fuel (see Eq. (5.12)).

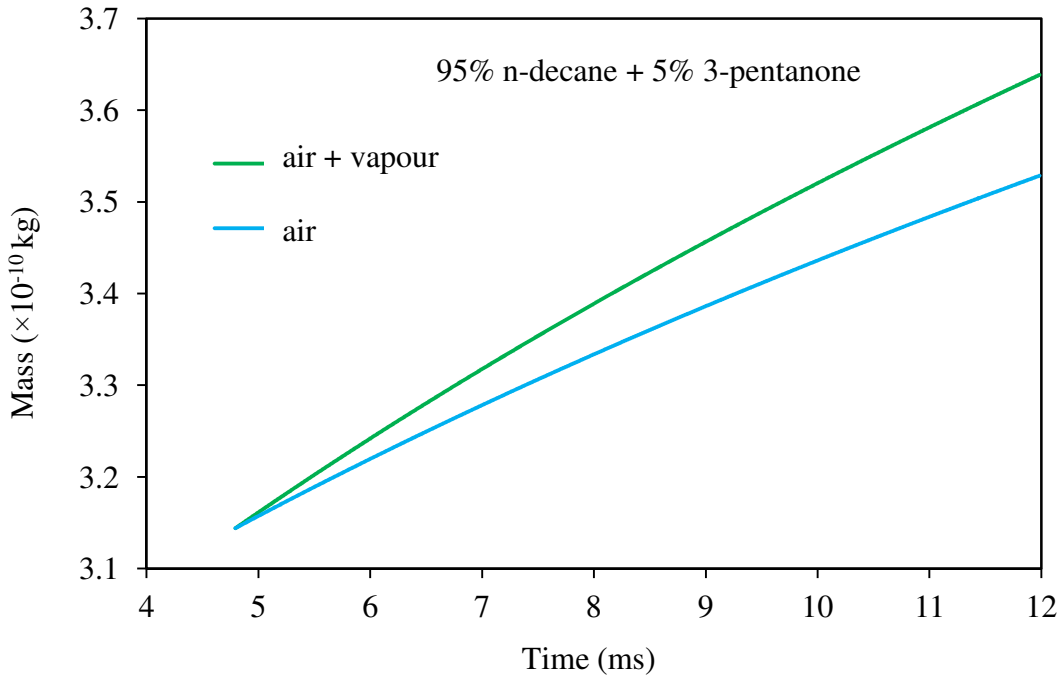


Fig. 5.12 The plots of the total mass of air and the mixture of air and vapour in the region of influence versus time predicted by the coupled solution for the same conditions as in Fig. 5.2.

The plots of time evolutions of the temperatures at the centre of the droplets, at the surface of the droplets and the average droplet temperatures, predicted by the coupled and one-way solutions for the 25% ethanol – 75% acetone mixture droplets, are shown in Fig. 5.13. The initial value of the ratio $r \equiv V_g/V_d$ was chosen to be 3500 in the case of ethanol/acetone mixture to ensure complete evaporation process if it is considered. Also, the coupled solutions show a slightly faster drop in temperature at the beginning of evaporation and a slower reduction at later times. This behaviour is different from the one described in Figs. 5.2-5.4 for the case of droplet heating in a hot gas. In that case, the coupled solution predicted visibly slower rates of droplet heating, compared with the predictions of the one-way solution. Most experimental plots lie between the average droplet temperature and the temperature at the centre of the droplet predicted by the coupled solution. The agreement between the predicted and experimental results looks marginally better for the coupled than for the one-way solution.

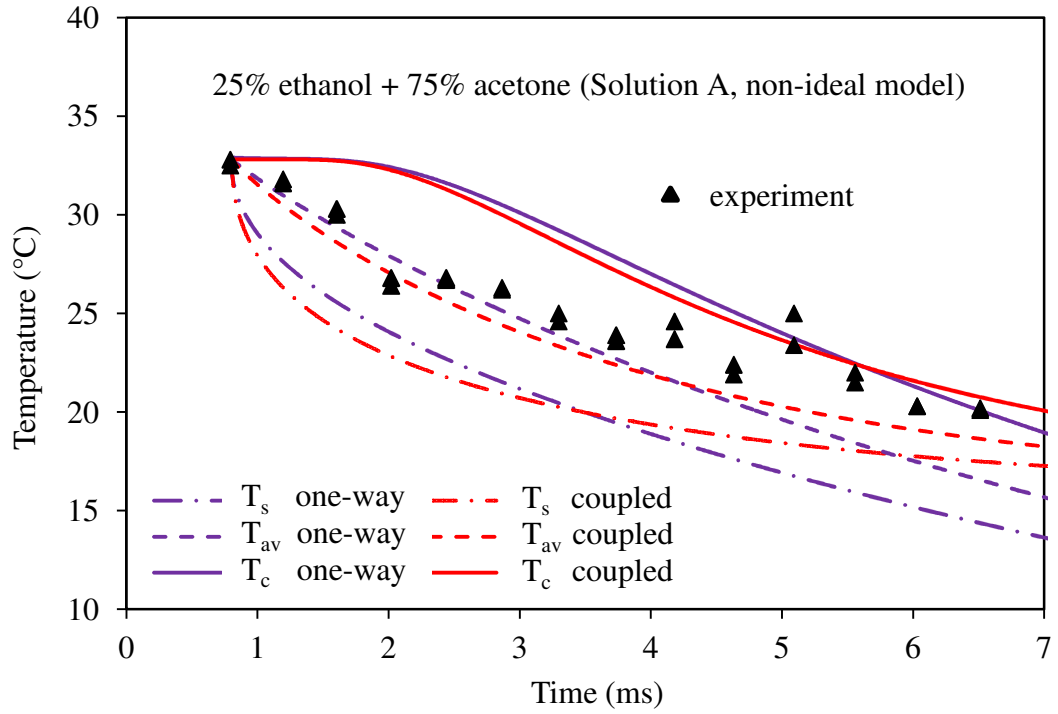


Fig. 5.13 The time evolution of droplet surface, average and centre temperatures ($T_s$, $T_{av}$ and $T_c$), predicted by Solution A for the non-ideal model, coupled and one-way solutions and experimentally observed temperatures for the 25% ethanol – 75% acetone mixture droplets. The initial parameters are the same as in Fig. 4.15.

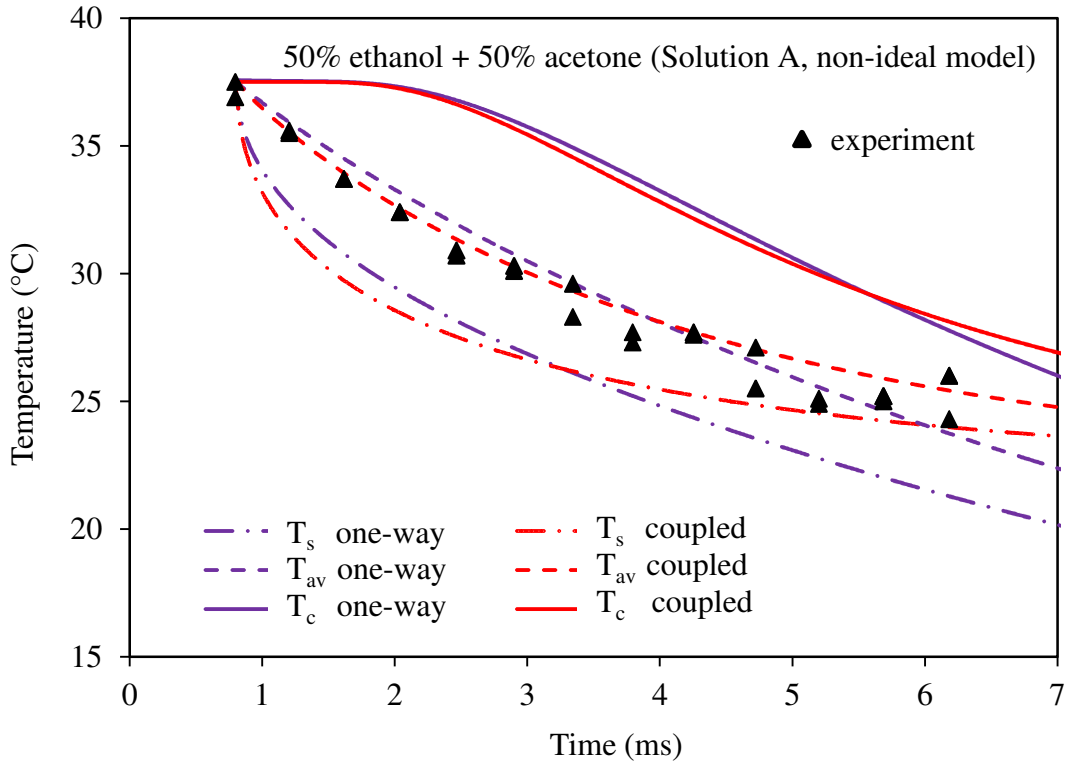


Fig. 5.14 The same as Fig. 5.13 but for 50% ethanol – 50% acetone mixture droplets. The initial parameters are the same as in Fig. 4.16.

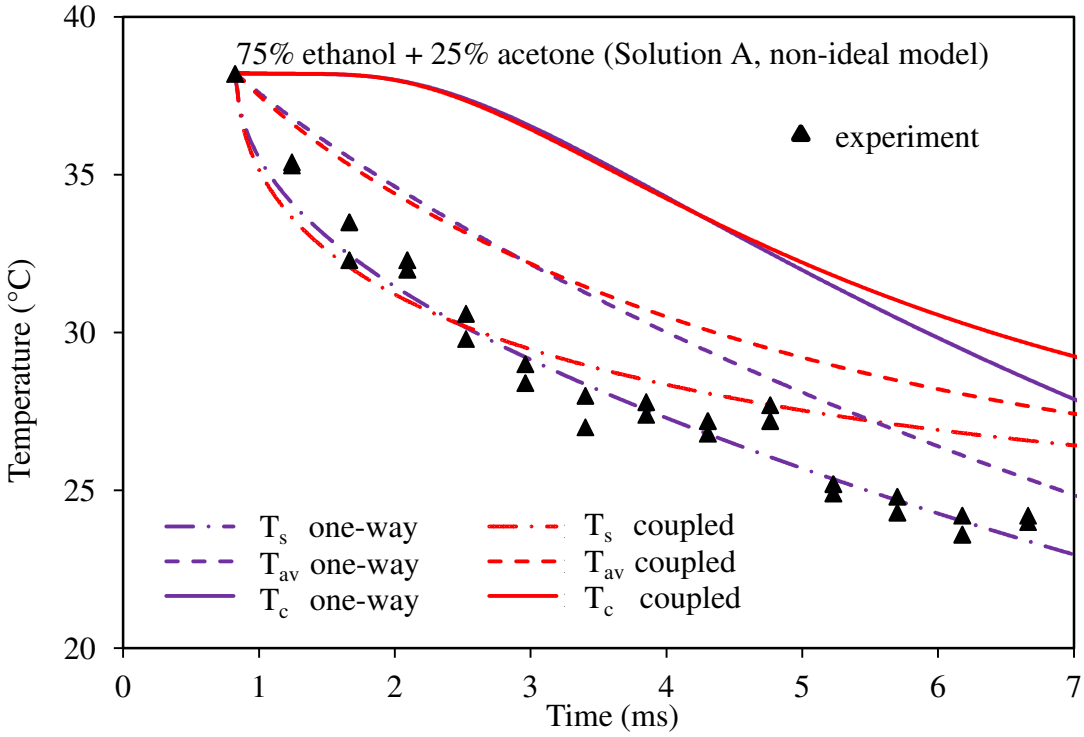


Fig. 5.15 The same as Figs. 5.13 and 5.14 but for 75% ethanol – 25% acetone mixture droplets. The initial parameters are the same as in Fig. 4.17.

Plots similar to those shown in Fig. 5.13, but for the 50% ethanol – 50% acetone mixture droplets, are shown in Fig. 5.14. The effects of the coupled solution on the trends are similar to those shown in Fig. 5.13. The experimentally observed values of temperature lie close to the average temperatures predicted by both the one-way and coupled solutions. The same plots as in Figs. 5.13 and 5.14, but for the 75% ethanol – 25% acetone mixture droplets, are shown in Fig. 5.15. The effects of the coupled solution on the trends are similar to those shown in Figs. 5.13 and 5.14. Note that in the case shown in Fig. 5.15, the deviation between the predicted and observed temperature values is larger for the coupled than for the one-way solution. The reason for this is not clear at the moment.

## 5.7 Accuracy versus CPU efficiency

In the analysis, reported in Chapters 3 and 4, we were concerned with the accuracy of the results, and chose the maximum number of terms in the series in the analytical solutions to temperature and species mass fractions. However, remembering that perhaps the most important practical application of the model described in Chapter 4 would be its potential implementation into CFD codes, and application of the latter to simulation of realistic engineering processes, finding a reasonable compromise between the accuracy of the model and its CPU efficiency

becomes more important than its accuracy alone. The accuracy and CPU efficiency of the model, depending on the number of terms in the series in the analytical solutions to temperature and species mass fractions, are investigated in this section. We focus on the analysis of the 95% decane – 5% 3-pentanone mixture droplets (Case 1). The conclusions referring to other mixtures are essentially the same as the ones for the above-mentioned mixture.

The relative errors were estimated based on the following equation:

$$\%\mathrm{Error}_n = \frac{\left(\sum_{i=1}^{i=i_{max}} (|F_{N=100} - F_{N=n}|/F_{N=100})\right)}{i_{max}}, \tag{5.17}$$

where $F$ stands for either temperature or mass fraction, $N$ is the number of terms in the series in the solution to the equation for temperature or mass fraction, $i$ refers to timesteps, $i_{max}$ is the maximal number of timesteps used in calculation (this number varied from about 700 to about 800). The errors were calculated relative to the values obtained when 100 terms in the expression for the temperature or mass fraction of n-decane were used. Higher order terms did not produce any effects on the results.

The plots of relative errors of the temperatures at the centre of the droplets ($T_c$), the surface of the droplets ($T_s$), the average droplet temperatures ($T_{av}$), predicted by the coupled solution, and the CPU requirement versus the number of terms in the series in the expression for droplet temperature ($n$) are presented in Fig. 5.16. 100 terms in the expression for the mass fraction of n-decane (Eq. D.38) were taken. All temperatures were measured in $^{o}$C. Calculations were performed on 3 GHz CPU, 3 GB RAM work station. As follows from this figure, the errors of calculating all temperatures, are practically equal to zero when the number of terms $n$ is close or larger than 20. Hence, 20 terms were used in the analysis presented in Section 5.6. The CPU time increased by about 50% when the number of terms in the expression for temperature increased from 20 to 100. This increase of the number of terms, however, does not lead to any increase in the accuracy of the results and cannot be justified. Note that the errors of calculating average temperature are more than an order of magnitude less than the errors of calculating droplet surface temperature and the temperature at the centre of the droplet. This is related to the fact that for small number of terms, small oscillations of temperature were observed near the centre of the droplets and its surface. These oscillations reduce substantially during the

integration along $R$ performed for the calculation of the droplet average temperature, Sazhin et al (2004).

$$F_{\rm av} = \frac{3}{R_d^3}\int_0^{R_d} R^2 F(R)\mathrm{d}R, \tag{5.18}$$

where $F$ stands for either temperature or mass fraction.

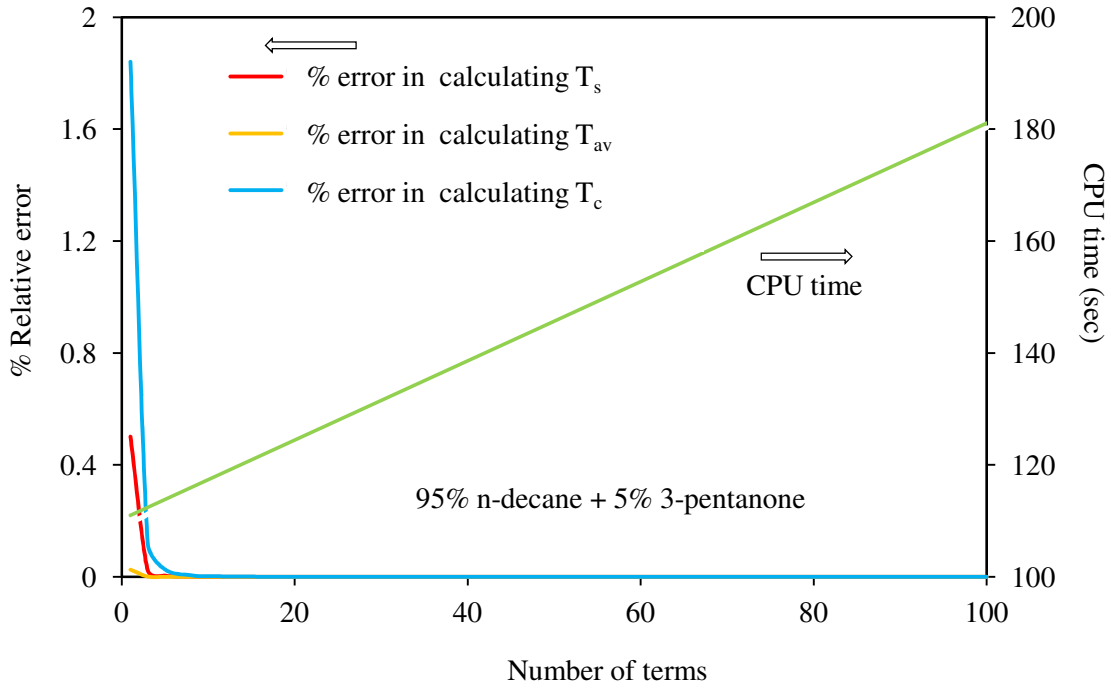


Fig. 5.16 The plots of relative errors (in percent) of calculation of droplet surface, average and central temperatures ($T_s$, $T_{\rm av}$ and $T_c$) and CPU time versus the number of terms in the solution to the temperature equation with the fixed number of terms in the solution to the species equation equal to 100 for the same conditions as in Fig. 5.2. Calculations were performed on 3 GHz CPU, 3 GB RAM work station.

Plots similar to those presented in Fig. 5.16, but for the mass fractions of n-decane, are shown in Fig. 5.17. In contrast to Fig. 5.16, the number of terms in the series in Eq. (D.38) varied, and the number of terms in the expression for the temperature Eq. (2.23) was assumed to be equal to 100. As can be seen from this figure, all errors of calculation of the mass fractions of n-decane are about two orders of magnitude less than the errors of calculation of droplet temperatures. As in the case of temperatures, the errors of calculating average mass fractions are more than an order of magnitude less than the errors of calculating the mass fractions at the surface and the centre of the droplets. The explanation of this phenomenon is the same as for the droplet temperature (see Fig. 5.16). As in the case of temperature, the errors in the case when the number of terms is about or more than 20, can be safely

ignored. The increase of CPU time when the number of terms increased from 20 to 100, was even more noticeable than in the case of temperature (this time almost doubled). As in the case of temperature, this increase in the number of terms could not be justified from the point of view of increased accuracy of the model.

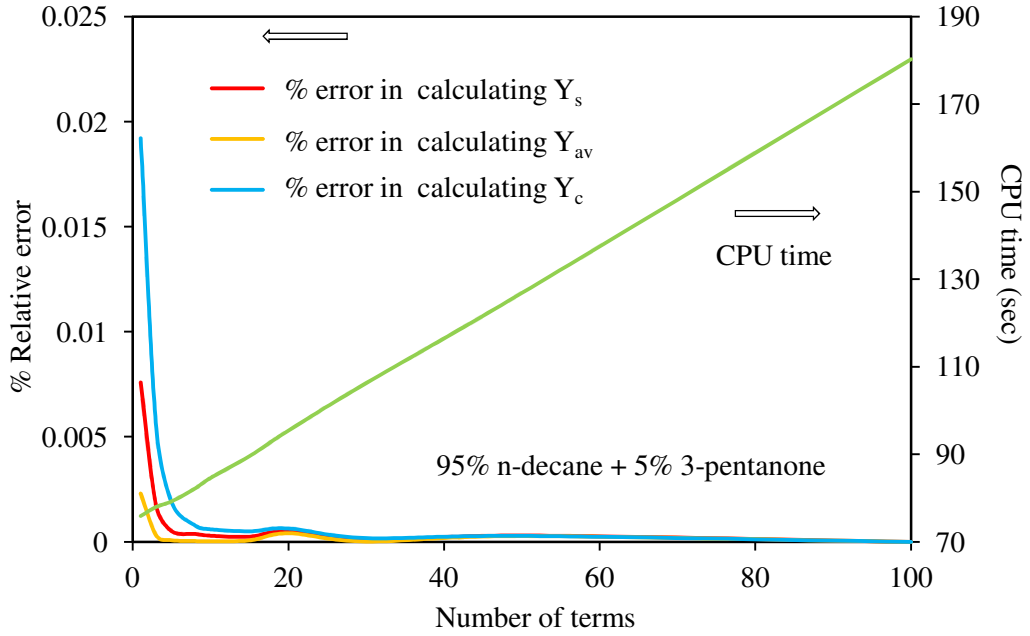


Fig. 5.17 The plots of relative errors (in percent) of calculation of liquid n-decane mass fractions at the surface of the droplet, average mass fraction of n-decane and its mass fraction at the centre of the droplet ($Y_s$, $Y_{av}$ and $Y_c$) and CPU time versus the number of terms in the solution to the species equation with fixed number of terms in the solution to the temperature equation equal to 100 for the same conditions as in Fig. 5.2. Calculations were performed on 3 GHz CPU, 3 GB RAM work station.

Plots similar to those shown in Fig. 5.17, but referring to the case when the numbers of terms in the series for temperature and mass fractions are equal, are presented in Figs. 5.18 and 5.19. As can be seen from these figures, the errors of estimating all mass fractions are less than about 0.02% even if the number of terms in both series is reduced to just three. Note that the increase in the number of these terms from five to twenty practically does not improve the accuracy of the prediction of the model. As in the case shown in Fig. 5.17, the CPU time, in the case when three terms are chosen, is more than an order of magnitude less than in the case when a hundred terms is chosen in both series.

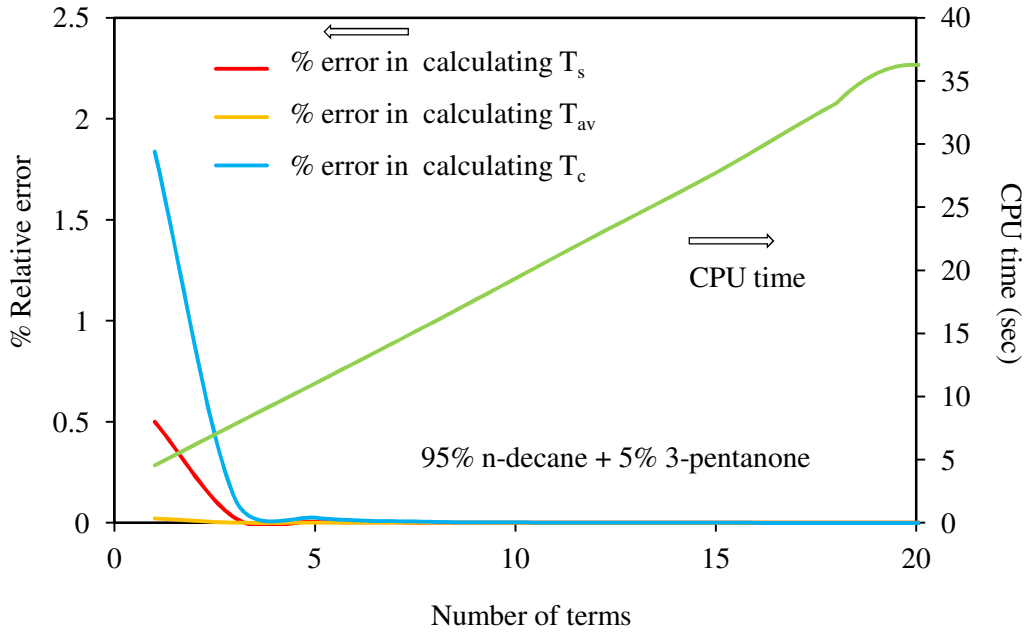


Fig. 5.18 The plots of relative errors (in percent) of calculation of droplet surface, average and central temperatures ($T_s$, $T_{av}$ and $T_c$) and CPU time versus the number of terms in the solutions to the temperature and species equations (these numbers are assumed equal) for the same conditions as in Fig. 5.2. Calculations were performed on 3 GHz CPU, 3 GB RAM work station.

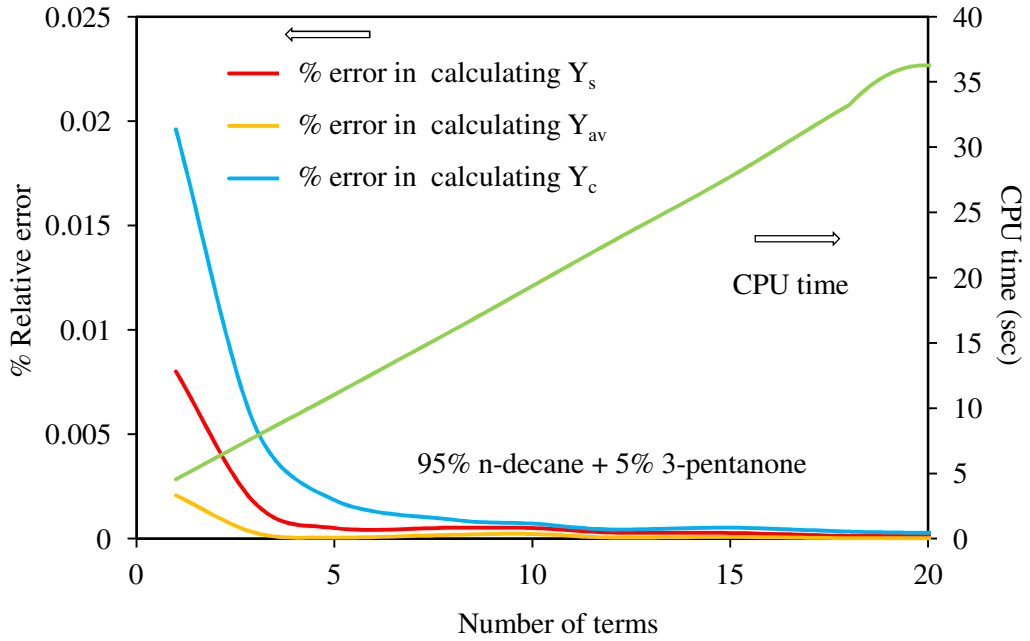


Fig. 5.19 The plots of relative errors (in percent) of calculation of liquid n-decane mass fractions at the surface of the droplet, average mass fraction and the mass fraction at the centre of the droplet ($Y_s$, $Y_{av}$ and $Y_c$) and CPU time versus the number of terms in the solutions to the temperature and species equations (these numbers are assumed equal) for the same conditions as in Fig. 5.2. Calculations were performed on 3 GHz CPU, 3 GB RAM work station.

Combining the results shown in Figs. 5.16-5.19, we can conclude that the model can accurately predict the values of droplet temperature and mass fractions of n-decane even if the number of terms in the series for temperature and mass fractions is reduced to three. This result is consistent with the earlier finding reported by Sazhin et al (2005b). Relatively low CPU time required for calculations makes this model potentially attractive for implementation into CFD codes.

As mentioned earlier, all plots presented so far refer to the case when the timestep was chosen equal to $10^{-5}$ s and the number of points along the radius, $N_R$, equal to 2000. The increase in the timestep is expected to decrease the accuracy of calculations as in any numerical code. In our case, however, the excessive reduction of this timestep can also lead to decrease in the accuracy of calculations due to the decrease in the Fourier numbers in the series in the analytical expressions for $T$ and $Y_{li}$. This decrease is expected to affect the convergence of these series. This effect is illustrated in Fig. 5.20, where the plots of droplet surface temperatures versus $N_R$ for different timesteps are presented for the 95% n-decane – 5% 3-pentanone mixture (Case 1) 5 ms after the start of calculations. As follows from this figure, the choice of the timestep $10^{-3}$ s leads to under-prediction of this temperature by more than 1 $^{o}$C for all $N_R$. For all timesteps in the range $10^{-6} - 10^{-4}$ s and $N_R \geq 1500$ the predicted temperature remains almost the same. For smaller $N_R$, the accuracy of calculations clearly deteriorates, especially for the timestep equal to $10^{-6}$ s. The plots, shown in Fig. 5.20, are similar to those obtained for other cases and other moments of time. Based on these plots, the values of the timestep $10^{-5}$ s and $N_R = 2000$ have been chosen. Note that the CPU time could be further reduced, practically without any detrimental effects on accuracy, if the timestep is increased to $10^{-4}$ s and $N_R$ is reduced to 1000.

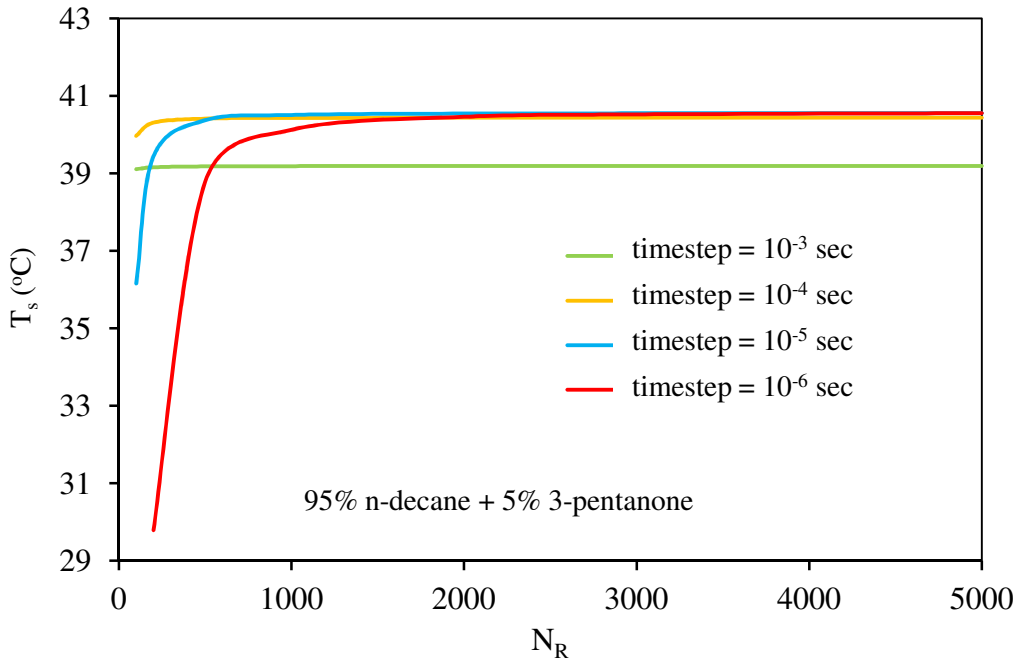


Fig. 5.20 The plots of the predicted droplet surface temperatures versus $N_R$ for different timesteps for the 95% n-decane – 5% 3-pentanone mixture (Case 1) at 5 ms after the start of calculations.

The parameter $r \equiv V_g/V_d$ was used as a fitting parameter to give the best fit with the experimental data. The calculations, for decane/3-pentanone droplet mixtures, were performed for $r \equiv V_g/V_d = 600$ (Figs. 5.2-5.4) where the best agreement with the experimental data for the three cases of mixtures under consideration (coupled solution) was achieved. The one-way calculations were performed for $r = 5\times10^4$. For this $r$ the results predicted by the coupled solution are indistinguishable from the results predicted by the one-way solution, described in Chapters 3 and 4. As can be seen from Fig. 5.21, if the value of $r$ is increased above $5 \times 10^4$ the results do not change and if the value of $r$ is below 600 no evaporation can take place (saturation condition $B_M = 0$).

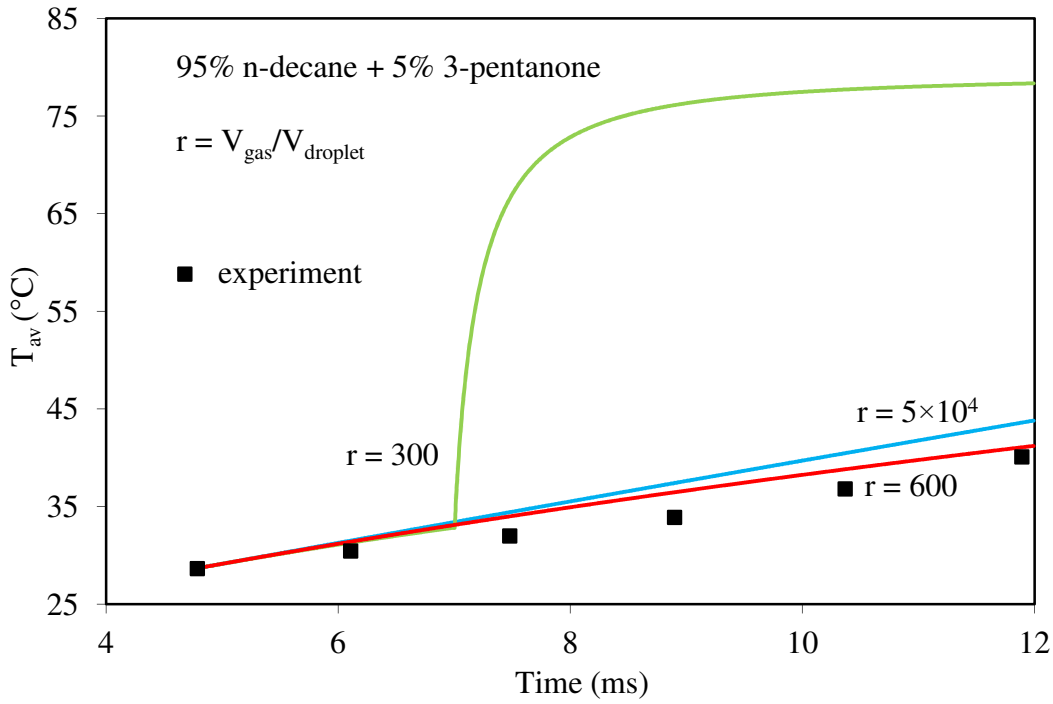


Fig. 5.21 The plots of average temperatures $T_{av}$ with different $r$ values indicated at the curve versus time for the same conditions as in Fig. 5.2.

## 5.8 Conclusions of Chapter 5

The earlier reported simplified model for multi-component droplet heating and evaporation, described in Chapter 4, is generalised to take into the coupling between the droplets and the ambient gas. Similarly to the original simplified model, the model described in this chapter takes into account droplet heating by convection from the ambient gas, the distribution of temperature inside the droplet, diffusion of liquid species inside the droplet, droplet swelling or contraction due to changing average temperature and the effects of recirculation in the moving droplets on heat and species mass diffusion within them. The effects of the non-unity activity coefficient are ignored (Raoult's law is assumed to be valid) and the interaction between droplets is taken into account based on the correlation suggested by Deprédurand et al (2010). The size of the gas volume, where the interaction between droplets and gas needs to be taken into account (region of influence), is estimated based on the characteristic thermal and mass diffusion scales. The model is applied to the analysis of the experimentally observed heating and evaporation of monodispersed n-decane/3-pentanone (Deprédurand et al, 2010) and ethanol/acetone (Maqua et al, 2008b) mixture droplets at atmospheric pressure. For the case of decane/3-pentanone mixture droplets (droplet heating), it is pointed out that the

effect of coupling leads to noticeably better agreement between the predictions of the model and the experimentally observed average droplet temperatures. In most cases, the experimentally observed droplet temperatures lie between the average and central temperatures, predicted by the coupled solution. The main effect of the coupled solution is linked with the reduction of the gas temperature in the region of influence. A deviation of up to about 0.5 $\mu$m between the experimentally observed and predicted droplet radii is related to the experimental margins. It is pointed out that the observed time evolution of droplet radii cannot be used for the validation of the model.

For the case of ethanol/acetone mixture droplets, at the initial stage of droplet cooling and evaporation, the coupled solution predicts visibly lower droplet temperatures, compared with the predictions of the one-way solution. At the later stage of droplet cooling and evaporation, the coupled solution predicts higher droplet temperatures, compared with the predictions of the one-way solution. In the case of acetone dominated mixture droplets (25% ethanol – 75% acetone) the agreement between the predicted and experimental results looks marginally better for the coupled than for the one-way solution.

It is pointed out that the number of terms in the series in the expressions for droplet temperature and species mass fraction can be reduced to just three, with possible errors less than about 0.5%. In this case the model can be recommended for implementation into CFD codes and used for various engineering applications, including those in internal combustion engines.

# 6 A quasi-discrete model for heating and evaporation of complex multi-component hydrocarbons fuel droplets

## 6.1 Introduction

As mentioned in Chapter 1, two main approaches to modelling multi-component droplets heating and evaporation have been suggested: those based on the analysis of individual components (Discrete Component 'DC' models) (Tong and Sirignano, 1986; Continllo and Sirignano, 1991; Klingsporn and Renz, 1994; Lage et al, 1995; Abraham and Magi, 1998; Aggarwal and Mongia, 2002; Maqua et al, 2008b), applicable in the case when a small number of components needs to be taken into account, and those based on the probabilistic analysis of a large number of components (e.g. Continuous Thermodynamics approach 'CT') (Tamim and Hallet, 1995; Lippert and Reitz, 1997; Hallet, 2000; Zhu and Reitz, 2002; Arias-Zugasti and Rosner, 2003; Abdel-Qader and Hallet, 2005; Zhang and Kong, 2009; Rivard and Brüggemann, 2010) and the Distillation Curve Model (Burger et al, 2003). In the second family of models a number of additional simplifying assumptions were used, including the assumption that species inside droplets mix infinitely quickly or do not mix at all.

A model containing features of both these groups of models has been suggested in (Laurent et al, 2009; Zhang and Kong, 2010). In all of these models, it was assumed that the species in droplets are well mixed. As follows from our analysis of heating and evaporation of bi-component droplets (Chapters 4 and 5), this assumption appears to be questionable.

In this chapter a new method of modelling heating and evaporation of multi-component droplets, suitable for the case when a large number of components is present in the droplets, is suggested. As in Laurent et al (2009), this method is based on the introduction of pseudo-components, but these pseudo-components are introduced in a way which differs from the one described in Laurent et al (2009). In contrast to the previously suggested models, designed for large numbers of components, the new model takes into account the diffusion of liquid species and thermal diffusion as in the classical DC models.

The new model, based on the introduction of the concept of quasi-components, is described in Section 6.2. The thermo-physical properties of quasi-components are

summarised in Section 6.3. The preliminary results of application of the new model to Diesel fuel droplets are presented and discussed in Section 6.4. Detailed results of application of the new model to Diesel and gasoline fuels are presented in Sections 6.5 and 6.6 respectively. The main results of this chapter are summarised in Section 6.7.

## 6.2 Quasi-discrete model

As in the case of Continuous Thermodynamics approach, the quasi-discrete model is based on the introduction of the distribution function $f_m(I)$ such that

$$\int_{I_1}^{I_2} f_m(I)\,\mathrm{d}I = 1, \tag{6.1}$$

where $I$ is the property of the component (usually taken as the molar mass $M$), $f_m$ characterises the relative contribution of the components having this property in the vicinity of $I$, $I_1$ and $I_2$ are limiting values of this property. For most practically important fuels $f_m(I)$ can be approximated by relatively simple functions (see Eq. (2.40)).

In most practically important cases the approximation for realistic multi-component fuel in the form (2.40) is valid only in the limited range of $I$: $I_1 > \gamma$ and $I_2 < \infty$, where $\gamma$ is the parameter that determines the original shift (Eq. (2.40)). In this case distribution (2.40) needs to be replaced by the following distribution:

$$f_m(I) = C_m \frac{(I-\gamma)^{\alpha-1}}{\beta^{\alpha}\Gamma(\alpha)} \exp\left[-\left(\frac{I-\gamma}{\beta}\right)\right], \tag{6.2}$$

where constant $C_m$ is defined from Condition (6.1) as

$$C_m = \left\{\int_{I_1}^{I_2} \frac{(I-\gamma)^{\alpha-1}}{\beta^{\alpha}\Gamma(\alpha)} \exp\left[-\left(\frac{I-\gamma}{\beta}\right)\right] \mathrm{d}I\right\}^{-1}. \tag{6.3}$$

Although molar mass is almost universally used to describe the property $I$, this choice is certainly far from being a unique one. For example, in Laurent et al (2009), this parameter was associated with the normal boiling points of individual components. Remembering that most practically important hydrocarbon fuels consist mainly of molecules of the type $C_nH_{2n+2}$, where $n \geq 1$ in the general case or $n \geq 5$ for liquid fuels, it is more practical to write the distribution function $f_m$ as a function of the carbon number $n$ rather than $M$, Arias-Zugasti and Rosner (2003). These two parameters are linked by the following equation:

$$M(n) = 14n + 2, \tag{6.4}$$

where $M$ is measured in kg/kmole.

Note that real life Diesel and gasoline fuels, apart from alkanes, contain significant amounts of alkenes, alkynes, naphthenes and aromatics. The contribution of these elements is not taken into account at this stage, and this is a serious limitation of our model.

Remembering (6.4), Eq. (6.2) can be rewritten as:

$$f_m(n) = C_m(n_0, n_f)\frac{(M(n)-\gamma)^{\alpha-1}}{\beta^{\alpha}\Gamma(\alpha)}\exp\left[-\left(\frac{M(n)-\gamma}{\beta}\right)\right], \tag{6.5}$$

where $n_0 \le n \le n_f$, subscripts $_0$ and $_f$ stand for initial and final,

$$C_m(n_0, n_f) = \left\{\int_{n_0}^{n_f}\frac{(M(n)-\gamma)^{\alpha-1}}{\beta^{\alpha}\Gamma(\alpha)}\exp\left[-\left(\frac{M(n)-\gamma}{\beta}\right)\right]\mathrm{d}n\right\}^{-1}. \tag{6.6}$$

This choice of $C_m$ assures that

$$\int_{n_o}^{n_f} f_m(n)\,\mathrm{d}n = 1. \tag{6.7}$$

Following Arias-Zugasti and Rosner (2003), we assume that transport and thermodynamic properties of hydrocarbon fuels are weak functions of $n$. In this case it would be sensible to assume that the properties of hydrocarbons in a certain narrow range of $n$ are about the same, and replace the continuous distribution (6.5) with a discrete one, consisting of $N_f$ quasi-components with carbon numbers:

$$\bar{n}_j = \frac{\int_{n_{j-1}}^{n_j} n f_m(n)\mathrm{d}n}{\int_{n_{j-1}}^{n_j} f_m(n)\mathrm{d}n}, \tag{6.8}$$

the corresponding molar fractions

$$X_j = \int_{n_{j-1}}^{n_j} f_m(n)\mathrm{d}n, \tag{6.9}$$

and mass fractions

$$Y_j = \frac{M(\bar{n}_j)X_j}{\sum_{j=1}^{j=N_f}[M(\bar{n}_j)X_j]}, \tag{6.10}$$

where $j$ is an integer in the range $1 \le j \le N_f$. Note that

$$\sum_{j=1}^{j=N_f} X_j = \sum_{j=1}^{j=N_f} Y_j = 1. \tag{6.11}$$

The choice of $n_j$ can be arbitrary. In our model we assume that all $n_j - n_{j-1}$ are equal, i.e. all quasi-components have the same range of values of $n$ (this range can consist of non integer values in the general case). For the case when $N_f = 1$ this approach reduces the analysis of multi-component droplets to mono-component ones.

These new quasi-components are not the actual physical hydrocarbon components ($\bar{n}_j$ are not integers in the general case). Hence, we call this model the

'quasi-discrete model'. These quasi-components will be treated as actual components in the conventional DC models, including taking into account diffusion of liquid species in droplets. This model is expected to be particularly useful when $N_f$ is much less than the number of actual species in the hydrocarbon mixture.

The analysis of multi-component droplet heating and evaporation using this model is essentially based on the approximations of thermo-physical properties of quasi-components for various $\bar{n}_j$. These are discussed in the next section.

## 6.3 Thermo-physical properties

### *6.3.1 Saturated vapour pressure*

Following Arias-Zugasti and Rosner (2003), the saturation vapour pressure in (MPa) is estimated using the Antoine equation:

$$p_{sat}(n) = \exp\left(A(n) - \frac{B(n)}{T_s - C(n)}\right), \tag{6.12}$$

where $A(n) = 6.318n^{0.05091}$, $B(n) = 1178n^{0.4652}$, $C(n) = 9.467n^{0.9143}$, $T_s$ is the droplet surface temperature in K. The approximations for $A(n)$, $B(n)$, $C(n)$ were derived for $4 < n < 17$, but we will assume that they can be applied for $n \geq 17$ as well if the contribution of hydrocarbon fuels with these $n$ is relatively small. Having replaced $n$ in Eq. (6.12) with $\bar{n}_j$, calculated by Eq. (6.8), we obtain the required values of $p_{sat}$ for all quasi-components. The mixtures will be treated as ideal (Raoult's law is assumed to be valid). In this case, partial pressures of individual quasi-components can be estimated as:

$$p_v(\bar{n}_j) = X_{lsi}(\bar{n}_j) p_{sat}(\bar{n}_j), \tag{6.13}$$

where $X_{lsi}$ is the molar fraction of liquid quasi-species at the surface of the droplet, $p_{sat}(\bar{n}_j)$ is determined by Eq. (6.12). The values of $p_{sat}(n)$ predicted by Eq. (6.12) for $n$=10 and $n$=12 (n-decane and n-dodecane) in the temperature range 300-500 K differed from those reported in Abramzon and Sazhin (2006) by not more than 6.05% and 5.62% respectively.

### *6.3.2 Latent heat of evaporation*

From the Clausius–Clapeyron equation it follows that (Arias-Zugasti and Rosner, 2003):

$$L(n) = -\frac{R_u}{M(n)} \frac{\mathrm{d} \ln p_{sat}(n)}{\mathrm{d}(1/T)}, \tag{6.14}$$

where $R_u$ is the universal gas constant. Remembering (6.12), Formula (6.14) can be rewritten as:

$$L(n) = \frac{R_u B(n) T_s^2}{M(n)(T_s - C(n))^2}. \quad (6.15)$$

The latter formula will be used in our analysis. Having replaced $n$ in Eq. (6.15) with $\bar{n}_j$, calculated by Eq. (6.8), we obtain the required values of $L(n)$ for all quasi-components.

The plots of $L(n)$ for temperatures in the range from 300 K to 500 K are shown in Fig. 6.1. As one can see from this figure, $L(n)$ increases with decreasing temperature as expected. For small $n$ ($n < 10$), $L(n)$ slowly decreases with increasing $n$, while at larger $n$ it increases with increasing $n$, and this increase is particularly strong for low temperatures. This is consistent with our expectation that heavier components are generally less volatile compared with the lighter ones. The values of $L(n)$ predicted by Eqs. (6.14) and (6.15) for $n$=10 and $n$=12 (n-decane and n-dodecane) in the temperature range 300-500K differed from those reported in Abramzon and Sazhin (2006) by not more than 4.82% and 3.52% respectively.

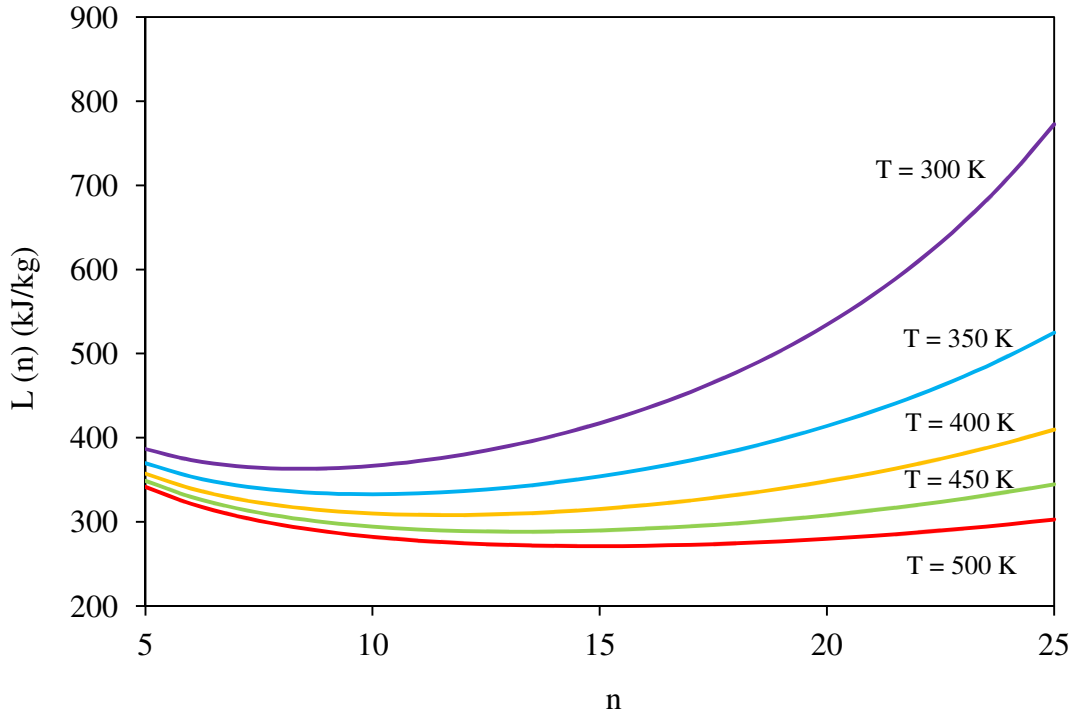


Fig. 6.1 The plots of $L(n)$ versus $n$ as predicted by Eq. (6.15).

### *6.3.3 Critical and boiling temperatures*

Using data provided in Poling et al (2000), the dependence of critical and boiling temperatures on $n$ is approximated by the following equations:

$$T_{cr}(n) = a_{cr} + b_{cr}n + c_{cr}n^2 + d_{cr}n^3, \quad (6.16)$$

$$T_b(n) = a_b + b_b n + c_b n^2 + d_b n^3, \quad (6.17)$$

where the coefficients are presented in Table 6.1.

| Coefficient | *a* | *b* | *c* | *d* |
|---|---|---|---|---|
| **Critical** | 242.3059898052 | 55.9186659144 | - 2.1883720897 | 0.0353374481 |
| **Boiling** | 118.3723701848 | 44.9138126355 | - 1.4047483216 | 0.0201382787 |

Table 6.1 The values of the coefficients in Eqs. (6.16) and (6.17).

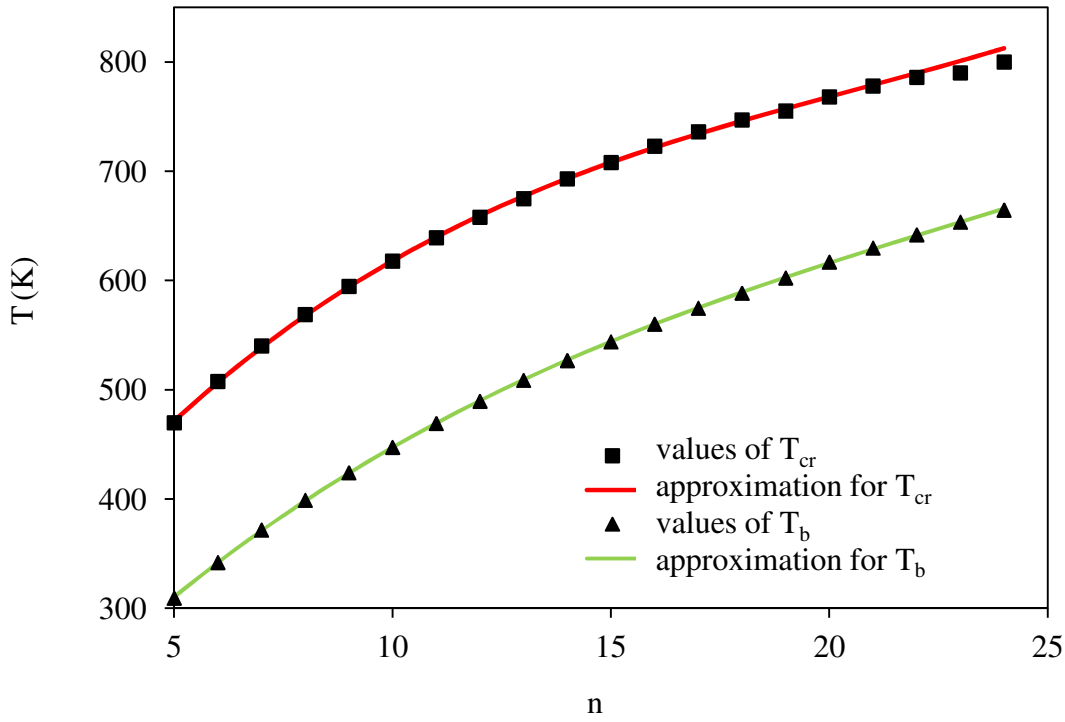


Fig. 6.2 The plots of $T_{cr}(n)$ and $T_b(n)$, and their Approximations (6.16) and (6.17), versus *n*.

The plots of $T_{cr}(n)$ and $T_b(n)$ are shown in Fig. 6.2 alongside the values of these parameters for individual *n* as reported in Poling et al (2000). As follows from this figure, Approximations (6.16) and (6.17) are reasonably accurate and can be used in our model. Having replaced *n* in Eqs. (6.16) and (6.17) with $\bar{n}_j$ we obtain the required values of $T_{cr}(n)$ and $T_b(n)$ for all quasi-components.

### *6.3.4 Liquid density*

Following Yaws (2008), the temperature dependence of the density of liquid n-alkanes in (kg/m$^3$) for $5 \leq n \leq 25$ is approximated as

$$\rho_l(n,T) = 1000 A_\rho B_\rho^{-\left(1-\frac{T}{T_{cr}(n)}\right)^{C_\rho}}, \quad (6.18)$$

where $T_{cr}(n)$ are the critical temperatures for n-alkanes (approximations for $T_{cr}(n)$ for $5 \le n \le 25$ are shown in Fig. 6.2 (Eq. (6.16)), the numerical values of $A_\rho$, $B_\rho$ and $C_\rho$ for individual values of $n$ are given in Yaws (2008). These values have been approximated by the following expressions:

$$\begin{cases} A_\rho = 0.00006196104 \times n + 0.234362 \\ B_\rho = 0.00004715697 \times n^2 - 0.00237693 \times n + 0.2768741 \\ C_\rho = 0.000597039 \times n + 0.2816916 \end{cases} \quad (6.19)$$

The range of applicability of Eq. (6.18) depends on the values of $n$. For $n$ = 5 this range was determined as 143.42-469.65 K; for $n$ = 10 this range was determined as 243.49-618.45 K; for $n$ = 25 this range was determined as 315.15-850.13 K (Yaws, 2008) (the upper limits are critical temperatures of the components). Remembering that the contribution of n-alkanes with $n$ close to 25 is relatively small, we will assume that Eqs. (6.18) and (6.19) are valid in the whole range from the room temperature until close to the critical temperature.

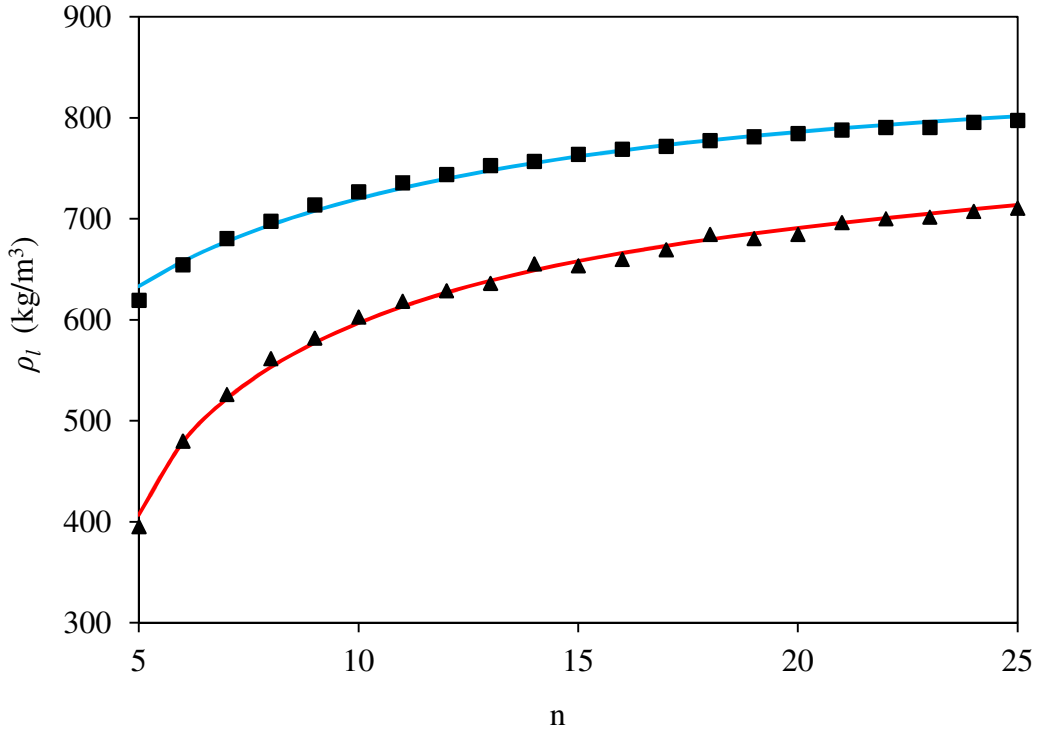


Fig. 6.3 The plots of $\rho_l$ versus $n$ for $T$ = 300 K and $T$ = 450 K, as inferred from Eq. (6.18) with coefficients $A_\rho$, $B_\rho$ and $C_\rho$ given by Yaws (2008) (filled squares for $T$ = 300 K and filled triangles for $T$ = 450 K), and approximated by Eqs. (6.19) (blue curve for $T$ = 300 K and red curve for $T$ = 450 K).

The plots of $\rho_l$ versus $n$ for $T$ = 300 K and $T$ = 450 K, as inferred from Eq. (6.18) with coefficients $A_\rho$, $B_\rho$ and $C_\rho$ given by Yaws (2008) (squares and triangles), and approximated by Eqs. (6.19) (blue and red curves) are shown in Fig. 6.3. As follows from this figure, the agreement between the values of liquid density predicted by Approximation (6.18) with the values of the coefficients given in Yaws (2008) and approximated by Eqs. (6.19) looks almost ideal. For temperatures of 300 and 450 K, the values of density inferred from Eq. (6.18) with coefficients given by Eqs. (6.19) differ by less than 0.51% and 0.76% respectively from the values of density inferred from Eq. (6.18) with coefficients given by Yaws (2008).

### *6.3.5 Liquid viscosity*

Following Mehrotra (1994), the temperature dependence of the dynamic viscosity of liquid n-alkanes in (Pa.s) for $4 \le n \le 44$ is approximated as

$$\mu_l(n,T) = 10^{-3}\,\langle 10^{[100(0.01T)^{b(n)}]} - 0.8\rangle, \tag{6.20}$$

where

$$b(n) = -5.745 + 0.616\ln(n) - 40.468n^{-1.5} \tag{6.21}$$

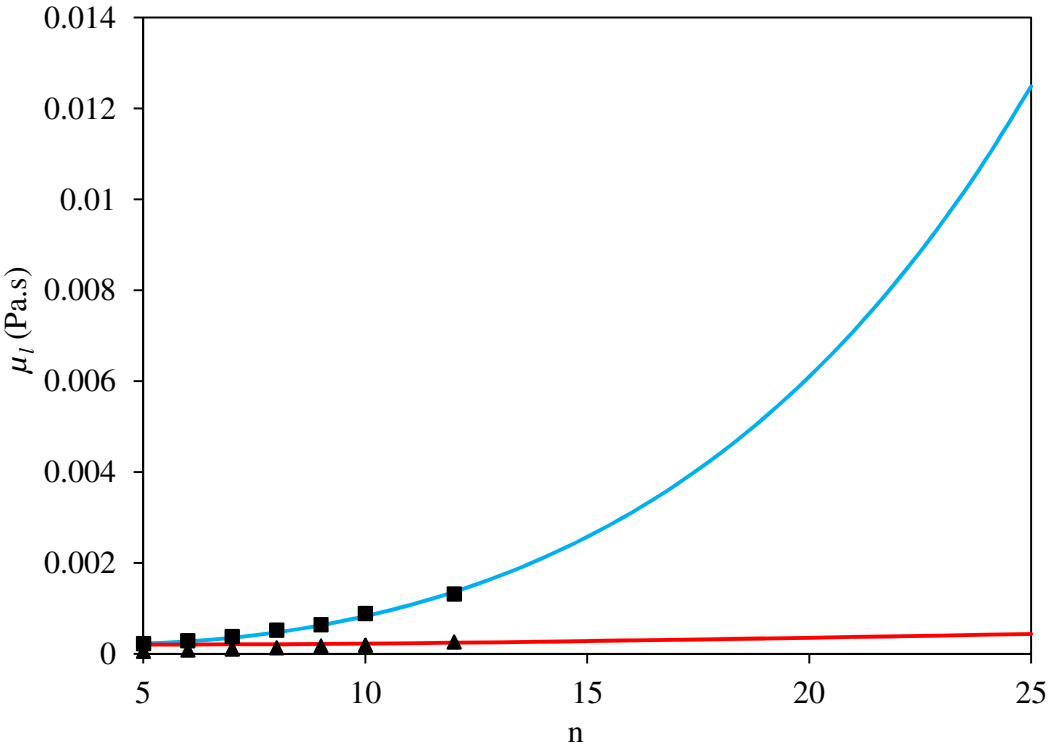


Fig. 6.4 The plots of $\mu_l$ versus $n$ for $T$ = 300 K and $T$ = 450 K, as inferred from Eqs. (6.20) and (6.21) (blue ($T$ = 300 K) and red ($T$ = 450 K) curves), and the corresponding values of $\mu_l$ in the range $5 \le n \le 12$, inferred from NIST website (filled squares ($T$ = 300 K) and filled triangles ($T$ = 450 K)).

The temperature range of the applicability of Approximations (6.20) and (6.21) was not explicitly specified in Mehrotra (1994), but the author of this paper demonstrated good agreement between the predictions of these approximations and experimental data in the range of temperatures from 10 °C to 100 °C.

The plots of $\mu_l$ versus $n$ for $T$ = 300 K and $T$ = 450 K, as inferred from Eqs. (6.20) and (6.21) (blue and red curves), and the corresponding values of $\mu_l$ in the range $5 \leq n \leq 12$, inferred from NIST website (National Institute of Standards and Technology) (squares ($T$ = 300 K) and triangles ($T$ = 450 K)), are shown in Fig. 6.4. As follows from this figure, the agreement between the values of liquid dynamic viscosity predicted by Approximations (6.20) and (6.21) and the results presented on the NIST website looks almost ideal. The differences between the results predicted by Eq. (6.20) and NIST data for 300 K and 450 K were found to be less than 5.13% and 40.16% respectively. Large errors in the latter case are linked with small values of $\mu$. Note that the values of dynamic viscosity affect droplet heating and evaporation only via the corrections to values of the thermal conductivity and diffusivity in the Effective Thermal Conductivity and Effective Diffusivity (ETC/ED) models. In most practically important cases, the influence of viscosity on the final result is expected to be very weak.

### *6.3.6 Heat capacity*

Following van Miltenburg (2000), the temperature dependence of the heat capacity of liquid n-alkanes in (J/(kg.K)) for $2 \leq n \leq 26$ is approximated as

$$c_l(n,T) = 1000\left(\frac{43.9+13.99(n-1)+0.0543(n-1)T}{M(n)}\right) \quad (6.22)$$

where $M(n)$ is defined by Eq. (6.4).

The temperature range of applicability of Eq. (6.22) was not clearly identified by van Miltenburg (2000) for all $n$, except to say that this approximation is not valid at temperatures close to the temperature of fusion. For $n$ = 16 and $n$ = 17 these ranges were identified as 340-400 K and 335-400 respectively. In the case of $n$ = 16 and $n$ = 25 the temperatures of fusion are equal to 295.1 K and 329.25 K respectively. However, remembering that the contribution of the n-alkanes with $n$ > 16, is very small, it will be assumed that Approximation (6.22) is valid in the whole temperature range from the room temperature onwards.

The plots of $c_l$ versus $n$ for $T$ = 300 K and $T$ = 450 K, as inferred from Eq. (6.22) (blue and red curves), and the corresponding experimental values of $c_l$ for $T$ = 300 K in the range $5 \leq n \leq 18$, inferred from NIST website (squares) and van Miltenburg (2000) (circles), are shown in Fig. 6.5. As follows from this figure, the agreement between the values of the liquid heat capacity predicted by Approximation (6.22) and the experimental results for $T$ = 300 K looks almost ideal. The difference between the results predicted by Eq. (6.22) and data reported in NIST website and van Miltenburg (2000) for 300 K was found to be less than 0.91%. We are not aware of experimental data for $T$ = 450 K.

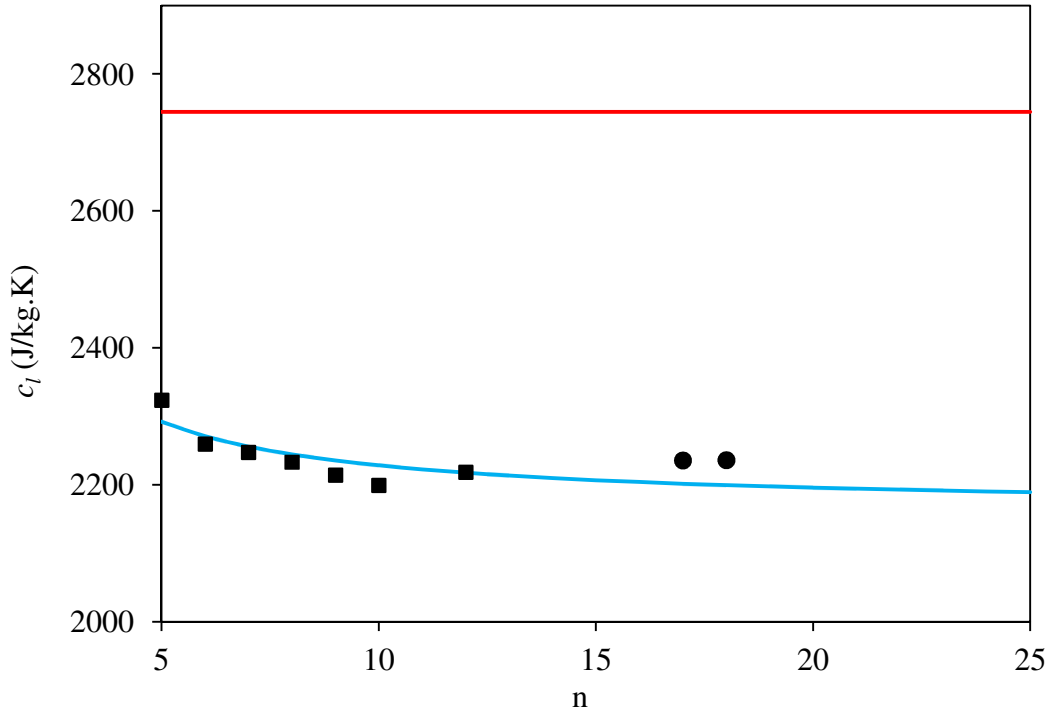


Fig. 6.5 The plots of $c_l$ versus $n$ for $T$ = 300 K and $T$ = 450 K, as inferred from Eq. (6.22) (blue ($T$ = 300 K) and red ($T$ = 450 K) curves), and the corresponding experimental values of $c_l$ for $T$ = 300 K in the range $5 \leq n \leq 18$, inferred from NIST website (filled squares) and van Miltenburg (2000) (filled circles).

### *6.3.7 Thermal conductivity*

Following Yaws (1995), the temperature dependence of thermal conductivity of liquid n-alkanes in (W/(m.K)) for $5 \leq n \leq 20$ is approximated as

$$k_l(n,T) = 10^{\left[A_k + B_k\left(1-\frac{T}{T_{cr}(n)}\right)^{2/7}\right]}, \qquad (6.23)$$

where $T_{cr}(n)$ are the critical temperatures for n-alkanes approximated by Eq. (6.16), the numerical values of $A_k$ and $B_k$ for individual values of $n$ are given in Yaws (1995). These values have been approximated by the following expressions:

$$\begin{cases} A_k(n) = 0.002911 \times n^2 - 0.071339 \times n - 1.319595 \\ B_k(n) = -0.002498 \times n^2 + 0.058720 \times n + 0.710698 \end{cases} \quad (6.24)$$

Although Approximations (6.23) and (6.24) have been derived for $5 \leq n \leq 20$, they are used in the whole range $5 \leq n \leq 25$. Possible errors imposed by these approximations in the range $21 \leq n \leq 25$ are expected to have very small effect on the final results as the mass fractions of n-alkanes in this range of $n$ is very small in Diesel fuel, and negligible in gasoline fuel.

The range of applicability of Eq. (6.23) depends on the values of $n$. For $n$ = 5 this range was determined as 143-446 K; for $n$ = 10 this range was determined as 243-588 K; for $n$ = 20 this range was determined as 310-729 K (Yaws, 1995). Remembering that the contribution of n-alkanes with $n \geq 20$ is relatively small, we have assumed that Eqs. (6.23) and (6.24) are valid in the whole range from the room temperature until close to the critical temperature, as in the case of Approximations (6.18) and (6.19).

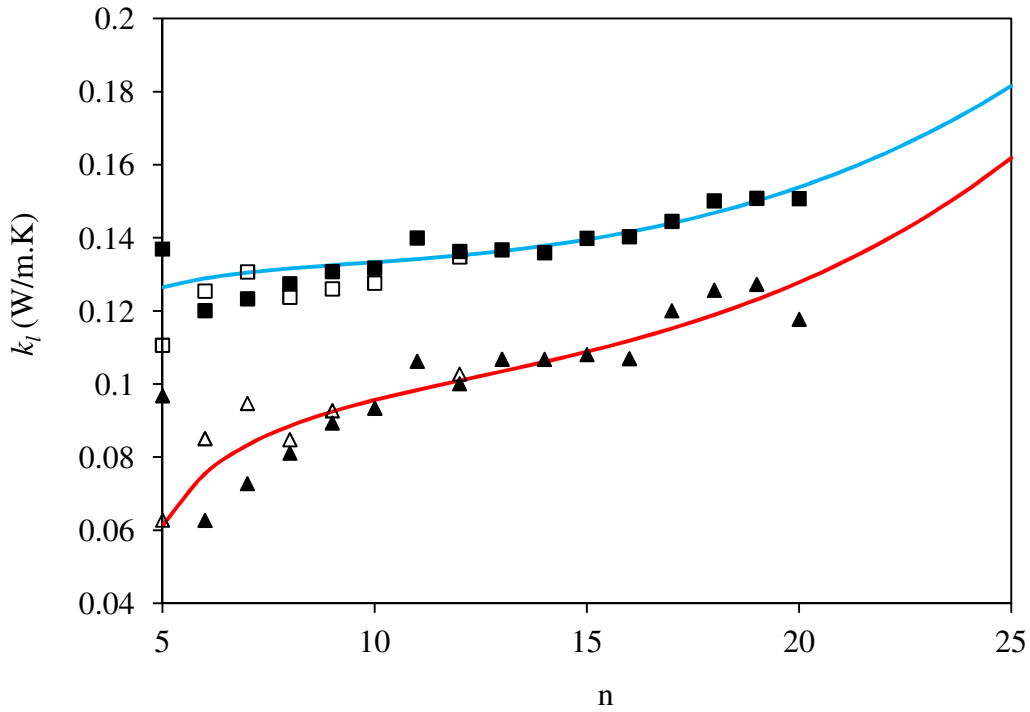


Fig. 6.6 The plots of $k_l$ versus $n$ for $T$ = 300 K and $T$ = 450 K, as inferred from Eq. (6.23) with coefficients $A_k$ and $B_k$ given by Yaws (1995) (filled squares ($T$ = 300 K) and filled triangles ($T$ = 450 K)) and approximated by Eqs. (6.24) (blue and red curves); the values of $k_l$ inferred from NIST website (squares ($T$ = 300 K) and triangles ($T$ = 450 K)).

The plots of $k_l$ versus $n$ for $T$ = 300 K and $T$ = 450 K, as inferred from Eq. (6.23) with coefficients $A_k$ and $B_k$ given by Yaws (1995) (filled squares ($T$ = 300 K)

and filled triangles ($T$ = 450 K)) and approximated by Eqs. (6.24) (blue and red curves) are shown in Fig. 6.6. In the same figure we have shown the values of $k_l$ inferred from NIST website (squares ($T$ = 300 K) and triangles ($T$ = 450 K)). As follows from this figure, the agreement between the values of thermal conductivity predicted by Approximation (6.23) with the values of the coefficients given in Yaws (1995) and approximated by Eqs. (6.24) looks almost ideal. Both these values agree well with the data reported in NIST website. For temperatures 300 and 450 K, the values of thermal conductivity inferred from Eq. (6.23) with coefficients given by Eqs. (6.24) differ by less than 2.46% and 7.80% respectively from the values of thermal conductivity inferred from Eq. (6.23) with coefficients given by Yaws (1995).

Note that during calculations, a small number of lighter components inside droplets could have temperatures exceeding their critical temperatures. In this case, the values of saturation pressure, latent heat of evaporation, density, viscosity, heat capacity and thermal conductivity were assumed equal to those at $T = T_{cr}$. This assumption allows us to avoid the analysis of heat and mass transfer in supercritical conditions, without imposing significant errors in our analysis due to the fact that the amount of components affected by this assumption is very small. Having replaced $n$ in Eqs. (6.18-6.24) with $\bar{n}_j$ (Eq. (6.8)) we obtain the required values of liquid density, viscosity, heat capacity and thermal conductivity for all quasi-components.

### *6.3.8 Diffusion coefficients*

In the case of mono-component droplets, the value of the diffusion coefficient of vapour in air $D_v$ can be estimated from the Wilke-Lee formula (Eq. (4.33)) (Poling et al, 2000).

Assuming that air is the dominant component in the air/fuel vapour mixture, the same formula will be used for multi-component droplets with molecular weight of vapour $M_v$ defined as

$$M_v = \frac{\sum_{j=1}^{j=N_f} M(\bar{n}_j) X_{vj}}{\sum_{j=1}^{j=N_f} X_{vj}}, \tag{6.25}$$

where the additional subscript $_v$ indicates that $X_j$ refers to the vapour phase. Parameters $\sigma_v$ and $\varepsilon_v/k_B$ , used in calculation of Eq. (4.33), are assumed to be equal to those of n-dodecane for the case of Diesel fuel and to those of n-octane for the case of gasoline fuel (Sazhin et al, 2005b) (see Appendix A), since no reliable

information referring to the dependence of these parameters on $n$ is available to the best of our knowledge.

Among various approximations for the diffusion coefficient for liquid $D_l$ we have chosen the Wilke-Chang approximation as illustrated in Appendix C (Eq. (C.9)).

### *6.3.9 Liquid and gas phase models*

As in previous Chapters 4 and 5, we used the Effective Thermal Conductivity (ETC) (Eqs. (2.13) and (2.23)) and Effective Diffusivity (ED) (Eqs. (4.8) and (D.38)) models for the liquid phase, and the model suggested in Abramzon and Sirignano (1989) (Eqs. (2.30) and (2.31)) for the gas phase. Whenever appropriate, the results will be compared with the prediction of the Infinite Thermal Conductivity (ITC) and Infinite Diffusivity (ID) models.

These models are described in detail in Chapters 3 and 4. In contrast to most previous studies, our analysis is based on the incorporation of the analytical solutions to the heat transfer and species diffusion equations inside droplets into a numerical code (Solution A in Chapter 4), rather than on the numerical solutions to these equations. The applicability of the ETC model to the analysis of droplet heating and evaporation has been demonstrated in Abramzon and Sirignano (1989) for the simplest case when the effects of thermal radiation and the dependence of transport coefficients on temperature are ignored and in Abramzon and Sazhin (2005, 2006) in the general case when both these affects are taken into account. The applicability of the ED model has been investigated in Delplanque et al (1991).

### *6.3.10 Parameters for the distribution functions*

Following Arias-Zugasti and Rosner (2003) we assume the values of parameters for the distribution function (6.5) for Diesel and gasoline fuels shown in Table 6.2.

| **Fuel** | $\alpha$ | $\beta$ **(kg/kmole)** | $\gamma$ **(kg/kmole)** | $n_0$ | $n_f$ |
|---|---|---|---|---|---|
| **Diesel** | 18.5 | 10 | 0 | 5 | 25 |
| **Gasoline** | 5.7 | 15 | 0 | 5 | 18 |

Table 6.2 The parameters of the distribution function (6.5) for Diesel and gasoline fuels.

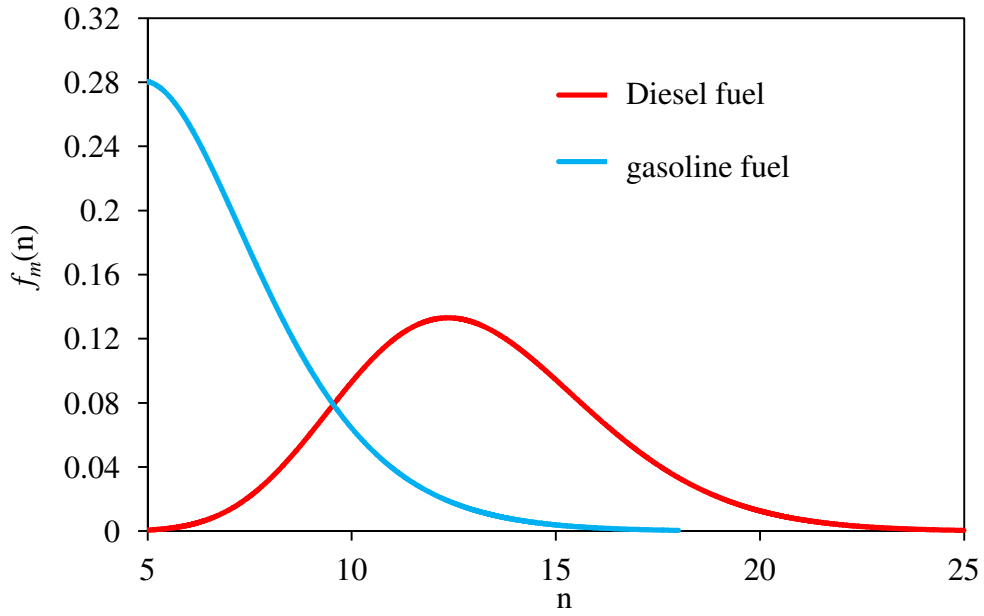


Fig. 6.7 The plots of $f_m(n)$ versus $n$ as predicted by Eq. (6.5) for Diesel (red) and gasoline (blue) fuels for the values of parameters given in Table 6.2.

The plots of $f_m(n)$ versus $n$ for Diesel and gasoline fuels for the values of parameters given in Table 6.2 are shown in Fig. 6.7. As follows from this figure, the forms of the plots of $f_m(n)$ versus $n$ for Diesel and gasoline fuels appear to be rather different. The values of $n$ for which $f_m(n)$ is maximal are equal to 12.4 and 5 for Diesel and gasoline fuels respectively. These values are different from the value of $\bar{n}_j = 12.5644$ for Diesel fuel and $\bar{n}_j = 7.0223$ for gasoline fuel for $n_{j-1} = n_0$ and $n_j = n_f$, as predicted by Eq. (6.8). Both these values are reasonably close to $n = 12$, referring to n-dodecane and $n = 8$, referring to n-octane, which are commonly considered as close approximations of Diesel and gasoline fuels respectively. The analysis of droplet heating and evaporation for both fuels will be performed separately below.

## 6.4 Preliminary results for Diesel fuel

Firstly, we assume that the dependence of liquid density, dynamic viscosity, heat capacity and thermal conductivity on $n$ can be ignored, and they are equal to those of n-dodecane for Diesel fuel (Sazhin et al, 2005b; 2006). The temperature dependence of these coefficients is taken into account (Appendix G). A sensitivity study of the n-dodecane properties are performed in Appendix G. This approach is consistent with the one used in Arias-Zugasti and Rosner (2003).

To illustrate the efficiency of the model, described above, we use the same values of parameters as in Sazhin et al (2006). Namely, we assume that the initial droplet temperature is equal to 300 K, and is homogeneous throughout its volume. Gas temperature is assumed to be equal to 880 K and gas pressure is assumed to be equal to 3 MPa. The initial composition of droplets is described by distribution function (6.5).

The plots of droplet surface temperature $T_s$ and droplet radius $R_d$ versus time for the initial droplet radius equal to 10 μm and velocity 1 m/s are shown in Fig. 6.8. The droplet velocity is assumed to be constant during the whole process. The calculations were performed for the case of $N_f$ = 1 (one quasi-component droplet) and $N_f$ = 20 (20 quasi-components droplet), using the ETC/ED and ITC/ID models.

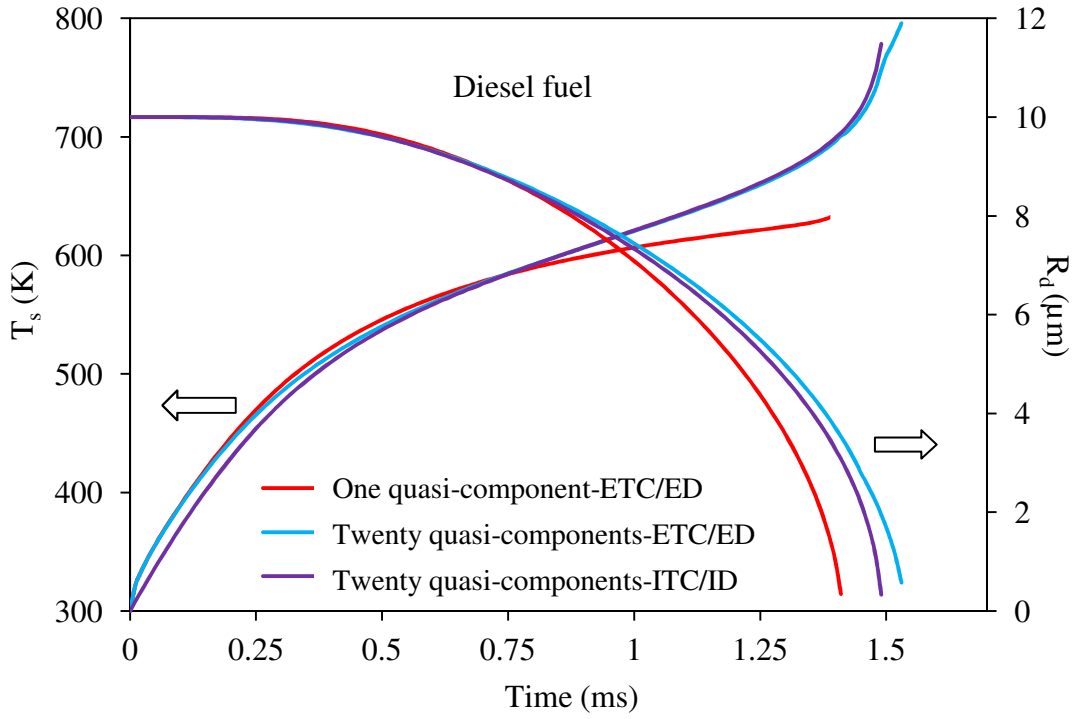


Fig. 6.8 The plots of $T_s$ and $R_d$, predicted by three models, versus time. The initial droplet radius and temperature are assumed to be equal to 10 μm and 300 K respectively, the droplet velocity is assumed to be equal to 1 m/s and its changes during the heating and evaporation process are ignored, gas temperature is assumed equal to 880 K. These are the models used for calculations: Effective Thermal Conductivity (ETC)/Effective Diffusivity (ED) model using one quasi-component (red), ETC/ED model using twenty quasi-components (blue), Infinite Thermal Conductivity (ITC)/Infinite Diffusivity (ID) model using twenty quasi-components (purple).

As one can see from this figure, the evaporation times and $T_s$, especially at the final stages of droplet heating and evaporation, predicted by the ETC/ED model,

using one and twenty quasi-components are noticeably different. The model, using twenty quasi-components predicts higher surface temperatures and longer evaporation time compared with the model using one quasi-component. This can be related to the fact that at the final stages of droplet evaporation the species with large $n$ become the dominant, as will be demonstrated later. These species evaporate more slowly than the species with lower $n$ and have higher wet bulb temperatures (see Fig. 6.1).

Also, there are noticeable differences in predictions of the ETC/ED and ITC/ID models, using twenty quasi-components, especially in the case of surface temperature at the initial stages of droplet heating and evaporation. The accurate prediction of this temperature is particularly important for prediction of the auto-ignition timing in Diesel engines (Sazhin et al, 2005b). This questions the reliability of the models for heating and evaporation of multi-component droplets, based on the ITC/ID approximations. As mentioned in the Introduction, these models are almost universally used for modelling these processes, especially when a large number of components are involved in the analysis.

The plots of $T_s$ and $R_d$ at time equal to 0.25 ms versus the number of quasi-components $N_f$, predicted by the ETC/ED and ITC/ID models, are shown in Fig. 6.9 for the same conditions as in Fig. 6.8. Symbols refer to those $N_f$ for which calculations were performed. As follows from this figure, for $N_f \geq 5$ the predicted $T_s$ and $R_d$ no longer depend on $N_f$. Hence, heating and evaporation of Diesel fuel droplets can be safely modelled using just 5 quasi-components. This number can even be reduced to 3 if errors less than about 0.3% can be tolerated. The errors due to the ITC/ID approximation in this case are significantly larger than those due to the choice of a small number of quasi-components, especially for the surface temperature. These errors cannot be ignored in most engineering applications, and this questions the applicability of the models using the ITC/ID approximation, including the widely used Continuous Thermodynamics models.

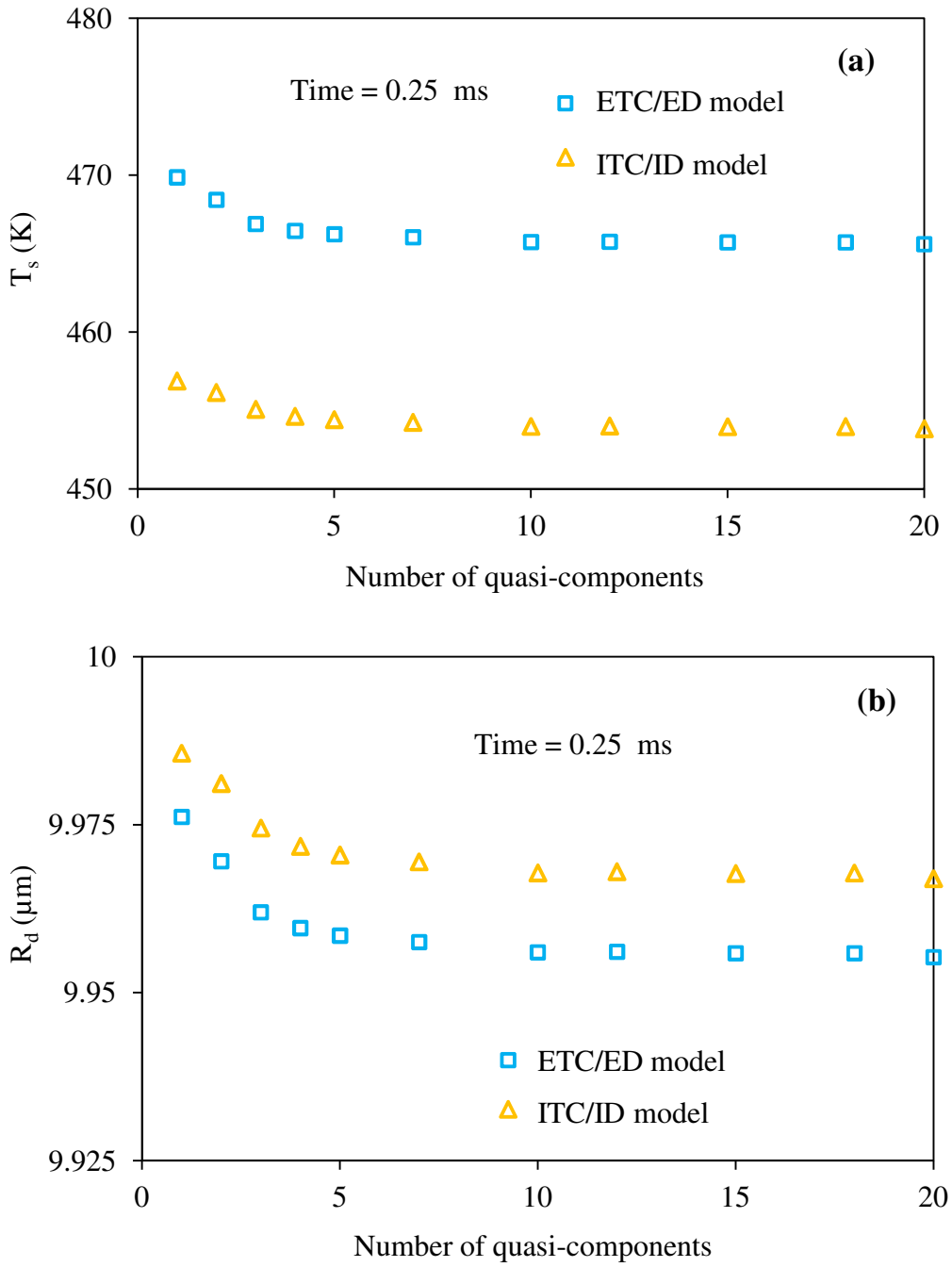


Fig. 6.9 The plots of $T_s$ (a) and $R_d$ (b) versus the number of quasi-components $N_f$ for the same conditions as in Fig. 6.8 at time 0.25 ms as predicted by the ETC/ED (squares) and ITC/ID (triangles) models.

Plots similar to those shown in Fig. 6.9 but at time equal to 1 ms are shown in Fig. 6.10. As one can see from this figure, both droplet surface temperature and radius can be well predicted if only 5 quasi-components are used. This number can even be reduced to 3 if errors of about 0.5% can be tolerated. In contrast to the case shown in Fig. 6.9, the droplet surface temperatures predicted by the ETC/ED and

ITC/ID models practically coincide, but the difference in predicted droplet radii is significantly larger than in the case shown in Fig. 6.9.

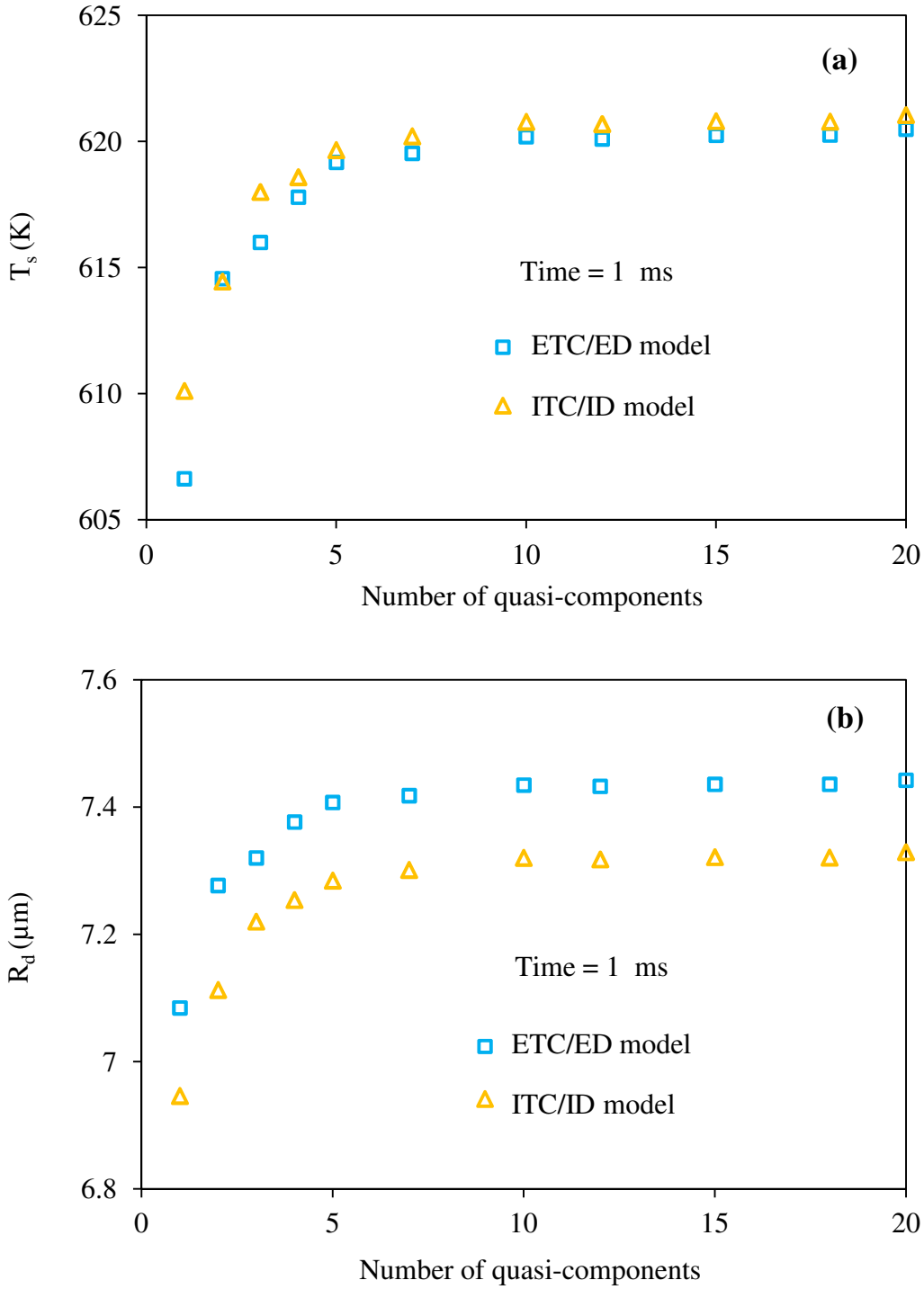


Fig. 6.10 The same as Fig. 6.9 but at time 1 ms.

The closeness of the temperatures predicted by ETC/ED and ITC/ID models at the later stages of droplet heating and evaporation can be related to the fact that at this stage the droplet temperature becomes almost homogeneous (see Fig. 6.15) and

the effects of temperature gradient inside droplets can be ignored. Smaller droplet radii predicted by the ITC/ID model, compared with the ETC/ED model, can be related to lower temperatures at the initial stages of droplet heating and evaporation predicted by the ITC/ID model compared with the ETC/ED model.

Comparing Figs. 6.9 and 6.10 one can see that at early stages of droplet heating and evaporation ($t$ = 0.25 ms), the predicted droplet radius reduces slightly with the increase in the number of quasi-components used, while at a later stage ($t$ = 1 ms) the opposite effect is observed. This could be related to the fact that at the early stages, droplet evaporation is controlled by the most volatile quasi-components, while at the later stages it is controlled by less volatile quasi-components. When the number of quasi-components increases then the volatility of the most volatile component increases and that of the least volatile decreases.

Plots similar to those shown in Fig. 6.8 but for the initial droplet radius equal to 25 μm are shown in Fig. 6.11. The conclusions which can be drawn from this figure are essentially the same as those obtained from Fig. 6.8.

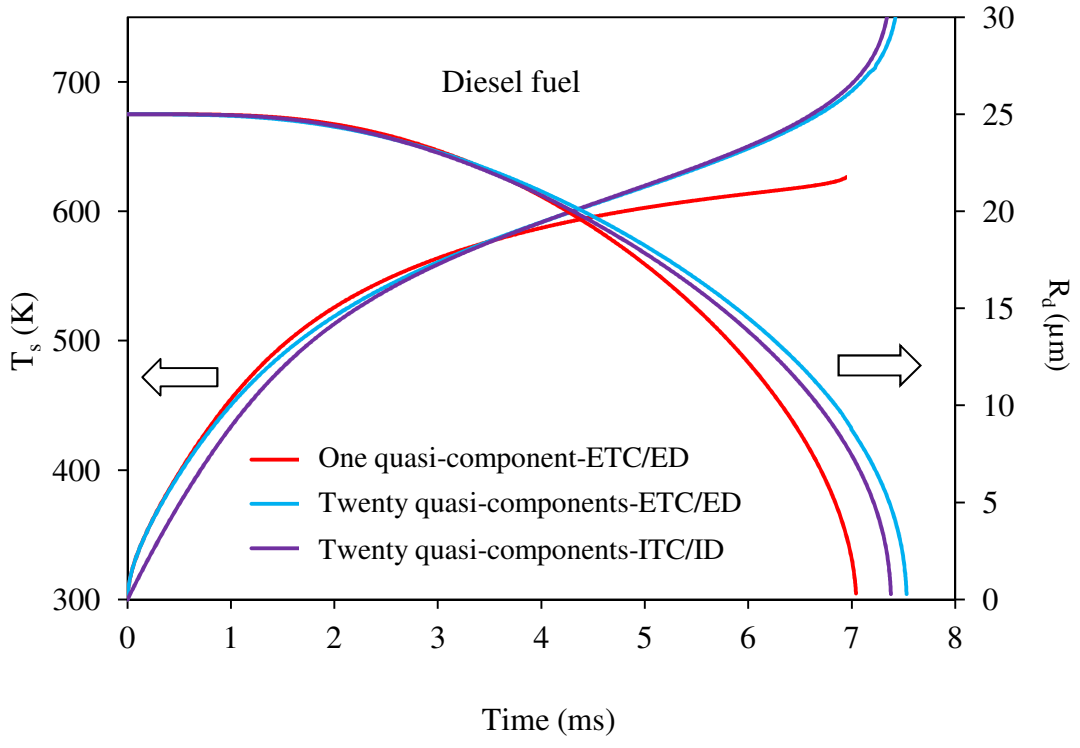


Fig. 6.11 The same as Fig. 6.8 but for the initial droplet radius equal to 25 μm.

Plots similar to those shown in Figs. 6.9 and 6.10 but for the initial droplet radius equal to 25 μm and at time equal to 2 ms are shown in Fig. 6.12. As can be seen from this figure, the choice of 5 or even 3 quasi-components is sufficient for

accurate prediction of droplet surface temperature and radius, in agreement with the results shown in Figs. 6.9 and 6.10. Also, in agreement with the results shown in Fig. 6.9, the droplet surface temperature predicted by the ITC/ID model is significantly (about 10 K) lower than the one predicted by the ETC/ED model. This provides an additional argument to support the application of the ETC/ED model rather than ITC/ID model.

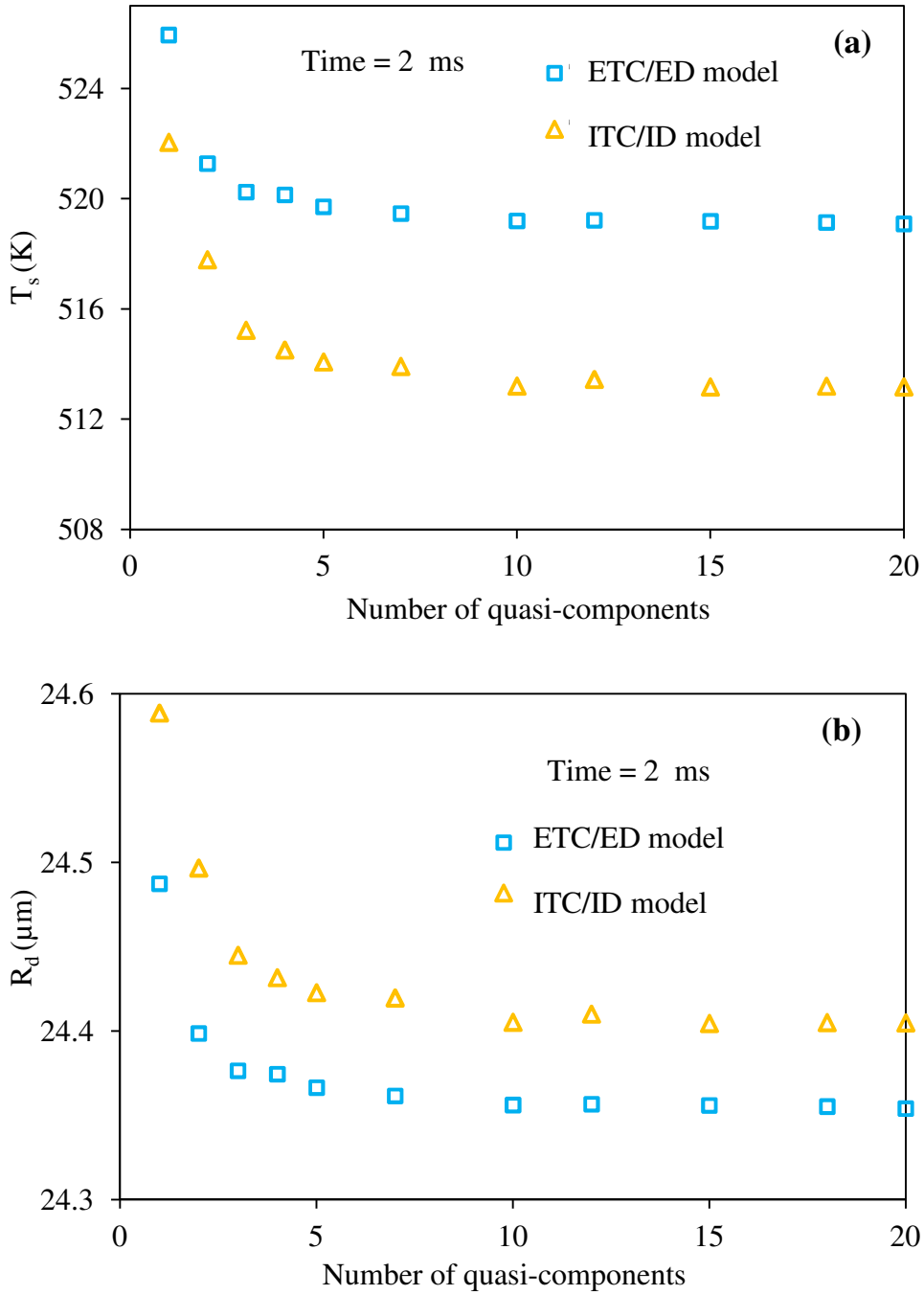


Fig. 6.12 The same as Figs. 6.9 and 6.10 but for the initial droplet radius equal to 25 μm and time equal to 2 ms.

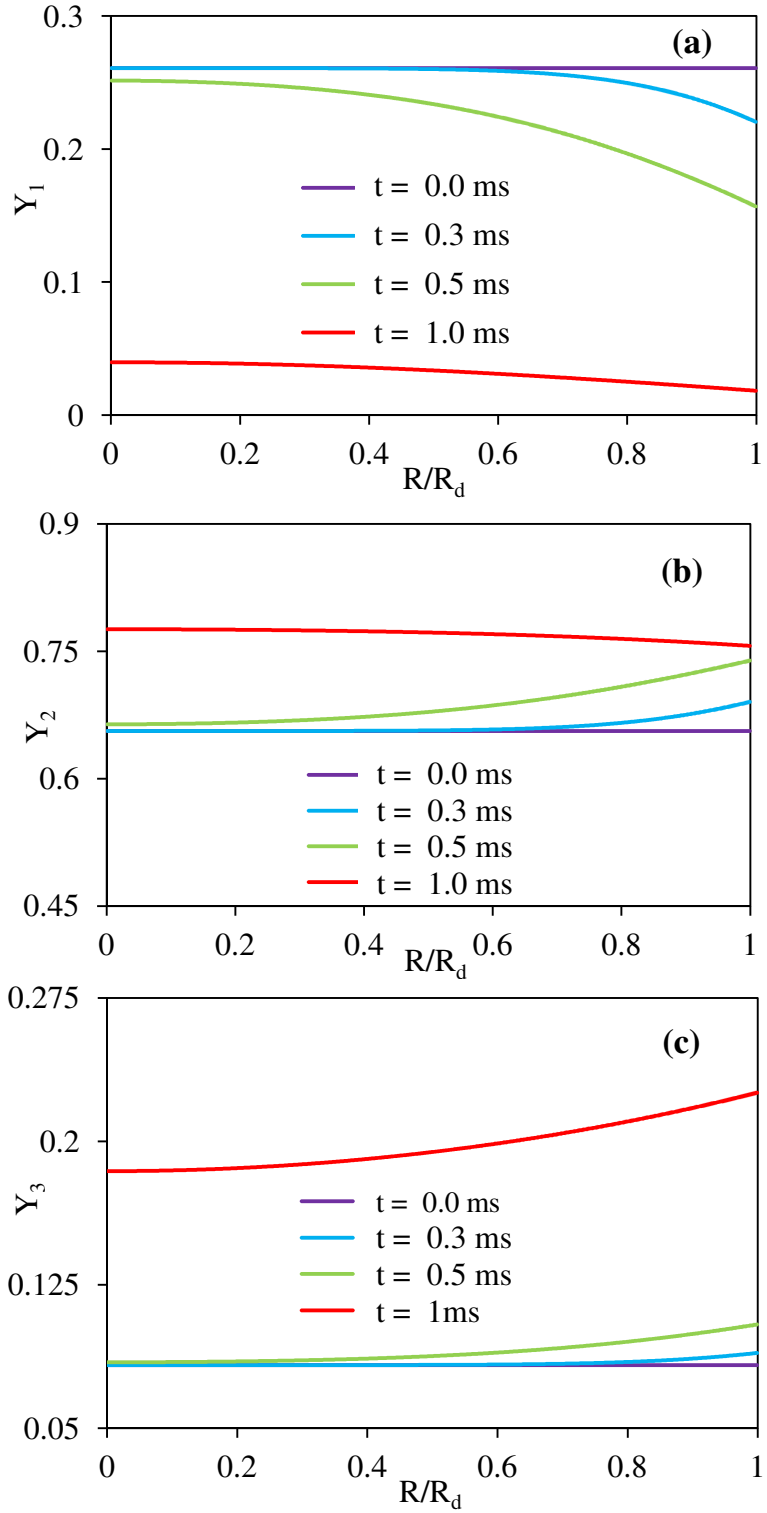


Fig. 6.13 The plots of $Y_i$ versus $R/R_d$ for three quasi-component droplets ($i$ = 1, 2, 3) at four moments of time as indicated near the curves. The same droplet and gas parameters as in Fig. 6.8 are used.

To illustrate the time evolution of the distribution of mass fractions of species inside droplets, we consider the case shown in Fig. 6.8 for three quasi-components. The plots of $Y_i$, where $i$ = 1, 2, 3, versus normalised radius $R/R_d$ for $t$ = 0, 0.3 ms, 0.5 ms and 1 ms are shown in Fig. 6.13. As one can see from this figure, the mass

fraction of the heaviest component $Y_3$ is always increasing with time, especially near the droplet surface. At the same time, the mass fraction of the lightest component ($Y_1$) decreases with time, and almost disappears at time 1 ms. The behaviour of the middle component ($Y_2$) is more complex. Initially, it increases with time, especially near the droplet surface, similarly to $Y_3$. At later times ($t \approx 1$ ms), however, it decreases with time, similarly to $Y_1$. These plots clearly show the significance of the gradients of concentration of all components at all times except the initial moment of time. This illustrates the limitations of the ID model, which is widely used in engineering applications.

The plots of $Y_{si}$ versus time of the same quasi-components as in Fig. 6.13 are presented in Fig. 6.14. The results presented in this figure are consistent with those shown in Fig. 6.13. The values of $Y_1$ monotonically decrease with time, while those of $Y_3$ monotonically increase with time. The values of $Y_2$ initially increase with time, but at later times they rapidly decrease with time. At times close to the moment when the droplet completely evaporates, only the quasi-component $Y_3$ remains. Since this quasi-component is the most slowly evaporating one, and has the highest wet bulb temperature, the model based on three quasi-components is expected to predict longer evaporation times and larger droplet surface temperatures at the final stages of droplet evaporation, compared with the model using one quasi-component. This result can be generalised to the case when the number of quasi-components is greater than 3. It is consistent with results shown in Figs. 6.8 and 6.11.

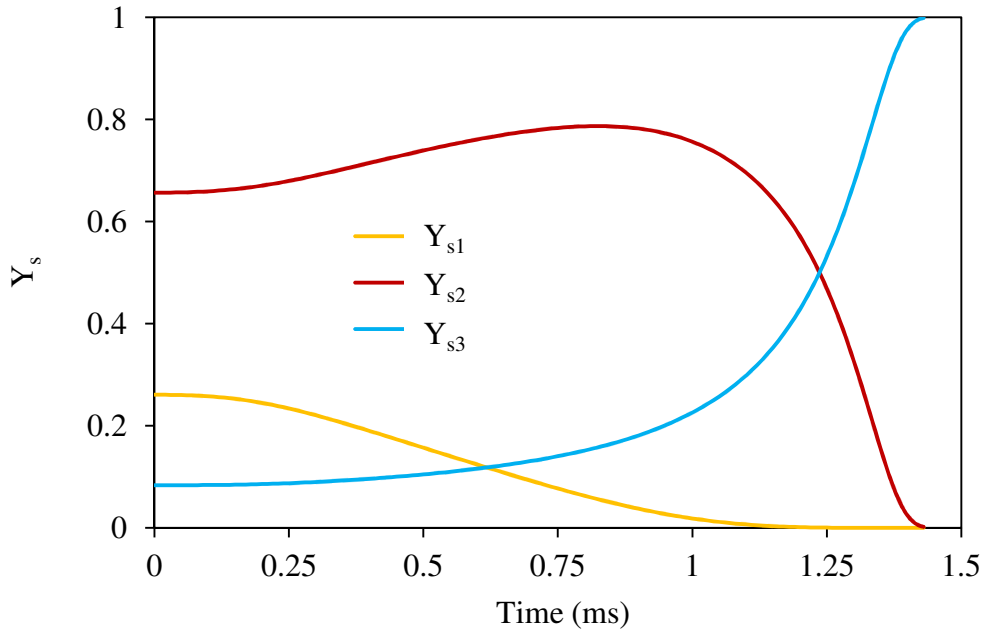


Fig. 6.14 The plots of $Y_{si}$ versus time of the same quasi-components as in Fig. 6.13.

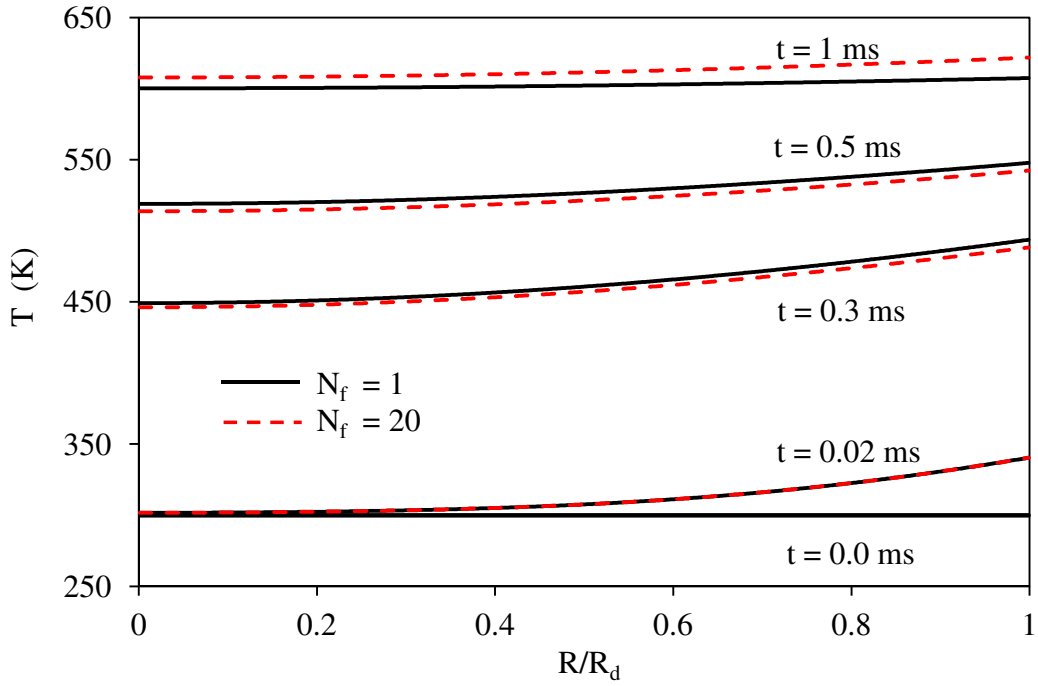


Fig. 6.15 The plots of $T_s$ versus $R/R_d$ for one quasi-component (solid) and twenty quasi-components (dashed) droplets at five moments of time as indicated near the curves. The same droplet and gas parameters as in Fig. 6.8 are used.

In Fig. 6.15 the time evolution of the distribution of temperature inside droplets is shown for the same case as in Fig. 6.8. Two cases are considered: one quasi-component and twenty quasi-components. As follows from this figure, in both cases, initially mainly the area close to the droplet surface is heated and a noticeable temperature gradient near the droplet surface can be clearly seen. At later times, however, the temperature inside the droplet becomes more homogeneous, which could justify the application of the ITC model. In agreement with Fig. 6.8, the model using twenty components predicts higher temperatures compared with the model using one quasi-component at $t$ = 1 ms.

## 6.5 Detailed results for Diesel fuel

In what follows the results of application of the quasi-discrete model to Diesel fuel, based on the new approximations for the temperature dependencies of liquid density, viscosity, heat capacity and thermal conductivity for n-alkanes ($C_nH_{2n+2}$) for $5 \leq n \leq 25$ (Eqs. (6.18) – (6.24)), are shown.

As in the previous section, we assume that the initial droplet temperature is equal to 300 K, and is homogeneous throughout its volume. Gas temperature is assumed to be equal to 880 K and gas pressure is assumed to be equal to 3 MPa. The

initial composition of droplets is described by distribution function (6.5) with the values of parameters for Diesel fuel given in Table 6.2, as shown in Fig. 6.7.

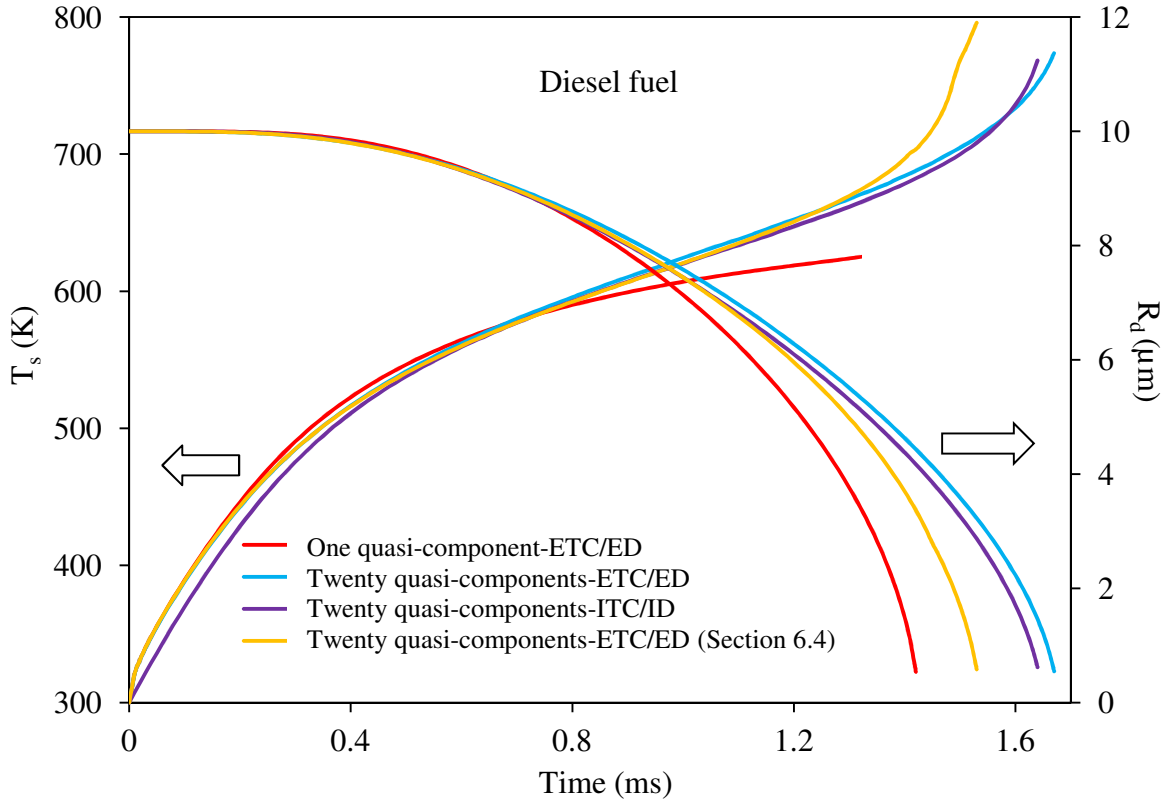


Fig. 6.16 The plots of $T_s$ and $R_d$, predicted by four models, versus time for the same conditions as in Fig. 6.8. These are the models used for calculations: ETC/ED model using one quasi-component and the approximations for liquid density, viscosity, heat capacity and thermal conductivity given in Section 6.3 (red), ETC/ED model using twenty quasi-components for liquid density, viscosity, heat capacity and thermal conductivity given in Section 6.3 (blue), ITC/ID model using twenty quasi-components for liquid density, viscosity, heat capacity and thermal conductivity given in Section 6.3 (purple) and ETC/ED model using twenty quasi-components for density, viscosity, heat capacity and thermal conductivity of the components assumed to be equal to those on n-dodecane (yellow-reproduced from Fig. 6.8).

The plots of droplet surface temperature $T_s$ and droplet radius $R_d$ versus time for the initial droplet radius equal to 10 μm and velocity 1 m/s are shown in Fig. 6.16. The droplet velocity is assumed to be constant during the whole process. The calculations were performed for the case of $N_f = 1$ (one quasi-component droplet, $n$ = 12.56) and $N_f = 20$ (twenty quasi-components droplet), using the ETC/ED and ITC/ID models. In the same figure, the plots of $T_s$ and $R_d$ versus time for $N_f = 20$, using the ETC/ED models, but assuming that the density, viscosity, heat capacity and thermal conductivity of all liquid components are the same and equal to those of

n-dodecane (as in Section 6.4) are shown. The conclusions drawn from this figure are the same as those obtained from Figs 6.8 and 6.11.

One can see from this figure that the results predicted by a simplified model used in Section 6.4 are noticeably different from those predicted by a more rigorous model used in this section. This shows the limitations of the earlier used simplified model for the density, viscosity, heat capacity and thermal conductivity of the liquid components.

Also, there are noticeable differences in predictions of the ETC/ED and ITC/ID models, using twenty quasi-components, especially in the case of the surface temperature at the initial stages of droplet heating and evaporation.

The plots of $T_s$ and $R_d$ at time equal to 0.5 ms versus the number of quasi-components $N_f$ , predicted by the ETC/ED and ITC/ID models, are shown in Fig. 6.17 for the same conditions as in Fig. 6.16. Symbols refer to those $N_f$ for which calculations were performed. As follows from this figure, for $N_f \geq 10$ the predicted $T_s$ and $R_d$ no longer depend on $N_f$. In fact the difference between the values of temperature and radius, predicted for $N_f = 5$ and $N_f = 20$, can be considered negligible compared with the difference between the values of temperature, predicted by the ETC/ED and ITC/ID models. Hence, heating and evaporation of Diesel fuel droplets can be safely modelled using just 5 quasi-components, in agreement with the results introduced in Section 6.4, obtained for time equal 0.25 ms using a simplified version of the quasi-discrete model. The errors due to the ITC/ID approximation for $N_f \geq 3$ are significantly larger than those due to the choice of a small number of quasi-components, especially for the surface temperature. These errors cannot be ignored in most engineering applications, and this questions the applicability of the models using the ITC/ID approximation, including the widely used Continuous Thermodynamics models.

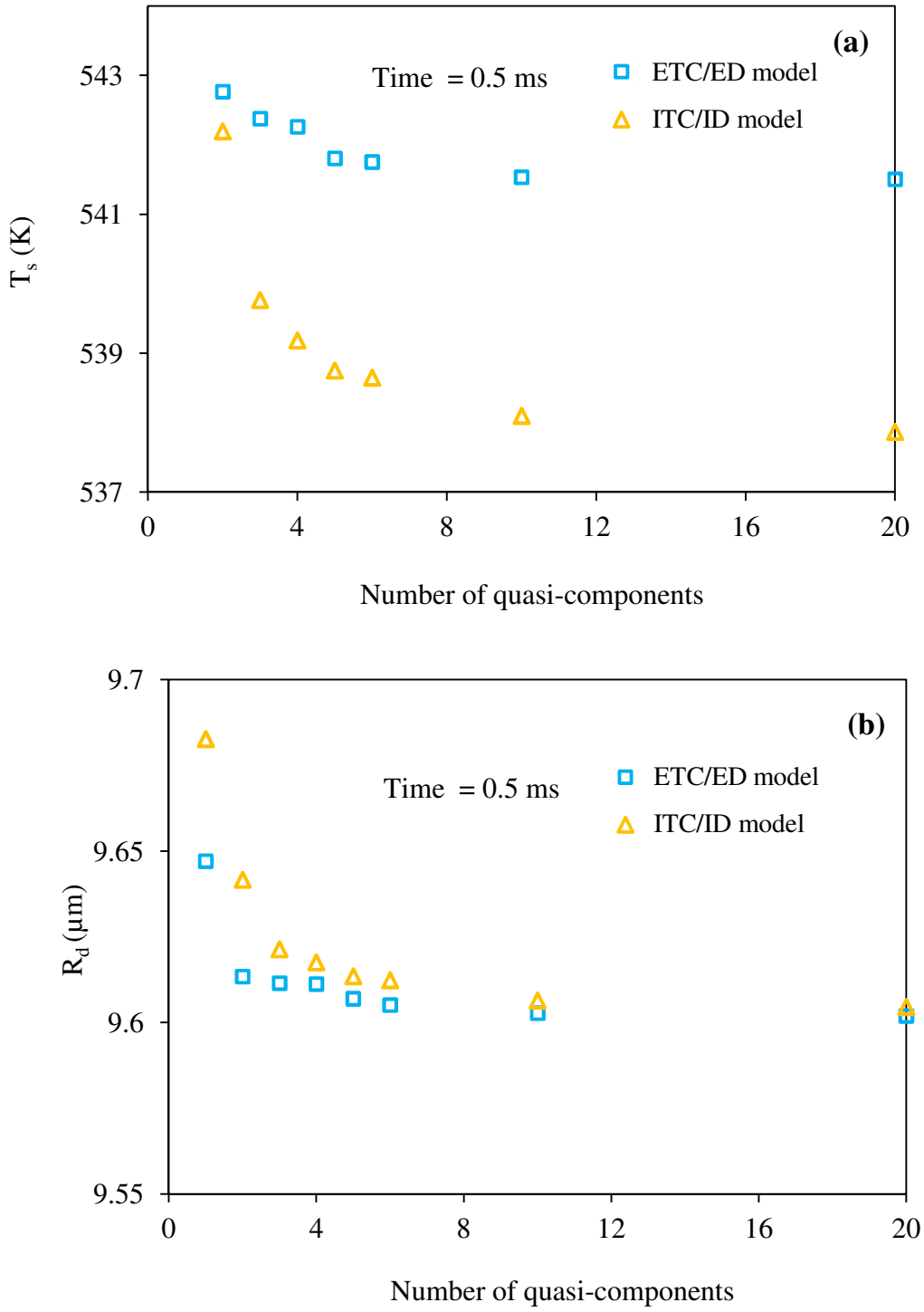


Fig. 6.17 The plots of $T_s$ (a) and $R_d$ (b) versus the number of quasi-components $N_f$ for the same conditions as in Fig. 6.16 at time 0.5 ms as predicted by the ETC/ED (squares) and ITC/ID (triangles) models.

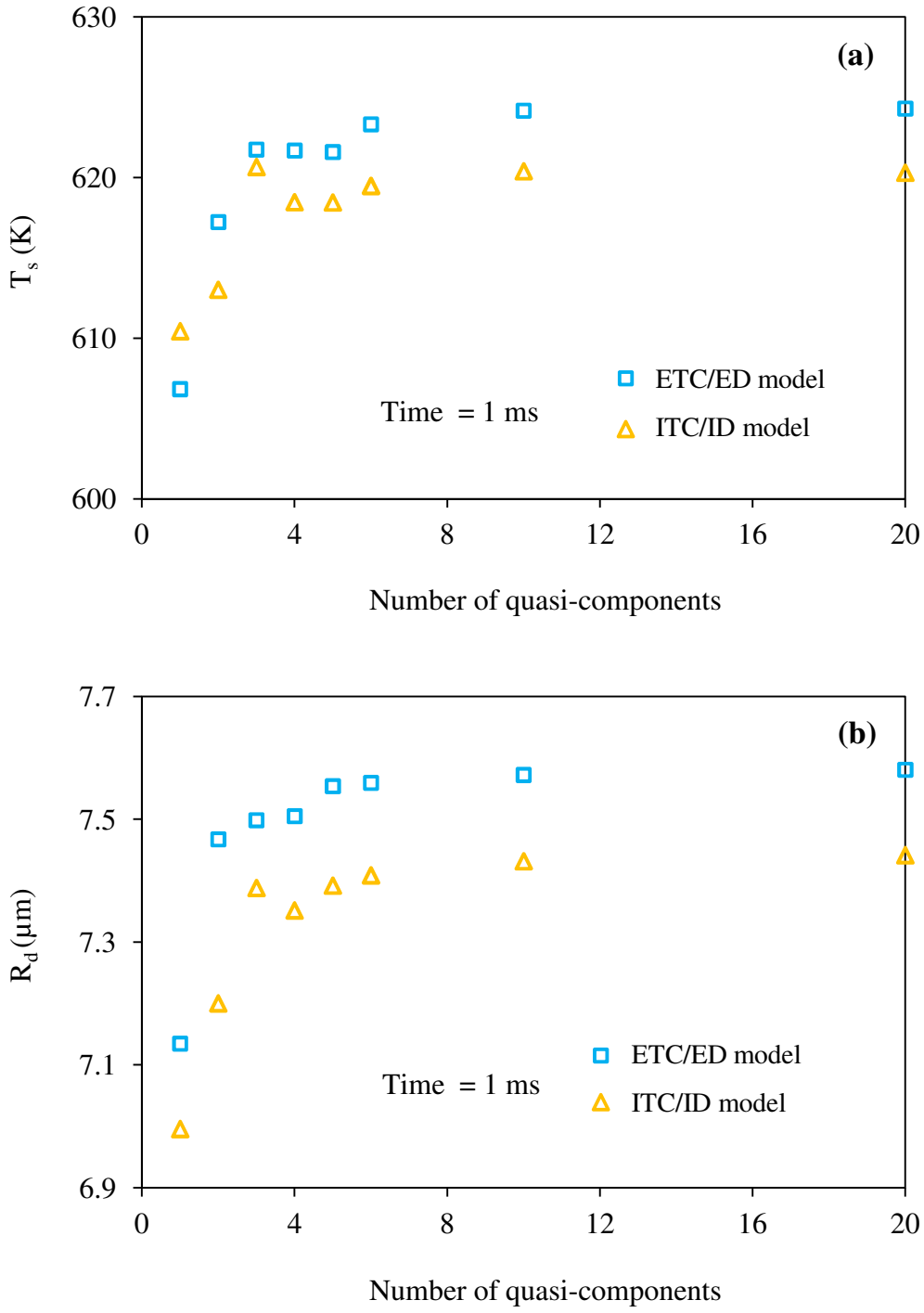


Fig. 6.18 The same as Fig. 6.17 but at time 1 ms.

Plots similar to those shown in Fig. 6.17 but at time equal to 1 ms are shown in Fig. 6.18. As one can see from this figure, both droplet surface temperature and radius can be well predicted if only 5 quasi-components are used. This number can even be reduced to 3 if errors of about 0.5% can be tolerated. In contrast to the case shown in Fig. 6.17, the droplet surface temperatures predicted by the ETC/ED and

ITC/ID models are rather close, but the difference in predicted droplet radii is significantly larger than in the case shown in Fig. 6.17.

In agreement with Section 6.4, smaller droplet radii are predicted by the ITC/ID model, compared with the ETC/ED model, at the final stages of droplet heating and evaporation due to low surface temperature predicted at the early stages of the evaporation.

Comparing Figs. 6.17 and 6.18 one can see that at early stages of droplet heating and evaporation ($t$ = 0.5 ms), the predicted droplet radius reduces slightly with the increase in the number of quasi-components used, while at a later stage ($t$ = 1 ms) the opposite effect is observed, in agreement with the results reported in Section 6.4.

## 6.6 Detailed results for gasoline fuel

Plots similar to those shown in Fig. 6.16, but for gasoline fuel, are presented in Fig. 6.19. The maximal number of quasi-components for gasoline fuel is 13. The initial conditions are assumed to be the same as in the case of Diesel fuel droplets to enable us to perform direct comparison between heating and evaporation of Diesel and gasoline fuel droplets in identical conditions. As in the case shown in Fig. 6.16, the droplet velocity is assumed to be constant during the whole process. The calculations were performed for the case of $N_f = 1$ (one quasi-component droplet, $\bar{n} = 7.0223$) and $N_f = 13$ (thirteen quasi-components droplet), using the ETC/ED and ITC/ID models. The density, viscosity, heat capacity and thermal conductivity of all liquid components are described in Section 6.3.

As in the case of Diesel fuel droplets, the evaporation times and $T_s$, especially at the final stages of droplet heating and evaporation, predicted by the ETC/ED models, using one and thirteen quasi-components are noticeably different. The model, using thirteen quasi-components predicts higher surface temperatures and longer evaporation time compared with the model using one quasi-component. As in the case of Diesel fuel droplets, this can be related to the fact that at the final stages of droplet evaporation the species with large $n$ become the dominant. These species evaporate more slowly than the species with lower $n$ and have higher wet bulb temperatures.

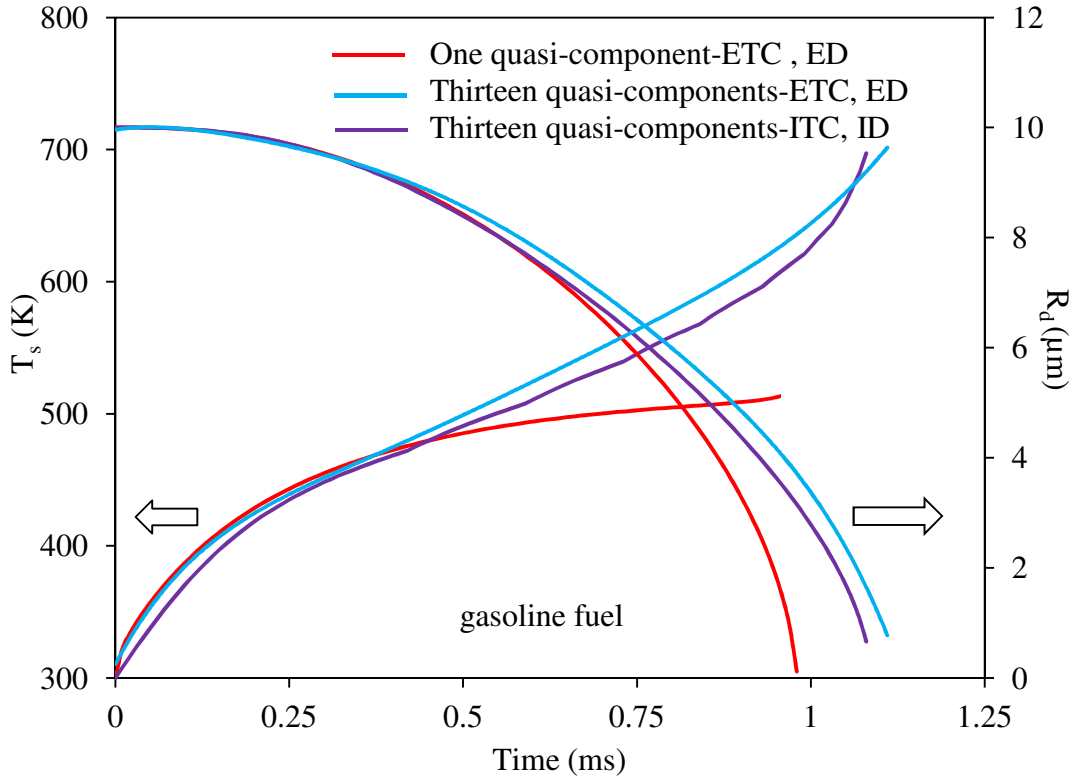


Fig. 6.19 The same as Fig. 6.16 for the first three curves but for the gasoline fuel with the maximal number of quasi-components $N_f = 13$. All plots are based on the approximations for liquid density, viscosity, heat capacity and thermal conductivity given in the Section 6.3.

The differences in predictions of the ETC/ED and ITC/ID models, using thirteen quasi-components, are more noticeable in the case of gasoline fuel droplets than in the case of Diesel fuel droplets. This difference can be seen not only at the initial stage of droplet heating and evaporation, but also at the later stages of these processes. This provides an additional support for our questioning of the reliability of the models for heating and evaporation of multi-component droplets, based on the ITC/ID approximations.

The plots of $T_s$ and $R_d$ at time equal to 0.2 ms versus the number of quasi-components $N_f$, predicted by the ETC/ED and ITC/ID models for gasoline droplets, are shown in Fig. 6.20 for the same conditions as in Fig. 6.19. As follows from this figure, for $N_f \geq 6$ the predicted $T_s$ and $R_d$ no longer depend on $N_f$. In fact the difference between the values of temperature and radius, predicted for $N_f = 3$ and $N_f = 13$, can be considered negligible compared with the difference between the values of temperature and radius, predicted by the ETC/ED and ITC/ID models. Hence, heating and evaporation of gasoline fuel droplets can be safely modelled using just 3 quasi-components. As in the case of Diesel fuel droplets, the errors due

to the ITC/ID approximation for $N_f \geq 3$ are significantly larger than those due to the choice of a small number of quasi-components, especially for the surface temperature.

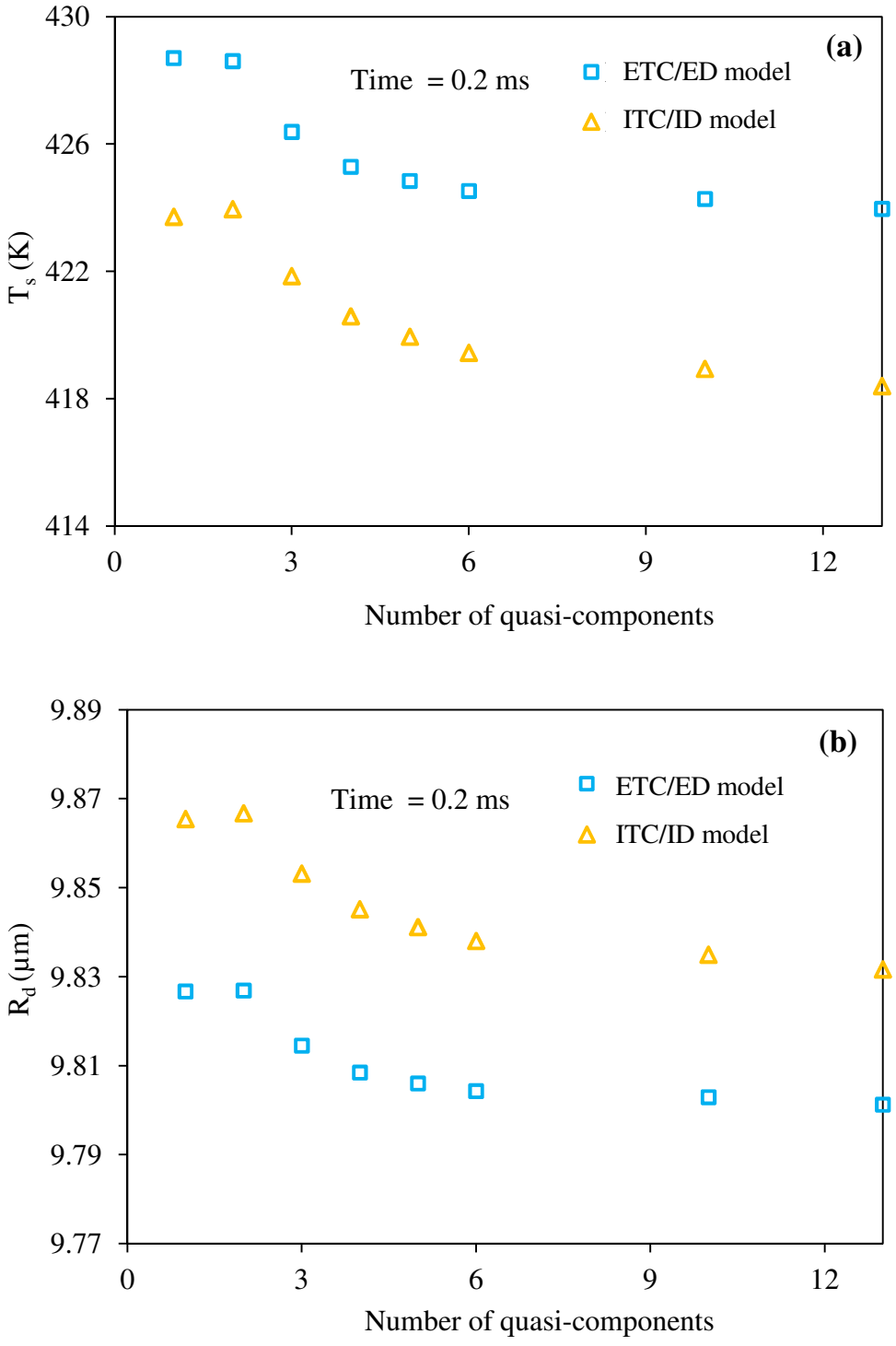


Fig. 6.20 The plots of $T_s$ (a) and $R_d$ (b) versus the number of quasi-components $N_f$ for the same conditions as in Fig. 6.19 at time 0.2 ms as predicted by the ETC/ED (squares) and ITC/ID (triangles) models.

Plots similar to those shown in Fig. 6.20 but at time equal to 0.75 ms are shown in Fig. 6.21. As one can see from this figure, both droplet surface temperature and radius can be well predicted by the ETC/ED model if only 3 quasi-components are used.

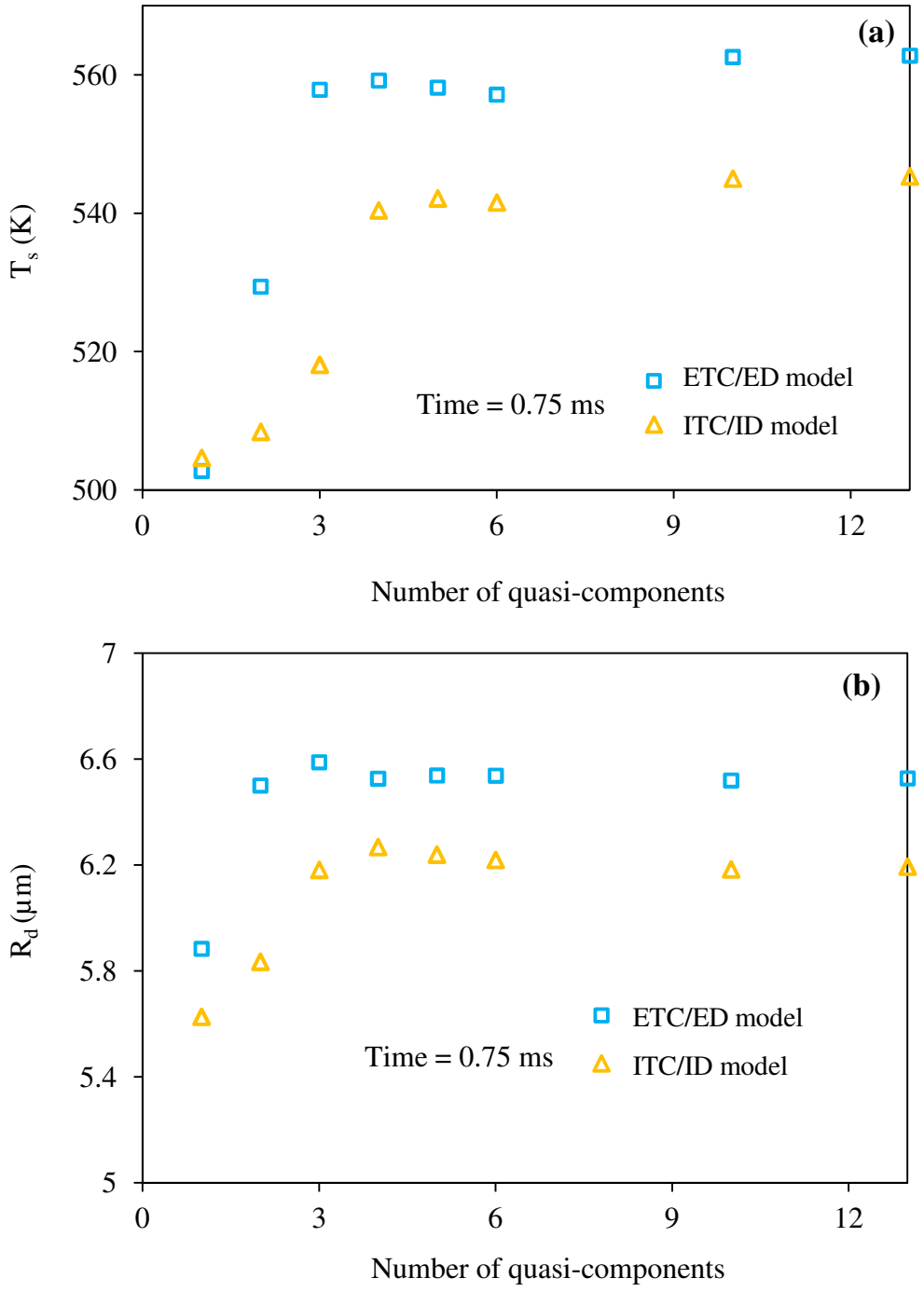


Fig. 6.21 The same as Fig. 6.20 but at time 0.75 ms.

Comparing Figs. 6.20 and 6.21 one can see that at the early stages of droplet heating and evaporation ($t$ = 0.2 ms), the predicted droplet radius reduces slightly

with the increase in the number of quasi-components used, while at a later stage ($t$ = 0.75 ms) the opposite effect is observed, in agreement with the results shown in Figs. 6.9, 6.10, 6.17 and 6.18.

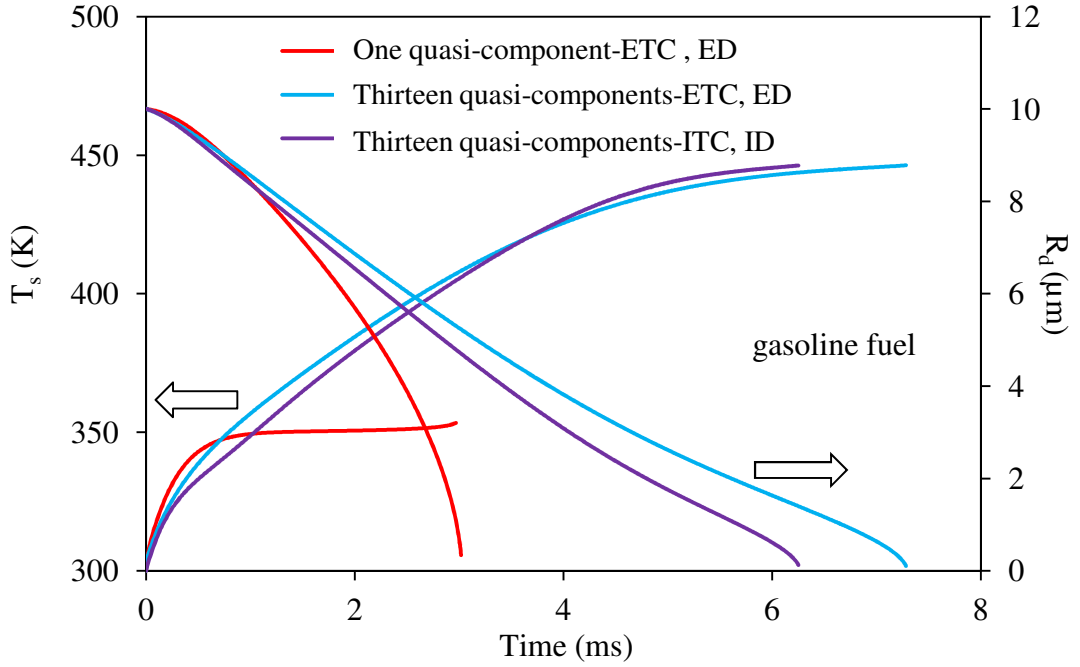


Fig. 6.22 The same as Fig. 6.21 but for the droplet velocity equal to 10 m/s, gas temperature equal to 450 K and pressure equal to 0.3 MPa.

Plots similar to those shown in Fig. 6.19, but for more realistic conditions in gasoline engines, are presented in Fig. 6.22. Following Basshuysen (2009), we assume that gas temperature is equal to 450 K, gas pressure is equal to 0.3 MPa and droplet velocity is equal to 10 m/s. As in the case shown in Fig. 6.19, we assume that the initial droplet temperature is equal to 300 K, and is homogeneous throughout its volume, while the droplet initial radius is equal to 10 μm.

Comparing Figs. 6.19 and 6.22, one can see that in the latter case the difference between the predicted temperatures and droplet radii for one and thirteen quasi-components is much more visible than in the former one. The same conclusion applies to the predictions of the ETC/ED and ITC/ID models. This can be attributed to much slower evaporation for the case shown in Fig. 6.22, compared with the case shown in Fig. 6.19. The general trends of the curves shown in Fig. 6.22 are similar to the ones shown in Fig. 6.19. In the case when thirteen quasi-components are considered, at the end of the evaporation process, mainly heavier components in droplets remain. These can reach higher temperatures and evaporate more slowly compared with the light and middle-range components.

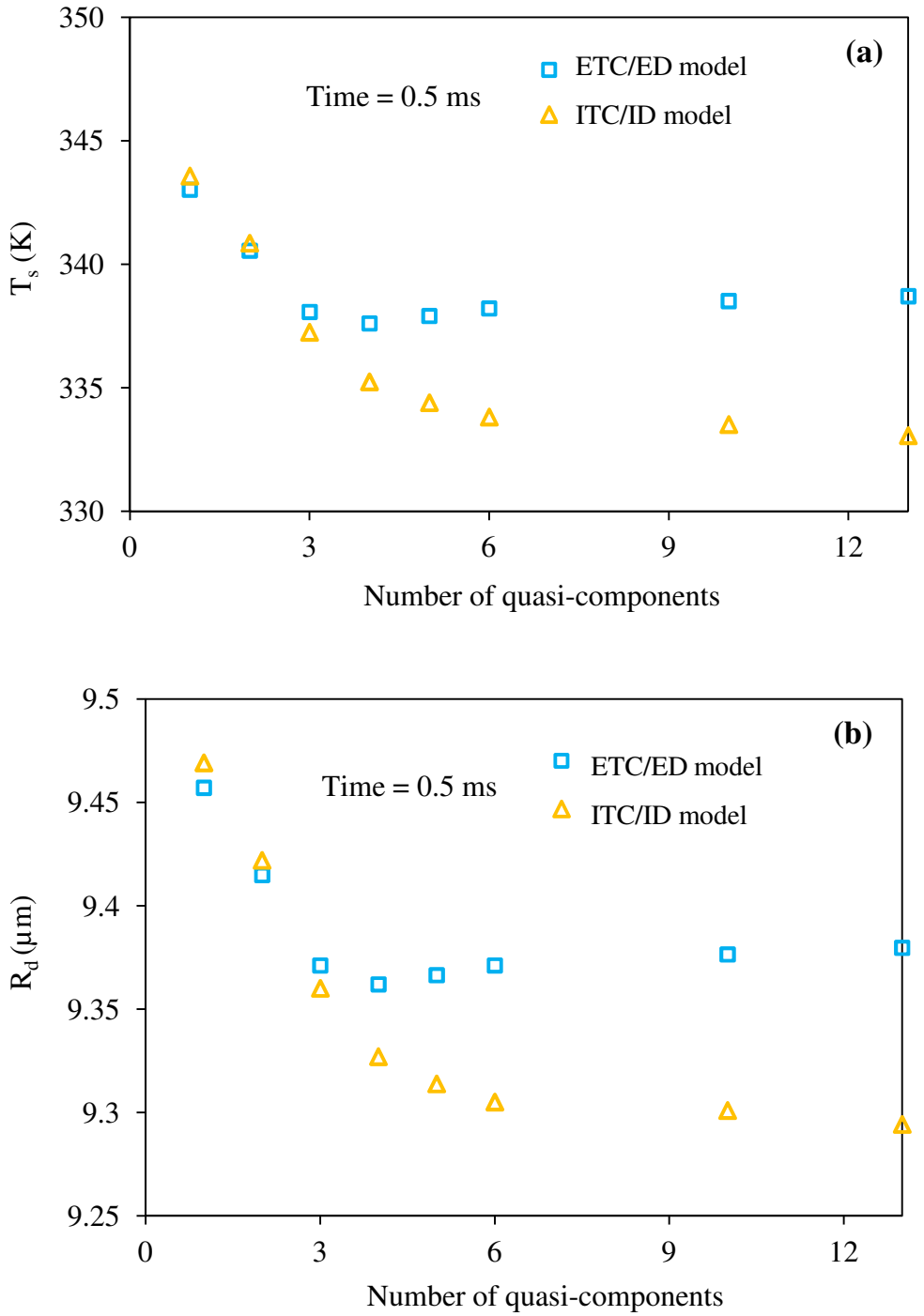


Fig. 6.23 The plots of $T_s$ (a) and $R_d$ (b) versus the number of quasi-components $N_f$ for the same conditions as in Fig. 6.22 at time 0.5 ms as predicted by the ETC/ED (squares) and ITC/ID (triangles) models.

The plots of $T_s$ and $R_d$ at time equal to 0.5 ms versus the number of quasi-components $N_f$ , predicted by the ETC/ED and ITC/ID models for gasoline droplets, are shown in Fig. 6.23 for the same conditions as in Fig. 6.22. As in the case shown in Figs. 6.17, 6.18, 6.20 and 6.21, for $N_f \geq 6$ the predicted $T_s$ and $R_d$ no longer

depend on $N_f$ . In fact this range can be extended to $N_f \geq 3$ at least for the ETC/ED model. In contrast to the cases shown in Figs. 6.17, 6.18, 6.20 and 6.21, the temperatures and radii, predicted by the ETC/ED and ITC/ID models, appear to be very close for small numbers of quasi-components. This can be related to the fact that in this case the temperature reaches the saturation level by the time 0.5 ms, when one or two components are considered.

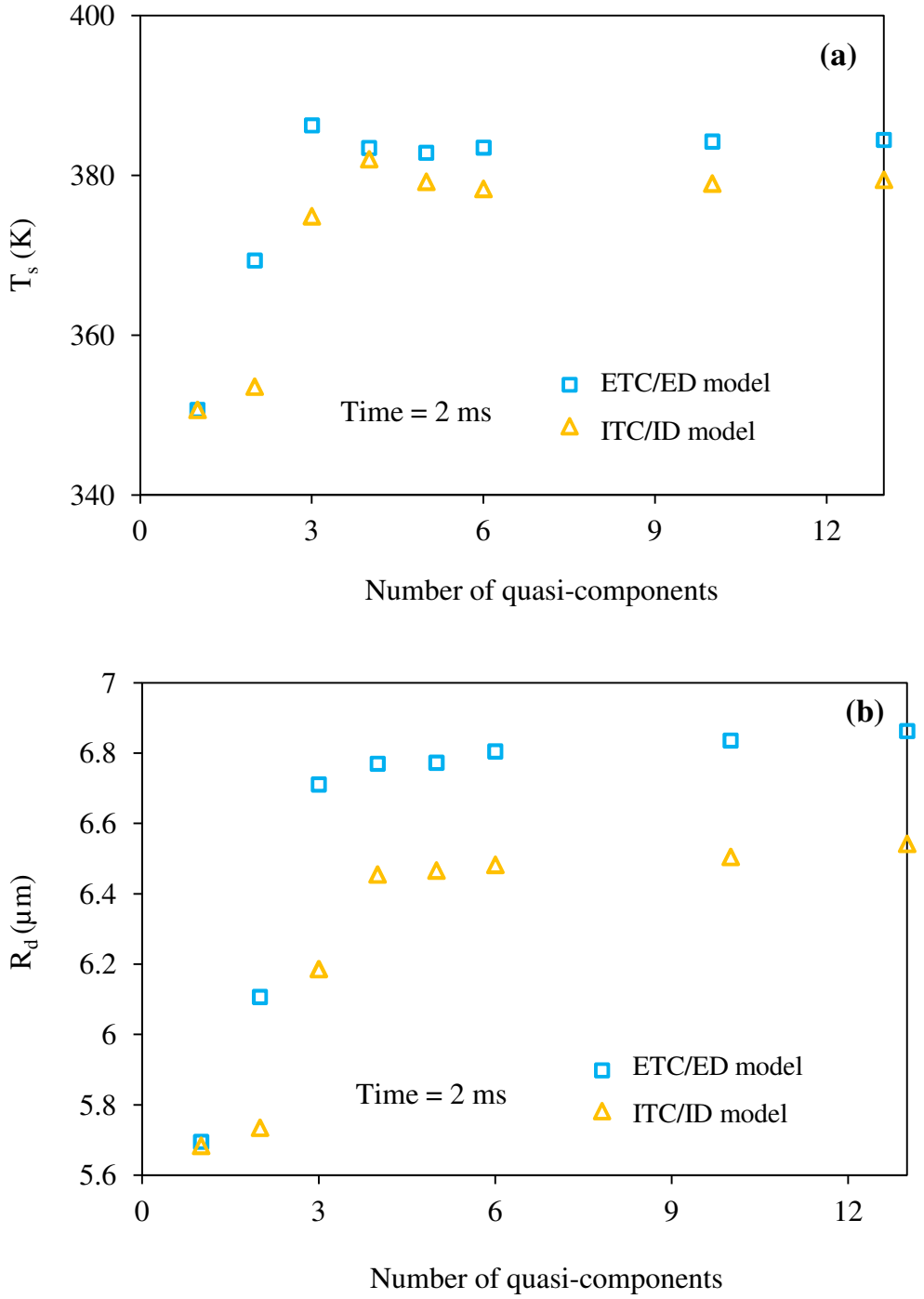


Fig. 6.24 The same as Fig. 6.23 but at time 2 ms.

Plots similar to those shown in Fig. 6.23 but at time equal to 2 ms are shown in Fig. 6.24. As in the case shown in Fig. 6.23, both droplet surface temperature and radius can be well predicted by the ETC/ED model if only 3 quasi-components are used. In contrast to the case shown in Fig. 6.23, the temperatures and radii, predicted by the ETC/ED and ITC/ID models, appear to be very close only for the case when one quasi-component is used.

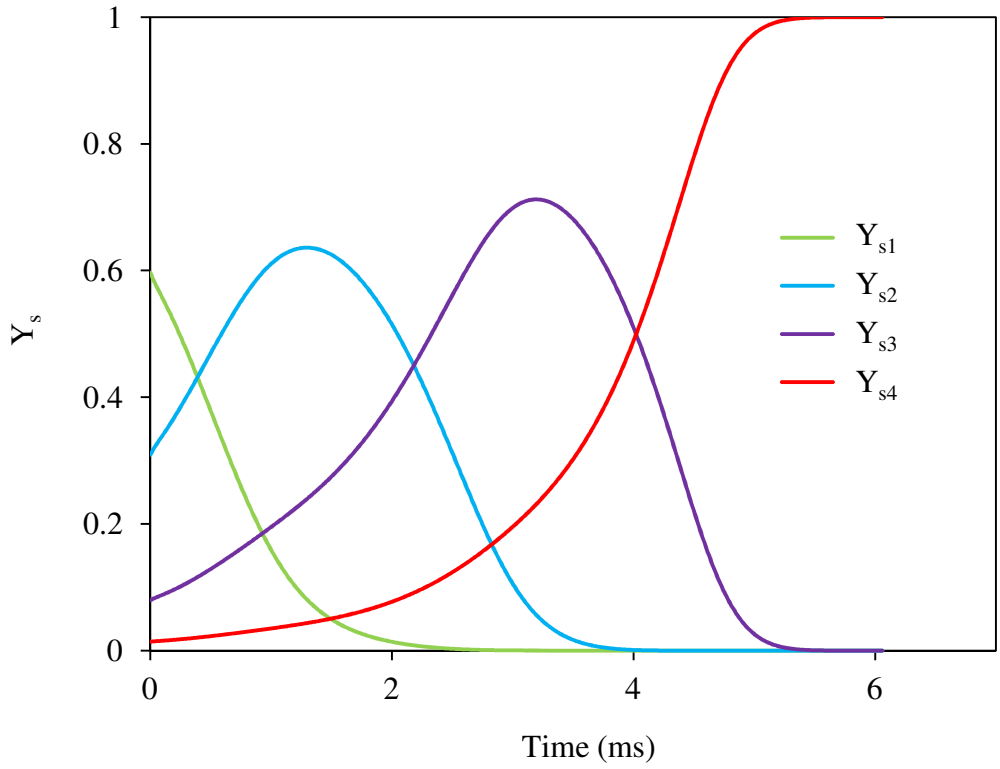


Fig. 6.25 The plots of $Y_{si}$ versus time for four quasi-components ($i$ = 1, 2, 3, 4) for the same case as shown in Fig. 6.22.

The plots of $Y_{si}$ versus time for the four quasi-components for the same case as shown in Fig. 6.22 are presented in Fig. 6.25. The results presented in this figure are consistent with those shown in Fig. 6.14 for Diesel fuel using a simplistic approach to approximate liquid density, viscosity, heat capacity and thermal conductivity of the liquid components. The values of $Y_{s1}$ monotonically decrease with time, while those of $Y_{s4}$ monotonically increase with time. The values of $Y_{s2}$ and $Y_{s3}$ initially increase with time, but at later times they rapidly decrease with time. At times close to the moment when the droplet completely evaporates, only the quasi-component $Y_{s4}$ remains.

## 6.7 Conclusions of Chapter 6

A new approach to modelling the heating and evaporation of multi-component droplets is suggested and tested for realistic Diesel and gasoline fuels droplets in engine-like conditions. The model is based upon the assumption that properties of components vary relatively slowly from one component to another and depend on a single parameter. This parameter is chosen to be the number of carbon atoms in the components ($n$). The components with relatively close $n$ are replaced by quasi-components with properties calculated as average properties of the *a priori* defined groups of actual components. Thus the analysis of the heating and evaporation of droplets consisting of many components is replaced by the analysis of the heating and evaporation of droplets consisting of relatively few quasi-components. In contrast to previously suggested approaches to modelling the heating and evaporation of droplets consisting of many components, the effects of temperature gradient and quasi-components diffusion inside droplets are taken into account.

Firstly the dependence of density, viscosity, heat capacity and thermal conductivity of all liquid components on the carbon number was ignored and assume to be equal to those of n-dodecane. The model, based on this approximation, is applied to Diesel fuel droplets. It is pointed out that droplet surface temperatures and radii, predicted by a rigorous model taking into account the effect of all 20 quasi-components, are almost the same as those predicted by the model using five quasi-components. Moreover, if errors less than about 1% can be tolerated, then the number of quasi-components used can be reduced to three. On the other hand, errors due to the assumptions that the droplet thermal conductivity and species diffusivities are infinitely large cannot be ignored in the general case. These errors are particularly important when the droplet surface temperature at the initial stage of heating is predicted. The time evolution of the distribution of temperature and species, predicted by the model, shows visible gradients of these parameters especially near the droplet surface at the initial stage of droplet heating and evaporation.

The model have been generalised to take into account the dependence of density, viscosity, heat capacity and thermal conductivity of all liquid components both on the carbon number and temperature. This model is applied to modelling of Diesel and gasoline fuels heating and evaporation.

In agreement with the simplified version of this model in which density, viscosity, heat capacity and thermal conductivity of all liquid components were assumed to be the same as for n-dodecane, it has been pointed out that for Diesel fuel droplet surface temperatures and radii, predicted by a rigorous model taking into account the effect of all twenty quasi-components, are close to those predicted by the model using five quasi-components. For the Effective Thermal Conductivity/ Effective Diffusivity (ETC/ED) model, the number of quasi-components used can be reduced to three. At the same time, the droplet surface temperature, and evaporation time predicted by the simplified model, and the rigorous model are noticeably different. The evaporation time predicted by the simplified model is about 10% shorter compared with the rigorous model. This justifies the need of taking into account the dependence of density, viscosity, heat capacity and thermal conductivity of liquid components both on the carbon number and temperature.

It is pointed out that in the case of gasoline fuels, with the maximal number of quasi-components equal to thirteen, a good approximation for the case of the ETC/ED model can be achieved based on the analysis of just three components. The difference in predictions of the thirteen and one component models appears to be particularly important in the case when droplets evaporate in gas at a relatively low temperature (450 K) and low pressure (0.3 MPa). In this case the evaporation time predicted by the one component model is less than half of the time predicted by the thirteen component model.

# 7 Conclusions and recommendations for future work

## 7.1 Conclusions

Heating and evaporation of monodisperse mono-component fuel droplets in ambient air at fixed temperature and atmospheric pressure have been studied numerically and validated against available experimental results. The effective thermal conductivity (ETC) model, which takes into account the finite thermal conductivity of droplets and recirculation inside them, has been used for the numerical modelling.

It is concluded that the ETC model, based on the analytical solution to the heat conduction equation inside droplets, can predict the observed average temperature of droplets with possible errors not exceeding several degrees, and observed droplet radii with possible errors not exceeding 2% in most cases. These results are consistent with those reported by Sazhin et al (2005a,b; 2006). Hence, this model can be recommended for implementation into CFD codes and used for multidimensional modelling of spray heating and evaporation based on these codes

The above-mentioned model has been generalised to take into account the effect of the presence of multiple components in fuel droplets on their heating and evaporation. This generalised model considers the effect of diffusion of liquid species inside the droplet and the non-unity activity coefficient (ideal and non-ideal models). The effects of recirculation in the moving droplets on heat and species diffusion within them are taken into account using the ETC and Effective Diffusivity (ED) models.

The predicted surface, average and central droplet temperatures have been compared with the experimentally measured droplet average temperatures for various mixtures of ethanol and acetone. It has been pointed out that there is a good agreement between the predicted and observed average temperatures in the case of pure acetone and acetone-rich mixtures. The temperatures predicted by the simplified model are reasonably close to the temperatures predicted by the earlier reported vortex model. Also, the temperatures predicted by the ideal and non-ideal models differ by not more than several degrees.

The above-mentioned simplified model for multi-component droplet heating and evaporation has been generalised to take into account the coupling between the

droplets and the ambient gas. The effects of the non-unity activity coefficient have been ignored (Raoult's law is assumed to be valid) and the interaction between droplets has been taken into account based on the correlation suggested by Deprédurand et al (2010). The model has been validated against experimental data for heating and evaporation of monodispersed n-decane/3-pentanone mixture droplets at atmospheric pressure. It has been pointed out that the effect of coupling leads to noticeably better agreement between the predictions of the model and the experimentally observed average droplet temperatures. In most cases, the experimentally observed droplet temperatures lie between the average and central temperatures predicted by the coupled solution. The main effect of the coupled solution has been linked with the reduction of the gas temperature in the region of influence. It has been pointed out that the number of terms in the series in the expressions for droplet temperature and species mass fraction can be reduced to just three, with possible errors less than about 0.5%. The model can be recommended for implementation into CFD codes and used for various engineering applications, including those in internal combustion engines.

The simplified model for heating and evaporation of multi-component droplets has been generalised to take into account the effect of the moving boundary on heat and mass diffusion within the droplet. The new model has been validated against the results predicted based on the numerical solutions to heat transfer and species diffusion equations. It has been noticed that both solutions (based on the analytical solutions to heat transfer and species diffusion equations and the numerical solutions to these equations) coincide.

A new model for droplet heating and evaporation of multi-component droplets with large number of components has been developed. The model is based upon the assumption that properties of components vary relatively slowly from one component to another and depend on a single parameter. This parameter is chosen to be the number of carbon atoms in the components ($n$). It is based on replacing the large number of actual components with a small number of quasi- components. This model is called the 'quasi-discrete model'. It has been assumed that the fuel consists only of n-alkanes in the form $C_nH_{2n+2}$. The liquid thermophysical properties of n-alkanes have been assumed to be the same as for n-dodecane except for the latent heat of evaporation and saturation vapour pressure. The model is applied to Diesel fuel. It is pointed out that droplet surface temperatures and radii, predicted by a

rigorous model taking into account the effect of all twenty quasi-components, are almost the same as those predicted by the model using five quasi-components. Moreover, if errors less than about 1% can be tolerated, then the number of quasi-components used can be reduced to three.

The quasi-discrete model has been extended to take into account the dependence of density, viscosity, specific heat and thermal conductivity of all liquid components on the number of carbon atoms. The extended quasi-discrete model has been applied to modelling of Diesel and gasoline fuel droplets. It has been pointed out that for Diesel and gasoline fuel droplets, surface temperatures and radii, predicted by a rigorous model, taking into account the effect of all twenty quasi-components, are close to those predicted by the model using five and three quasi-components respectively. The evaporation time predicted by the previous version of the quasi-discrete model is shown to be about 10% shorter compared with the extended model. This confirms the need to take into account the dependence of density, viscosity, heat capacity and thermal conductivity of liquid components both on the carbon number and temperature.

## 7.2 Recommendations for future work

The model for heating and evaporation of multi-component droplets needs to be implemented into ANSYS FLUENT CFD code and validated against engine-like conditions.

The effect of radiation on heating and evaporation of multi-component fuel droplets needs to be taken into account.

The kinetic effects on heating and evaporation of multi-component fuel droplets need to be taken into account.

The effect of other hydrocarbons families and fuel additives on the heating and evaporation process needs to be considered.

It is suggested that the concept of the quasi-discrete model is applied to the modelling of heating and evaporation of biofuel droplets.

It is suggested that the effect that the existence of many components has on the break-up process be studied.

## References

Abdelghaffar W.A. (2005), *Modelling of fuel droplet heating in diesel engines*, PhD Thesis, University of Brighton, Brighton, UK.

Abdelghaffar W. A., Karimi K. and Heikal M. R. (2006), *Fuel Spray Penetration in High Pressure Diesel Engines*, SAE 07SFL-15.

Abdelghaffar W.A., Elwardany A.E. and Sazhin S.S. (2010), *Modelling of the processes in Diesel engine-like conditions: effects of fuel heating and evaporation*, Atomization and Sprays, 20(8), 737-747.

Abdelghaffar W.A., Elwardany A.E. and Sazhin S.S. (2011), *Effect of fuel droplet break-up, heating and evaporation in Diesel engines*, World Congress on Engineering, London, UK, 6-7 July 2011, Vol. 3, p. 2485-2490. Publisher: Newswood Limited International Association of Engineers (IAENG), Hong Kong.

Abdel-Qader Z. and Hallett W.L.H. (2005), *The role of liquid mixing in evaporation of complex multicomponent mixtures: modelling using continuous thermodynamics*, Chemical Engineering Sciences 60, 1629-1640.

Abraham J. and Magi V. (1998), *A model for multicomponent droplet vaporization in sprays*, SAE Paper No. 980511.

Abramzon B. and Sirignano W.A. (1987), *Approximate theory of a single droplet vaporization in a convective field: effects of variable properties, Stefan flow and transient liquid heating*, Proceedings of 2nd ASME-JSME Thermal Engineering Joint Conference, Hawaii, 1, 11-18.

Abramzon B. and Sirignano W.A. (1989), *Droplet vaporization model for spray combustion calculation*, Int. J. Heat and Mass Transfer 32, 1605-1618.

Abramzon B. and Sazhin S. (2005), *Droplet vaporization model in the presence of thermal radiation*, Int. J. Heat Mass Transfer 48, 1868–1873.

Abramzon B. and Sazhin S. (2006), *Convective vaporization of fuel droplets with thermal radiation absorption*, Fuel 85, 32–46.

Aggarwal S.K. and Mongia H.C. (2002), *Multicomponent and high-pressure effects on droplet vaporization*, ASME J. Engineering for Gas Turbines and Power 124, 248-255.

Amsden A.A. (1993), *KIVA-3: A KIVA program with block-structured mesh for complex geometries*, Los Alamos Nat. Laboratory, New Mexico.

Amsden A.A., O'Rourke P.J. and Butler T.D. (1987), *KIVA II: A computer program for chemically reactive flows with sprays*, SAE 872072.

Arias-Zugasti M. and Rosner D. E. (2003), *Multicomponent fuel droplet vaporization and combustion using spectral theory for a continuous mixture*, Combustion and Flame 135, 271-284.

Ashgriz N. (2011), *Handbook of Atomization and Sprays Theory and Applications*, Chapter 12. Springer New York.

Atkins P. and de Paula J. (2002), *Atkins' Physical Chemistry*, seventh edition, Oxford University Press.

Barata J. (2008), *Modelling of biofuel droplets dispersion and evaporation*, Renewable Energy 33, 769-779.

Basshuysen R.V. (2009), *Gasoline engine with direct injection: processes, systems, development, potential*, 1st Edition, GWV Fachverlage GmbH, Wiesbaden (978-8348, 0670-3).

Bertoli C. and na Migliaccio M. (1999), *A finite conductivity model for diesel spray evaporation and computations*, Int. J. Heat and Fluid Flow 20, 552-561.

Bird R.B., Stewart E.W. and Lightfoot E.N. (2002), *Transport Phenomena*, 2nd edition. New York, Chichester: Wiley and Sons.

Brenn G., Deviprasath L. J., Durst F. and Fink C. (2007), *Evaporation of acoustically levitated multi-component liquid droplets*, Int. J. Heat Mass Transfer 50, 5073-5086.

Burger M., Schmehl R., Prommersberger K., Schäfer O., Koch R. and Wittig S. (2003), *Droplet evaporation modelling by the distillation curve model: accounting for kerosene fuel and elevated pressures*, Int. J. Heat Mass Transfer 46, 4403–4412.

Carslaw H.S. and Jaeger J.C. (1986), *Conduction of Heat in Solids*, Clarendon Press, Oxford.

Castanet G. (2004), *Etude aérothermique d'un jet de gouttes monodispersé en évaporation et en combustion à l'aide de méthodes optiques*. Thèse présentée pour l'obtention du grade de Docteur de l'Université Henri Poincaré, Vandoeuvre-Les-Nancy.

Castanet G., Lavieille P., Lemoine F., Lebounce M., Atthasit A., Biscos Y. and Lavergne G. (2002), *Energetic Budget on an Evaporating Monodisperse Droplet Stream Using Combined Optical Methods: Evaluation of The Convective Heat Transfer*, Int. J. Heat and Mass Transfer 45, 5053-5067.

Castanet G., Lavieille P., Lebounce M. and Lemoine F. (2003), *Measurement of the temperature distribution within monodisperse combusting droplets in linear streams using two-colour laser-induced fluorescence*, Experiments in Fluids 35, 563-571.

Castanet G., Lebouché M. and Lemoine F. (2005), *Heat and mass transfer of combusting monodisperse droplets in a linear stream*, Int. J. Heat Mass Transfer 48, 3261–3275.

Castanet G., Maqua C., Orain M., Grisch F. and Lemoine F. (2007), *Investigation of heat and mass transfer between the two phases of an evaporating droplet stream using laser-induced fluorescence techniques: comparison with modelling*, Int. J. Heat Mass Transfer 50, 3670–3683.

Chin J.S. and Lefebvre A.H. (1983a), *Steady-state evaporation characteristics of hydrocarbon fuel drops,* AIAA-21-10, 1437-1443.

Chin J.S. and Lefebvre A.H. (1983b), *The role of the heat-up period in fuel drop evaporation*, AIAA-83-0068, 1-10.

Continillo G. and Sirignano W.A. (1991), *Unsteady, spherically-symmetric flame propagation through multicomponent fuel spray clouds*, in: G. Angelino, L. De Luca, W.A. Sirignano (Eds.), Modern Research Topics in Aerospace Propulsion, Springer-Verlag, 173–198.

Delplanque J.-P., Rangel R.H. and Sirignano W.A. (1991), *Liquid-waste incineration in a parallel-stream configuration: effect of auxiliary fuel*, Prog. Aeronaut. Astronaut. 132, 164–184.

Deprédurand V. (2009), *Approche experimentale de l' évaporation de sprays de combustibles multicomposants*, Thèse présentée pour l'obtention du grade de Docteur de l'Institut National Polytechnique de Lorraine, Vandoeuvre-Les- Nancy.

Deprédurand V., Miron P., Labergue A., Wolff M., Castanet G. and Lemoine F. (2008), *A temperature sensitive tracer suitable for two-colour laser-induced fluorescence thermometry applied to evaporating droplets*, Measurement Science Technology 19(10), 1–12.

Deprédurand V., Castanet G. and Lemoine F. (2010), *Heat and mass transfer in evaporating droplets in interaction: influence of the fuel*, Int. J. Heat Mass Trans 53, 3495–3502.

Dombrovsky L.A. and Sazhin S.S. (2003a), *A parabolic Temperature Profile Model for Heating of Droplets*, ASME J. Heat Transfer 125, 535-537.

Dombrovsky L.A. and Sazhin S.S. (2003b), *A simplified non-isothermal model for droplet heating and evaporation*, Int. Communications in Heat and Mass Transfer 30, 787-796.

Elwardany A.E. (2009), *Modelling of heat, mass transfer and break up processes in Diesel fuel droplets*, MSc thesis, University of Alexandria, Alexandria, Egypt.

Elwardany A.E., Sazhin S.S., Castanet G., Lemoine F. and Heikal M.R. (2011), *The modelling of heating and evaporation of mono-component, bi-component and multi-*

*component droplets*, Proceedings of the ILASS-Europe, Estoril, Portugal, 5-7 September 2011.

Elwardany A.E., Gusev I.G., Castanet G., Lemoine F. and Sazhin S.S. (2012), *Mono- and multi-component droplet cooling/heating and evaporation: comparative analysis of numerical models*, Atomization and Sprays (accepted).

Elwardany A.E. and Sazhin S.S. (2012), *A quasi-discrete model for droplet heating and evaporation: application to Diesel and gasoline fuels*, Fuel (accepted).

Faeth G.M. (1983), *Evaporation and combustion of sprays*, Progress in Energy and Combustion Science 9, 1–76.

Faghri A. and Zhang Y. (2006), *Transport phenomena in multiphase systems*, Burlington: Elsevier.

Fieberg C., Reichelt L., Martin D., Renz U. and Kneer R. (2009), Experimental and numerical investigation of droplet evaporation under diesel engine conditions, Int. J. Heat Mass Transfer 52, 3738-3746.

Flynn P. F., Durrett R. P., Hunter G. L., zur Loye A. O., Akinyemi O. C., Dec J. E. and Westbrook C. K. (1999), *Diesel Combustion: An Integrated View Combining Laser Diagnostics, Chemical Kinetics, and Empirical Validation*, SAE 1999-01-0509.

Ghosh J., Mukhopadhyay A., Rao G.V. and Sanyal D. (2008), *Analysis of evaporation of dense cluster of bicomponent fuel droplets in a spray using spherical cell model*, Int. J. Thermal Sciences 47, 584-590.

Gökalp I., Chauveau C., Berrekam H. and Ramos-Arroyo N.A. (1994), *Vaporization of miscible binary fuel droplets under laminar and turbulent convective conditions,* Atomization Spray 4, 661–676.

Gusev I.G., Krutitskii P.A., Sazhin S.S. and Elwardany A.E. (2012), *New solutions to species diffusion equation in the presence of the moving boundary*, Int. J. Heat Mass Transfer 55, 2014-2021.

Hallett W.L.H. (1997), *A simple quasi-steady droplet evaporation model using continuous thermodynamics*, The Combustion Institute, Spring Technical Meeting.

Hallett W.L.H. (2000), *A simple model for the vaporization of droplets with large number of components*, Combustion and Flame 121, 334-344.

Hallett W.L.H. and Legault N.V. (2011), *Modelling of biodiesel droplet evaporation using continuous thermodynamics*, Fuel 90, 1221-1228.

Han Z., Reitz R. D., Claybaker P. J. and Rutland C. J. (1996), *Modeling the effects of intake flow structure on fuel/air mixing in a direct-injected spark-ignition engine*, SAE Paper 961192.

Harstad K. and Bellan J. (2004), *Modeling evaporation of Jet A, JP-7, and RP-1 drops at 1– 15 bars*, Combust. Flame 137, 163–177.

Heywood J. B. (1988), *Internal Combustion Engines Fundamentals*, McGraw-Hill Book Company, New York.

Incropera F.P. and DeWitt D.P. (2002), *Fundamentals of Heat and Mass Transfer*, 5th edition. John Wiley and Sons.

Karimi K., Sazhina E.M., Abdelghaffar W.A., Crua C., Cowell T., Heikal M.R. and Gold M.R. (2006), *Developments in Diesel Spray Characterisation and Modelling*, THIESEL Conference on Thermo- and Fluid Dynamic Processes in Diesel engines, Spain, Session A.1 (CD).

Kennaird D.A., Crua C., Heikal M.R., Gold M.R. and Jackson N.S. (2002), *In-Cylinder Penetration and Break-up of Diesel Sprays Using a Common-Rail Injection System*, SAE 01-1626.

Klingsporn M. and Renz U. (1994), *Vaporization of a binary unsteady spray at high temperature and high pressure*, Int. J. Heat Mass Transfer 37 (Suppl. 1) 265–272.

Knig G., Anders K. and Frohn A. (1986), *A new light-scattering technique to measure the diameter of periodically generated moving droplets*, J. Aerosol Science 17, 157-167.

Kristyadi T., Deprédurand V., Castanet G., Lemoine F., Sazhin S.S., Elwardany A., Sazhina E.M. and Heikal M.R. (2010), *Monodisperse monocomponent fuel droplet heating and evaporation*, Fuel 89, 3995–4001

Kuo K.K. (1986), *Principles of Combustion*, John Wiley and Sons.

Lage P.L.C. (2007), *The quadrature method of moments for continuous thermodynamics*, Comput. Chem. Eng. 31, 782–799.

Lage P.L.C., Hackenberg C.M. and Rangel R.H. (1995), *Nonideal vaporization of dilating binary droplets with radiation absorption*, Combust. Flame 101, 36– 44.

Laurent C., Lavergne G. and Villedieu P. (2009), *Continuous thermodynamics for droplet vaporization: comparison between Gamma-PDF model and QMoM*, C.R. Mech. 337 449–457.

Lavieille P., Lemoine F., Lavergne G., Virepinte. J.F. and Lebouche M. (2000) *Temperature measurements on droplets in monodisperse stream using laser-induced fluorescence*. Experiments in Fluids, 29, 429-437.

Lavieille P., Lemoine F., Lebouché M. and Lavergne G. (2001), *Evaporating and combusting droplet temperature measurement using two colors laser induced fluorescence*. Exp Fluids 31, 45–55.

Lavieille P., Lemoine F. and Lebouché M. (2002a), *Investigation on temperature of evaporating droplets in linear stream using two-color laser-induced fluorescence*. Combust Sci Technol 174, 117–42.

Laveille P., Lemoine F. and Lebouché M. (2002b) *Measurement of the temperature distribution over a combusting droplet in monodisperse stream using two-colour laser-induced fluorescence*. Proceedings of the 12th International Heat Transfer Conference, 2, 917, Elsevier (available on CD).

Laveille P., Delconte A., Blondel D., Lebouché M. and Lemoine F. (2004), *Non-intrusive temperature measurements using three-color laser-induced fluorescence*, Exp Fluids 36, 706-716.

Lippert A.M. and Reitz R.D. (1997), *Modelling of Multicomponent Fuels using Continuous Distributions with Application to Droplet Evaporation and Sprays*, SAE Technical Paper 972882.

Maqua C. (2007), *Contribution à la compréhension de l'évaporation de gouttes de combustible bi-composant à l'aide de méthodes optique*, Thèse, Nancy- Université.

Maqua C., Castanet G., Doué N., Lavergne G. and Lemoine F. (2006), *Temperature measurements of binary droplets using three color laser-induced fluorescence*, Exp. Fluids 40, 786797.

Maqua C., Castanet G., Grisch F., Lemoine F., Kristyadi T. and Sazhin S.S. (2008a), *Monodisperse droplet heating and evaporation: experimental study and modelling*, Int. J. Heat Mass Transfer 51, 3932–45.

Maqua C., Castanet G. and Lemoine F. (2008b), *Bi-component droplets evaporation: temperature measurements and modelling*, Fuel 87, 2932–2942.

Maxwell J.B. (1950), *Data book on hydrocarbons: application to process engineering*, New York: D. van Nostrand Company, INC.

Mehrotra A.K. (1994), *Correlation and prediction of the viscosity of pure hydrocarbon*, The Canadian Journal of Chemical Engineering 72, 554-557.

Michaelides E.E. (2006), *Particles, Bubbles and Drops*, Singapore: World Scientific.

Mitchell S.L., Vynnycky M., Gusev I.G. and Sazhin S.S. (2011), *An accurate numerical solution for the transient heating of an evaporating spherical droplet*, Applied Mathematics and Computation 217, 9219-9233.

Morin C., Chauveau C. and Gökalp I. (2000). *Droplet vaporisation characteristics of vegetable oil derived biofuels at high temperatures*. Exp. Therm. Fluid Sci. 21, 41–50.

Morsi S.A. and Alexander A.J. (1972), *An Investigation of Particle Trajectories in Two-Phase Flow Systems*. J. Fluid Mech., 55(2), 193–208.

NIST: http://webbook.nist.gov/chemistry/.

Nomura J., Ujiie Y., Rath H.J., Sato J., and Kono M. (1996), *Experimental Study on High Pressure Droplet Evaporation Using Microgravity Conditions*, 26th Int. Symposium on Combustion, The Combustion Institute, 1267-1273.

Poling B.E., Prausnitz J.M. and O'Connell J., (2000), *The Properties of Gases and Liquids*, New York: McGraw-Hill.

Polyanin A.D., Kutepov A.M., Vyazmin A.V. and Kazenin D.A. (2002), *Hydrodynamics mass and heat transfer in chemical engineering*, London and New York: Taylor and Francis.

Ra Y. and Reitz R.D., (2009), *A vaporization model for discrete multi-component fuel sprays*, Int. J. MultiPhase Flow 35, 101-117.

Reitz R.D. and Rutland C.J. (1995), *Development and Testing of Diesel Engine CFD Models*, Progress in Energy and Combustion Science 21, 173-196.

Rivard E. and Brüggemann D. (2010), *Numerical investigation of semi-continuous mixture droplet vaporization*, Chem. Eng. Sci. 65 5137–5145.

Sazhin S.S. (2006), *Advanced models of fuel droplet heating and evaporation*, Progress Energy Combustion Science 32, 162–214.

Sazhin S. S. (2009), *Modelling of Sprays Using Computational Fluid Dynamics Codes*, Pollack Periodica, 4(1), 5-16.

Sazhin S.S. and Krutitskii P.A. (2003), *A conduction model for transient heating of fuel droplets*, Proceedings of the 3d International ISAAC (International Society for Analysis, Applications and Computations) Congress (August 20 - 25, 2001, Berlin).

Sazhin S.S., Krutitskii P.A., Abdelghaffar W.A., Sazhina E.M., Mikhalovsky S.V., Meikle S.T. and Heikal M.R. (2004), *Transient heating of diesel fuel droplets*, Int. J. Heat Mass Transfer 47, 3327–3340.

Sazhin S.S., Abdelghaffar W.A., Krutitskii P.A., Sazhina E.M. and Heikal M.R. (2005a), *New approaches to numerical modelling of droplet transient heating and evaporation*, Int. J. Heat Mass Transfer 48, 4215–4228.

Sazhin, S.S., Abdelghaffar, W.A., Sazhina, E.M., and Heikal M.R. (2005b), *Models for droplet transient heating: Effects on droplet evaporation, ignition, and break-up*, Int. J. Thermal Sciences 44, 610-622.

Sazhin S.S., Kristyadi T., Abdelghaffar, W.A. and Heikal M.R. (2006), *Models for fuel droplet heating and evaporation: Comparative analysis*, Fuel 85, 1613–1630.

Sazhin S.S., Krutitskii P.A., Martynov S.B., Mason D., Heikal M.R. and Sazhina E.M. (2007), *Transient heating of a semitransparent spherical body*, Int. J. Thermal Sciences 46, 444-457.

Sazhin S. S., Martynov S. B., Kristyadi T., Crua C. and Heikal M. R. (2008), *Diesel fuel spray penetration, heating, evaporation and ignition: modelling versus experimentation*, Int. J. Engineering Systems Modelling and Simulation, 1-1, 1–19.

Sazhin S.S., Krutitskii P.A., Gusev I.G. and Heikal M.R. (2010a), *Transient heating of an evaporating droplet*, Int. J. Heat Mass Transfer 53, 2826–2836.

Sazhin S.S., Elwardany A.E., Krutitskii P.A., Castanet G., Lemoine F., Sazhina E.M. and Heikal M.R. (2010b), *A simplified model for bi-component droplet heating and evaporation*, Int. J. Heat Mass Transfer 53, 4495–4505.

Sazhin S.S., Shishkova I.N., Gusev I.G., Elwardany A., Krutitskii P.A. and Heikal M. (2010c) *Fuel droplet heating and evaporation: new hydrodynamic and kinetic models*, Proceedings of the 14th International Heat Transfer Conferences, Washington 8-13 August 2010, paper IHTC14-22320.

Sazhin S.S., Krutitskii P.A., Elwardany A., Castanet G., Lemoine F. and Heikal M. (2010d) *An analytical solution to the spherically symmetric species diffusion equation: application to modelling of heating and evaporation of bi-component droplets*, Proceedings of the ILASS--Europe 2010, Brno, Czech Republic, 6-8 September 2010, paper ID: 29.

Sazhin S.S., Elwardany A.E., Krutitskii P.A., Deprédurand V., Castanet G., Lemoine F., Sazhina E.M. and Heikal M.R. (2011a), *Multi-component droplet heating and evaporation: numerical simulation versus experimental data*, Int. J. Thermal Sciences, 50, 1164-1180.

Sazhin S.S., Shishkova I.N., Elwardany A., Gusev I.G. and Heikal M. (2011b) *Modelling of droplet heating and evaporation: recent results and unsolved problems*, Journal of Physics, Conference Series, International Workshop on Multi-Rate Processes & Hysteresis in Mathematics, Physics and Information Sciences. University of Pecs, Hungary, May 31 - June 3, 2010 . Published by Institute of Physics (UK).

Sazhin S.S., Elwardany A.E., Sazhina E.M. and Heikal M.R. (2011c), *A quasi-discrete model for heating and evaporation of complex multi-component hydrocarbons fuel droplets*, Int. J. Heat Mass Transfer, 54, 4325-4332.

Sazhin S.S., Krutitskii P.A., Gusev I.G. and Heikal M.R. (2011d), *Transient heating of an evaporating droplet with presumed time evolution of its radius*, Int. J. Heat Mass Transfer, 54 (5-6), 1278-1288.

Sazhina E.M., Sazhin S.S., Heikal M.R., Babushok V.I. and Johns R. (2000), *A detailed modelling of the spray ignition process in diesel engines*, Combustion Science Technology 160, 317–344.

Sirignano W.A. (1983), *Fuel droplet vaporization and spray combustion theory*, Progress in Energy and Combustion Science 9, 291–322.

Sirignano W.A. (1999), *Fluid Dynamics and Transport of Droplets and Sprays*, Cambridge University press.

Sirignano W.A. and Wu G. (2008), *Multicomponent-liquid-fuel vaporization with complex configuration*, Int. J. Heat Mass Transfer 51, 4759–4774.

Stengele J., Willmann M. and Wittig S. (1997), *Experimental and theoretical study of droplet vaporization in high pressure environment*, ASME Paper 97-GT-151.

Tamim J. and Hallett W.L.H. (1995), *Continuous thermodynamics model for multicomponent vaporization*, Chemical Engineering Science 50, 2933–2942.

Tong A.Y. and Sirignano W.A. (1986), *Multicomponent transient droplet vaporization with internal circulation: integral equation formulation*, Numer. Heat Transfer 10, 253–278.

Tonini S., Gavaises M. and Theodorakakos A. (2008), *Modelling of high-pressure dense diesel sprays with adaptive local grid refinement*, Int. J. Heat and Fluid Flow 29, 427-448.

van Beeck J. and Riethmuller M. (1997), *Rainbow interferometry with wire diffraction for simultaneous measurement of droplet temperature, size and velocity*. Part Part Syst Charact 14, 186-192.

van Miltenburg J.C. (2000), *Fitting the heat capacity of liquid n-alkanes: new measurements of n-heptadecane and n-octadecane*, Thermochimica Acta (343) 57-62.

Yaws C.L. (1995), *Handbook of thermal conductivity,* Vol (2): Organic compounds, $C_5$ to $C_7$ and Vol (3): Organic compounds, $C_8$ to $C_{28}$. Gulf Publishing Company, Houston, London, Paris, Zurich, Tokyo.

Yaws C.L. (Editor), (2008), *Thermophysical properties of chemicals and hydrocarbons*, William Andrew Inc.

Zhang L. and Kong S-C. (2009), *modelling of multi-component fuel vaporization and combustion for gasoline and diesel spray*, Chemical Engineering Science 64, 3688-3696.

Zhang L. and Kong S-C. (2010), *Vaporization modeling of petrolium-biofuel drop using a hybrid multi-component approach*, Combustion and Flame 157, 2165-2174

Zhu G-S. and Reitz R.D. (2002), *A model for high-pressure vaporization of droplets of complex liquid mixtures using continuous thermodynamics*, Int. J. Heat Mass Transfer 45, 495–507.

# Appendices

## Appendix A. Binary diffusion coefficient for fuel vapour

The binary diffusion coefficient for fuels (Chapter 3) was estimated using the following equation (Bird et al, 2002):

$$D_v = 1.8583 \times 10^{-7} \sqrt{T^3 \left(\frac{1}{M_v} + \frac{1}{M_a}\right)} \frac{1}{p\sigma_{va}^2 \Omega_D(T^*)} \ , \qquad \text{(A.1)}$$

where $D_v$ is in m$^2$/s, $T$ is temperature in K, $p$ is in atm (1 atm = 0.101 MPa), $\sigma_{va} = (\sigma_v + \sigma_a)/2$ is the minimal distance between molecules in Angstrom, $\Omega_D$ is the collision integral, the values of which depends on the normalised temperature $T^* = k_B T/\varepsilon_{va}$, $k_B$ is the Boltzmann constant, $\varepsilon_{va} = \sqrt{\varepsilon_v \varepsilon_a}$; the subscript $_a$ indicates air. Note that the formula for the binary diffusion coefficient used by Poling et al (2000) differs from the one presented above in terms of the value of the coefficient (they used 1.8623 instead of 1.8583). The difference between the values of this coefficient predicted by two formulae (0.2%) can be safely ignored in most practical applications. Note that there is a typo in Eq. (B5) of Sazhin et al (2006). $\sigma_a = 3.617$ Angstrom, $\varepsilon_a/k_B = 97.0$ K (see Table E.1 in Bird et al, 2002).

Once the value of $T^*$ had been found, the collision integral $\Omega_D$ could be obtained from Table E.2 of Bird et al (2002). However, it is more convenient to use the analytical approximation of $\Omega_D$ given by the following equation (Poling et al, 2000; Bird et al, 2002):

$$\Omega_D = \frac{1.06036}{(T^*)^{0.15610}} + \frac{0.19300}{\exp(0.47635T^*)} + \frac{1.03587}{\exp(1.52996T^*)} + \frac{1.76474}{\exp(3.89411T^*)}. \qquad \text{(A.2)}$$

For the binary diffusion coefficient of n-decane ($C_{10}H_{22}$) the following approximation was used (Abramzon and Sazhin, 2006):

$$D_v = 5.46 \times 10^{-6} \frac{1}{1.01p} \left(\frac{T}{300}\right), \qquad \text{(A.3)}$$

where $p$ is in atm, as in Eq. (A.1).

| Fuel | Ref. | Formula | Molar mass (kg/kmol) | Boiling temperature (K) | Critical Temperature (K) | $\sigma_f$ (Angstrom) | $\varepsilon_f/k_B$ (K) |
|---|---|---|---|---|---|---|---|
| **Acetone** | Bird et al (200) and Poling et al (2000) | $C_3H_6O$ | 58.080 | 329.22 | 508.1 | 4.600 | 560.2 |
| **Ethanol** | | $C_2H_6O$ | 46.069 | 351.8 | 516.2 | 4.530 | 362.6 |
| **n-Heptane** | | $C_7H_{16}$ | 100.204 | 371.4 | 540.17 | 5.949 | 399.3 |
| **3-Pentanone** | | $C_5H_{10}O$ | 86.134 | 375.14 | 561.5 | 4.22 | 351.562 |
| **n-Dodecane** | | $C_{12}H_{26}$ | 170.338 | 489.48 | 658 | 6.5972 | 454.6768 |
| **n-Decane** | | $C_{10}H_{22}$ | 142.29 | 477.3 | 617.3 | 7.38 | 548.895 |
| **n-Octane** | | $C_8H_{18}$ | 114.23 | 398.82 | 568.7 | 7.035 | 361 |

Table A.1 The values of molar masses, boiling temperatures, critical temperatures, $\sigma_f$ and $\varepsilon_f/k_B$ for acetone, ethanol, n-heptane, 3-pentanone, n-dodecane, n-decane and n-octane, as inferred from various sources.

## Appendix B. Physical properties of fuels and air

### *Appendix B1. Physical properties of acetone*

Liquid thermal conductivity in W/(m.K) is approximated as (Maqua, 2007)

$$k_{l,ac} = 0.3133614225 - 0.8163 \times 10^{-3} \times T + 0.1 \times 10^{-5} \times T^2. \quad \text{(B.1)}$$

Liquid dynamic viscosity in Pa.s is approximated as (Maqua, 2007)

$$\mu_{l,ac} = 0.3183313525 \times 10^{-2} - 0.16297359 \times 10^{-4} \times T + 0.223333 \times 10^{-4} \times T^2. \quad \text{(B.2)}$$

Specific heat capacity of liquid in J/(kg.K) is approximated as (Maqua, 2007)

$$c_{l,ac} = 2165.234225 - 2.963 \times T + 0.01 \times T^2. \quad \text{(B.3)}$$

Density of the liquid in kg/m$^3$ is approximated as (Maqua, 2007)

$$\rho_{l,ac} = 986.5303588 - 0.6014966034 \times T - 0.2754046133 \times 10^{-3} \times T^2. \quad \text{(B.4)}$$

Vapour thermal conductivity in W/(m.K) is approximated as (Maqua, 2007)

$$k_{v,ac} = 0.1143468 \times \left(\frac{T}{273.15}\right)^{2-0.3428433650 \times T^2}. \quad \text{(B.5)}$$

Vapour dynamic viscosity in Pa.s is approximated as (Maqua, 2007)

$$\mu_{v,ac} = -0.44932 \times 10^{-11} \times T^2 + 0.3090958 \times 10^{-7} \times T - 0.157988444 \times 10^{-5}. \quad \text{(B.6)}$$

Specific heat capacity of vapour in J/(kg.K) is approximated as (Maqua, 2007)

$$c_{p,v,ac} = 7.047344 \times 10^{-6} \times T^3 - 9.9229425 \times 10^{-3} \times T^2 + 8.211229 \times T - 458.00814. \quad \text{(B.7)}$$

Density of the vapour in kg/m$^3$ is approximated as (Maqua, 2007)

$$\rho_{v,ac} = \frac{707.7943354}{T}. \quad \text{(B.8)}$$

Latent heat of vaporization in J/kg is approximated as (Deprédurand, 2009)

$$L_{ac} = 489 \times 10^3 \times \left(\frac{T_{cr}-T}{T_{cr}-T_b}\right)^{0.38}, \quad \text{(B.9)}$$

when $T < T_{cr}$ and zero otherwise, where $T$ is in K.

### *Appendix B2. Physical properties of ethanol*

Liquid thermal conductivity in W/(m.K) is approximated as (Deprédurand, 2009)

$$k_{l,eth} = 0.61572 - 0.24127\times10^{-2}\times T + 0.31333\times10^{-5}\times T^2. \quad \text{(B.10)}$$

Liquid dynamic viscosity in Pa.s is approximated as (Deprédurand, 2009)

$$\mu_{l,eth} = 10^{\left(\frac{686.64}{T}-5.282\right)}. \quad \text{(B.11)}$$

Specific heat capacity of liquid in J/(kg.K) is approximated as (Deprédurand, 2009)

$$c_{l,eth} = 15039 - 130.53\times T + 0.4143\times T^2 - 0.39583\times T^3. \quad \text{(B.12)}$$

Density of the liquid in kg/m$^3$ is approximated as (Deprédurand, 2009)

$$\rho_{l,eth} = 1053.6 - 0.925 \times T. \quad \text{(B.13)}$$

Vapour thermal conductivity in W/(m.K) is approximated as (Deprédurand, 2009)

$$k_{v,eth} = 1.8037\times10^{-3} + 7.419\times10^{-6}\times T + 1.1536\times10^{-7}\times T^2. \quad \text{(B.14)}$$

Vapour dynamic viscosity in Pa.s is approximated as (Deprédurand, 2009)

$$\mu_{v,eth} = 0.29211\times10^{-7}\times T - 0.19757\times10^{-6}. \quad \text{(B.15)}$$

Specific heat capacity of vapour in J/(kg.K) is approximated as (Deprédurand, 2009)

$$c_{p,v,eth} = 469.67 + 4.2301 \times T - 1.5571 \times 10^{-3} \times T^2. \quad \text{(B.16)}$$

Density of the vapour in kg/m$^3$ is approximated as (Deprédurand, 2009)

$$\rho_{v,eth} = 0.5541 \times 10^{-2} \times \frac{p_{gas}}{T}. \quad \text{(B.17)}$$

Latent heat of vaporization in J/kg is approximated as (Deprédurand, 2009)

$$L_{eth} = 120.91 \times 10^3 \times (T_{cr} - T)^{0.38}, \quad \text{(B.18)}$$

when $T < T_{cr}$ and zero otherwise, where $T$ is in K.

***Appendix B3. Physical properties of n-decane***

Liquid thermal conductivity in W/(m.K) is approximated as (Abramzon and Sazhin, 2006)

$$k_{l,n-dec} = 0.1334 - 0.000237 \times (T - 300). \quad \text{(B.19)}$$

Liquid dynamic viscosity in Pa.s is approximated as (Abramzon and Sazhin, 2006)

$$\mu_{l,n-dec} = 0.001 \times \exp\left(4.803 \times \frac{300}{T} - 5.0276\right). \quad \text{(B.20)}$$

Specific heat capacity of liquid in J/(kg.K) is approximated as (Abramzon and Sazhin, 2006)

$$c_{l,n-dec} = 1000 \times \left(2.138 + 0.0021 \times (T - 300)\right). \quad \text{(B.21)}$$

Density of the liquid in kg/m$^3$ is approximated as (Abramzon and Sazhin, 2006)

$$\rho_{l,n-dec} = 724.74 - 0.8081 \times (T - 300). \quad \text{(B.22)}$$

Vapour thermal conductivity in W/(m.K) is approximated as (Abramzon and Sazhin, 2006)

$$k_{v,n-dec} = 0.012142 \times \left(\frac{T}{300}\right)^{1.8}. \quad \text{(B.23)}$$

Vapour dynamic viscosity in Pa.s is approximated as (Abramzon and Sazhin, 2006)

$$\mu_{v,n-dec} = 10^{-5} \times \left(0.564 + 0.00175 \times (T - 300)\right). \quad \text{(B.24)}$$

Specific heat capacity of vapour in J/(kg.K) is approximated as (Abramzon and Sazhin, 2006)

$$c_{p,v,n-dec} = 10^3 \times \left(0.0209 \times \left(\frac{\mathrm{T}}{300}\right)^3 - 0.3296 \times \left(\frac{\mathrm{T}}{300}\right)^2 + 2.0135 \times \left(\frac{\mathrm{T}}{300}\right) - 0.0471\right). \quad \text{(B.25)}$$

Density of the vapour in kg/m$^3$ is approximated as (Deprédurand, 2009)

$$\rho_{n-dec,v} = 0.01711 \times \frac{P_g}{T}. \quad \text{(B.26)}$$

Latent heat of vaporization in J/kg is approximated as (Abramzon and Sazhin, 2006)

$$L_{n-dec} = 39.578 \times 10^3 \times (T_{cr} - T)^{0.38}, \quad \text{(B.27)}$$

when $T < T_{cr}$ and zero otherwise, where $T$ is in K.

***Appendix B4. Physical properties of 3-pentanone***

Liquid thermal conductivity in W/(m.K) is approximated as (Deprédurand, 2009)

$$k_{l,3-pen} = 0.19859 - 0.000095781 \times T - 0.00000031088 \times T^2. \quad \text{(B.28)}$$

Liquid dynamic viscosity in Pa.s is approximated as (Deprédurand, 2009)

$$\mu_{l,3-pen} = 0.001 \times \exp\left(\frac{979.8}{T} - 4.123\right). \quad \text{(B.29)}$$

Specific heat capacity of liquid in J/(kg.K) is approximated as (Deprédurand, 2009)

$$c_{l,3-pen} = 1000 \times (-1.85557 + 0.025782 \times T - 0.00004 \times T^2) . \quad \text{(B.30)}$$

Density of the liquid in kg/m$^3$ is approximated as (Deprédurand, 2009)

$$\rho_{l,3-pen} = 1142 - 1.1042 \times T. \quad \text{(B.31)}$$

Vapour thermal conductivity in W/(m.K) is approximated as (Deprédurand, 2009)

$$k_{v,3-pen} = 0.00000012351 \times \mathrm{T}^2 - 0.000004287 \times \mathrm{T} + 0.0015107. \quad \text{(B.32)}$$

Vapour dynamic viscosity in Pa.s is approximated as (Deprédurand, 2009)

$$\mu_{v,3-pen} = 10^{-6} \times (-0.51069 + 0.024793 \times T - 0.0000041232 \times T^2). \quad \text{(B.33)}$$

Specific heat capacity of vapour in J/(kg.K) is approximated as (Deprédurand, 2009)

$$c_{p,v,3-pen} = -0.0014539 \times \mathrm{T}^2 + 4.1145 \times \mathrm{T} + 430.42 . \quad \text{(B.34)}$$

Density of the vapour in kg/m$^3$ is approximated as (Deprédurand, 2009)

$$\rho_{3-pen,v} = \frac{p_g}{(8.314/(0.086134 \times T))} . \quad \text{(B.35)}$$

Latent heat of vaporization in J/kg is approximated as (Deprédurand, 2009)

$$L_{3-pen} = \frac{10^6}{86.134} \times (-0.000046310709 \times T^2 - 0.03468689 \times T + 52.97188), \quad \text{(B.36)}$$

when $T < T_{cr}$ and zero otherwise, where $T$ is in K.

***Appendix B5. Physical properties of n-heptane***

Liquid thermal conductivity in W/(m.K)is approximated using data from Maxwell, (1950) and presented as Sazhin et al (2006)

$$k_{l,n-hep} = 0.122 - 0.137 \times \tilde{T} , \quad \text{(B.37)}$$

where $\tilde{T} = \frac{T-300}{300}$ is the normalized temperature.

Liquid dynamic viscosity in Pa.s is approximated as (Deprédurand, 2009)

$$\mu_{l,n-hep} = 10^{-2} \times (-0.000002003 \times T^3 + 0.001847595 \times T^2 - 0.563410432 \times T + 57.27836218). \quad \text{(B.38)}$$

Specific heat capacity of liquid in J/(kg.K) is approximated following Maxwell (1950) and Sazhin et al (2006)

$$c_{l,n-hep} = 2.25 \times 10^3 + 1.11 \times 10^3 \times \tilde{T} + 1.87 \times 10^3 \times \tilde{T}^2 - 4.89 \times 10^3 \times \tilde{T}^3 + 5.16 \times 10^3 \times \tilde{T}^4 . \quad \text{(B.39)}$$

Density of the liquid in kg/m$^3$ is approximated following Maxwell (1950) and Sazhin et al. (2006)

$$\rho_{l,n-hep} = 678.93 - 248.73 \times \tilde{T} - 251.16 \times \tilde{T}^2 + 735.16 \times \tilde{T}^3 - 882.37 \times \tilde{T}^4, \quad (B.40)$$

when $\tilde{T} \leq 0.793$ , and

$$\rho_{l,n-hep} = -3.16 \times 10^5 + 8.04 \times 10^5 \times \tilde{T} - 5.1 \times 10^5 \times \tilde{T}^2 , \quad (B.41)$$

when $\tilde{T} > 0.793$.

Vapour thermal conductivity in W/(m.K) is approximated as (Maxwell, 1950)

$$k_{v,n-hep} = 4.3933 \times 10^{-9} \times T^3 - 5.4311 \times 10^{-6} \times T^2 + 2.3685 \times 10^{-3} \times T - 0.33101 , \quad (B.42)$$

when $> 373$ K , and

$$k_{v,n-hep} = 7.5 \times 10^{-5} \times T^2 + 2.6 \times 10^{-2} \times T + 4.19 , \quad (B.43)$$

when $T \leq 373$ K.

Vapour dynamic viscosity in Pa.s is approximated as (Deprédurand, 2009)

$$\mu_{v,n-hep} = 10^{-6} \times (-0.43965 + 0.022776 \times T - 0.0000039093 \times T^2). \quad (B.44)$$

Specific heat capacity of vapour in J/(kg.K) is approximated as (Maxwell, 1950)

$$c_{p,v,3-pen} = 1662.5 + 1.28 \times 10^3 \times \tilde{T} + 121.75 \times \tilde{T}^2 - 240.64 \times \tilde{T}^3 + 52.22 \times \tilde{T}^4. \quad (B.45)$$

Density of the vapour in kg/m$^3$ is approximated as (Deprédurand, 2009)

$$\rho_{n-hep,v} = \frac{0.100205 \times 101325}{8.314 \times T} . \quad (B.46)$$

Latent heat of vaporization in J/kg is approximated as (Deprédurand, 2009)

$$L_{n-hep} = 317.8 \times 10^3 \left(\frac{\tilde{T}_{cr} - \tilde{T}}{\tilde{T}_{cr} - \tilde{T}_b}\right)^{0.38}, \quad (B.47)$$

when $\tilde{T} < \tilde{T}_{cr}$ and zero otherwise, $\tilde{T}_{cr} = 0.8$ and $\tilde{T}_b = 0.238$ (Poling et al, 2000).

### *Appendix B6. Physical properties of n-dodecane*

The properties of n-dodecane used in Chapter 3 are as follows:

Liquid thermal conductivity in W/(m.K)is approximated as (Deprédurand, 2009)

$$k_{l,n-dodec} = 0.1405 - 0.00022 \times (T - 300). \quad (B.48)$$

Liquid Dynamic viscosity in Pa.s is approximated as (Deprédurand, 2009):

$$\mu_{l,n-dodec} = 0.001 \times \exp\left(631.63 \times \left(\frac{1}{T} - \frac{1}{318.78}\right)\right). \quad (B.49)$$

Specific heat capacity of liquid in J/(kg.K) is approximated as (Maxwell, 1950; Sazhin et al, 2006)

$$c_{l,n-dodec} = 2172.5 + 1260.5 \times \tilde{T} - 63.38 \times \tilde{T}^2 + 45.17 \times \tilde{T}^3. \quad (B.50)$$

Density of the liquid in kg/m$^3$ is approximated as (Maxwell, 1950)

$$\rho_{l,n-dodec} = 744.96 - 230.42 \times \tilde{T} + 40.90 \times \tilde{T}^2 - 88.7 \times \tilde{T}^3. \quad \text{(B.51)}$$

Latent heat of vaporization in J/kg is approximated as (Poling et al, 2000)

$$L_{n-dodec} = 4.45 \times 10^5 + 334.92 \times \tilde{T} + 1.01 \times 10^5 \times \tilde{T}^2 + 9.96 \times 10^4 \times \tilde{T}^3 - 1.17 \times 10^5 \times \tilde{T}^4. \quad \text{(B.52)}$$

when $\tilde{T} < \tilde{T}_{cr}$ and zero otherwise.

***Appendix B7. Physical properties of air***

Air thermal conductivity in W/(m.K) is approximated as (Incropera and DeWitt, 2002)

$$k_a = 10^{-3} \times (-0.00006 \times T^2 + 0.113 \times T - 2.2), \quad \text{(B.53)}$$

where 250 K $\leq T \leq$ 350 K, and it is approximated as (Incropera and DeWitt, 2002)

$$k_a = 10^{-3} \times (-0.00000000125 \times T^4 + 0.00000244918 \times T^3 - 0.00153675321 \times T^2 + 0.43343841945 \times T - 22.50161033466), \quad \text{(B.54)}$$

where 250 K $\leq T \leq$ 800 K.

Air dynamic viscosity in Pa.s is approximated (Incropera and DeWitt, 2002)

$$\mu_a = 10^{-7} \times (-0.00028 \times T^2 + 0.654 \times T + 13.6), \quad \text{(B.55)}$$

where 250 K $\leq T \leq$ 350 K, and it is approximated as (Incropera and DeWitt, 2002)

$$\mu_a = 10^{-7} \times (-0.00019342657 \times T^2 + 0.58086013986 \times T + 27.72412587413), \quad \text{(B.56)}$$

where 250 K $\leq T \leq$ 800 K.

Specific heat capacity of air in J/(kg.K) is approximated as (Incropera and DeWitt, 2002)

$$c_{p,a} = 10^{-3} \times (0.0000002 \times T^2 - 0.00009 \times T + 1.016), \quad \text{(B.57)}$$

where 250 K $\leq T \leq$ 350 K, and it is approximated as (Incropera and DeWitt, 2002)

$$c_{p,a} = 10^{-3} \times (-0.00000000044 \times T^3 + 0.00000092454 \times T^2 - 0.00040771821 \times T + 1.05729181929), \quad \text{(B.58)}$$

where 250 K $\leq T \leq$ 800 K.

Density of air in kg/m$^3$ is approximated as (Incropera and DeWitt, 2002)

$$\rho_a = 0.0000134 \times T^2 - 0.012025 \times T + 3.5647, \quad \text{(B.59)}$$

where 250 K $\leq T \leq$ 350 K, and it is approximated as (Incropera and DeWitt, 2002)

$$\rho_a = -0.00000000685 \times T^3 + 0.00001408584 \times T^2 - 0.01034857135 \times T + 3.19595945166, \quad \text{(B.60)}$$

where $250\ \text{K} \leq T \leq 800\ \text{K}$.

## Appendix C. Physical properties for a mixture

### *Appendix C1. Liquid thermal conductivity for a mixture*

A number of approximate formulae for thermal conductivity in multi-component liquids are reviewed in Poling et al (2000). The simplest Filippov equation, valid for binary mixtures, was used in Chapter 3:

$$k_l = Y_1 k_{l1} + Y_2 k_{l1} - 0.72 Y_1 Y_2 |k_{l1} - k_{l2}|, \quad \text{(C.1)}$$

where $Y_1$ and $Y_2$ are mass fractions for species 1 and 2, $k_{l1}$ and $k_{l2}$ are thermal conductivities of species 1 and 2.

For Chapters 4-6, the Vredeveld equation, valid for non-aqueous systems in which the ratio of thermal conductivities does not exceed two, was used:

$$k_l = (\textstyle\sum_i Y_i k_{li}^{-2})^{-1/2}, \quad \text{(C.2)}$$

where $Y_i$ are mass fractions for species $i$, $k_{li}$ are thermal conductivities of species $i$.

### *Appendix C2. Liquid kinematic viscosity for a mixture*

A number of approximate formulae for dynamic viscosity of multi-component liquids ($\mu_l$) are reviewed by Poling et al (2000). It was shown that the approach suggested by Grunberg and Nissan is the most accurate and convenient in practical applications. In the case of a bi-component liquid, this approach is based on the following equation:

$$\ln \mu_l = X_1 \ln \mu_{l1} + X_2 \ln \mu_{l2} - G_{12} X_1 X_2, \quad \text{(C.3)}$$

where $X_{1,2}$ are molar fractions of species 1 and 2. The values of $G_{12}$ depend on the type of species involved (Poling et al, 2000). In this study, following Maqua (2007), we use a simplified version of Eq. (C.3) assuming that $G_{12} = 0$. In this case Eq. (C.3) is simplified to:

$$\mu_l = \exp(X_1 \ln \mu_{l1} + X_2 \ln \mu_{l2}). \quad \text{(C.4)}$$

The kinematic viscosity is obtained from Eq. (C.4) by dividing $\mu_l$ by $\rho_l$ which is calculated as follows:

$$\rho_l = \left(\frac{Y_1}{\rho_{l1}} + \frac{Y_2}{\rho_{l2}}\right)^{-1}, \quad \text{(C.5)}$$

where $Y_1$ and $Y_2$ are mass fractions for species 1 and 2, $\rho_{l1}$ and $\rho_{l2}$ are liquid densities of species 1 and 2.

### *Appendix C3. Specific heat capacity for a mixture*

The specific heat capacity of the mixture $c_l$ was estimated as

$$c_l = \sum_i Y_i\, c_{li}, \quad \text{(C.6)}$$

where $Y_i$ are mass fractions for species $i$, $c_{li}$ are specific heat capacities of species $i$.

### *Appendix C4. Liquid diffusivity for a mixture*

As in the case of liquid thermal conductivity and liquid viscosity, various approximations for liquid diffusivity for a mixture were discussed in Poling et al (2000). One of the simplest approximations was given by the Sanchez and Clifton formula:

$$D_{12} = [X_1 D_{12}^0 + X_2 D_{21}^0](1 - \overline{m} + \overline{m}\bar{a}), \quad \text{(C.7)}$$

where the parameter $\overline{m}$ is to be found from one mixture datum point, $\bar{a}$ is the thermodynamic factor defined as:

$$\bar{a} = \left.\frac{\partial a_1}{\partial X_1}\right|_{T,P} = \left.\frac{\partial a_2}{\partial X_2}\right|_{T,P}.$$

$a_{1,2}$ are the activities of species 1 and 2, $D_{12}^0$ and $D_{21}^0$ are diffusivities of dilute solute 1 in solvent 2, and dilute solute 2 in solvent 1.

Since both $\overline{m}$ and $\bar{a}$ are close to 1, Formula (C.7) can be simplified to:

$$D_{12} = X_1 D_{12}^0 + X_2 D_{21}^0. \quad \text{(C.8)}$$

Among various approximations for $D_{12}^0$ and $D_{21}^0$ we have chosen the Wilke–Chang approximation given by the following formula:

$$D_{AB}^0 = \frac{7.4\times10^{-12}\sqrt{\varphi M_B}T}{\mu_B V_A^{0.6}}, \quad \text{(C.9)}$$

where $D_{AB}^0$ is the mutual diffusion coefficient of solute $A$ at very low concentrations in solvent $B$, m$^2$/s, $M_B$ is the molar mass of solvent $B$, kg/kmol, $T$ temperature in K, $\mu_B$ dynamic viscosity of solvent $B$, cP (1 cP = $10^{-3}$ kg m$^{-1}$ s$^{-1}$), $V_A$ is the molar volume of solute $A$ at its normal boiling temperature, cm$^3$/mol calculated as in Eq. (4.35), $\varphi$ is the associated factor of solvent $B$ ($\varphi = 1.5$ if $B$ is ethanol, $\varphi = 1$ if $B$ is acetone).

When calculating $D_{12}$ based on Eq. (C.8) the values of $X_1$, $X_2$ and $T$, averaged over the whole volume of droplets, were used. These parameters were updated at each timestep.

### *Appendix C5. Latent heat of vaporization for a mixture*

The latent heat of vaporization of a mixture $L$ was estimated as (Sazhin, 2006)

$$L = \sum_i \epsilon_i L_i \,, \tag{C.10}$$

where $\epsilon_i = \epsilon_i(t)$ is the evaporation rate of species $i$, calculated based on Eq. (3.4), $L_i$ is the latent heat of vaporization of species $i$.

### *Appendix C6. Heat conductivity and dynamic viscosity of gaseous mixture*

The thermal heat conductivity of a gaseous mixture was estimated as (Maqua, 2007)

$$k_{mix} = \sum_{i=1}^{N} \left(\frac{x_i k_i}{S_i}\right), \tag{C.11}$$

and the dynamic viscosity of a gaseous mixture was estimated as (Maqua, 2007):

$$\mu_{mix} = \sum_{i=1}^{N} \left(\frac{x_i \mu_i}{S_i}\right), \tag{C.12}$$

$$S_i = \sum_{j=1}^{N} x_j A_{ij}, \tag{C.13}$$

$$A_{ij} = \frac{\left[1+\sqrt{\mu_i M_j/\mu_j M_i}\left(M_i/M_j\right)^{1/4}\right]^2}{\sqrt{8\left(1+\frac{M_i}{M_j}\right)}}, \tag{C.14}$$

where $x_i$ are molar fractions for species $i$, $k_i$ are thermal heat conductivities of species $i$, $\mu_i$ are dynamic viscosities of species $i$ and $M_i$ are molar masses of the species $i$.

## Appendix D. The Sturm-Liouville problem

In what follows, the details of the solution to Eq. (4.4) ($Y_{li}(t,R)$) for $t \geq 0$ and $0 \leq R < R_d$ are given. Remembering the physical background of the problem, we will look for a solution which is continuously differentiable twice in the whole domain.

Rewriting the boundary condition (4.5) in the form:

$$\left(\frac{\partial Y_{li}}{\partial R} - \frac{\alpha}{D_l} Y_{li}\right)\Big|_{R=R_d} = -\frac{\alpha \epsilon_i(t)}{D_l} \,. \tag{D.1}$$

The initial condition is $Y_{li}(t = 0) = Y_{li0}(R)$.

We look for the solution to Eq. (4.4) in the form:

$$Y_{li}(t, R) = y(t, R) + \epsilon(t), \tag{D.2}$$

where the subscript *i* at ϵ is omitted to simplify the notation.

Having substituted (D.2) into Eq. (4.4) and the boundary condition (D.1) we can rewrite this equation and the corresponding boundary and initial conditions in the form:

$$\frac{\partial y}{\partial t} = D_l \left(\frac{\partial^2 y}{\partial R^2} + \frac{2}{R}\frac{\partial y}{\partial R}\right) - \frac{d\epsilon(t)}{dt}, \tag{D.3}$$

$$\left(\frac{\partial y}{\partial R} - \frac{\alpha}{D_l} y\right)\Big|_{R=R_d} = 0, \tag{D.4}$$

$$y|_{t=0} = Y_{li0}(R) - \epsilon(0) \equiv Y_{li0}(R) - \epsilon_0 . \tag{D.5}$$

Introduction of the new variable, following Sazhin et al (2004),

$$u(t, R) = y(t, R)R$$

allows the rewriting of Eq. (D.3) and the corresponding boundary and initial conditions in the form:

$$\frac{\partial u}{\partial t} = \mathrm{D}_l \frac{\partial^2 u}{\partial R^2} - R\frac{d\epsilon(t)}{dt}, \tag{D.6}$$

$$u|_{R=0} = \left(\frac{\partial u}{\partial R} + \frac{h_0}{R_d} u\right)\Big|_{R=R_d} = 0, \tag{D.7}$$

$$u|_{t=0} = R(Y_{li0}(R) - \epsilon_0) , \tag{D.8}$$

where:

$$h_0 = -\left(1 + \frac{\alpha R_d}{\mathrm{D}_l}\right).$$

Note that the change of the variable from *y* to *u* leads to the need for a second boundary condition at $R = 0$. The assumption that the solution is continuously differentiable twice implies that *y* is finite everywhere in the domain $0 \le R < R_d$. Hence, the boundary condition (D.7) at $R = 0$. The solution to the problem (D.6) - (D.8) for $h_0 > -1$ was earlier reported by Sazhin et al (2004). Here the focus will be on the case $h_0 < -1$, which is directly relevant to the problem of diffusion of species inside droplets.

We look for the solution to Eq. (D.6) in the form:

$$u = \sum_{n=0}^{\infty} \Theta_n(t) v_n(R), \tag{D.9}$$

where $v_n(R)$ is the full set of non-trivial solutions to the equation:

$$\frac{\partial^2 v}{\partial R^2} + pv = 0, \tag{D.10}$$

subject to the boundary conditions:

$$v|_{R=0} = \left(\frac{\partial v}{\partial R} + \frac{h_0}{R_d} v\right)\Big|_{R=R_d} = 0. \quad \text{(D.11)}$$

Eq. (D.10) with boundary conditions (D.11) is the well known Sturm-Liouville problem. The first task is to find eigen values $p$ for this problem. The cases $p = 0$, $p < 0$ and $p > 0$ will be considered separately.

***The Sturm-Liouville problem for p = 0***

For $p = 0$ the general solution to Eq. (D.10) can be presented as $v = A+BR$. The condition $v|_{R=0} = 0$ implies that $A = 0$. The boundary condition at $R = R_d$ leads to the following equation $B(1+h_0) = 0$. Since $h_0 \in (-\infty, -1)$, the latter equation is satisfied only when $B = 0$. This leads to the trivial solution $v = 0$ which is disregarded in our analysis. Hence, Eq. (D.10) has no non-trivial solutions for $p = 0$.

***The Sturm-Liouville problem for p < 0***

Assuming that $p = -\lambda^2 < 0$ we write the general solution to (D.10) as:

$$v(R) = A\cosh\left(\lambda\frac{R}{R_d}\right) + B\sinh\left(\lambda\frac{R}{R_d}\right), \quad \text{(D.12)}$$

where $A$ and $B$ are arbitrary constants.

The boundary condition at $R = 0$ (see (D.11)) implies that $A = 0$. The boundary condition at $R = R_d$ leads to the following equation:

$$\frac{B}{R_d}(\lambda\cosh\lambda + h_0\sinh\lambda) = 0. \quad \text{(D.13)}$$

$B$ in this equation is not equal to zero as we do not consider the trivial solution $v = 0$. Hence, Eq. (D.12) can be re-written as:

$$\tanh\lambda = -\frac{\lambda}{h_0}. \quad \text{(D.14)}$$

It is easy to show that for $h_0 \in (-\infty, -1)$ Eq. (D.14) has three solutions $\lambda = 0; \pm\lambda_0$, where $\lambda_0 \in (0, +\infty)$, and it has no solutions for $h_0 > -1$. The solution $\lambda = 0$ leads to the trivial solution $v = 0$, which is disregarded in our analysis. The solutions $\lambda = \pm\lambda_0$ lead to Solutions (D.12) (eigen functions) which differ only by the sign of $B$. Since the value of the coefficient $B$ is determined by the normalisation condition only (see below), the solution $\lambda = -\lambda_0$ can be disregarded. Hence, we can conclude that the solution of Eq. (D.14) gives only one eigen value $\lambda = \lambda_0 > 0$ and the corresponding eigen function

$$v_0(R) = \sinh\left(\lambda_0\frac{R}{R_d}\right), \quad \text{(D.15)}$$

where the normalisation leading to $B = 1$ has been chosen.

The direct calculation of the integrals, taking into account Condition (D.14), leads to the following expression for the norm of $v_0$:

$$\|v_0\|^2 = \int_0^{R_d} v_0^2(R)dR = -\frac{R_d}{2}\left[1 + \frac{\mathrm{h_0}}{h_0^2 - \lambda_0^2}\right]. \quad \text{(D.16)}$$

***The Sturm-Liouville problem for p > 0***

Assuming that $p = \lambda^2 > 0$ we write the general solution to (D.10) as:

$$v(R) = A\cos\left(\lambda\frac{R}{R_d}\right) + B\sin\left(\lambda\frac{R}{R_d}\right), \quad \text{(D.17)}$$

where *A* and *B* are arbitrary constants.

The boundary condition at $R = 0$ (see (D.11)) implies that $A = 0$. The boundary condition at $R = R_d$ leads to the following equation:

$$\frac{B}{R_d}(\lambda\cos\lambda + h_0\sin\lambda) = 0. \quad \text{(D.18)}$$

*B* in this equation is not equal to zero as we do not consider the trivial solution $v = 0$. Hence, Eq. (D.18) can be re-written as:

$$\tan\lambda = -\frac{\lambda}{h_0}. \quad \text{(D.19)}$$

As in the case $p < 0$ we disregard the solutions to this equation corresponding to zero and negative $\lambda$. A countable set of positive solutions to this equation (positive eigenvalues) $\lambda_n$ are arranged in ascending order:

$$0 < \lambda_1 < \lambda_2 < \lambda_3 < \ldots..$$

The corresponding eigen function can be presented as:

$$v_n(R) = \sin\left(\lambda_n\frac{R}{R_d}\right), \quad \text{(D.20)}$$

where the normalisation leading to $B = 1$ has been chosen as in the case $p < 0$.

The direct calculation of the integrals, taking into account Condition (D.19), leads to the following expression for the norm of $v_n$ for $n \geq 1$:

$$\|v_n\|^2 = \int_0^{R_d} v_n^2(R)d = \frac{R_d}{2}\left[1 + \frac{\mathrm{h_0}}{h_0^2 - \lambda_0^2}\right]. \quad \text{(D.21)}$$

The norm (D.21) differs from the norm chosen in Sazhin et al (2004) by the factor Rd (see their Eq. (A4)). This does not affect the final solution.

*Orthogonality of the eigen functions*

The orthogonality of functions of $v_n$ $(n \geq 1)$ was shown in Sazhin et al (2004). To show that functions $v_0$ and $v_n$ $(n \geq 1)$ are orthogonal, we need to calculate the following integral:

$$I = \int_0^{R_d} \sinh\left(\lambda_0\frac{R}{R_d}\right)\sin\left(\lambda_n\frac{R}{R_d}\right)\mathrm{d}R, \quad \text{(D.22)}$$

where $n \geq 1$.

Using integration by parts twice when calculating the integral on the right hand side of Eq. (D.22) can be rearranged to:

$$I = -\frac{R_d}{\lambda_n}\left[\sinh\lambda_0 \cos\lambda_n - \frac{\lambda_0}{\lambda_n}\cosh\lambda_0 \sin\lambda_n + \frac{\lambda_0^2}{\lambda_n R_d} I\right], \tag{D.23}$$

where *I* in the right hand side of this equation is the same as in (D.22).

Eq. (D.23) can be rearranged to:

$$I = -\frac{\frac{R_d}{\lambda_n}\left[\frac{\sinh\lambda_0}{\cosh\lambda_0} - \frac{\lambda_0 \sin\lambda_n}{\lambda_n \cos\lambda_n}\right]\cosh\lambda_0 \cos\lambda_n}{1+\left(\frac{\lambda_0}{\lambda_n}\right)^2}. \tag{D.24}$$

Remembering Eqs. (D.14) and (D.18), we can see that *I* defined by Eq. (D.24) is equal to zero. This implies that functions $v_n$ are orthogonal for $n \geq 0$ and we can write:

$$\int_0^{R_d} v_n(R) v_m(R) \mathrm{d}R = \delta_{nm} \|v_n\|^2, \tag{D.25}$$

where $n \geq 0$ and $m \geq 0$, $\|v_n\|^2$ is defined by (D.16) when $n = 0$ and (D.21) when $n \geq 1$.

*Expansion of R in a Fourier series with respect to functions $v_n$*

Before using Eq. (D.9) for the solution of Eq. (D.6) the presentation of *R* as a Fourier series with respect to functions $v_n$ should be presented:

$$R = \sum_{n=0}^{\infty} \mathrm{Q}_n v_n(R) \ , \tag{D.26}$$

where

$$Q_n = \frac{1}{\|v_n\|^2}\int_0^{R_d} R v_n(R)\, \mathrm{d}R, \tag{D.27}$$

Direct calculation of the integrals in the right hand side of (D.27) leads to the following explicit expressions for $Q_n$:

$$Q_n = \begin{cases} -\frac{1}{\|v_0\|^2}\left(\frac{R_d}{\lambda_0}\right)^2 (1+h_0)\sinh\lambda_0 & when \ \ n = 0 \\ \frac{1}{\|v_n\|^2}\left(\frac{R_d}{\lambda_n}\right)^2 (1+h_0)\sin\lambda_n & when \ \ n \geq 1 \end{cases} \tag{D.28}$$

*Calculation of coefficients $\Theta_n$(t) in Eq. (D.9)*

Having substituted Expressions (D.9) and (D.26) into Eq. (D.6), the latter equation can be rewritten in the form:

$$\sum_{n=0}^{\infty} \Theta_n'(t) v_n(R) = D_l \sum_{n=0}^{\infty} \Theta_n(t) v_n''(R) - \epsilon'(t) \sum_{n=0}^{\infty} \mathrm{Q}_n v_n(R)\,, \tag{D.29}$$

where

$$\Theta_n' = \frac{\mathrm{d}\Theta_n}{\mathrm{d}t};\ v_n''(R) = \frac{\mathrm{d}^2 v_n}{\mathrm{d}R^2};\ \epsilon'(t) = \frac{\mathrm{d}\epsilon}{\mathrm{d}t} \equiv \epsilon'$$

Since the expansion in the series with respect to $v_n$ (Fourier series) is unique, Eq. (D.29) is satisfied only when it is satisfied for each term in this expansion. Remembering that:

$$v_0'' = \left(\frac{\lambda_0}{R_d}\right)^2 v_0 \text{ and } v_n'' = \left(\frac{\lambda_n}{R_d}\right)^2 v_n \ (n \geq 1),$$

It can be seen that this implies that:

$$\Theta_0'(t) = D_l \left(\frac{\lambda_0}{R_d}\right)^2 \Theta_0(t) - \epsilon' Q_0, \tag{D.30}$$

$$\Theta_n'(t) = -D_l \left(\frac{\lambda_n}{R_d}\right)^2 \Theta_n(t) - \epsilon' Q_n, \tag{D.31}$$

when $n \geq 1$.

Eqs. (D.30) and (D.31) need to be solved subject to the initial conditions for $\Theta_n(t)$ $(n \geq 1)$. To find these initial conditions we substitute (D.9) into the initial condition (D.8) and expand $RY_{li0}(R)$ into a Fourier series with respect to $v_n$. Remembering that the expansion with respect to $v_n$ is unique, this leads to the following equation for $\Theta_n(0)$:

$$\Theta_n(0) = q_{in} - \epsilon(0) Q_n, \tag{D.32}$$

where $Q_n$ is defined by (D.27),

$$q_{in} = \frac{1}{\|v_n\|^2} \int_0^{R_d} RY_{li0}(R) v_n(R) \mathrm{d}R \ , \tag{D.33}$$

$n \geq 0$.

The solutions to Eqs. (D.30) and (D.31) subject to the initial condition (D.32) can be presented in the form:

$$\Theta_0(t) = \exp\left[D_l \left(\frac{\lambda_0}{R_d}\right)^2 t\right] [q_{i0} - \epsilon(0) Q_0]$$
$$- Q_0 \int_0^t \frac{\mathrm{d}\epsilon(\tau)}{\mathrm{d}\tau} \exp\left[D_l \left(\frac{\lambda_0}{R_d}\right)^2 (t - \tau)\right] \mathrm{d}\tau \ , \tag{D.34}$$

where $n = 0$,

$$\Theta_n(t) = \exp\left[- D_l \left(\frac{\lambda_n}{R_d}\right)^2 t\right] [q_{in} - \epsilon(0) Q_n]$$
$$- Q_n \int_0^t \frac{\mathrm{d}\epsilon(\tau)}{\mathrm{d}\tau} \exp\left[-D_l \left(\frac{\lambda_n}{R_d}\right)^2 (t - \tau)\right] \mathrm{d}\tau, \tag{D.35}$$

where $n \geq 1$.

*The final solution*

Having substituted (D.15), (D.20), (D.34) and (D.35), into (D.9), we can present the final solution to Eq. (4.4), satisfying boundary condition (4.5) and the corresponding initial condition in the form:

$$Y_{li} = \epsilon_i + \frac{1}{R}\left\{\left[\exp\left[D_l\left(\frac{\lambda_0}{R_d}\right)^2 t\right][q_{i0} - \epsilon_i(0)Q_0] - Q_0\int_0^t \frac{d\epsilon_i(\tau)}{d\tau}\exp\left[D_l\left(\frac{\lambda_0}{R_d}\right)^2(t-\tau)\right]d\tau\right]\sinh\left(\lambda_0\frac{R}{R_d}\right) + \sum_{n=1}^{\infty}\left[\exp\left[-D_l\left(\frac{\lambda_n}{R_d}\right)^2 t\right][q_{in} - \epsilon_i(0)Q_n] - Q_n\int_0^t \frac{\mathrm{d}\epsilon_i(\tau)}{\mathrm{d}\tau}\exp\left[-D_l\left(\frac{\lambda_n}{R_d}\right)^2(t-\tau)\right]d\tau\right]\sin\left(\lambda_n\frac{R}{R_d}\right)\right\}, \quad \text{(D.36)}$$

where $Q_n$, $q_{in}, \lambda_0$ and $\lambda_n$ $(n \geq 1)$ are defined by Eqs. (D.28), (D.33), (D.14) and (D.19) respectively; the subscript *i* at $\epsilon$ has been restored.

Note that Expression (D.36) contains the term which exponentially increases with time. This, however, will not lead to an unphysical solution to Eq. (4.4), since this equation is valid only for $0 \leq Y_{li} \leq 1$. Once $Y_{li}$ reaches one of its limiting values it will remain equal to this value.

If the Solution (D.36) is applied to individual short timesteps, the time dependence of $\frac{d\epsilon_i(\tau)}{d\tau}$ during this timestep can be ignored and it can be assumed that:

$$\frac{d\epsilon_i(\tau)}{d\tau} = \left.\frac{d\epsilon_i(\tau)}{d\tau}\right|_{t=0} \equiv \epsilon_i'.$$

This allows the simplification of Expression (D.36) to:

$$Y_{li} = \epsilon_i + \frac{1}{R}\left\{\left[\exp\left[D_l\left(\frac{\lambda_0}{R_d}\right)^2 t\right]\left[q_{i0} - Q_0\left(\epsilon_i(0) + \frac{R_d^2}{D_l\lambda_0^2}\epsilon_i'\right)\right] + Q_0\frac{R_d^2}{D_l\lambda_0^2}\epsilon_i'\right]\sinh\left(\lambda_0\frac{R}{R_d}\right) + \sum_{n=1}^{\infty}\left[\exp\left[-D_l\left(\frac{\lambda_n}{R_d}\right)^2 t\right]\left[q_{in} - Q_n(\epsilon_i(0))\right] - Q_n\frac{R_d^2}{D_l\lambda_n^2}\epsilon_i'\right]\sin\left(\lambda_n\frac{R}{R_d}\right)\right\}. \quad \text{(D.37)}$$

If we ignore the time dependence of $\epsilon_i$ then Expression (D.37) can be simplified to:

$$Y_{li} = \epsilon_i + \frac{1}{R}\left\{\left[\exp\left[D_l\left(\frac{\lambda_0}{R_d}\right)^2 t\right][q_{i0} - Q_0\epsilon_i]\right]\sinh\left(\lambda_0\frac{R}{R_d}\right) + \sum_{n=1}^{\infty}\left[\exp\left[-D_l\left(\frac{\lambda_n}{R_d}\right)^2 t\right][q_{in} - Q_n\epsilon_i]\right]\sin\left(\lambda_n\frac{R}{R_d}\right)\right\}. \quad \text{(D.38)}$$

The assumption that the time dependence of $\epsilon_i$ can be ignored during the timestep will be used in my analysis. This allows us to build our calculations on Eq. (D.38)

## Appendix E. Activity coefficients for the ethanol–acetone mixtures

The activity coefficient ($\gamma_i$) for any liquid mixture is related to the excess of Gibbs free energy per unit mole ($G^E$) by the following formula (Atkins and de Paula , 2002):

$$\ln \gamma_i = \frac{1}{R_u T} \frac{\partial (n_{l,total} G^E)}{\partial n_{li}}, \tag{E.1}$$

where $R_u$ is the universal gas constant, $T$ is temperature in K, $n_{l,total} = \sum_i n_{li}$; $n_{li}$ is the molar concentration of the $i^{\text{th}}$ component in the liquid phase.

$$n_{l,total} G^E = R_u T \frac{n_{l1} n_{l2}}{n_{l1}+n_{l2}} \left[ \frac{\alpha n_{l2}}{n_{l1}+n_{l2}} + \frac{\beta n_{l1}}{n_{l1}+n_{l2}} - \frac{\delta n_{l1} n_{l2}}{(n_{l1}+n_{l2})^2} \right], \tag{E.2}$$

where $\alpha = \frac{546.3}{T} - 0.9897$, $\beta = \frac{543.3}{T} - 0.9483$, $\delta = \frac{15.63}{T} + 0.0759$.

Having substituted (E.2) into (E.1) the following expressions for $\gamma_1 = \gamma_{eth}$ and $\gamma_2 = \gamma_{ac}$ are obtained:

$$\left.\begin{array}{l} \gamma_1 = \exp\left[X_{l2}^2 \left[\alpha + 2(\beta - \alpha - \delta) X_{l1} + 3\delta X_{l1}^2\right]\right] \\ \gamma_2 = \exp\left[X_{l1}^2 \left[\beta + 2(\alpha - \beta - \delta) X_{l2} + 3\delta X_{l2}^2\right]\right] \end{array}\right\}. \tag{E.3}$$

Expressions (E.3) were used in Eq. (4.10).

## Appendix F. Approximations of the measured droplet velocities in Chapter 4

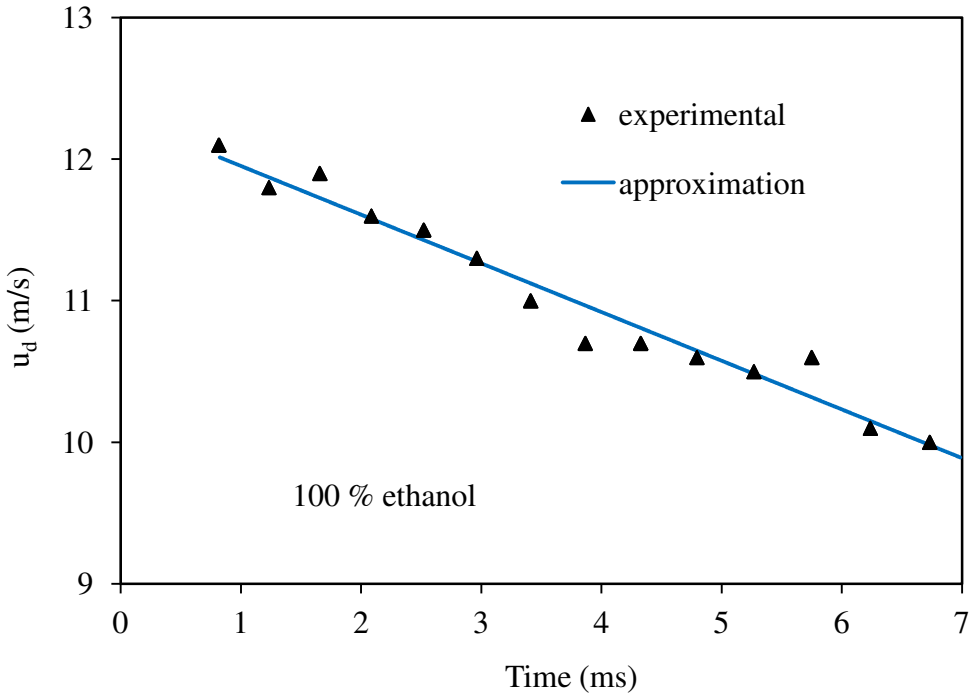


Fig. F1 The same as Fig. 4.1 but for pure ethanol droplets.

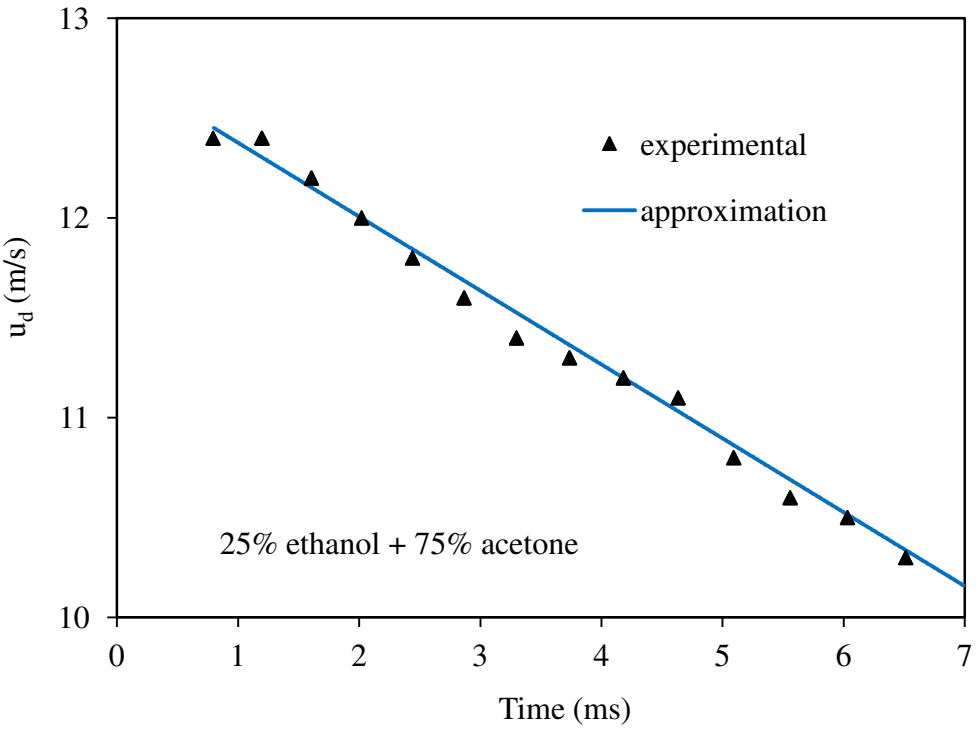


Fig. F2 The same as Figs. 4.1 and F1 but for 25% ethanol-75% acetone mixture droplets.

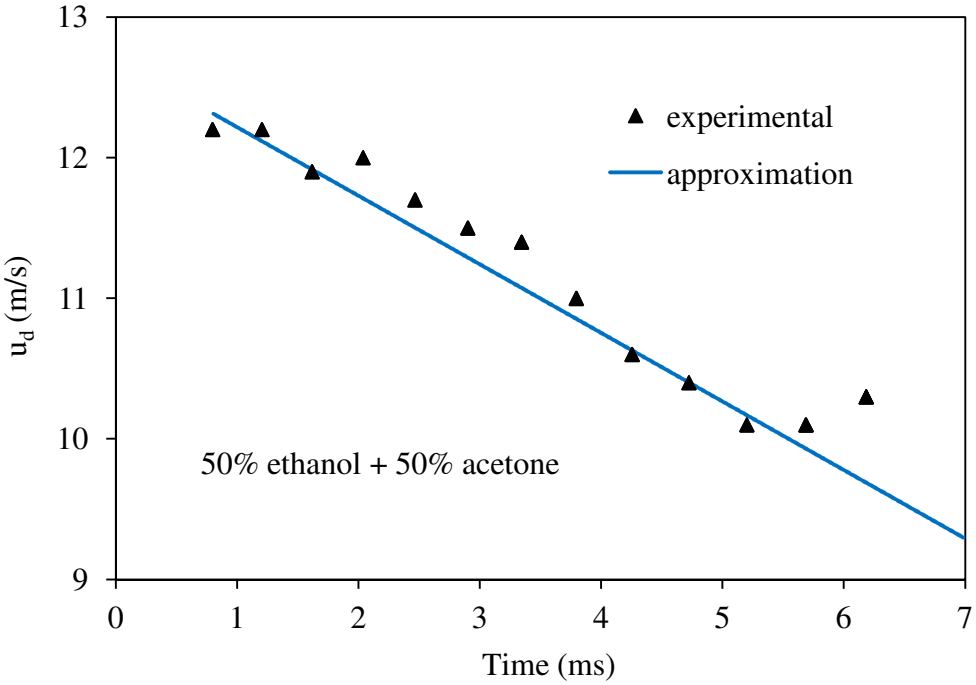


Fig. F3 The same as Fig. F2 but for 50% ethanol-50% acetone mixture droplets.

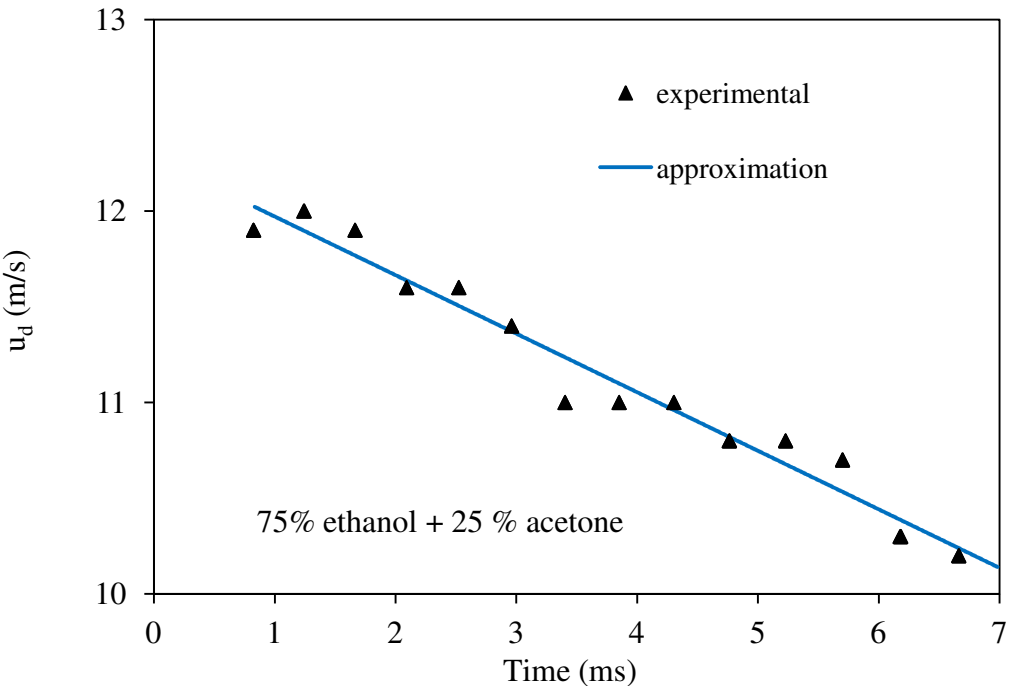


Fig. F4 The same as Figs. F2 and F3 but for 75% ethanol-25% acetone mixture droplets.

**Appendix G. Sensitivity study of n-dodecane properties used in Chapter 6**

The properties of n-dodecane used in calculations of Chapter 6 are the same as reproduced by Sazhin et al (2005b). A sensitivity study based on the temperature dependence of n-dodecane properties is to be shown in this Appendix. The comparison is based on the properties presented in Appendix B and used in Chapter 3 (used by Deprédurand, 2009), the approximations of the properties that we got from NIST website (National Institute of Standards and Technology) http://webbook.nist.gov/chemistry/name-ser.html and the properties used by Sazhin et al (2005b).

The liquid density of is approximated as Sazhin et al (2005b) (kg/m$^3$):

$$\rho = 1104.98 + T\left(-1.9277 + T(0.003411 - 3.2851 \times 10^{-6}T)\right). \quad \text{(G.1)}$$

The approximation of the liquid density reproduced from NIST website is:

$$\rho = -4.334713357484130 \times 10^{-6} \times T^3 + 4.759233595856190 \times 10^{-3} \times T^2 - 2.488051596744170 \times T + 1.180345044278340 \times 10^3. \quad \text{(G.2)}$$

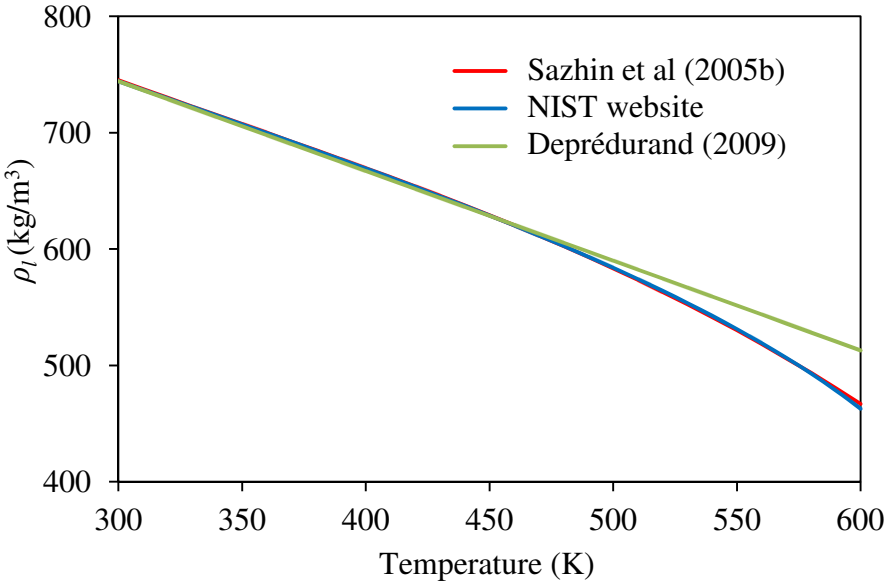


Fig. G1 The plots of liquid density ($\rho_l$) of n-dodecane from different sources (indicated in the curve) versus temperature.

The heat capacity of liquid n-dodecane is approximated as (Sazhin et al, 2005b) (J/(kg.K)):

$$c_l = 803.42 + T\big(5.076 + T(-0.0022124 + 0.000001673T)\big)\,. \qquad \text{(G.3)}$$

The polynomial approximation of the heat capacity of liquid n-dodecane as reproduced from NIST website:

$$c_l = 1.48202380136249 \times 10^{-7} \times T^4 - 2.52261390358263 \times 10^{-4} \times T^3 + 0.160796521364528 \times T^2 - 41.4034976491586 \times T + 5785.5370245135\,. \qquad \text{(G.4)}$$

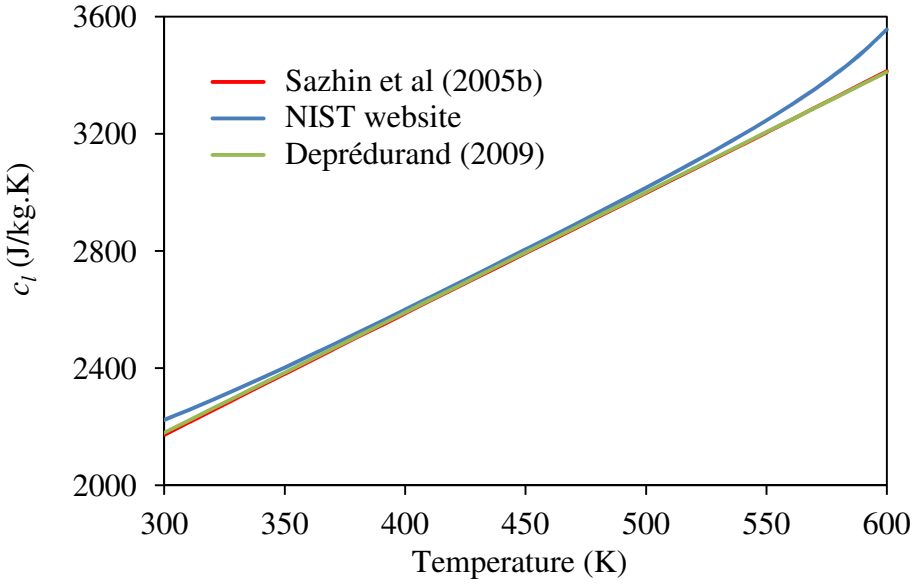


Fig. G2 the same as Fig. G1 but for liquid specific heat, $c_l$.

The liquid viscosity of n-dodecane used is (Sazhin et al, 2005b) (Pa.s):

$$\mu = 10^{-6} \times \rho \times (\exp(\exp(15.1 - 2.6 \times \ln T)) - 1.07). \quad \text{(G.5)}$$

The approximation of the liquid viscosity reproduced from NIST website:

$$\mu = 1.406649218688310 \times 10^{-17} \times T^6 - 4.08104594410045 \times 10^{-14} \times T^5 + 4.91879227224549 \times 10^{-11} \times T^4 - 3.15596557014197 \times 10^{-8} \times T^3 + 1.13885766634288 \times 10^{-5} \times T^2 - 2.19828783711901 \times 10^{-3} \times T + 0.178428752661574. \quad \text{(G.6)}$$

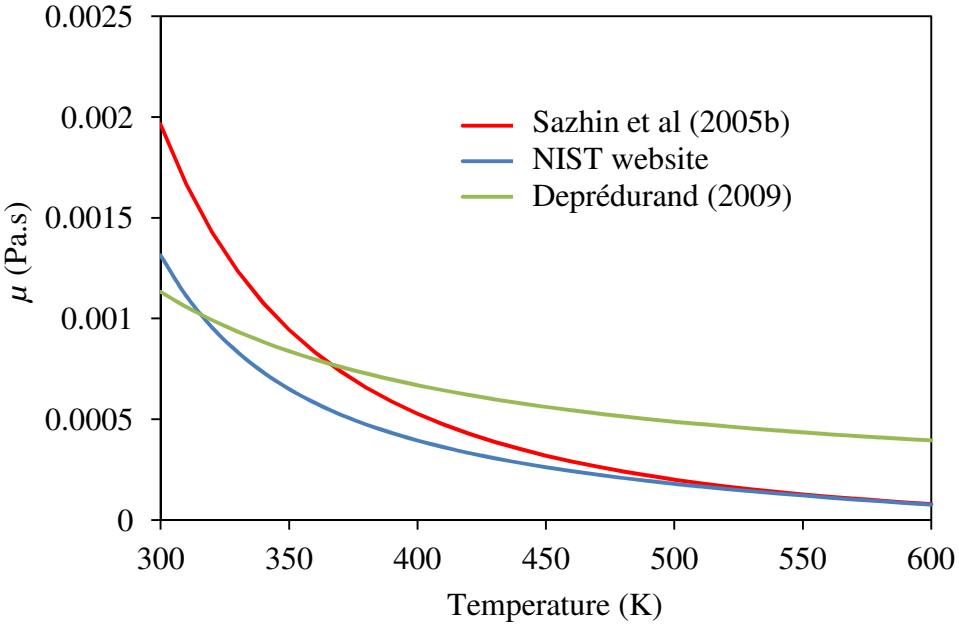


Fig. G3 The same as Figs. G1 and G2 but for liquid viscosity, $\mu$.

The liquid thermal conductivity of n-dodecane as used by Sazhin et al (2005b) was fitted by the following equation:

$$k_l = -4.9946 \times 10^{-10} \times T^3 + 5.3841 \times 10^{-7} \times T^2 - 4.16075 \times 10^{-4} \times T + 0.22924116. \quad \text{(G.7)}$$

The approximation of the thermal conductivity of n-dodecane reproduced from NIST website

$$k_l = 8.13209121245732 \times 10^{-8} \times T^2 - 0.000273057208008894 \times T + 0.209151530311457\ . \quad \text{(G.8)}$$

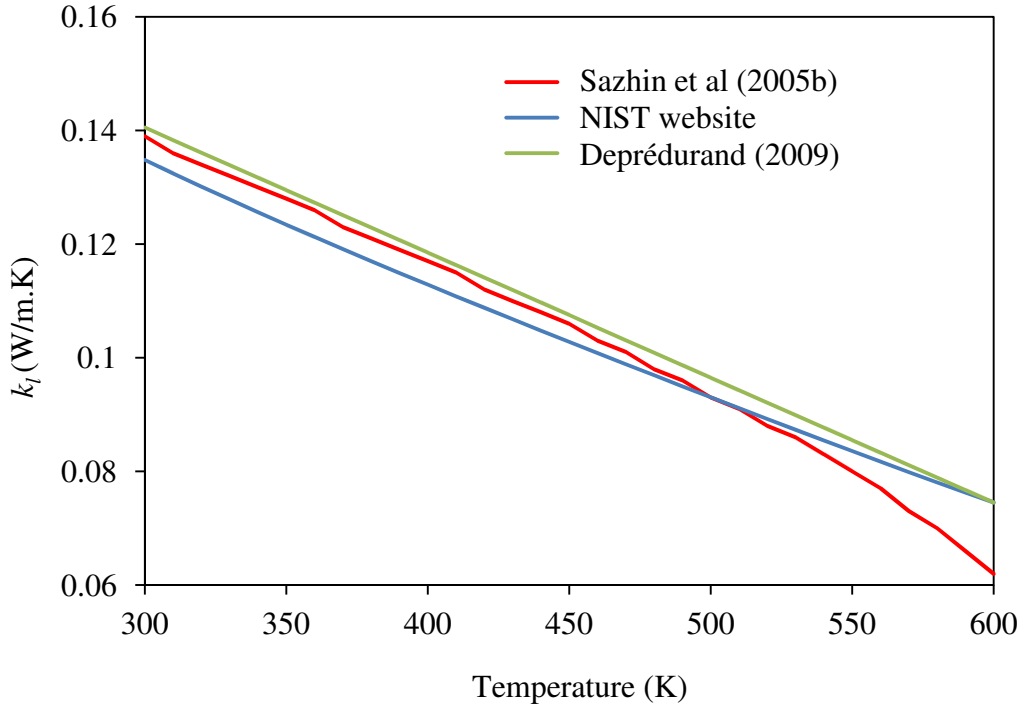


Fig. G4 The same as Figs. G1-G3 but for liquid thermal conductivity, $k_l$.